Advanced Optical Metrology

Geoscience | Corrosion | Particles | Additive Manufacturing: Metallurgy, Cut Analysis & Porosity

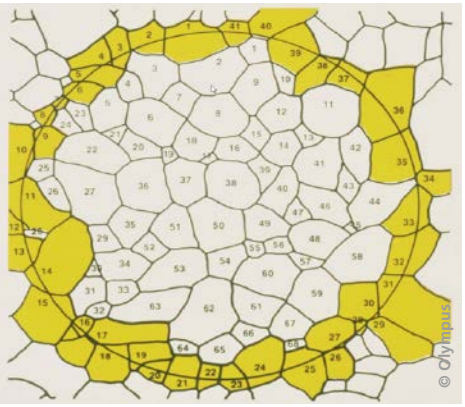

EVIDENT™
OLYMPUS

WILEY

Contents

Imprint

© Wiley-VCH GmbH
Boschstr. 12,
69469 Weinheim, Germany
Email: info@wiley-vch.de
Editor-in-Chief: Dr. Christina Poggel

Dear reader,

Optical metrology is the science of measuring the properties of objects and materials using optical techniques, such as light intensity, wavelength, and polarization. It is used in a wide range of fields, from metallurgy and corrosion science to particles and geosciences. As the world becomes increasingly reliant on optical and electronic devices, the need for accurate and precise optical metrology will only grow.

Optical metrology techniques are based on the interaction of light with the object or material being measured. This interaction can be used to measure a broad range of properties, such as shape, size, refractive index, and chemical composition. Additionally, optical metrology can be used to measure the optical properties of materials, such as absorption and scattering coefficients. There are a variety of devices that can be used including interferometers, spectrophotometers, and microscopes. A variety of software packages exist that can be used to process and analyze the data collected.

Optical metrology is a rapidly growing field, with new applications being developed all the time. Some of the most promising applications are in 3D printing, where optical metrology can be used to control the printing process and ensure that the finished product meets the required specifications. Some future applications of optical metrology include measuring the thickness of thin films, characterizing nanoparticles, and measuring the 3D shape of objects.

With this in mind, the long-lasting partnership between Evident and Wiley Analytical Science brings you the assembly of a second compendium with six eBooks that highlights the most advanced and leading research in the fields of geosciences, corrosion, particles, and additive manufacturing. In more than 20 article digests, you can find the most recent methods of imaging particles and other trending research, such as the use of nanoparticles for light storage, the corrosion behavior of steel, and many more.

Advanced Optical Metrology is a project that is designed to help improve communication between fundamental research and industrial applications. This project involves collecting and organizing existing information on the topic to make it more accessible and useful for both researchers and practitioners. The project is constantly expanding the online platform with a variety of resources, including a searchable database of optical metrology papers, a repository of teaching materials, and even instructions on how to publish scientific achievements.

If you would like to contribute to the platform, or have any ideas and suggestions, please feel free to contact us at website@advancedopticalmetrology.com.

Yours sincerely,
Dr. Cecilia Kruszynski
Technical Editor of Wiley Analytical Science

Advanced Optical Metrology

Part IV

Geoscience

Geoscience

Geoscience is the scientific study of the Earth — more precisely, the study of the materials, structures, evolution, and dynamics of the Earth, including its organisms, natural minerals, and energy resources. Geoscientists routinely investigate the composition and molecular structure of soils, rocks, sediments, minerals, and other geological samples. Geoscientists employ many analytical techniques to characterize these materials and samples — among them X-ray analytical techniques such as X-ray fluorescence (XRF) and X-ray diffractometry (XRD) [1,2].

XRF is the most frequently used analysis technique for determining the elemental composition of rock, sediment, and other earth material samples [3]. In XRF, the sample is bombarded with a high-energy X-ray beam, leading to the ionization of its component atoms and the dislodgment of an inner-shell electron. The resulting electron-hole in the inner shell is then filled by an outer-shell electron accompanied by the release of energy in the form of a photon. The emitted radiation has a lower energy than the absorbed radiation and is termed 'fluorescence'. The energy of the emitted radiation reflects the energy difference between the two shells involved. As these transitions occur at discrete energies unique to a specific element and its local environment, the emitted characteristic fluorescence can be used to determine the elements in a sample and after calibration, its concentration. Thus, XRF analysis can determine the elemental/chemical composition of a sample but fails to differentiate between the different compounds present in the sample.

Like XRF, XRD measures the response of X-rays interacting with a sample to identify substances. XRD leverages the fact that crystalline materials (e.g., minerals) exhibit a certain degree of periodicity in their structural arrangement [4]. When a monochromatic X-ray beam irradiates a crystalline sample, the X-rays collide with the sample's electrons, leading to constructive interference (i.e., diffraction) as long as the Bragg's Law ($n\lambda = 2d \sin\theta$) is satisfied. The law relates the wavelength of the incident beam to the diffraction angle and the distance between the lattice planes of the atoms arranged in the crystalline sample. Each material produces a unique diffraction pattern by which it can be identified. Such diffraction patterns can be compared and matched with those of known structures (e.g., various minerals) maintained in the International Center for Diffraction Data (ICDD) database. In contrast to XRF, XRD identifies and quantifies crystalline compounds or phases in a sample and determines its degree of crystallinity and amorphous content. Thus, the methods are complementary to each other. For example, XRF could measure the total concentration of a specific element (e.g., Ca) in a given geological sample, while XRD could determine and differentiate between the compounds in which this element exists (e.g., CaO vs. $CaCO_3$).

Both techniques have been widely applied in different fields of geoscience for decades, with portable versions of XRF and XRD (pXRF and pXRD, respectively) allowing for fast in situ screenings and analyses [5].

This introduction will briefly describe the advances in pXRF and pXRD, the implication of both methods for geoscience, and their application in soil and rock analysis. The following digest articles will focus on the application of pXRF in geological settings.

1. ADVANCES IN PXRF AND PXRD AND THEIR IMPLICATIONS FOR GEOSCIENCE

With advancements in hardware and software technologies (i.e., X-ray tubes, detectors, and processors), pXRF and pXRD devices have become important qualitative and quantitative characterization tools for analyzing geological materials.

Early pXRF spectrometers usually comprised radioactive isotopes as their excitation source and Si-PIN diode detectors, but in later generations, the radioactive isotope sources and PIN diode detectors were replaced by small X-ray tubes and silicon drift detectors, respectively [3,7]. Several generations of improvement have led to the current standard for pXRF, featuring relatively low detection limits, high sensitivity, low background noise, high temperature stability, high resolution at high count rates, and fast processing times. Portable XRF devices have many advantages over traditional lab-based techniques, including, of course, portability, allowing for *in situ* data collection; little to no sample preparation, facilitating the scanning process; wide dynamic range and multi-element capability, enabling accurate and precise quantification of many elements; and speed, allowing for fast decision-making on site. Moreover, pXRF is a non-destructive technique, allowing for multiple measurements of the same sample and the use of analyzed samples for future use. Using a pXRF device, geoscientists can quickly cover large study areas, increasing the sampling density and advancing decision-making. Modern pXRF devices have integrated GPS receivers that are used to georeference the collected data, enabling rapid spatial visualization using a geographic information system (https://www.olympus-ims.com/en/handheld-xrf-for-soil-surveys-geochemistry-of-rock-outcrops-soils-and-sediments/).

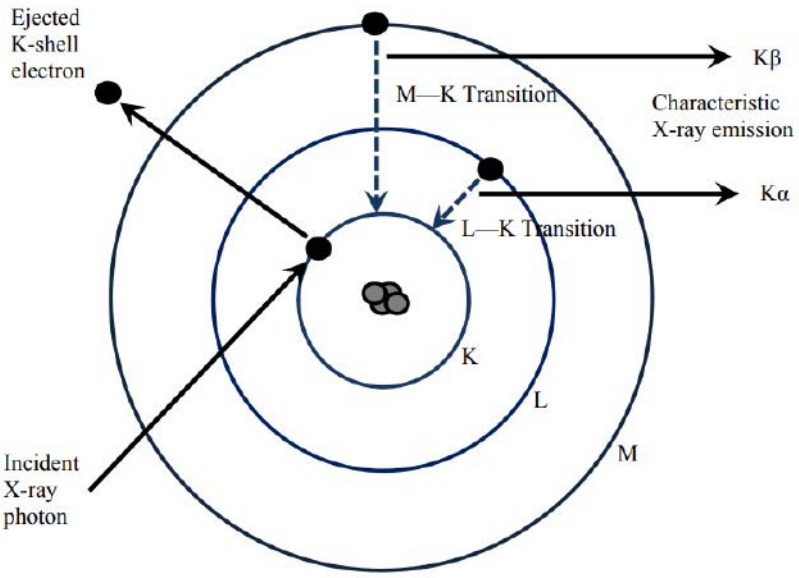

Figure 1: Fundamental principles of XRF. When an electron void in the K shell is filled by an electron from the L or M shell, the emitted photon is termed Kα or Kβ, respectively. The figure is taken from reference [6].

Due to these beneficial properties, pXRF devices are widely used in geoscience. Besides the scientific and experimental benefits, pXRF is a highly cost-effective technique; according to an ASX-listed explorer, a saving of $2.75 million over a three-year period was achieved by employing pXRF devices for testing 100,000 samples instead of costly lab-based techniques (https://www.olympus-ims.com/en/handheld-xrf-for-soil-surveys-geochemistry-of-rock-outcrops-soils-and-sediments/). Likewise, the First Mining Finance Corporation used pXRF devices for assessing soil geochemistry within their Sonora projects (Mexico); the estimated costs were approximately 3–5 times less than those of traditional wet chemistry analysis at commercial labs (https://www.olympus-ims.com/en/customer-case-study-soil-geochemistry-by-pxrf-at-the-sonora-project-mexico/).

The digest article "Portable X-ray fluorescence spectrometry analysis of soils" reviews further advantages and disadvantages of pXRF and provides helpful, practical tips and recommendations for its application in the geoscientific field. The remaining digest articles in this eBook demonstrate the high quality of pXRF data obtained from geo-

scientificl samples, which are comparable to those of traditional analytical techniques.

Like pXRF, pXRD has benefited from technological advances, especially from the automation of data processing and the use of vibrating sample holders and CCD-based cameras. Portable XRD devices now offer fast, accurate, and cost-effective analysis of geological samples [5]. Although pXRD devices are larger and heavier than handheld pXRF devices, they can be operated in the field. The ability to identify minerals in situ by pXRD promotes more accurate geological logging and provides valuable insights into geological systems. In contrast to pXRF, pXRD is generally limited to crystalline materials and is thus primarily used for the characterization and identification of crystalline materials in soils and sediments. Nonetheless, it is a commonly used and proven technique to identify and quantify the mineralogical composition of raw materials [8]. However, geoscientists have concluded that pXRD data alone is insufficient for soil mineral identification and thus should be combined with other techniques [9].

2. APPLICATION OF PXRF AND PXRD IN SOIL AND ROCK ANALYSIS

Given the importance of the elemental composition of soils and rocks, the application of pXRF is rapidly expanding in soil and rock analysis. The obtained elemental data can be used to predict soil and rock physical and chemical properties, such as salinity, pH, and cation-exchange capability [3]. Gazley *et al.* [10] presented a rapid and robust pXRF-based workflow to aid exploration in a regolith-dominated terrane. The authors obtained a large dataset from the Western Mount Isa Inlier, Queensland, Australia, including data from soil, rock, and rotary air blast samples. Portable XRF data obtained from the soil samples were comparable to laboratory data for most elements (Cu and Zn within 2% of laboratory data; Mn, Rb, and Sr within 8% of laboratory data; and Fe, Al, K, and Ca within 25% of laboratory data). However, the Pb content in the soil estimated by pXRF was 77% less than that estimated by the laboratory. This underestimation was due to an erroneous Pb concentration reported by the pXRF device because of energy peaks overlap between Fe (pile up) and Pb. The rotary air blast dataset showed a similar trend to the soil dataset (Pb overestimated by 69%), and the rock dataset, which was uncorrected, correlated unexpectedly well with the laboratory data for many elements. Thus, the authors concluded that the use of pXRF enables dynamic exploration campaigns in regolith-dominated terranes at a relatively low cost, with decision-making being possible while the drill rig is still in the study area.

Ahmed *et al.* [11] used pXRF to evaluate the ore-forming potential of intrusive rocks in different porphyry Cu environments by assessing their Sr/Y and Sr/MnO contents, which are effective discriminators between ore-forming and unprospective intrusions. For this purpose, pXRF data were collected from pulp powders and rock slabs from six porphyry Cu districts. Calibrated pXRF data obtained from pulp powders correlated very well with those of conventional methods (within 16%). In contrast, pXRF data obtained from rock slabs correlated less well with those of conventional methods (within 37%). This discrepancy in the data between the samples was due to homogeneity differences (in terms of grain size and mineralogy) between pulp powder and rock slabs. Nevertheless, pXRF represents a rapid and cost-effective alternative to traditional methods for collecting Sr, Mn, and Y data to determine the ore-forming potential of intrusions.

Portable XRF can also be applied in geological oceanography to study the geological history of the ocean floor. Ivanova *et al.* [12] used pXRF, in combination with other techniques, to analyze the sediment cores from the summit and the northeastern slope of the Ioffe Drift, which is located in the Antarctic Bottom Water pathway. The study was conducted to identify hiatuses in the contourite records, determine their duration, and refine the stratigraphy of the upper sediment cover overlaying the Ioffe Drift area. The Ca/Ti and Ca/Al ratios were determined by pXRF as they represent biogenic/terrigenous material ratios, reflecting the changes in terrigenous sediment contribution. Abrupt changes in the XRF data were used to infer potential long- and short-term hiatus/erosional events over the last ~ 3 million years. The authors demonstrated that continuous pXRF scanning, in combination with other techniques, is an excellent approach to identifying hiatuses, even short-lived ones.

Portable XRD is particularly useful for on-site mineralogical analysis and geological exploration. For example, in the Indika project, pXRD was used for testing critical mineral identification in two study areas in northern Finland [13]. Using pXRD, the authors successfully detected common rock-forming minerals, such

as albite, amphiboles, muscovite, and quartz, and indicator minerals for both study areas in till and weathered bedrock samples. However, as mentioned before, the authors also noted that the pXRD data alone was not reliable enough without employing complementary methods. Another study demonstrated that pXRD could be applied to identify hydrothermally modified mineral fissures, which can be used to track the formation conditions for ore deposits and other geothermal systems [14].

Besides being largely used individually, pXRF and pXRD were also combined to investigate a large set of complex geological samples [15]. Coupled pXRF-pXRD analysis delivered both elemental (XRF) and mineralogical (XRD) information of high quality, making it a promising method for the exploration of lithologies, hydrothermal alterations, and ores.

REFERENCES:

[1] *T. D. T. Oyedotun, Geol Ecol. Landsc. 2018, 2, 148.*

[2] *B. Lavina, P. Dera, R. T. Downs, Rev. Mineral. Geochem. 2014, 78, 1.*

[3] *D. C. Weindorf, N. Bakr, Y. Zhu, Adv. Agron. 2014, 128, 1.*

[4] *D. M. Moore, R. C. Reynolds Jr., in X-Ray diffraction and the identification and analysis of clay minerals, Oxford University Press, New York, 1997.*

[5] *B. Lamiere, Y. A. Uvarova, Geochem. Explor. Env. A. 2020, 20, 205.*

[6] *D. J. Kalnicky, R. Singhvi, J. Hazard. Mat. 2001, 83, 93.*

[7] *D. C. Weindorf, S. Chakraborty, Soil Sci. Soc. Am. J. 2020, 84, 1384.*

[8] *P. S. Nayak, B. K. Singh, Bull. Mater. Sci. 2007, 30, 235.*

[9] *V. Singh, H. M. Agrawal, Radiat. Phys. Chem. 2012, 81, 1796.*

[10] *M. F. Gazley, L. C. Bonnett, L. A. Fisher, W. Salama, J. H. Price, Aus. J. Earth Sci. 2017, 64, 903.*

[11] *A. Ahmed, A. J. Crawford, C. Leslie, J. Phillips, T. Wells, A. Garay, S. B. Hood, D. R. Cooke, Geochem. Explor. Env. A. 2020, 20, 81.*

[12] *E. Ivanova, D. Borisov, O. Dmitrenko, I. Murdmaa, Mar. Pet. Geol. 2020, 111, 624.*

[13] *P. Sarala, H. Koskinen, Geologi 2018, 70, 58.*

[14] *D. A, Burkett, I. T. Graham, C. R. Ward, Canad. Mineral. 2015, 53, 429.*

[15] *Y. A. Uvarova, J. S. Cleverly, A. Baensch, M. Verrall, Coupled XRF and XRD analyses for efficient and rapid characterization of geological materials: Applications for the mineral exploration and mining industry, conference paper at the 21st General Meeting of the International Mineralogical Association (IMA), Johannesburg, 2014.*

01 Portable X-Ray Fluorescence Spectrometry Analysis of Soils

D. C. Weindorf and S. Chakraborty

ABSTRACT

Portable X-ray fluorescence (pXRF) spectrometry is a proximal sensing technique whereby low-power X-rays are used to make elemental determinations in soils. The technique is rapid, portable, and provides multi-elemental analysis with results generally comparable to traditional laboratory-based techniques. Elemental data from pXRF can then be either used directly for soil parameter assessment or as a proxy for predicting other soil parameters of interest via simple or multiple linear regression. Importantly, pXRF has some limitations that must be considered in the context of soil analysis. Notwithstanding those limitations, pXRF has proven effective in numerous agronomic, pedological, and environmental quality assessment applications.

RATIONALE FOR GENERAL PROCEDURE

The elemental composition of soil is one of its most fundamental chemical parameters, affecting its reaction, salinity, cation-exchange capacity (CEC), nutrient cycling, and pollutant transport. Early forays into soil chemical analysis relied on colorimetric wet chemistry methods such as titration or colorimetry [1]. In recent decades, these simplistic measurements gave way to methods offering greater accuracy and precision: atomic absorption spectrometry (AAS) and inductively coupled plasma atomic emission spectroscopy (ICP–AES). While the latter is the analytical standard for contemporary elemental analysis, both methods have some limitations; specifically, they require digestion of soil with caustic chemicals such as nitric or hydrochloric acids for partial digestion [2] or hydrofluoric acid for total digestion [3]. Therefore, these approaches require considerable time, energy, consumables, and laboratory-based equipment.

By contrast, X-ray fluorescence (XRF) was originally developed as a laboratory-based technique [4], but it has since been miniaturized into small, portable units capable of making quality elemental determinations in situ with minimal sample preprocessing. The energies of most X-rays reflect the core-electron-binding energies of atoms; thus, the atomic number strongly influences XRF effectiveness [5]. XRF describes the emission of fluorescent photons from a sample that has been irradiated by high-energy X-rays. As the emitted (fluorescent) secondary X-rays have discrete energies unique to a particular element and its local environment, X-ray absorption (or emission) can be used for elemental determination in soils. Using the rela-

tionship between emission wavelength and atomic number, specific elements can be identified and quantified in a sample [6].

Early portable XRF (pXRF) instruments often featured radioactive isotopes as their excitation sources (e.g., Cd^{109} or Fe^{55}) and featured Si-PIN diode detectors [6]. In later generations, these radioactive isotope sources were replaced by miniaturized tube-based X-ray sources, and Si-PIN diodes were replaced by silicon drift detectors, with the latter presenting tremendous advances in pXRF accuracy and precision. For purposes of discussion and methodology, all comments hereafter refer to experiences with an Olympus® DELTA™ Premium (DP-6000) pXRF configured with a 4 W Rh X-ray tube operated at 10–40 keV.

REVIEW OF EXISTING PROCEDURES: STRENGTHS, LIMITATIONS, INTERFERENCES

The use of pXRF for soil analysis offers many strengths relative to traditional laboratory-based methods but also some limitations. One of the greatest advantages of pXRF is its field portability as it is configured as a handheld meter that can be taken to the field for in situ soil analysis. Scanning time varies widely but is typically in the order of ~60 to 90 seconds. Longer scanning times (up to 300 seconds) increase the accuracy of elemental readings. Also, pXRF can be operated by rechargeable Li-ion batteries, thus requiring no conventional electrical power supply on-site. Portable XRF offers a wide dynamic range of elemental quantification from low mg kg^{-1} to high percentage levels, with no need for dilutions or restandardization. Lastly, pXRF analysis is multi-elemental, providing simultaneous analysis of ~20 elements. However, the detection limits of each element vary based on the atomic number and size of the electron cloud. Generally, elements with larger atomic numbers are measured more accurately than those with lower ones. For example, light elements such as P might have a limit of detection (LOD) of~ ±5000 mg kg^{-1}, whereas heavy elements such as U might have a LOD of ± 5 mg kg^{-1} (**Figure 1**).

Figure 1: Periodic table of elements showing LODs for Olympus X-ray fluorescence analyzers.

Figure 2: Hydraulic probe sampling tube with slot accommodating the aperture of a pXRF device for field scanning at fixed depths.

Despite numerous advantages, pXRF has several limitations. First, pXRF is variably affected by soil moisture. Literature points to a critical value of 20% moisture, a threshold above which drying or moisture correction should be considered. Weindorf et al. [7] noted that pXRF data quality was substantively reduced when evaluating frozen soils laden with ice relative to their dry counterparts.

Second, interelemental interferences are well documented. For example, As and Pb feature a shared spectral peak, making isolation and identification cumbersome [8]. Importantly, pXRF fails to distinguish elemental valence (e.g., Fe^{2+} vs. Fe^{3+}) and merely reports total elemental concentration. Portable XRF also cannot read light elements (e.g., $Z \leq 11$ Na). This is particularly limiting in soil analysis when the consideration of Na is important. However, some contemporary approaches have sought to overcome those limitations using other elemental data as proxies for the light elements of interest. In most pXRF instruments, the aperture through which X-rays are emitted and fluorescence is detected is relatively small (~2 cm). Applied to highly heterogeneous matrices in soils, results can vary dramatically over only a few lateral centimeters in a soil profile. Finally, pXRF lacks very low LODs (very low or high mg kg^{-1}) required for some investigations, where AAS or ICP–AES will remain the analytical standard for the foreseeable future.

INDIVIDUAL STEPS IN THE PREFERRED ANALYSIS, INCLUDING JUSTIFICATION

When conducting pXRF analysis of soil samples, several variables must be considered for optimal performance. First, the instrument must be properly standardized. The Olympus® DELTA™ pXRF features a calibration alloy clip (316 clip). Scanning the clip allows the instrument to lock into a standardized substance recognized by the integrated computer. Given the inherent heterogeneity in many soil samples, steps must be taken to ensure that pXRF scanning adequately reflects the composition of the soil being evaluated. When scanning in situ, the soil should be evaluated for concretions, nodules, or irregularities that may disproportionately affect pXRF performance; such areas should be avoided. The nose of the pXRF should be placed in direct contact with the soil, such that it makes good contact with a flat surface. In some instances, this may involve using a knife to gently scrape the soil to create a flat surface for scanning. To adequately capture variability within a given soil horizon, investigators should take multiple scans, physically repositioning the instrument between each scan to collect data on multiple points within a horizon. Excessive soil moisture (≥20%) denudes fluorescence received by the instrument [9]; thus, field evaluation of soil is best undertaken when soils are dry. In addition to scanning soil profiles, it can be convenient to scan soil cores collected with a hydraulic probe; the evaluation slot of the collection tube nicely accommodates the instrument's aperture (**Figure 2**). If field measurements are not essential, it may be preferable to scan soil samples ex situ after drying and grinding. Ex situ processing achieves two goals: reduction/elimination of soil moisture and sample homogenization. Scanning time is an important consideration as a longer scanning time produces optimized results. However, investigators must evaluate the need for reasonable sample throughput versus pXRF accuracy. Many soil evaluations typically use between 60 and 90 seconds for scanning [4]. A good practice for evaluating the quality of pXRF data is to scan the National Institute of Standards and Technology (NIST)-certified reference soil standards. A recovery percentage (pXRF determined/NIST-certified value) can then be calculated and reported with the pXRF data collected. Notably, pXRF tends to over- or underreport some elements, but many elements achieve results within 10% of NIST-certified values.

Figure 3: Hands-free pXRF operation using a hooded sample stage for special applications (left) and a bipod stand (right).

Although most instruments operate at low power (10–40 KeV), the operator must undergo proper radiation safety training to ensure safe operation as pXRF still produces ionizing radiation. The penetration depth of the X-rays produced by pXRF instruments is commonly a few mm. Thus, exposing skin or body parts to X-rays should be avoided. Furthermore, many states have licensing requirements for the use of radiation-producing devices that sometimes require the operator to wear a dosimetry badge to monitor X-ray exposure levels. Leakage of X-rays, which can be detected with a Geiger counter, most commonly occurs near the instrument's aperture if it fails to make planar contact with the sample being scanned. For comfort in prolonged use or specialized scanning applications, a bipod or sample stage can be used to position the pXRF for hands-free operation (**Figure 3**).

DATA QUALITY AND PROCESSING

Portable XRF for in-field environmental studies has repeatedly proven useful for directly predicting metal concentrations in soil. For example, Radu and Diamond [10] reported strong coefficients of determination (R^2) for Pb (0.99), As (0.99), Cu (0.95), and Zn (0.84) between pXRF and AAS. Furthermore, pXRF has shown potential for environmental quality assessment of peri-urban agriculture, exhibiting reasonably strong correlations with ICP results of several trace elements [11]. However, pXRF elemental data can also be used as a proxy for predicting other soil properties.

Traditionally, scientists have utilized simple linear regression (SLR) and multiple linear regression (MLR) for establishing correlations between pXRF measured elements and physicochemical soil properties measured via standard laboratory procedures. For example, Sharma et al. [12] used pXRF for pH determination using elemental data as a proxy for soil pH. They used SLR and MLR to develop models associating pure elemental data from pXRF and pXRF elemental data with auxiliary input data (clay content, sand content, organic matter content). While MLR with auxiliary input data produced the best predictive model (R^2 = 0.82; RMSE = 0.541), MLR with pure pXRF elemental data provided a reasonable predictability (R^2 = 0.77; RMSE = 0.685). Notably, SLR could not produce a robust predictive model. Several other studies also included the development of SLR and/or MLR models (with or without auxiliary input data) to predict and find correlations between pXRF elemental data and traditionally lab-measured soil properties, such as soil CEC [13], soil salinity (electrical conductivity) [14], and soil gypsum content [15]. In all cases, the model(s) produced at least acceptable R^2 values, ranging from 0.83 to 0.95 (see the full article for a complete reference list and detailed description of the studies).

Both SLR and MLR are commonly used techniques relating pXRF elemental data to standard laboratory characterization data for the physicochemical parameters of

interest. We recommend splitting the datasets into modeling (~70%) and validation (~30%) datasets when constructing a predictive model to assess model performance before using on unknown samples.

RECOMMENDATIONS

For common soil studies, ex situ scanning in the laboratory after drying and grinding of soil samples is preferable as this eliminates potential interference from soil moisture and provides increased sample homogeneity. As a balance between analytical accuracy and sufficient sample processing throughput, a scanning time of ~60 to 90 seconds is recommended for most soil applications. However, if lower LODs are essential, extending the scanning time can optimize pXRF performance. The Olympus® DELTA™ pXRF features several modes for analysis (Soil, Geochem, Mining, Alloy). These modes offer different packages of elements used in various applications. For most common soil science applications, Soil mode works quite well. More exotic studies of pollution sources or mine soil tailings may benefit from Mining or Alloy modes. In some instances, scanning with more than one mode can be useful, where certain elements are reported more accurately by one mode than another. These modes use various energies and filters to produce fluorescence signatures of various elements. The use of specialized filters may also enhance instrument performance for certain applications in which background scatter or interference can be isolated, allowing better performance [16].

SAMPLE APPLICATIONS AND CASE STUDIES, INCLUDING CALCULATIONS

To date, pXRF has been used to quantify elemental concentrations in several media [4]. While early pXRF studies focused on geologic, metallurgical, or archeological uses, newer soil science and agronomy applications have developed rapidly in recent years. Portable XRF is a good method for use in instances where the chemical properties of soils are of importance. Portable XRF will not provide LODs as low as traditional ICP–AES or ICP–MS analysis. Portable XRF reports total elemental concentration in soils, while techniques such as ICP–AES depend on the success of the digestion used to extract elements into solution. However, pXRF can provide in situ data of reasonable accuracy, with minimal to no sample preparation in ~60 to 90 seconds. Also, pXRF may be useful in certain specialized applications where nondestructive analysis is required or matrices that do not lend themselves readily to traditional soil physicochemical analysis. Similar to spectral data collected by visible and near-infrared (VisNIR) spectroscopy, once collected, pXRF elemental data can be used to predict many physicochemical soil parameters. Universal predictive models can be used with some degree of accuracy, but for optimal results, it is advisable to collect pXRF elemental data, process the soil samples by traditional laboratory analysis, and then develop customized predictive models for a given area. In most cases, a customized model will show considerable accuracy across a given region as long as the general geological and soil properties remain similar. Importantly, the samples used in constructing the model should reflect the variability the investigator seeks to directly predict from the pXRF data. For example, if two substantively different soils are studied, two different models should be developed.

Most models are built on MLR, using elemental data as proxies for the parameter of interest. In developing the predictive model, the investigator should collect a robust dataset ($n \geq 100$ or more), reflective of all variability likely to be encountered in future analysis with the model. Randomly, 30% of the samples should be removed from the dataset for independent validation, with 70% of the samples used for model calibration. Calibration performances can be observed in terms of R^2, RMSE, bias, residual prediction deviation, and ratio of performance to inter-quartile range.

Alternatively, concatenating pXRF elemental data with spectral data from other proximal sensors like visible VisNIR diffuse reflectance spectroscopy can be used in advanced algorithms like penalized spline regression (PSR), partial least squares regression, and random forest regression (RF) to predict several soil parameters with high accuracy [17]. The addition of remote sensing data has also been shown to increase model prediction accuracy [18]. Besides, an advanced combined modeling approach (PSR + RF) can be used in which PSR is used to fit the training set (containing VisNIR spectra only) using full cross-validation to choose the tuning parameter. Next, RF can be used to fit the residuals of the PSR model on the PXRF elemental data. The final predicted value represents the combination of PSR and RF predicted values [19].

REFERENCES:

[1] *C. B. Fliermans, T. D. Brock, Soil Science 1973, 115, 120.*

[2] *USEPA, Method 3050B: Acid digestion of sediments, sludges, and soils, 1996, www.epa.gov.*

[3] *USEPA, Method 3052: Microwave assisted acid digestion of siliceous and organically based matrices, 1996, www.epa.gov.*

[4] *D. C. Weindorf, N. Bakr, Y. Zhu, Adv. Agron. 2014, 128, 1.*

[5] *W. P. Gates, in Handbook of clay science, Elsevier, New York, 2006.*

[6] *D. J. Kalnicky, R. Singhvi, J. Hazard. Mat. 2001, 83, 93.*

[7] *D. C. Weindorf, N. Bakr, Y. Zhu, A. McWhirt, A., C. L. Ping, G. Michaelson, C. Nelson, K. Shook, S. Nuss, Pedosphere 2014, 24, 1.*

[8] *A. Whirt, C. D. Weindorf, Y. Zhu, Compost Sci. Util. 2012, 20, 185.*

[9] *S. Piorek, in Current protocols in field analytical chemistry, John Wiley & Sons, New York, 1998.*

[10] *T. Radu, D. Diamond, J. Hazard. Mater. 2009, 171, 1168.*

[11] *D. C. Weindorf, Y. Zhu, S. Chakraborty, N. Bakr, B. Huang, Environ. Monit. Assess. 2012, 184, 217.*

[12] *A. Sharma, D. C. Weindorf, T. Man, A. Aldabaa, S. Chakraborty, Geoderma 2014, 232–234, 141.*

[13] *A. Sharma, D.C. Weindorf, D. D. Wang, S. Chakraborty, Geoderma 2015, 239–240, 130.*

[14] *S. Swanhart, D. C. Weindorf, S. Chakraborty, N. Bakr, Y. Zhu, C. Nelson, K. Shook, A. Acree, Soil Science 2014, 179, 417.*

[15] *D. C. Weindorf, J. Herrero, C. Castañeda, N. Bakr, S. Swanhart, Soil Sci. Soc. Am. J. 2013, 77, 2071.*

[16] *S. Bichlmeier, K. Janssens, J. Heckel, D. Gibson, P. Hoffmann, H. M. Ortner, X-Ray Spectrom. 2001, 30, 8.*

[17] *D. D. Wang, S. Chakraborty, D. C. Weindorf, B. Li, A. Sharma, S. Paul, M. N. Ali, Geoderma 2015, 243–244, 157.*

[18] *A. A. A. Aldabaa, D. C. Weindorf, S. Chakraborty, A. Sharma, Geoderma 2015, 239–240, 34.*

[19] *S. Chakraborty, D. C. Weindorf, B. Li, A. A. A. Aldabaa, R. K. Ghosh, S. Paul, M. N. Ali, Sci. Total Environ. 2015, 514, 399.*

02 Impact of Sample Preparation Methods for Characterizing the Geochemistry of Soils and Sediments by Portable X-Ray Fluorescence

K. Goff, R. J. Schaetzl, S. Chakraborty, *et al.*

ABSTRACT

We examined the impact of three different sample preparation methods on bulk soil geochemistry data obtained from a portable X-ray fluorescence (pXRF) spectrometer. We generated data from a soil core recovered from the surface, downward into unaltered loess, and into a buried soil at a site in eastern Iowa. Samples were scanned (i) directly from field-moist soil cores; (ii) after drying, grinding, and being loosely massed in plastic cups; and (iii) as pressed powder pellets. Data derived using these methods were compared with data obtained from a standard benchtop X-ray fluorescence (XRF) unit. Generally, the results indicated that data from pressed powder pellets provide the best correlation to benchtop XRF data, although the results were sometimes element- or compound-specific. CaO, Fe_2O_3, and K_2O generally provided the strongest correlations between pXRF and XRF data; SiO_2 data were more problematic. Field-moist pXRF scans generally underestimated element concentrations, but the correlations between pXRF and benchtop XRF measurements were greatly improved after applying pXRF-derived calibration standards. In summary, although element/compound data provided by pXRF showed significant relationships to benchtop XRF data, the results are improved with proper sample preparation and usually by calibrating the pXRF data against known standards.

INTRODUCTION

X-ray fluorescence (XRF) spectroscopy is an analytical technique used to determine the elemental composition of a sample using high-energy X-rays. When bombarded with X-rays, different elements can be identified by the characteristic fluorescent energy they emit (X-ray fluorescence). Thus, X-ray fluorescence offers a rapid and cost-efficient way to generate multielement analytical data.

Researchers are increasingly using portable X-ray fluorescence (pXRF) instruments in the field and laboratory [1]. Many studies have demonstrated that pXRF measurements correlate well with data obtained using conventional methods, such as benchtop XRF [2]. Portable XRF instruments can generate robust, accurate, and repeatable data and are applicable to various environmental applications [3].

As with any new method, researchers actively attempt to determine its overall accuracy and main error sources. Unfortunately, no universally agreed-upon protocol for pXRF sample preparation exists, specifically for analyses of soils or finely ground geological samples. Nonetheless, the Soil Survey Staff [4] has observed that the results from soil analyses are more reproducible if the sample has been air dried, homogenized, and finely ground (<75 µm). By comparison, the Soil Science Society of America method for pXRF analysis of soils advocates drying and grinding to pass a 2 mm sieve [5]. The present study addresses this issue by evaluating the effects of different sample preparation techniques on pXRF data.

For soil investigations, some studies have obtained data by placing the instrument directly onto a field-moist core [6]. Moisture in the sample attenuates the fluorescence, usually leading to underestimation of elemental data [7]. However, moisture levels of <20% generally cause a minimal error in elemental determinations [8]. For example, Stockmann et al. [6] calculated geochemical weathering indices using elemental pXRF data. Although the indices varied greatly between field-moist vs. dried samples, the depth trends showed similar patterns.

Although the accuracy of pXRF measurements from field-moist samples continues to be explored, most researchers conduct their analyses in a laboratory setting. Laboratory preparations typically involve combinations of drying, sieving, and grinding the samples before pXRF analysis [9]. Other researchers physically compact each sample in a standard-sized container, forming a pressed powder pellet, before analysis.

Few studies have examined the efficacy of various sample pretreatments on the overall accuracy of the data. The objective of this study was to examine the effects of three different preparation methods on pXRF data from three soil samples: (i) field-moist soils, (ii) dried and ground powders, and (iii) pressed pellets. Data generated using these preparation methods were compared with traditional benchtop XRF data to determine the effects of sample pretreatment on final data accuracy.

METHODS

Samples from Clear Creek, a tributary of the Iowa River in eastern Iowa, were selected for the study. The Clear Creek Watershed is located within the Southern Iowa Drift Plain [10] and represents a hilly, dissected landscape underlain by Pre-Illinoian tills, with a mantle of loess. At the site, a 7.6 cm diameter core (5.0 m in length) was collected from a site on an upper shoulder slope. A detailed description of the study area and soil is present in the full article of this digest.

Three different pXRF preparation methods (field-moist condition, dried and ground to a powder, and pressed pellets) were compared to evaluate their efficacy for accurately determining soil/sediment geochemistry and weathering zones for the cores. A benchtop XRF unit was used as a comparative standard to establish the bulk chemical composition of the samples. Samples analyzed on the benchtop XRF had been initially removed from the scraped surfaces of the cores, dried at 50 °C (122 °F) for 12 hours, and ground to a fine powder. Subsamples of ~0.2–0.5 g were further ground to pass a 75 µm sieve, pressed into pellets, and made into homogeneous glass disks by fusion of the sample and a lithium tetraborate/lithium metaborate mixture [11]. XRF analyses were conducted for seven elements (Si, Al, Zr, K, Ca, Ti, Fe, and Mn) at SGS Canada Inc., in Mississauga, Ontario. Quality control was achieved using SiO_2 blanks, duplicates, and certified reference materials [11].

Portable XRF analyses were performed in Geochem Mode using an Olympus® DELTA™ Professional pXRF unit. The unit was operated on line at 110 VAC, without special filters, with a dwell time of 30 seconds, and under nor-

Analyzed element	Detection limit
Ti	10 ppm
Si	1.0%
Al	1.0%
Mn	10 ppm
K	50 ppm
Fe	10 ppm
Ca	50 ppm

Table 1: Detection limits of the Olympus pXRF spectrometer for the seven elements reported in this study.

mal atmospheric conditions. Instrument resolution was 150 eV per channel with a pulse density of 100,000 cps. Resulting waveforms were processed with the proprietary Olympus X-act Count Digital Pulse Processor and integrated software [12]. Each time the pXRF was initialized, a 316 alloy coin was used for factory calibration. Detection limits for pXRF analyses vary by element (**Table 1**).

Initial scanning was completed by placing the pXRF device directly on the moist core at ≤10 cm intervals after any outer sediment material had been scraped away and the exterior area flattened with a knife. If a horizon break occurred, the sample increment was lessened so that no sample was taken from different horizon types. The remainder of the analyses were conducted on dried samples. In the laboratory, ~100 g samples were ground. Subsamples of ~20 g were then powdered, placed in 2.5 cm diameter plastic cups with at least 2 cm of material, covered with a 3.0 µm thin mylar film, and lightly tamped to achieve a level surface before pXRF analysis. Portable XRF analyses were also conducted on pucks formed by compressing the sediment in 0.4 × 3 cm stainless steel cups using a stainless steel hydraulic press at 25 tons of pressure per square inch (pressed powder pellets). Four replicate scans were conducted on each sample for each method; all data reported are mean elemental data. Portable XRF data were converted to oxide values using standard conversion factors for SiO_2, Al_2O_3, K_2O, CaO, TiO_2, Fe_2O_3, and MnO. Four soil standard reference materials from the National Institute of Standards and Technology (NIST; https://www.nist.gov/srm; AGV-2, BIR-1, BCR-2, JA-1) were examined to develop linear calibration curves for selected elements/oxides using the Lucas-Tooth Calibration Method [13]. The average value of each standard, based on five analyses, was then compared with the known values reported by Jochum *et al.* [14]. An in-house standard of Peoria loess, which was geochemically similar to the core materials, was used as a fifth standard.

RESULTS AND DISCUSSION

Data derived from pXRF and benchtop XRF were often quite different; SiO_2 and Fe_2O_3 data were especially problematic (**Table 2**). Using three different sample preparation methods (moist core, dried and ground powder, and a pressed powder pellet), we sought to understand which method yields the most accurate pXRF results relative to data from the traditional benchtop XRF instrument. We assumed that benchtop XRF data most accurately characterize the overall bulk chemical composition of the soils. Benchtop XRF data may still suffer from overlapping fluorescence energies of different elements, limiting data interpretability. Furthermore, "light" elemental detection remains challenging given their weak fluorescent energies and atmospheric attenuation issues.

To that end, pXRF data from three different pretreatments were compared with benchtop XRF data. Example data from the Old Scotch core are shown in **Figure 1**. Generally, CaO, TiO_2, and MnO data from the pXRF correlated best with benchtop XRF data, and for these compounds, the correlations were strongest when using the pressed powder method. Nonetheless, many of the data are element-specific, and thus the optimal sample preparation method is not the same for the seven elements/compounds. Portable XRF routinely overestimated the contents of Fe_2O_3 and Al_2O_3 and generally underesti-

		pXRF
Compound	**Benchtop XRF**	**(average of 55 runs)**
	– wt% –	
Al_2O_3	8.71	8.13
SiO_2	70.30	52.24
K_2O	1.76	1.40
CaO	3.69	4.04
TiO_2	0.66	0.74
Fe_2O_3	2.96	3.80
MnO	0.07	0.07

Table 2: Elemental contents for an in-house standard of Peoria Loess, as determined by benchtop XRF and pXRF.

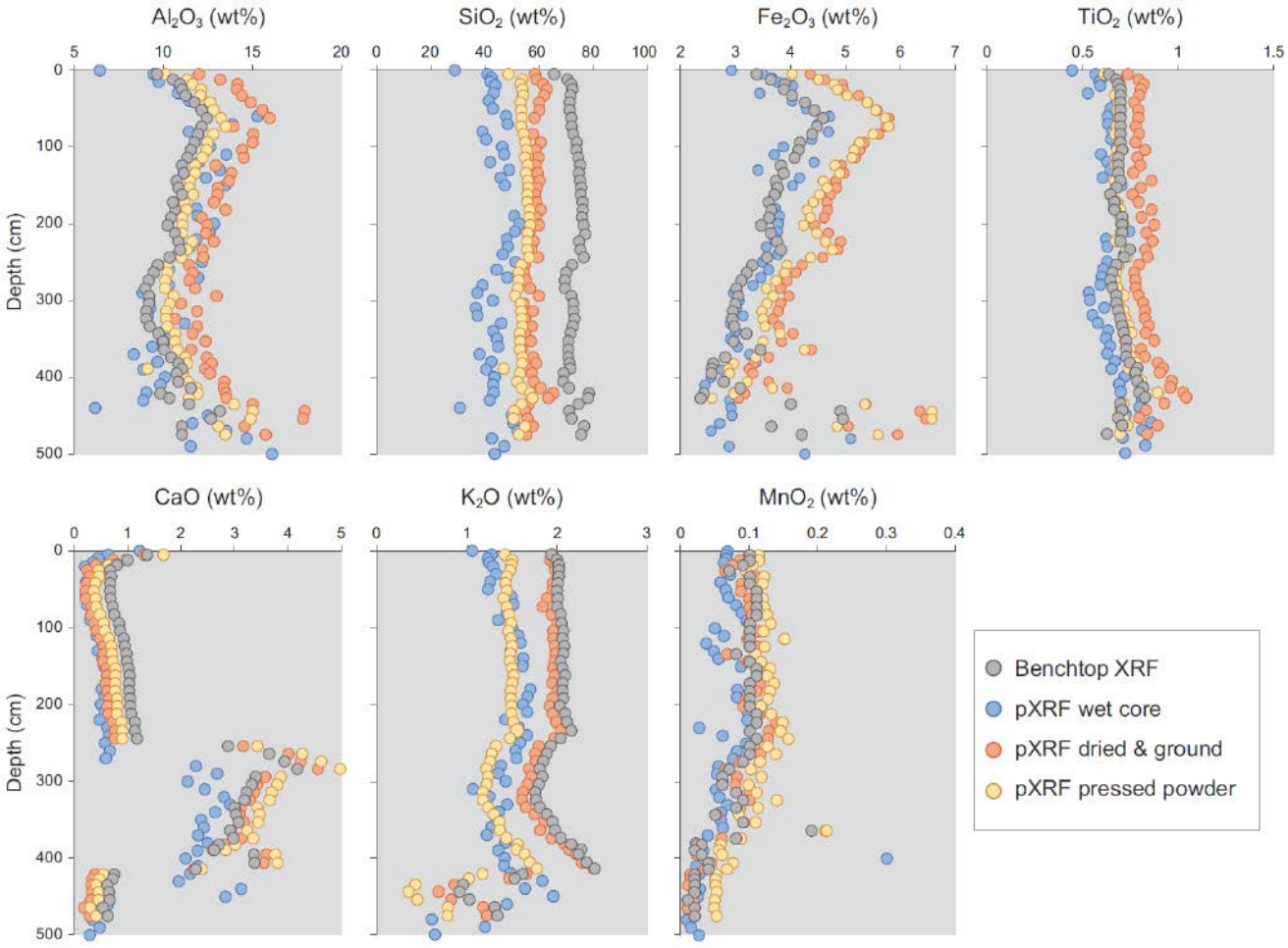

Figure 1: Depth plots of energy dispersive pXRF and benchtop XRF data for seven different oxides (Old Scotch core).

mated those of CaO and K_2O (**Figure 1**). Several researchers have reported a tendency of pXRF to overestimate Fe concentrations [15], a trend observed in the present study on all but the wet core samples (**Figure 1**). A possible explanation for the latter is that many closely spaced K- and L-lines occur in the low-energy region, causing spectral interferences [16]; however, as moisture attenuates fluorescence, that attenuation probably compensated for the overestimation of Fe in the present study. Generally, the accuracy of the data increased for most elements using the pressed powder pellet method. Thus, these data will be used as the pXRF component from this point forward.

Correlations of (pressed powder) pXRF vs. benchtop XRF data indicate that the highest R^2 values were obtained for CaO (0.997), Fe_2O_3 (0.983), and K_2O (0.981); analyses for Al_2O_3 (0.746), TiO_2 (0.666), and SiO_2 (0.136) yielded lower correlations. Low correlation values for SiO_2 probably reflect variable attenuation of low-frequency X-rays during pXRF analysis, whereas the slightly lower correlation values for TiO_2 might reflect an uneven distribution of Fe-Ti oxides in the samples because of their overall lower concentrations.

Linear calibrations were developed for elements that appeared to vary consistently between benchtop XRF and pXRF analyses using four NIST standards and the in-house Peoria Loess standard (**Figure 2**). The linear regressions were then used to correct (calibrate) the pXRF data. Based on the standards shown in **Figure 2**, these calibrations are for major oxides: CaO, MnO, MgO, Fe_2O_3, P_2O_5, K_2O, and TiO_2. They produced well-correlated

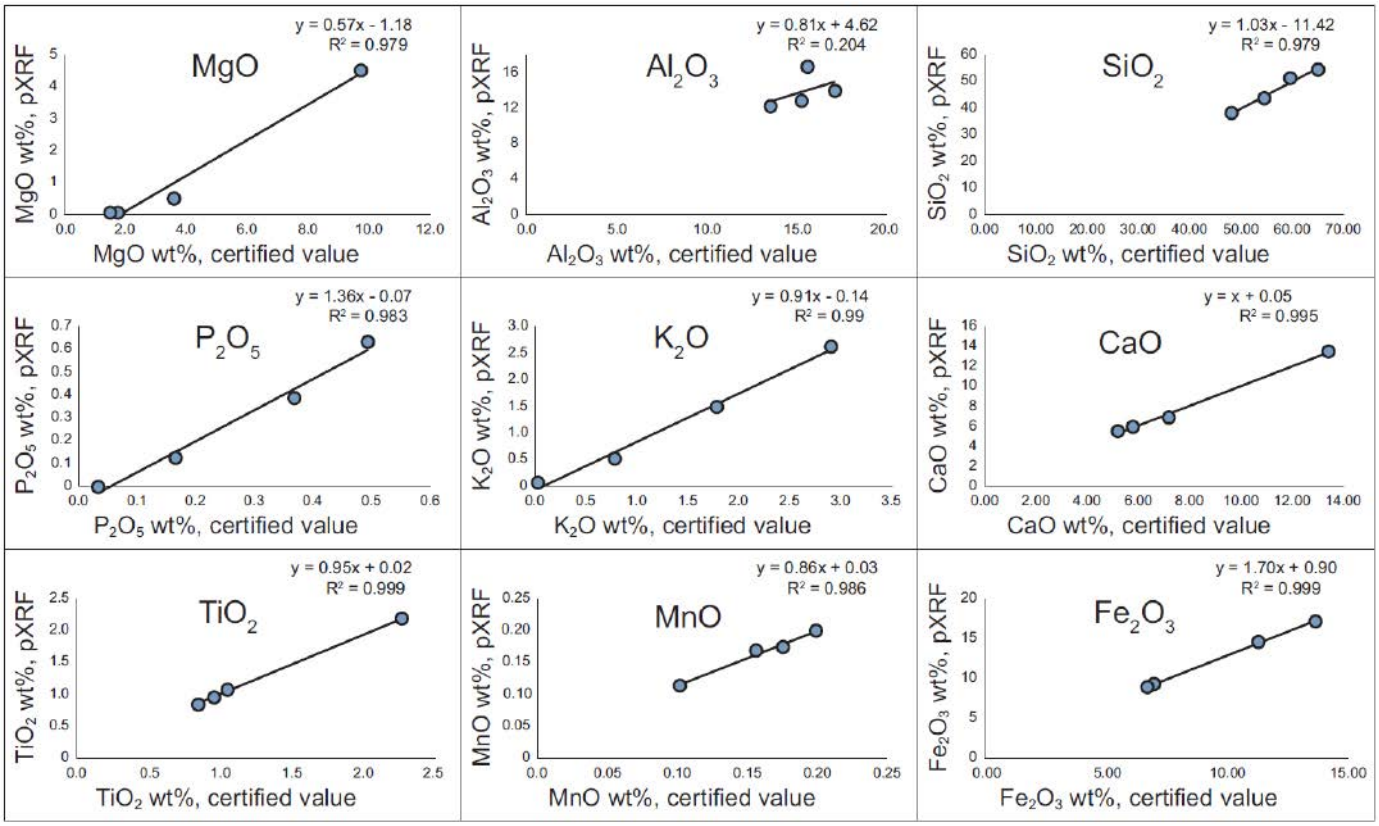

Figure 2: Calibrations developed for correcting energy dispersive pXRF data, using data from this study, four NIST standards, and an internal Peoria Loess standard.

	Equation	R^2	Equation	R^2
Oxide	**Calibrated pXRF data**		**Raw pXRF data**	
SiO_2	$y = 0.60x + 9.64$	0.60	$y = 0.35x + 31.92$	0.13
TiO_2	$y = 0.97x + 0.02$	0.72	$y = 1.25x - 0.04$	0.66
Al_2O_3	$y = 1.06x + 0.19$	0.72	$y = 1.37x - 1.40$	0.74
MnO	$y = 0.89x + 0.03$	0.90	$y = 1.07x - 0.004$	0.91
K_2O	$y = 0.94x - 0.47$	0.98	$y = 1.06x - 0.22$	0.98
Fe_2O_3	$y = 1.47x + 0.92$	0.98	$y = 1.30x - 0.06$	0.98
CaO	$y = 1.28x - 0.47$	0.99	$y = 0.88x - 0.41$	0.99

Table 3: Linear regression equations comparing calibrated and raw pXRF data to benchtop XRF data, using data from the Old Scotch core pressed pellet samples.

calibrations. Except for SiO_2, the correlation coefficients are >0.7, with most being >0.9.

Table 3 illustrates the improvements in correlation between the uncalibrated vs. calibrated pXRF data of the samples. Although most of the data were improved using the calibration functions, data for some elements were only slightly improved or even slightly worsened. Despite producing substantial improvement in R^2 values for SiO_2 by pXRF correction, the concordance between benchtop XRF and calibrated pXRF SiO_2 data was still moderate at best (R^2 = 0.60). **Figure 3** shows the changes in the data for four elements obtained by applying the calibrations in **Figure 2** to the raw pXRF data.

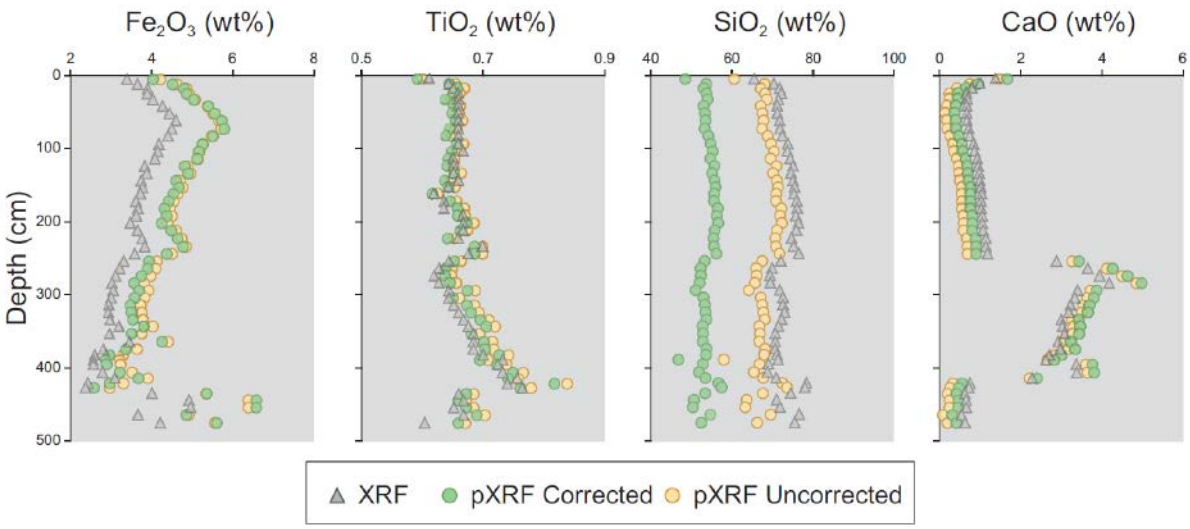

Figure 3: Depth plots showing agreement between calibrated and raw pXRF vs. benchtop XRF data for Fe_2O_3, TiO_2, SiO_2, and CaO values for the Old Scotch core.

Results indicate that the overall accuracy of the Olympus® pXRF data is very good but somewhat element-dependent. For example, the comparatively poor performance of some elements may create problems for determining weathering ratios, many of which are dependent on Al or Si oxide contents and often use Ti as an indicator of the contents of the slowly weatherable mineral tourmaline [17]. Likely, the contents of light elements such as Mg, Al, and Si are more difficult to determine accurately because the emitted X-rays are more easily attenuated by the atmosphere. As a result, these elements have lower R2 values and poorer calibrations due to the low-energy condition and the inability of the current pXRF technology to properly correct this issue (**Table 3**).

The accuracy of raw pXRF data can be improved for most oxides by calibrations. Such linear calibrations should ideally have a slope of 1.0 and an intercept at the origin. The calibrations in this study differ significantly from these values, likely reflecting the inaccuracy of the internal calibration technique of the Olympus® instrument and issues related to X-ray attenuation, fluorescence, and interference. Thus, many pXRF data may have good correlations but are offset by XRF data derived from benchtop instruments (**Figure 1**). Improvements in these calibrations could be achieved using more standards and standards with higher variability in composition. Particularly concerning is that applying calibrations to known standards did not improve the Si data (**Figure 3**).

The intensity of characteristic fluorescence decreases with increasing soil moisture due to strong X-ray absorption by soil water [5]. Therefore, dried, ground, and sieved soil samples should theoretically provide increased homogeneity by averaging out the effect of microscale inclusions and similar substances, such as Fe/Mn concretions. However, compression of dried/ground powders may also artificially inflate pXRF elemental readings by accentuating the number of atoms per unit area in contact with the X-ray beam. Indeed, the average bulk density of the pressed powder pellets was significantly higher (2.56 g cm^{-3}) than the average bulk density of the cores (1.69 g cm^{-3}).

CONCLUSION

In this study, soil/sediment samples from cores taken in loess soils in eastern Iowa were evaluated by pXRF spectrometry using three different pretreatments: (i) field-moist soils (no pretreatment), (ii) dried/ground powder, and (iii) pressed powder pellets. Results from the pXRF were compared with benchtop XRF data. Portable XRF data from pressed powder pellets performed best for certain elements/oxides and generally provided the strongest correlations between pXRF and XRF data. Data correlations for some other elements were less

robust. Scanning of field-moist samples consistently underestimated the concentrations of certain elements/oxides due to fluorescence attenuation. Therefore, soil samples should be dried, ground, sieved, and, in some cases, pressed into dense pellets before pXRF analysis.

Application of calibrations developed from standard materials to adjust pXRF data resulted in considerable improvements, leading to data that more closely align with benchtop XRF data. However, more work is needed to simultaneously consider the influence of moisture, sample bulk density, pXRF operational parameterization, and correction of reported pXRF data with local calibration samples. Those limitations notwithstanding, pXRF remains a powerful tool for rapid in situ analysis of soils and ground geologic sediments.

REFERENCES:

[1] *S. Chakraborty, B. Li, D. C. Weindorf, S. Deb, A. Acree, P. De, P. Panda, Geoderma 2019, 338, 5.*

[2] *A. M. W. Hunt, R. J. Speakman, J. Archaeol. Sci. 2015, 53, 626.*

[3] *D. C. Weindorf, N. Bakr, Y. Zhu, Adv. Agron. 2014, 128, 1.*

[4] *Soil Survey Staff, in Kellogg soil survey laboratory methods manual, Natl. Soil Surv. Ctr., Lincoln, 2014.*

[5] *D. C. Weindorf, S. Chakraborty, Soil Sci Soc Am J. 2020, 84, 1384.*

[6] *U. Stockmann, S. R. Cattle, B. Minasny, A. B. McBratney, Catena 2016, 139, 220.*

[7] *H. Sahraoui, M. Hachicha, J. Fundam. Appl. Sci. 2017, 9, 468.*

[8] *USEPA, Method 6200: Field portable X-ray fluorescence spectrometry for the determination of elemental concentrations in soil and sediment, 2007, www.epa.gov.*

[9] *B. M. Duda, D. C. Weindorf, S. Chakraborty, B. Li, T. Man, L. Paulette, S. Deb, Geoderma 2017, 298, 78.*

[10] *J. C. Prior, in Landforms of Iowa. University of Iowa Press, Iowa City, 1991.*

[11] *SGS Canada Inc., Sample preparation and XRF procedure, Mississauga, 2016.*

[12] *Olympus Corporation, XRF and XRD Analyzers DELTA Premium, Tokyo, 2017.*

[13] *M. J. Adams, J. R. Allen, J. Anal. At. Spectrom. 1998, 13, 119.*

[14] *K. P. Jochum, U. Nohl, K. Herwig, E. Lammel, B. Stoll, A. W. Hofmann, Geostand. Geoanal. Res. 2005, 29, 333.*

[15] *J. Koch, S. Chakraborty, N. Li, J. Moore-Kucera, P. Van Deventer, A. Daniell, C. Faul, T. Man, D. Pearson, B. Duda, C. A. Weindorf, D. C. Weindorf, J. Geochem. Explor. 2017, 181, 45.*

[16] *D. Gallhofer, B. G. Lottermoser, Minerals 2018, 8, 320.*

[17] *B. Buggle, B. Glaser, U. Hambach, N. Gerasimenko, S. Markovic, Quat. Int. 2011, 240, 12.*

03 Semiquantitative Evaluation of Secondary Carbonates via Portable X-Ray Fluorescence Spectrometry

S. Chakraborty, D. C. Weindorf, C. A. Weindorf, *et al.*

ABSTRACT

Secondary $CaCO_3$ is commonly found in soils of arid and semiarid regions in variable states of development. Historically, a qualitative scale featuring various stages of development has been applied when evaluating carbonate-laden soils. By contrast, this study used portable X-ray fluorescence (pXRF) spectrometry to determine the Ca concentration of 75 soil samples from four US states in relation to the developmental stage, as determined independently by five pedologists from the USDA–NRCS Soil Survey Staff. Although experienced, the evaluators unanimously agreed on the carbonate development stage of only 22.6% of the samples while evaluating the samples ex situ. Portable XRF-determined Ca content generally increased from Development Stage I through VI for intact aggregates and ground soil samples. The widest variation in Ca content was found in Stage III for both conditions. No substantive differences in Ca content were observed between Stages V and VI. A strong positive correlation was observed between the Ca content of intact aggregates vs. ground soil samples ($r = 0.89$). Both support vector machine classification, and interpretable rules were used to classify secondary carbonate development stages using total Ca concentrations for intact aggregates and ground soil. Using scans of both conditions offers stronger predictive ability than either condition independently. Portable XRF provides an important analytical tool for field soil scientists to evaluate soils containing Ca as part of $CaCO_3$.

INTRODUCTION

Soils featuring secondary carbonates are common in semiarid and arid regions. $CaCO_3$ is a mineral of limited solubility, often originally derived from the mineral calcite or Ca-containing rocks. As mineral and rock forms of $CaCO_3$ degrade, they can serve as parent material for various soils. For example, Alfisols, Mollisols, and Inceptisols of the Southern High Plains of Texas are largely eolian in nature, and all contain substantive subsoil secondary $CaCO_3$, originating from the northern Chihuahuan Desert (via prevailing winds from the south). The solubility of $CaCO_3$ is influenced by variable CO_2 pressure, pH, temperature, and salinity. Often in the presence of active acidity inherited from atmospheric sources (e.g., H_2CO_3) or plant respiration, $CaCO_3$ dissolves to free Ca^{2+} and HCO_3^- ions that readily translocate within the soil as part of the soil solution [1]. As water in the soil solution begins to evaporate, the solubility product is exceeded, and $CaCO_3$ begins to precipitate, leading to the development of lower portions of the solum as Bk, Bkk, Bkkm, Ck, or, more rarely, Ak horizons. Collectively, these horizons often constitute diagnostically recognized calcic horizons [2].

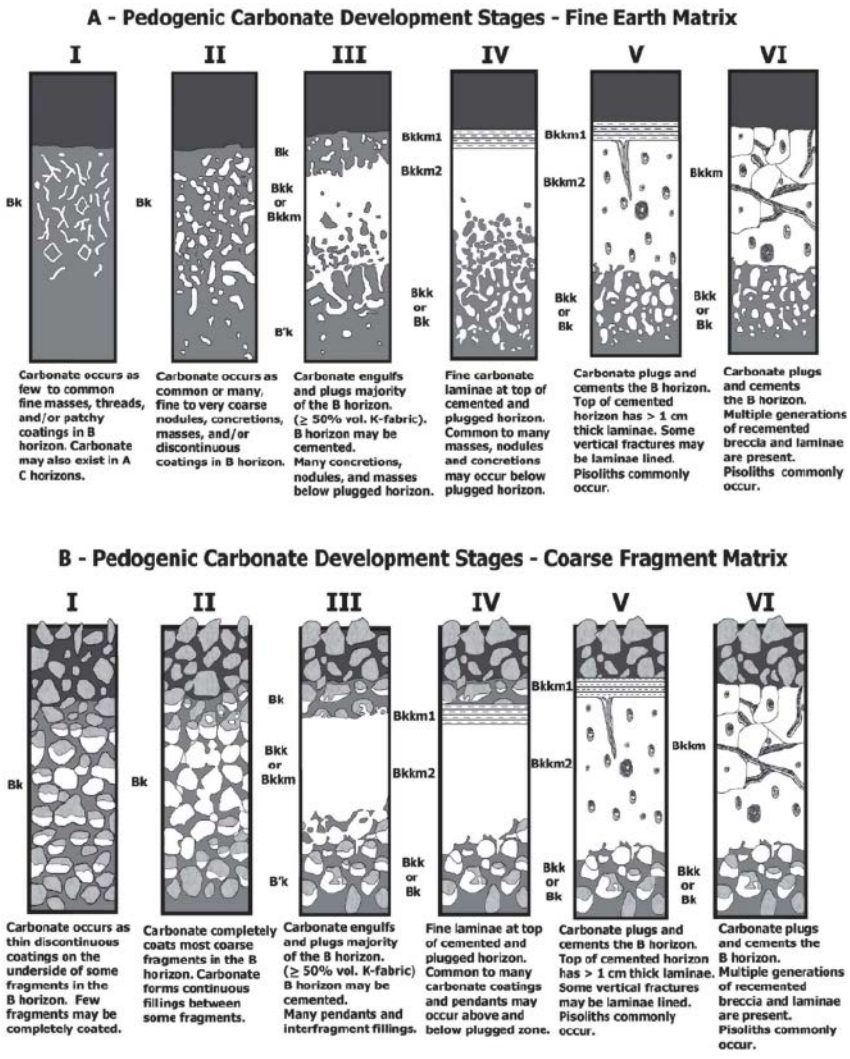

Figure 1: Pedogenic carbonate development stages for (A) fine earth matrix and (B) coarse fragment matrix [3].

The Soil Survey Staff commonly uses morphological attributes (e.g., identifiable carbonates) and qualitative descriptions of soil horizons for establishing the quantity of secondary carbonates observed either in a fine earth or coarse fragment matrix in the field (**Figure 1**) [3]. Similarly, previous studies have investigated carbonates in soils, recognizing and describing up to six carbonate development stages [4–6]. Although useful, these descriptions lack the objectivity of being quantitative measures. In contrast, $CaCO_3$ can be measured in the laboratory; however, the two most commonly applied methods—gasometry and titration—do not lend themselves easily to field quantification [7].

Recently, portable X-ray fluorescence (pXRF) spectrometry has been shown to be adept at elemental quantification in situ. For example, using reagent-grade Ca under laboratory conditions, Zhu and Weindorf [8] found an R^2 of 0.986 comparing pXRF-determined Ca levels with true Ca contents. The pXRF approach has also been successfully applied to enhanced pedon horizonation [9], identification of lithologic discontinuities [10], assessment of soil cation exchange capacity [11], soil pH [12], and salinity of both soil [13] and water [14]. The accuracy, speed, nondestructiveness, and inexpensiveness of pXRF offer formidable advantages over traditional laboratory-based analytical approaches [15].

The pXRF approach cannot distinguish between the primary (rock/mineral) and secondary (Bk/Bkk) source of Ca in $CaCO_3$-containing soil horizons as it provides only elemental data on total Ca concentration. However, the enrichment of a soil horizon with $CaCO_3$ via pedogenesis may be assessed rapidly in situ. Such assessment is important for identifying diagnostic calcic horizons, which are defined by the $CaCO_3$ concentration relative to adjacent horizons. We hypothesized that total Ca contents in soil aggregates may provide insight into the pedogenic development stages of secondary

Parameter	*n*
Sampling location	
Colorado	
Colorado County	2
Kansas	
Decatur County	1
Norton County	2
Wallace County	12
New Mexico	
Chaves County	4
Lincoln County	16
Texas	
Garza County	6
Lubbock County	24
Scurry County	4
Yoakum County	4
Total	75
Developmental stage	
1.0–1.4	12
1.5–2.4	12
2.5–3.4	23
3.5–4.4	12
4.5–5.4	10
5.5–6.0	6
Total	75

Table 1: Qualitative assessment of secondary $CaCO_3$ development stage and sampling location of Bk, Bkk, Bkkm, and Ck horizons.

soil carbonates. Thus, we aimed to explore the extent to which pXRF-quantified Ca can explain secondary carbonate development stages.

METHODS

A total of 75 soil samples were collected across semiarid and arid regions of New Mexico, Texas, Colorado, and Kansas (**Table 1**). Sampling was done mostly in Bk, Bkk, Bkkm, and/or Ck horizons observed as road cuts. In some instances, soil pits were excavated to a depth of 1 m and then sampled. Soil sampling was done in accordance with [3], whereby subsoil aggregates were kept intact and placed in sealed plastic containers for transport to the laboratory.

LABORATORY ANALYSES

Upon receipt in the laboratory, samples were dried as intact aggregates for 5 days at 35 °C (95 °F) until air dry as soil moisture attenuates fluorescence [9]. With **Figure 1** provided as a reference, the secondary carbonate development stage of all samples was independently evaluated ex situ by five members of the USDA–NRCS Soil Survey Staff with a combined experience of 90 years. The rankings of each soil scientist were averaged to generate a mean score for each sample (**Table 1**). For comparative analysis, rounding of the mean score was performed to place a given sample into a class.

Ten selected soil samples were subjected to powder X-ray diffraction for mineralogical analysis. The 10 samples represented one sample from each county in which sampling occurred, and all six developmental stages were evaluated.

PORTABLE X-RAY FLUORESCENCE SCANNING

For pXRF, samples were scanned as intact aggregates using an Olympus® DELTA™ Premium (DP-6000) pXRF spectrometer. The spectrometer was positioned in a portable hooded test stand. Soil samples were placed on a Prolene thin film and positioned directly on the aperture of the pXRF, allowing for scanning of intact aggregates with irregular edges without exposure to stray X-rays. For samples showing considerable heterogeneity in secondary $CaCO_3$ distribution, the most carbonate-laden accumulation visible in the aggregate was scanned. Scanning was conducted in Geochem mode (two beams) at 40 seconds per beam, with elemental Ca as the target element of interest. After scanning all intact aggregates, samples were ground and rescanned as powders. Instrument performance was verified via the scanning of two NIST-certified reference soils.

Support vector machine (SVM) classification was implemented for statistical analysis to classify secondary carbonate development stages using total Ca concentrations in intact aggregates (Ca-intact) and ground soil (Ca-ground) samples. Radial kernel SVM was used, incorporating Ca-intact, Ca-ground, and Ca-intact + Ca-ground as explanatory variables. Tenfold cross-validation was used to select the optimal tuning parameters in SVM (cost and kernel width).

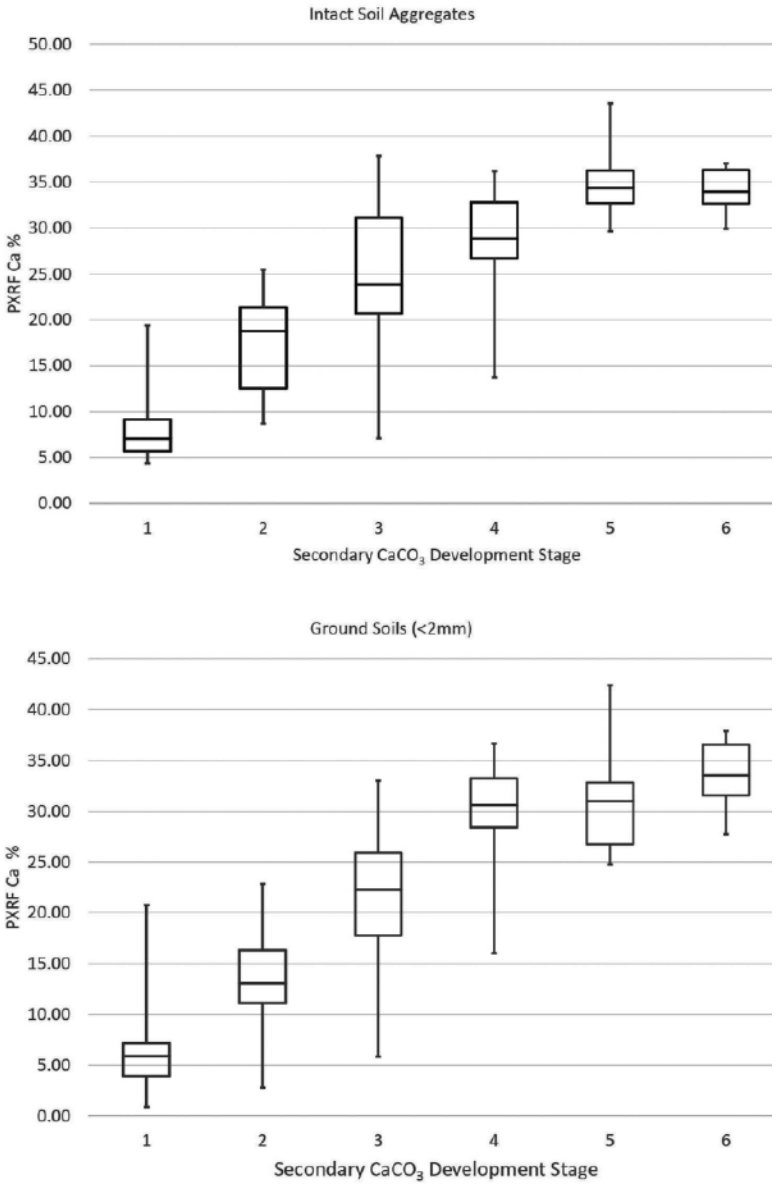

Figure 2: Median, quartiles, maximum, and minimum values of pXRF-Ca for Ca-intact (above) and Ca-ground (below) soils grouped by the visually determined developmental stages of carbonate-laden soils from Texas, New Mexico, Kansas, and Colorado.

Stage	Rule
I	{Ca.Intact – Ca.Ground > 0} AND {Ca.Intact + Ca.Ground < 20}
II	{Ca.Intact – Ca.Ground > 0} AND {20 < Ca.Intact + Ca.Ground < 40}
III	Variable
IV	{Ca.Intact – Ca.Ground < 0} AND {40 < Ca.Intact + Ca.Ground}
V	{Ca.Intact – Ca.Ground > 0} AND {55 < Ca.Intact + Ca.Ground}
VI	{60 < Ca.Intact + Ca.Ground}

Table 2: Rules for identifying six secondary carbonate development stages for carbonate-laden soils.

The full article of this digest includes a more detailed description of the SVM approach.

RESULTS AND DISCUSSION

Qualitative assessment of the secondary carbonate development stage showed considerable disagreement among the panel of evaluators. Unanimous agreement was found on only 16 samples (22.6%). Fair agreement was defined by one or more panelist(s) placing a given sample in adjacent carbonate development stages. Poor agreement was defined by panelists placing a given sample in three adjacent development stages. Fair and poor agreement among panelists was observed for 46 (61.3%) and 12 (16%) samples, respectively.

X-ray diffraction generally revealed a larger diversity in mineralogy and lower total Ca content at lower developmental stages. As the carbonate development stage increased, the mineralogy became increasingly dominated by $CaCO_3$ and SiO_2. For example, a Stage III sample from Lincoln County, New Mexico, featured 42.6% $CaCO_3$ and 33.9% SiO_2 and included smaller quantities of phengite, anorthite, birnessite, and vermiculite. By contrast, a Stage VI sample from Lubbock County, Texas, featured 94.3% $CaCO_3$ and 5.7% SiO_2; no other minerals were identified.

Field-intact aggregate scans of soil Ca via pXRF showed clear differences between samples classified as carbonate development Stages I–V, with less difference between Stages V and VI (**Figure 2**). Importantly, pXRF reports only total soil Ca content, so it cannot distinguish between primary and secondary $CaCO_3$ or determine the degree of induration. Careful attention must be given to field-intact soil aggregates because secondary carbonate precipitation is often influenced by the wetting front, soil structure, and soil porosity [4]. For example, it is quite common to find secondary carbonates deposited on the face of structural aggregates while the matrix remains carbonate-free [16]. Thus, scanning the carbonate-laded prism face may cause an overestimation of the carbonate development stage relative to the overall soil volume. However, scanning soils both as intact aggregates and <2-mm powders provides an important differential measure that can be used for carbonate stage assessment (**Table 2**).

Pearson correlation testing exhibited a high positive correlation between Ca-intact and

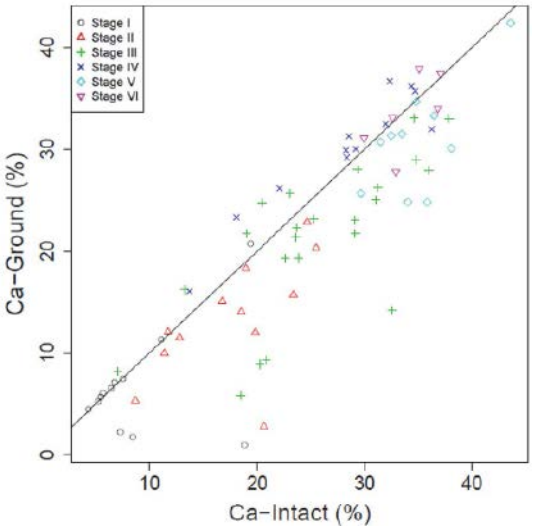

Figure 3: Scatterplot exhibiting correlation between Ca-intact and Ca-ground for carbonate-laden soils.

Ca-ground (r = 0.89, **Figure 3**). Moreover, **Figure 4** shows the basis for some interpretable rules (**Table 2**) that were devised for explaining different secondary carbonate development stages using Ca-intact and Ca-ground values. A box was used to identify each stage in the scatterplot. This was motivated by the fact that each box can be expressed by "IF AND THEN" language, with intervals on each variable. For example, Stage I's box can be expressed as IF (Ca-intact – Ca-ground is >0) AND (Ca-intact + Ca-ground is <20), THEN the sample is most likely to be Stage I (**Figure 4** and **Table 2**). Stage I was the easiest to identify, whereas Stage III was the most variable; these results are consistent with the variability

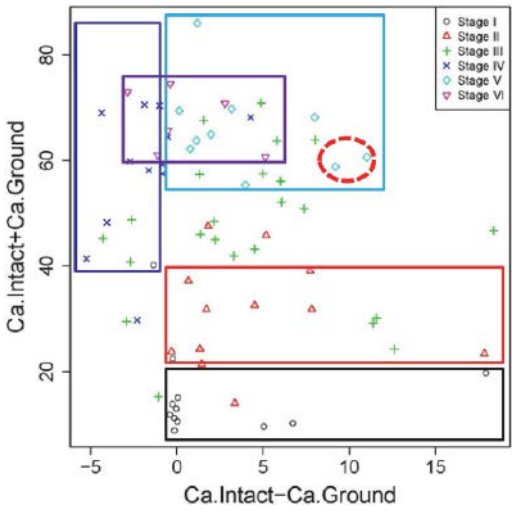

Figure 4: Scatterplot used for establishing the rules for explaining different secondary carbonate development stages for carbonate-laden soils.

observed in Ca content (**Figure 2**). Conversely, Stages IV–VI appeared very close (**Figures 2** and **4**). Notably, although Stages IV and V were very close to each other, Stage IV was above the $y = x$ line (**Figure 3**), indicating Ca-ground > Ca-intact, whereas the opposite trend was observed in Stage V. These trends indicate the benefit of using both pXRF-sensed variables in classifying carbonate developmental stages. The results further indicate that pXRF scanning can be used to identify several carbonate developmental stages. Based on our results and the original concepts [3], revision to the carbonate development stages may be warranted. For example, Stages V and VI may be combined into a single developmental stage because their Ca content and morphological features were generally similar.

Using Ca-intact + Ca-ground, SVM achieved the lowest 10-fold cross-validation error (0.491). Conversely, while using Ca-intact and Ca-ground independently, SVM achieved 0.521 and 0.527 cross-validation errors, respectively. Hence, using two variables together provides better results than either variable alone. Notably, 83.3% (n = 10), 83.3% (n = 10), 91.03% (n = 21), 91.66% (n = 11), 60% (n = 6), and 33.33% (n = 2) of the samples were correctly classified for Stages I, II, III, IV, V, and VI, respectively. **Figure 5** shows the resultant nonlinear SVM classification plot. The region outside the data range is the extrapolation area, which is useless and artificial (e.g., yellow region in the top left corner). The plot indicates that Stage III (yellow region) had the largest area within the data range, indicating the largest variation for Ca-intact and Ca-ground. Further, the Stage I region (dark green) was mainly located at the lower-left corner, indicating that Stage I samples had the smallest Ca-intact and Ca-ground values. The Stage II region (green) is next to Stage I, confirming that samples from both groups were relatively close together. The Stage VI region (white) implies that Stage VI samples had the largest value in both variables. The narrow nature of the diagonal Stage V region can be attributed to the two samples from Stage V, which were close to the diagonal area (red circle in **Figure 4**). Further, Stages IV, V, and VI were relatively close to each other, exhibiting larger Ca-intact and Ca-ground values than Stages I and II (**Figures 2** and **4**). However, Stage IV and V were separated by the diagonal lines, implying that Stage IV samples had larger Ca-ground values than Ca-intact, whereas Stage V samples showed the opposite trend. Therefore, it can be concluded that Stages I and II were relatively easy to identify.

CONCLUSION

In summary, 75 carbonate-laden soils were subjected to pXRF scanning to provide semi-quantitative information on the carbonate development stage. The results indicate that Ca concentration increases steadily with the carbonate development stage. This was true for both intact aggregates and ground powder samples. Stage III carbonate development demonstrated the widest variability in Ca content. Intact aggregates showed almost no difference in Ca content between Stages V and VI. SVM analysis realistically classified carbonate development stages using total Ca concentrations in intact aggregates and ground soil samples. Portable XRF was generally shown to be a useful tool in establishing the developmental stage of secondary carbonates in soils.

REFERENCES:

[1] *C. C. Reeves, J. Geol. 1970, 78, 352.*

[2] *Soil Survey Staff, in Keys to soil taxonomy, Natl. Soil Surv. Ctr., Lincoln, 2014.*

[3] *P. J. Schoeneberger, D. A. Wysocki, E. C. Benham, E.C., in Field book for describing and sampling soils, Natl. Soil Surv. Ctr., Lincoln, NE, 2012.*

[4] *H. W. Hawker, Soil Sci. 1927, 23, 475.*

[5] *M. N. Machette, in Calcic soils of the southwestern United States, Geol. Soc. Am., Boulder, 1985.*

[6] *A. M. Alonso-Zarza, P. G. Silva, J. L. Goy, C. Zazo, Geomorphology 1998, 24, 147.*

[7] *R. H. Loeppert, D. L. Suarez, in Methods of soil analysis. Part 3—Chemical methods, SSSA and ASA, Madison, 1996.*

[8] *Y. Zhu, D. C. Weindorf, Soil Sci. 2009, 174, 151.*

[9] *D. C. Weindorf, Y. Zhu, B. Haggard, J. Lofton, S. Chakraborty, N. Bakr, W. T. Zhang, W. C. Weindorf, M. Legoria, Soil Sci. Soc. Am. J. 2012, 76, 522,*

[10] *D. C. Weindorf, S. Chakraborty, A. A. A. Aldabaa, L. Paulette, G. Corti, S. Cocco, E. Micheli, D. Wang, B. Li, T. Man, A. Sharma, T. Person, Soil Sci. Soc. Am. J. 79, 1704.*

[11] *A. Sharma, D. C. Weindorf, D.D. Wang, S. Chakraborty, Geoderma 2015, 239–240, 130.*

[12] *A. Sharma, D. C. Weindorf, T. Man, A. A. A. Aldabaa, S. Chakraborty, Geoderma 2014, 232–234, 141.*

[13] *S. Swanhart, D. C. Weindorf, S. Chakraborty, N. Bakr, Y. Zhu, C. Nelson, K. Shook, A. Acree, Soil Sci. 2014, 179, 417.*

[14] *D. Pearson, S. Chakraborty, B. Duda, B.Li, D. C. Weindorf, S. Deb, E. Brevik, D. P. Ray, J. Hydrol. 2017, 544, 172.*

[15] *D. C. Weindorf, N. Bakr, Y. Zhu, Adv. Agron. 2014, 128, 1.*

[16] *R. J. Schaetzl, S. Anderson, in Soils: Genesis and geomorphology, Cambridge Univ. Press, New York, 2005.*

04 Using EMI and P-XRF to Characterize the Magnetic Properties and the Concentration of Metals in Soils Formed over Different Lithologies

S. Doolittle, J. Chibirka, E. Muñiz, *et al.*

ABSTRACT

Two sites located in the Northern Piedmont of Pennsylvania suspected to have different levels of magnetic susceptibility (*k*) were examined using electromagnetic induction (EMI) and portable X-ray fluorescence (pXRF). One site is underlain by micaceous schist and serpentinite; the other site by micaceous schist only. The responses of an EM38-MK2-1 meter and the estimated *k* were greater and more variable at the site underlain by serpentinite and micaceous schist. Also, the average concentrations of Fe, Cr, Ni, and Ti were significantly higher at this site, and significant correlations were derived between the concentrations of several metals and the in-phase response and *k* of the upper 30 cm of the soil. These correlations were generally lower and less significant at the site underlain by micaceous schist alone. As *k* is associated with greater amounts of ferromagnetic constituents in soils, the greater concentration of Fe measured with pXRF at the site underlain by micaceous schist and serpentinite helps explain the greater averaged and more variable EMI responses measured with the EM38-MK2-1 meter at this site. The contrast in the EMI and pXRF data between these two sites was associated with differences in the mineralogy and lithologies of serpentinite- and nonserpentinite-derived soils.

INTRODUCTION

Little is known about the magnetic properties of soils and their spatial variability, but they are largely determined by the presence of iron oxides in different forms and concentrations [1]. The magnetic susceptibility (k) indicates the presence of iron-bearing minerals in soils and rocks. As *k* describes a material's ability to become magnetized, it is roughly proportional to the concentration of ferromagnetic minerals. However, the in-phase (IP) response of electromagnetic induction (EMI) sensors is also used to measure the magnetic properties of soils [2].

EMI surveys traditionally focus on the electrical properties of soils, neglecting the magnetic ones. In general, *k* of most soils is low and has negligible effects on electromagnetic field strengths; however, in magnetic soils, the presence of ferromagnetic minerals interferes with the efficiency of magnetic and electromagnetic sensors in detecting buried metallic objects [1].

The interpretation of *k* and IP data obtained from EMI sensors remains challenging due to various technical and environmental limitations, especially EMI sensor drift [3], arbitrary "zero level" [4], limited exploration depths [5], and changes in the sign (±) of the response at certain depths and in relation to the target position [6]. Regarding the latter, for EMI sensors operating in the vertical dipole orientation (VDO), the IP response experiences a sign change with depth [2]. For example, for the EM38 meter operating in the VDO, the response is positive for the upper 60 cm of the soil profile and weakly negative below 60 cm [2].

In the Piedmont of southeastern Pennsylvania and northeastern Maryland, areas of metamorphosed ultramafic rocks, which include serpentinite, occur along the state line [7]. Serpentinite is a Fe- and Mg-rich, subsiliceous rock formed principally through the metamorphic alteration of dunite, peridotite, or pyroxenite [8]. Soils formed over serpentinite have high Mg and low Ca levels, are low in essential nutrients, and have high concentrations of heavy metals [9]. During an EMI soil investigation conducted on a serpentine barren in southeast Pennsylvania, considerable variations in the IP and quadrature-phase (QP) responses were recorded. The cause of these unexpected results was attributed to the *k* of the soils formed over ultramafic rocks. As a result of these observations, a study was initiated to better understand the EMI response on soils formed over different lithologies in the northern Piedmont of southeastern Pennsylvania and determine whether the concentrations of different metals in these soils could be linked to the response of an EMI meter and *k*.

METHODS

Two study sites, Nottingham Park (39.7375° N, 76.0326° W) and Cochranville (39.8735° N, 75.9315° W), were selected for this study. These sites are located about 12 miles apart in southwestern Chester County, Pennsylvania. The soils on these two sites formed over different lithologies. The Nottingham Park site consists of two portions (Glenelg and Chrome soils) and is located over ultramafic rocks and schist. The Cochranville site consists mainly of Glenelg soil is situated over schist. The full article of this digest includes a detailed description of both sites.

Pedestrian surveys were completed across each site with the EM38-MK2-1 meter (Geonics Limited) operated in the VDO and a continuous recording mode with measurements collected at a rate of 1 s^{-1}. The meter's long axis was orientated parallel to the traverse direction and held about 5 cm above the ground surface. Walking in a back and forth manner across each site along essentially parallel traverse lines, a total of 4465 and 4874 apparent electrical conductivity (EC_a) and IP measurements were recorded with the EM38-MK2 meter at the Nottingham Park and Cochranville sites, respectively. The Geonics DAS70 Data Acquisition System was used with the EM38-MK2-1 meter to record and store both EMI and GPS data. At the time of the EMI surveys, soils were moist throughout.

At each study site, a minimum number of soil sampling points were selected by submitting the IP EMI data to the Response Surface Sampling Design (RSSD) program of the ESAP (ECe Sampling, Assessment, and Prediction) software. RSSD was used to statistically select a small number of sample locations based on the observed magnitudes and spatial distribution of the IP EMI data; 12 and 7 optimal sampling points were identified at the Nottingham Park and Cochranville sites, respectively.

Two additional measurements were made at each of the optimal sampling points with the EM38-MK2–1 at different heights (0 and 150 cm). Using these data, *k* of the soil was estimated following the procedures of Geonics

Figure 1: Scanning a sample for elemental characterization with a pXRF spectrometer operated in benchtop mode.

Limited [5]. Small grab samples were collected from the 0 to 30 cm and 30 to 60 cm depth intervals at each sampling point. The samples were dried and analyzed in sampling bags positioned at a constant distance from the portable X-ray fluorescence (pXRF) spectrometer mounted on a portable workstation (**Figure 1**). A DELTA™ Standard pXRF spectrometer (Olympus®) was used to determine the concentrations of 15 metals (K, Ca, Ti, Cr, Mn, Fe, Co, Cu, Zn, As, Rb, Sr, Zn, Ba, and Pb) in the samples from each site. The spectrometer was calibrated, and each sample was scanned for 60 seconds. For each sample, scans were repeated three times, and an average value was calculated.

	EC_a	IP	*k*
	mS m^{-1}	ppt	10^{-6} x SI
Min.	2.58	–171.64	–2850
25%-tile	10.86	–30.00	869
75%-tile	17.07	17.03	9562
Max.	31.29	358.52	44802
Mean	14.26	1.81	9077
SD	4.77	55.42	13748

Table 1: Basic statistics for the EMI data collected at the Nottingham Park site.

RESULTS AND DISCUSSION

Electromagnetic Induction

A statistical summary of the EMI data collected at the Nottingham Park site is shown in **Table 1**. The EC_a averaged 14.3 mS m^{-1}, ranging from 2.6 to 31.3 mS m^{-1}. The comparatively low averaged EC_a was assumed to reflect the effects of soil weathering and the relatively shallow depths to bedrock. The IP data averaged 1.8 ppt, with an exceptionally large range of -172 to 359 ppt. The *k* averaged 9077 × 10^{-6}, ranging from -2850 to 44802 × 10^{-6}. The unusually large ranges in the IP response and *k* were attributed to the presence of iron-bearing minerals in soils and rocks. Similar variations have been observed in urban areas (e.g., anthropogenic soils) where the induced electric currents are significantly affected by the presence of metallic artifacts (e.g., pipes). No evidence was found of former structures, mining activities, or cultural deposits within the Nottingham Park site.

Figure 2 shows the spatial distributions of the EC_a and IP data collected at the Nottingham Park site. In each plot, segmented lineations with more extreme and anomalous values can be identified. These lineations suggest layers of contrasting lithology and mineralogy.

In the IP data plot (**Figure 2**), the higher amplitude (±) anomalies indicate "stronger" source objects. A "stronger" source object may be more conductive or magnetic, larger, and/or located closer to the surface. The amplitudes of the anomalies also depend on the source objects' orientation in the earth's magnetic field. This is especially true for elongate bodies such as veins of highly magnetic materials.

Table 2 lists the basic statistics for the EMI data collected at the Cochranville site. EC_a averaged 10.3 mS/m^{-1}, ranging from -0.1 to 15.5 mS m^{-1}. The IP data averaged -24.8 ppt, ranging from -48.0 to 10.1 ppt, and *k* averaged 1897 × 10^{-6}, ranging from 798 to 5016 × 10^{-6}. EC_a/IP measurements and *k* estimates were noticeably lower in magnitude and less variable at the Cochranville site than at the Nottingham Park site. The contrast in the EMI data between these two sites indicates differences in mineralogy and lithologies.

Figure 3 shows the spatial distributions of EC_a and IP data at the Cochranville site. Spatial patterns are nondescript except for a noticeable cluster of anomalous values in

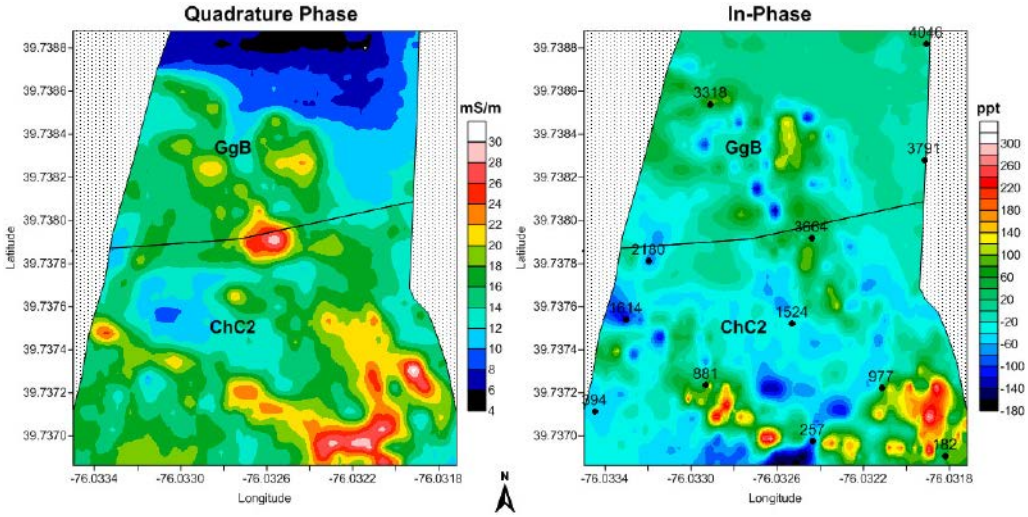

Figure 2: Plots of the Nottingham Park site showing spatial variations in EC_a (QP component) and susceptibility (IP component). The soil line was imported from the Web Soil Survey. Numbers and point symbols on the IP plot label the locations of the twelve optimal sample points.

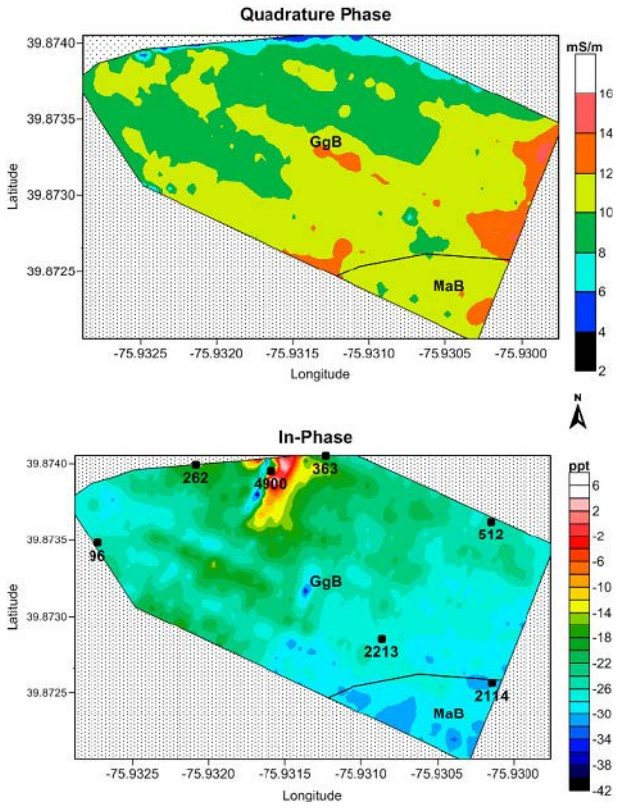

Figure 3: Plots of the Cochranville site showing spatial variations in EC_a (QP component) and susceptibility (IP component). The soil line was imported from the Web Soil Survey. Numbers and point symbols on the IP plot label the locations of the seven optimal sample points.

the extreme north-central portion of the site in the IP data plot. A small outcropping of the Peters Creek schist was evident in the vicinity of this anomalous pattern, and the area was associated with shallower depths to rock and contrasts in mineralogy.

X-Ray Fluorescence

At both sites, the concentrations of different metals varied over several orders of magnitude. Spatial and depth variability in these concentrations was evident at each site. Noticeable differences in the concentrations of each metal were also evident between the sites. The full article of this digest contains tables with the concentration of every measured element in the samples collected at both sites and depth intervals.

At both sites and depth intervals, Fe was the most abundant element. The average concentration of Fe increased with increasing soil depth. However, the average concentra-

	EC_a	IP	*k*
	mS m^{-1}	ppt	10^{-6} x SI
Min.	–0.12	–47.97	798
25%-tile	9.41	–28.05	1112
75%-tile	11.29	–22.58	2052
Max.	15.51	10.08	5016
Mean	10.31	–24.76	1897
SD	1.67	4.95	1490

Table 2: Basic statistics for the EMI data collected at the Cochranville site.

tion of Fe for the 0- to 60-cm depth interval was about 152% higher at the Nottingham Park site than at the Cochranville site. At both sites, the concentration of Ca decreased with increasing soil depth. At the Nottingham Park site, the mapped Chrome soil is known for its low Ca/Mg ratios [10]. However, the average concentration of Ca for the 0- to 60-cm depth interval was about 188% higher at the Nottingham Park site than at the Cochranville site.

The Chrome soil, which forms over serpentinite, typically has high Ni and Cr concentrations [9,10]. The average concentration of Cr for the 0- to 60-cm depth interval was about 11 times higher at the Nottingham Park site than at the Cochranville site. Although less abundant, the average concentration of Ni was markedly higher at the Nottingham Park site than at the Cochranville site (960 and <20 mg kg^{-1}, respectively).

Correlation between EMI and P-XRF Data

Because of the small number of soil samples obtained from each site, nonparametric statistics were used to access the relationship between EMI and pXRF data. **Table 3** summarizes the correlations between EMI and pXRF data for both depth intervals at the Nottingham Park site (only the eight most abundant metals are listed).

For the quadrature response (EC_a), correlations were mostly nonsignificant. However, a moderate and significant ($P = 0.05$) correlation was measured between EC_a and Mn. For the 30 to 60 cm depth interval, correlations between the different metals and EC_a were generally higher. Significant correlations were observed between EC_a and Cr, Mn, Fe, Co, and Ni. When operated in the VDO, the EM38-MK2-1 meter is relatively insensitive to materials at the surface, and its maximum sensitivity is at a depth of

	IP	*k*	K	Ca	Ti	Cr	Mn	Fe	Co	Ni
						0–30 cm				
ECa	–0.139	–0.444	–0.140	–0.133	0.007	0.402	–0.699*	–0.255	–0.280	–0.039
IP		0.661*	–0.629*	0.496	–0.643*	0.608	0.853***	0.867***	0.881***	0.874
k			–	0.857**	–0.789	0.399	0.602	0.525	0.561	0.566
						30–60 cm				
ECa	0.043	–0.354	–0.616	0.270	–0.470	0.639*	0.739**	0.684*	0.693*	0.711*
IP		0.625*	–0.546	0.325	–0.764*	0.427	0.491	0.418	0.382	0.654*
k			–0.148	0.325	–0.170	0.143	0.070	–0.084	–0.011	0.220

Table 3: Spearman's rank correlation coefficients for different EMI responses and element concentrations within the Nottingham Park site.

*, **, *** indicates significance at the $P = 0.055$, 0.01, and 0.001 levels, respectively.

about 40 cm. This depth–sensitivity may partially explain the higher correlation between EC_a and the metals in the 30 to 60 cm depth interval. At the Nottingham Park site, for the 0 to 30 cm depth interval, strong and significant ($P = 0.001$) correlations can be observed between the IP response and the Mn, Fe, and Co contents. For the 30 to 60 cm depth interval, less significant and mostly lower correlations were obtained between the IP response and the concentration of various metals. The relative abundance of Fe in the Chrome and Glenelg soils and the relatively high correlation between IP response and this metal support the premise that the soils and underlying ultramafic rocks contain significant amounts of ferromagnetic and/or paramagnetic minerals that affect the response of EMI sensors.

For the samples obtained from the upper 30 cm at the Nottingham Park site, significant ($P = 0.01$) correlations exist between *k* and the concentration of Ca. Nonsignificant correlations were obtained between *k* and the concentrations of the other metals. For samples collected from the 30 to 60 cm depth interval, correlations between *k* and the concentrations of the measured metals were nonsignificant.

Table 4 lists the correlations between EMI and pXRF data at the Cochranville site. For the 0 to 30 cm depth interval, strong, negative, and significant ($P = 0.01$) correlations were obtained between EC_a and the Mn and Fe contents; however, this relationship cannot be explained at this time. For the 30 to 60 cm depth interval, correlations were mostly nonsignificant between EC_a and the eight most abundant metals at the Cochranville site.

For both depth intervals, a significant correlation ($P = 0.05$) was obtained only between the IP response and Mn content. Compared with those at the Nottingham Park site, correlations were lower and nonsignificant between the IP response and Fe. Factors responsible for the lower and nonsignificant correlations may include lower Fe concentrations in the samples, effects of other physical parameters, and human-controlled variables related to differences in land management on the EMI response at the Cochranville site.

At the Cochranville site, significant correlations were obtained between *k* and the concentrations of Mn and K/Mn in the 0 to 30 cm and 30 to 60 cm depth intervals, respectively.

CONCLUSION

This study determined and associated the concentrations of different metals in soils formed over different lithologies in the Northern Piedmont of southeastern Pennsylvania with the responses of an EMI meter. The IP and QP responses of an EM38- MK2-1 meter and the estimated *k* were greater and more variable at the site underlain by micaceous schist and serpentinite than those at the site underlain by micaceous schist alone. The contrast in the EMI response and *k* between the two sites was associated with mineralogy and lithology differences. Spatial and depth variabilities in metal concentrations were evident at each

	IP	*k*	K	Ca	Ti	Mn	Fe	Co	Zr	Ba
						0–30 cm				
ECa	–0.509	–0.705	–0.547	–0.278	–0.402	–0.848*	–0.759*	–0.277	0.723	–0.045
IP		0.911	0.446	0.643	0.357	0.821*	0.482	0.232	–0.393	0.250
k			0.536	0.571	0.464	0.857*	0.571	0.214	–0.714	0.107
						30–60 cm				
ECa	–0.714	–0.589	–0.750	0.321	–0.107	–0.750	–0.536	–0.027	0.464	–0.598
IP		0.911	0.750	–0.143	0.000	0.786*	0.607	–0.027	–0.357	0.402
k			0.875**	0.071	0.375	0.821*	0.679	0.179	–0.571	0.232

Table 4: Spearman's rank correlation coefficients for different EMI responses and element concentrations within the Cochranville site.

*, ** indicates significance at the $P = 0.055$, and 0.01 levels, respectively.

site. Noticeable differences in the concentrations of each metal were also evident between the sites. Fe was the most abundant metal at both sites. However, the average concentration of Fe for the 0 to 60 cm depth interval was about 152% higher at the site underlain by micaceous schist and serpentinite than that at the site underlain by micaceous schists alone. At the first-mentioned site, for the 0 to 30 cm depth interval, strong and significant correlations were observed between the concentration of several metals and the IP response and *k*. These correlations were lower and mostly nonsignificant at the site underlain by micaceous schists only. For both sites, the correlations between the various metals and EC_a were mostly nonsignificant. The contrast in the EMI and pXRF data between these two sites was largely associated with differences in *k*, mineralogy, and lithologies.

REFERENCES:

[1] *R. L. Van Dam, J. M. H. Hendrickx, B. Harrison, B. Borchers, D. J. Norman, S. Ndur, C. Jasper, P. Niemeye, R. Nartney, D. Vega, L. Calvo, J. E. Simms, Proc. SPIE. 2004, 5415, 665.*

[2] *R. Dalan, in Remote Sensing – Applications, Alabama Press, Tuscaloosa, 2006.*

[3] *A. Tabbagh, in Seeing the Unseen—Geophysics and Landscape Archaeology, Taylor & Francis Group, London, 2009.*

[4] *R. E. North, J. E. Simms, SAGEEP 2007, 20, 264.*

[5] *Geonics Limited, EM38-MK2-1 ground conductivity meter operating manual, Geonics Ltd., Mississauga, 2009.*

[6] *A. Tabbagh, Archaeometry 1986, 28, 185.*

[7] *M. L. Crawford, W. A. Crawford, A. L. Hoersch, M. E. Wagner, in The Geology of Pennsylvania, Pennsylvania Geological Survey and Pittsburgh Geological Society, Harrisburg, 1999.*

[8] *J. D. Istok, M.E. Hayward, Soil Sci. Soc. Am. J. 1982, 46, 1106.*

[9] *J. L. Burgess, S. Lev, C. M. Swan, K. Szlavecz, Northeastern Naturalist 2009, 16, 366.*

[10] *M. C. Rabenhorst, J.E. Foss, Soil Sci. Soc. Am. J. 1981, 45, 1160.*

XRF and XRD Instruments for Geoscience

Both X-ray fluorescence (XRF) and X-ray diffraction (XRD) are frequently used analysis techniques for the analysis of rock, sediment, and other earth material samples. Geoscientists in the field use portable equipment to get real-time material chemistry (XRF) and mineralogy (XRD) of geo-logical samples as well as microscopes for traditional optical mineralogy and petrology. You can learn more about the functional principles of these instruments in the introduction on page 3.

XRF is a powerful, nondestructive technique for measuring elemental composition from magnesium (Mg) to uranium (U), from parts per million to 100%. Compact and portable XRF machines offer accurate, rapid elemental analysis on the go, making them an essential piece of equipment for anyone looking for laboratoryquality results. Prescreening using XRF enables priority sample selection for laboratory analysis, maximizing analytical budgets.

Whereas XRF instruments are used for the quantification of a specific element, XRD analyzers can identify and quantify crystalline compounds or phases in a sample. Portable XRD instru-ments allow the identification of all mineral phases in the field in realtime. Both complimentary methods together allow the coverage of large areas very quickly and enable users to make decisions in the field.

Five XRF Accessories for Mining and Geochemical Analysis Field Kit Handheld XRF analyzers can provide immediate, onsite elemental measurements for a range of mining and geochemical analysis applications, including mineral exploration, ore grade control, and environmental monitoring.

1. VANTA WORK STATION

The Vanta Work Station is a fully interlocked system that enables you to set up your handheld XRF analyzer on a benchtop or as a portable field laboratory. Simply power on the system, click the analyzer into place, close the lid, and start the test through a wireless connection or USB. While the test runs, you can perform other tasks and stay productive.

2. VANTA SOIL FOOT

Another helpful tool for hands-free analysis is the Vanta Soil Foot, which provides a stable three-point support for your XRF analyzer. This compact, cost-effective accessory is useful for the longer test times required in some mining and geochemical analysis applications.

3. VANTA FIELD STAND

If you need to test small items such as samples in cups or bags, then look no further than the Vanta Field Stand. The lightweight, portable test stand and shielded sample chamber are easy to set up, use, and pack away in just a few steps.

4. VANTA HOLSTER

Keep your XRF analyzer securely by your side and ready when you need it with the Vanta Holster.

5. VANTA TRANSPORT CASE

All Vanta handheld XRF analyzers come with a rugged, hard-shell transport case that can endure tough mining and field conditions. But if you ever need a replacement, just head to our web-store to order a new case.

You can find all mining and geology solutions of Olympus at https://www.olympus-ims.com/en/solutions/mining-geology

Geoscience: The Natural Sciences of the Earth

Geoscience includes all the natural sciences related to the structure, morphology, evolution, and dynamics of the Earth. Among them, geology deals with the origin, formation, and evolution of Earth, including its component materials and their structure. For geologists, grains and sediment are important since their study and analysis represent a powerful tool in classifying rocks or for describing a site's geomorphic setting. Characterizing the physical properties of grains, for example, is critical to determine the suitability of sediment for various uses or in the study of its geologic history. The main physical properties of grains are their size and size distribution, color, shape, and composition.

A basic tool for geoscientists is the optical microscope, which enables the magnification of sample images for analysis and careful inspection. The Olympus DSX1000 digital microscope is ideal for this application due to its large collection of easily interchangeable lenses, six observation methods available at the push of a button, fast macro to micro viewing, and accurate measurements thanks to a telecentric optical system.

Geoscientists study many types of sediments, including grains in a wide range of sizes and shapes. For example, gravel-sized particles have a nominal diameter of 2 mm, sand-sized particles have diameters ranging from ca. 2 mm to 62.5 µm, and clay is composed of particles having diameters less than 2 µm.[1] On the other hand, sands, for example, are usually composed of grains/units having different sizes and shapes, as shown in Figure 1. The wide range of sizes necessitates working with several magnifications and objectives with a range of working distances. Smaller samples require higher magnifications and objectives with shorter working distances. With conventional digital microscopes, this can be challenging since the objective can crash into the sample, potentially damaging it. This problem is solved with the DSX1000 digital microscope since its long working distance objectives enable the observation of uneven samples. These objectives are convenient for 3D samples since they combine the resolution of standard objectives with very long working distances, keeping the grains far from the optic to reduce the risk of damage.

Two important physical parameters of geological samples are their color and texture since they can be critical in the identification of the different minerals that compose the sample. Darkfield microscopy is the preferred method for imaging natural colors. On the other hand, accurate identification of texture requires a detailed observation of surface details, which necessitates illuminating the sample from above. The DSX1000 digital microscope can simultaneously work in brightfield and darkfield illumination methods from different directions. This feature, called MIX illumination,

Saint Vincent Paradise Beach, Caribbean Sea, Saint Vincent
Mineral sand with volcanic minerals
Field of view: 2.5 mm

makes the DSX1000 digital microscope ideal for the observation of geological samples.

Another important advantage the microscope offers to geoscience is its ability to acquire Z-stacks (focus stacking), which is a technique to combine images taken at different focus distances. The result is an image with a greater depth of field than any of the individual images. This is of particular interest for samples that have rough surfaces or with marked reliefs, like rocks or sediments.

For geoscientists, the DSX1000 digital microscope is a powerful tool for inspection geological sample. It combines low-magnification and high-magnification systems, offering a wide-magnification range in a single easy-to-use instrument. Moreover, the microscope possesses high-resolution, long working distance objectives that facilitate the capture of high-resolution, high-magnification images, enabling the inspection of fine details in the geological samples. In addition, the long working distance objectives provide ample space between the lens and sample to make observations without risking the optics. And with six observation methods available at all magnifications by simply pushing a button, the DSX1000 digital microscope offers geoscientists tremendous flexibility.

REFERENCES:

[1] *Wentworth, C. K. A Scale of Grade and Class Terms for Clastic Sediments. J. Geol. 30, 377–392 (1922).*

[2] *Rebecca Chandler. Discovering the Unseen Beauty of Sand Under a Digital Microscope. https://www.olympus-ims.com/en/insight/discovering-the-unseen-beauty-of-sand-under-a-digital-microscope/ (2021).*

What you can also find in this eBook

Another recent research article on the application of portable X-Ray fluorescence spectroscopy for soil analysis. Learn more about how this method was used to scan soils of three agricultural fields in New Mexico after the Gold King Mine spill on **page 49** of this eBook.

05 The Unseen Beauty of Sand Under a Digital Microscope

© Becky Swora - Adobe-Stock.com

Annegret Janovsky is a senior specialist for industrial microscopy at Olympus who uses her imaging expertise for a unique hobby: microscopic sand photography. In her spare time, she collects sands from beaches around the world to produce beautiful, detailed images of their grains using our DSX1000 digital microscope.

In the following pages of this eBook, you will find eleven selected images from the more than three hundred that the cristallographer and her friends and family have collected over the years; we talked to Annegret about her favorite ones.

Was there any particular time you got interested in looking at sand?

Annegret: In 2015, I remembered sand I saw 25 years ago on my first travel with my future husband. And there was such a lovely lake in Scotland, it was called Loch Achilty. But back then we did not know the name of that lake. And at its bank, we found a sand I had never seen before. It was so crazy because it was not such a bright sand such as from the Mediterranean Sea or the Baltic Sea. Also, it was violet. I was so fascinated by this sand, but in those days, I never thought about collecting it or imaging it.

Later, when we got the first digital microscopes at Olympus, I was looking for good samples to see the quality of the images. I remembered this sand, but it took a while before I was able to collect any. We had to go back to Scotland to look for this lake. But there was no help on the Internet; nobody knew anything about this lake with violet sand. However, after two days, we were lucky and found this special sand again. And yes, after collecting a small amount of violet sand, I was interested in its composition, so I had a look using a DSX1000 digital microscope, and it was very interesting.

This was the beginning of my sand collection.

That is a nice way of getting into a new field of imaging and a new hobby at the same time. Since then, have you been collecting different types of sand on different holidays and travels?

Annegret: Yes, of course. But my colleagues, family, and friends all know of my hobby, so they collect sand for me when they travel. Currently, I have a collection of over 300 sands. Sometimes they are very similar to other sands I already have, but most of the sands are very interesting. Within almost every new sand is a new world.

The images in this eBook are only a sample of everything you have. Can you tell us more about the image of the violet sand on page 6?

Annegret: Yes, this is my very first sand, the one I mentioned before from Loch Achilty. On the large image at the bottom, you can see a macro photo of the lake. This is a pure mineral sand. It is violet, and, of course, has bright or natural colored grains. But there is also a range of dark grains included.

X-ray diffractometry analysis performed by one of my Olympus colleagues using our TERRA™ pXRD instrument have shown that the purple sand grains are garnets.

Loch Achilty, Scotland, UK
Mineral sand
Field of view: 3.2 mm

Star Sand, Taketomi Island, East China Sea, Japan
Biogenic sand made of forams
Field of view: 14 mm

The next image on page 7 is very interesting. What is the secret behind the shape of this sand?

Annegret: My two most important sands are the purple one we just discussed, as it was my first sand, and this sand, which is from Taketomi, a Japanese island in the East China Sea. It is so impressive—can you see the stars? This is organic sand, and it is composed of the shells of foraminifera—microscopic organisms that form hard shells of various shapes. These grains are particularly amazing as the whole shell is formed by a single-celled organism.

This is fascinating. How big are these grains?

Annegret: The foraminifera are relatively large at 2–3 mm each, so this image was taken using a 3x XLOB objective from Olympus. These objectives are useful for 3D samples because they combine the resolution of standard material objectives with very long working distances, reducing the risk of sand grains hitting the optics!

Toronto Islands,
Lake Ontario, Canada
Heavy mineral sand with pink and red garnets, black magnetite
Field of view: 2 mm

The next image that is really impressive is the one on page 8. What is the story behind that one?

Annegret: This is a sand that was collected by my daughter. It is from Lake Ontario near Toronto, Canada. In the large image you can see the photo of the beach with this reddish and black material. The reddish grains are garnets and the black ones are magnetite. It is a typical heavy mineral sand. Due to their weight, heavy minerals like garnet or magnetite can be accumulated on beaches, with lighter minerals being carried away by wind or by water.

This sand was imaged using a 10x XLOB objective. As with the first image, these grains are small and have interesting colors. From my experience of imaging different materials, I knew that darkfield microscopy is best for imaging natural colors. It is also useful to have a light source above the sample to capture surface details. The DSX1000 allows simultaneous brightfield and darkfield illumination from different directions, which is ideal for these types of samples. In fact, all of the images featured here were taken using MIX illumination.

Figure 1: Organic sand collected from Lahinch in Ireland. This sand is composed of units having several sizes and shapes, forming a heterogeneous mix of purely biogenic components.[2]

Another fascinating image is the one shown on page 9. Where did you find this sand?

Annegret: This is sand from Lahinch in Ireland, and it's completely different from the heavy mineral sand in the last photo from Lake Ontario and from the sand from Loch Achilty, as it is composed of biogenic components. Therefore, it is not possible to find out the origin of all the broken bits and pieces you can see in the image. They could be shells, foraminifera, or other organic materials; I don't know. But you can see a glassy, Y-shaped piece in the center of the image; this is a sponge spicule. And in the left bottom corner, there is another interesting shape. It is a fragment of a sea urchin spine.

A crucial advantage to using the DSX1000 digital microscope for imaging sand is its ability to acquire Z-stacks—all of the images here were acquired using focus stacking.

Lahinch, Atlantic Ocean, Ireland
Biogenic sand with a Y-shaped sponge spicule, sea urchin spine
Field of view: 2.5 mm

CURRICULUM VITAE DR. ANNEGRET JANOVSKY

Work experience

Since January 2021	Product Marketing Manager Industrial Microscopy EMEA SSD, Olympus Europa SE & Co. KG (OEKG)
April 2017 – December 2020	Sales Specialist Industrial Microscopy, OLYMPUS Deutschland GmbH
June 2015 – March 2017	Territory Manager Manufacturing, Sales of all industrial product lines (NDT, RVI, ANI and Microscopy), OLYMPUS Deutschland GmbH
Mai 2002 – June 2015	Sales Microscopy in Material and Life Science, OLYMPUS Deutschland GmbH

Education

09/1997 – 08/1999	PhD studies at the University of Leipzig Graduation with the academic degree Dr.rer.nat in Mineralogy
09/1988 – 07/1993	Studies of Crystallography at the University of Leipzig Graduation as "Diplom-Kristallographin" Main focus on Mineralogy and Microscopy
Additional Skills/ Hobby	Microphotography: Grains of sand

Brandon river mouth, Ireland
Mineral sand
Field of view: 3 mm

Massa Carrara, Mediterranean Sea, Italy
Mineral sand
Field of view: 2.5 mm

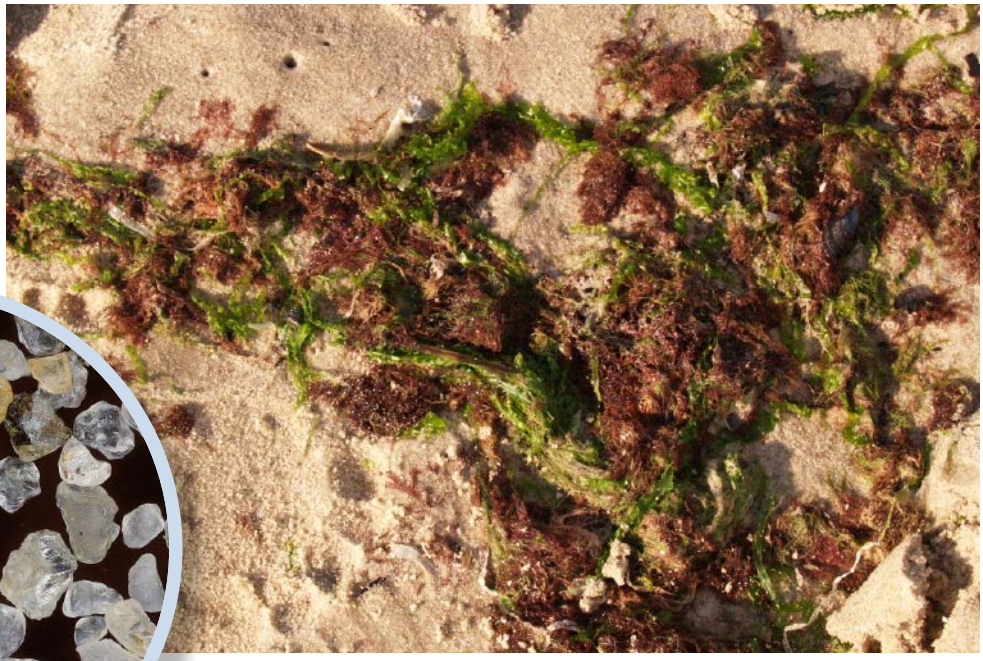

Warnemünde,
Baltic Sea, Germany
Mineral sand, mainly quartz
Field of view: 3.1 mm

Hurghada, Red Sea, Egypt
Biogenic sand with forams
Field of view: 12.8 mm

Godafoss Waterfall, Iceland
Volcanic glass
Field of view: 1 mm

Playa del Verodal, El Hierro, Canary Islands, Spain
Volcanic mineral sand
Field of view: 8 mm

Whitefish Lake, Montana, USA
Mineral sand
Field of view: 8.1 mm

06 Portable X-Ray Fluorescence Spectroscopy Analysis of Agricultural Soils After the Gold King Mine Spill

G. Jha, S. Mukhopadhyay, *et al.*

ABSTRACT

In 2015, a million liters of heavy metal–contaminated water spilled into the Animas River from the Gold King Mine (Colorado, USA), attracting national attention about the water quality and agricultural production in the affected areas. In response to the concerns, surface soil elemental concentrations were analyzed in three New Mexico agricultural fields to determine potential threats to agronomic production. The irrigated fields were scanned using portable X-ray fluorescence (pXRF) spectrometry to monitor the spatiotemporal variability of lead (Pb), arsenic (As), copper (Cu), and chromium (Cr) before and after the growing season for 3 years. The geostatistical model with the lowest RMSE was chosen as the optimal model. The spatial dependence between the measured values exhibited strong to moderate autocorrelation for all metals except for As, for which spatial dependence was strong to weak. Some areas exceeded the soil screening limit of 7.07 mg As kg^{-1}. All sampling locations were below the screening limit at last sampling time in 2019. Mixed models used for temporal analysis showed a significant decrease only in As below the screening value at the end of the study. Results indicate that the agricultural soils were below the soil screening guideline values.

1 INTRODUCTION

On August 5, 2015, an inadvertent breach of the Gold King Mine (GKM) released ~11.3 million L of acid mine drainage into Cement Creek at the headwaters of the Animas River.[1] Approximately 2032 kg lead (Pb), 499 kg zinc (Zn), and 93 kg arsenic (As), among others, were released and flowed downstream.[2] The GKM is "one of an estimated 23000 abandoned mines dotting the state of Colorado".[3] The USEPA notes that "mining operations have greatly disturbed the land, adding to existing highly mineralized conditions in many areas that cause acidic conditions that release heavy metals to the surrounding environment".[3] They specifically note the prevalence of aluminum (Al), lead (Pb), zinc (Zn), cadmium (Cd), copper (Cu), iron (Fe), and manganese (Mn) as contributing polluters to surface water, subsurface water, surface soils, and stream sediments.

In northwestern New Mexico, alfalfa hay, pumpkin, watermelon, pepper, tomato, and other specialty crops are of strong economic importance. The irrigation water is delivered to farms through a series of community ditches or canals. At the time of the GKM spill, most farmers immediately closed their irrigation gates and ditches, allowing the most pollutant-laden water to pass down the river without entering their irrigation systems.

A substantive portion of the released metals were associated with suspended solids in the river. Sediments rich in Fe, Al, and other metals, however, were deposited as reddish orange sludge along the banks and throughout the river channel. A rapid assessment of the elemental concentration of riverbank sludge, irrigated croplands, and upland (non-irrigated) soils of the river valley affected and unaffected by the GKM was conducted.

In this assessment, Fe, Cu, Zn, As, and Pb increased in the order of control (non-irrigated) soils < irrigated soils < riverbank alluvium < riverbank sludge. Additionally, the riverbank sludge had concentrations of Pb (n = 9) that ranged from 509 to 859 mg kg^{-1}, all above the USEPA residential screening limit of 400 mg kg^{-1}. Therefore, a comprehensive monitoring plan was initiated out of concern that as hydrologic pulses occur, the metal-laden sludge deposited on the bottom of the river would become resuspended, enter the irrigation systems, and lead to an increase in toxic metal concentration in soils used for farming.

The deleterious effects of toxic metals to human health are well documented. Briefly, the main health effects associated with high levels of elements include nervous system disorders, liver and kidney failure and damage, anemia, cancer, cardiomyopathy, gastroenteritis, osteomalacia, brain damage, hematologic effects, hypertension, intestine tract distress, and tissue lesions, among others.[4]

Widespread concern exists as to the safety of produce if irrigated with potentially metal-laden water from the Animas River. The objective of this study was to perform a spatio-temporal analysis of elemental concentrations in agricultural soils of the Animas River watershed over a period of three cropping seasons (2017–2019) and compare monitored values to determine their potential threat to agronomic production. We hypothesized that the soil concentrations of several elements would increase over time in response to irrigation with water from the Animas River.

2 MATERIALS AND METHODS

2.1 General study area

The study was conducted on irrigated farm fields in San Juan County, NM. Geologically, the area is comprised of shale, sandstone, limestone, dolomite, and volcanic rock outcrops. Soils of the area are Alfisols, Aridisols, Entisols, and a few Mollisols. Soil temperature regime is dominantly mesic, with an aridic or ustic-aridic moisture regime.[5] The Koppen climate classification of the area is BSk (cold semiarid).[6] Soils feature carbonatic, mixed, or smectitic mineralogy. In this arid to semi-arid climate, almost all crops must be irrigated to produce sufficient yields. The soil series on the studied fields are described as Fruitland, Turley, and Garland.

2.2 Fieldwork

Three irrigated farm fields of 30, 17, and 8 ha were evaluated as part of this study. With the perimeter of each field, a random sampling scheme was established in ArcGIS (ESRI), which created a sampling density of ~3.2 points ha^{-1}. This resulted in a total of 175 points (two fields with 50 points each and one field with 75 points). The pre-determined sampling locations were downloaded into an eTrex (Garmin) handheld global positioning receiver for field geolocation. Elemental data collection was performed using a DP-6000 portable X-ray fluorescence (pXRF) spectrometer (Olympus®).

[7] Prior to operation, the instrument is checked with a stainless steel alloy, then operated on line power (110 VAC) using a portable power inverter at 15–40 keV. The instrument was operated in Soil Mode at 30 s per beam such that one complete scan was completed in 90 s. Validation of instrument performance was accomplished via National Institutes of Standards and Technology (NIST)-certified reference materials. The average recovery percentages were determined for all four sampling times during the study that did not vary by more than 15% from the actual certified values for the elemental concentrations.

The pXRF field sampling was conducted over 3 years. The Animas River watershed has only one growing season (from mid-April to mid-November). Portable XRF scans in November were considered to represent both post-growing conditions for the current season and pre-growing conditions for next growing season. Scanning was performed in an identical manner at the same sampling locations to allow for temporal analysis.

2.3 Statistical analysis

Descriptive statistics and correlation analysis of pXRF metal(loid) was analyzed in R studio (version 3.4.1). Pearson's correlation matrix was plotted using the *corrplot* function combined with the significance test ($p \leq .05$) in *Hmisc* package. Temporal changes in metal(loid) s were assessed in SAS version 9.4 using a design-based linear mixed model approach with sampling time as the fixed effect and random effects for field and the sampling time by field interaction. Additionally, a repeated statement fitted an unstructured covariance of the repeated measurements (the four sampling times) from the randomly chosen but repeatedly sampled locations within fields. When time was significant, pairwise comparisons among the four measurement times used model-based estimates and standard errors. Significance was set at $p \leq .05$. Temporal analysis of significant changes in metal(loid) concentrations were analyzed using SAS version 9.4.

2.4 Geostatistical analysis and spatiotemporal mapping

Spatiotemporal variability maps were interpolated for four metal(loid)s of concern using pXRF total concentrations sampling four times over a period of three growing seasons. Three different models were fit to total metal(loid) concentrations of As, Cr, Pb, and Cu. Root mean square error was considered as a measure of model performance, and the model with the lowest RMSE value was selected for each metalloid as the best fitted model for kriging interpolation[8]. Semivariogram parameters were interpreted to understand the insights of the fitted model. Sill is the variance on the dataset without knowing the spatial location, and nugget is the amount of variance that is not explained by the model as the distance between observations approaches zero (Allan, 2018). Nugget to sill ratios were interpreted to understand the strength of spatial dependence between sampling points. Semivariogram ranges were also interpreted as the range of spatial autocorrelation determining the strength of metal concentrations scanned using pXRF at one geographic location in the field relative to another scanning location separated by a distance. Spatial maps were interpolated using ordinary kriging in ArcGIS version 10.2.2 (ESRI) using the weighted averages of the known concentrations of metal(loid)s.

3 RESULTS AND DISCUSSION

3.1 Summary statistics

Total mean soil elemental concentrations were detected in the order Pb > Cu > Cr > As for each growing season. The Pb and Cu concentrations at all locations were below the soil screening levels of 400 and 3100 mg kg^{-1}, respectively. During the pre-growing 2017 season, the average total metal concentrations in the three fields were 50 mg kg–1 (Pb), 23 mg kg^{-1} (Cu), 17 mg kg^{-1} (Cr), and 8 mg kg^{-1} (As). In observing the maximum, median, and mean concentration values for As, at least one or more sampled locations exceeded the soil screening limit (SSL) value of 7.07 mg kg^{-1} recommended by the New Mexico Environment Department.[9] In total, 46.3% (number of locations exceeded/total number of scanning locations = 81/175) sampling locations exceeded the SSL for As during the 2017 pre-growing study period, and 43.4% (76/175) samples exceeded the SSL in the 2017 post-growing season. In the 2018 and 2019 post-growing seasons, the percentage of locations that exceeded the SSL values was reduced to 16.6% (29/175) and 7.4% (13/175), suggesting temporal decreases.

3.2 Correlation analysis between elements analyzed using pXRF

Several metals showed significant correlations with each other in the soil matrix. Combining the data from all three fields, Cu and Pb were positively correlated with significant correlation coefficient values ranging from .76 to .90 when metal concentrations pooled for all three fields were correlated and compared respective to the four sampling times.

These results were similar to the findings by other researchers using pXRF for multi-elemental analysis with strong correlations between Pb and Cu.[10,11] Cu and Cr, Pb and Cr, As and Cr, and As and Cu showed weak or moderate correlations with each other or sometimes negative correlations. Additional works in the Animas River watershed after the GKM spill established that there was an association between Pb, Cu, and Zn and Fe-minerals such as jarosite, goethite, and clays in sediment.[12]

3.3 Spatiotemporal variability of metals in agricultural fields

Figures 1–4 depict the spatial distribution of the four metal(loid)s of interest interpolated over the four sampling dates. There were some hotspots of As in the fields until the third sampling date. All soil As concentrations were below the SSL of 7.07 mg kg^{-1} and therefore were considered below the risk assessment guidelines during the last sampling date in the 2019 post-growing season (**Figure 1**).

Cr concentration increased in the soil collected during the last sampling time for all three fields (**Figure 2**). This increase was more noticeable in fields 1K and 3K, which were under pivot irrigation. Field 2S, which was under furrow irrigation, had an increase in Cr at some locations. Regions of higher Pb concentration also showed high Cu concentration. However, Cu (**Figure 4**) does not show much variability after any irrigation season. Lead and Cu show similar adsorption behavior and tend to coexist in soil,13 however, lead tends to become less soluble with increasing pH of soil solution as more calcium carbonate is added through irrigation

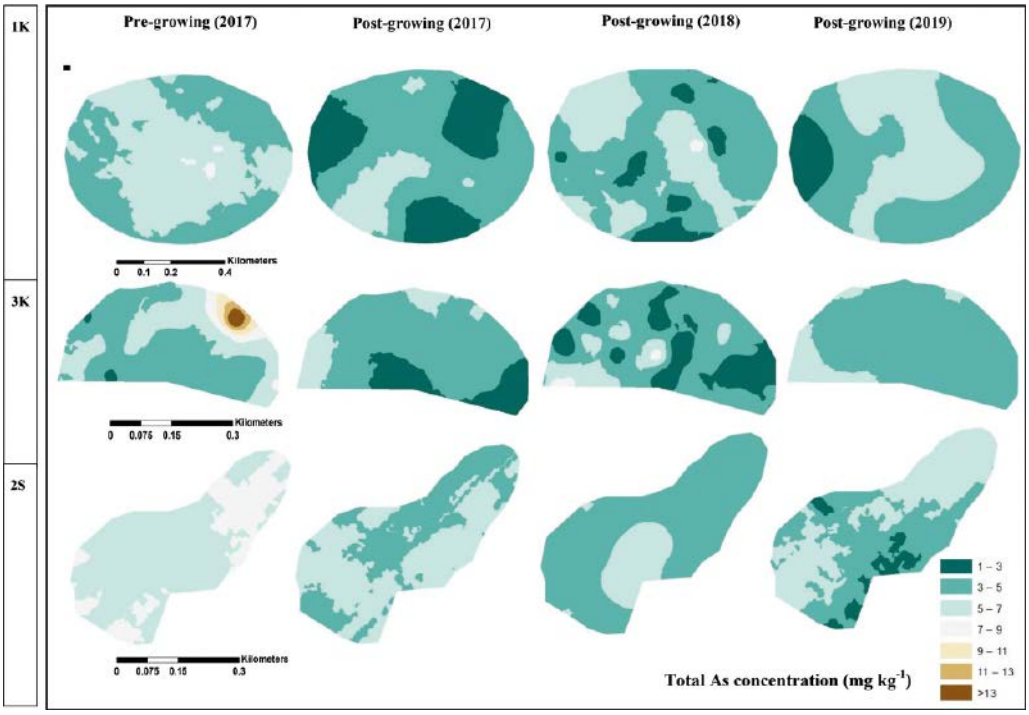

Figure 1: Spatial variability interpolation maps of total As concentration in three agricultural fields under irrigated conditions for four sampling dates from 2017 to 2019.

water. River water was collected near the inlet irrigation gates for three growing seasons and analyzed for all metal concentrations, showing values below the USEPA screening levels.

Samples located closer to each other by distances less than the range are spatially correlated and contribute to kriging predictions.[14] The nugget to sill ratios for As were moderate for fields 1K and 2S. The nugget to sill ratio for field 3K was moderate for pre- and post-growing 2017 and strong for post-growing 2018 but was weak for post-growing 2019. Nugget to sill ratios for Cr, Pb, and Cu were moderate to strong.

Weak spatial dependence of As is due to variability at scales smaller than the two closest sampling points in any one field. The inability to capture small-scale variability for As in this study was also due to the increasing number of nondetectable As readings using the pXRF. The nugget to sill ratio for Cr, Cu, and Pb showed strong to moderate spatial dependence during all four sampling times for all three fields. The spatial dependence estimated using semivariogram parameters are predictions at unsampled locations in the field based on the known values from sampled locations.

Maps based on kriging predictions can be used for future study by sampling locations less than the range in fields. In furrow-irrigated fields, it is important to understand that redox conditions might be different in the top of ridges and bottom of furrows. In this study, samples were scanned from random locations with a mix of both ridge and furrows without any biased separation. Therefore, it is important to sample both locations in furrow-irrigated systems to get a proper representation of elemental concentration in future studies.

3.4 Temporal analysis

At the time of the GKM spill it was hypothesized that there would be a surge in metal concentrations in agricultural field soils as irrigation resumed once the irrigation ban was lifted. There was a significant increase in total Cr concentration at the end of three growing seasons. We also measured a significant decrease

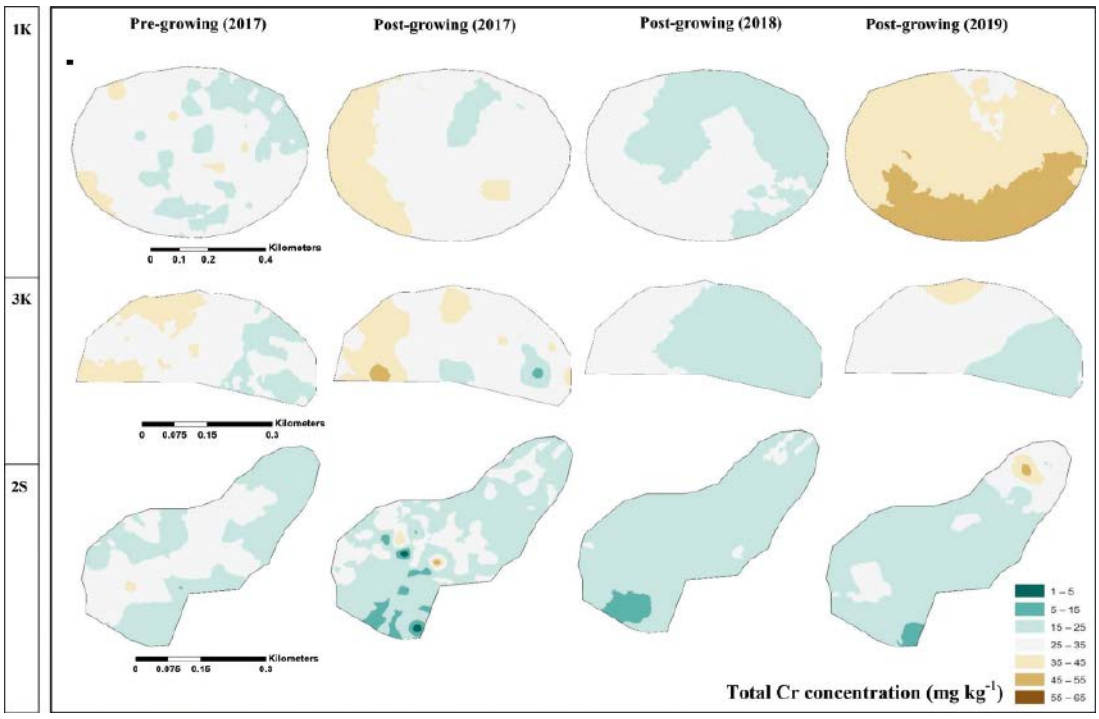

Figure 2: Spatial variability interpolation maps of total Cr concentration in three agricultural fields under irrigated conditions for four sampling dates from 2017 to 2019.

in total As and Pb at the third sampling date in post-growing 2018 (**Figures 1** and **2**).

Contrary to the hypothesis of this study, As decreased 2.3 ± 0.3 mg kg^{-1} from March 2017 to November 2019. The estimated As (5.3 ± 0.2 mg kg^{-1}) after three growing seasons decreased to below the soil screening level. However, there was a significant increase (9.4 ± 1.3 mg kg^{-1}) in mean Cr concentration. This study did not analyze the oxidation state of Cr and focused only on total concentration. It is recommended for future studies to look into Cr speciation and how it interacts with soil matrix and plants. Decreases in average Cu concentrations (1.7 ± 0.9 mg kg^{-1}) were not significant, whereas decreases in mean Pb concentration (1.0 ± 2.9 mg kg^{-1}) were significant between March 2017 and November 2018 but not between March 2017 and November 2019. Both Cu and Pb were below the soil screening level for all fields sampled at all sampling times.

4 CONCLUSIONS

This study evaluated agricultural fields in the Animas River watershed, NM, for four potential metal(loid) contaminants of concern (Pb, As, Cu, Cr) following the GKM spill of 2015. Portable X-ray fluorescence was used to determine metal(loid)s at a total of 175 sampling locations spread across three fields over 3 yr. Geostatistical models were fit to each metal(loid) for each agricultural field for each sampling date. Spatial interpolation was used to infer spatial variation, and mixed models were used to infer the temporal variation in metal(loid) concentrations. Spatial interpolation revealed an overall decrease in surface soil As concentration between 2017 and 2019. However, there were some areas in the fields where As concentrations still exceeded the regional soil screening limits of 7.07 mg kg^{-1} for the first three sampling times. Arsenic concentration in soils decreased to significantly below the soil screening value (7.07 mg kg^{-1}) by the end of 2019 growing season for all fields. We found

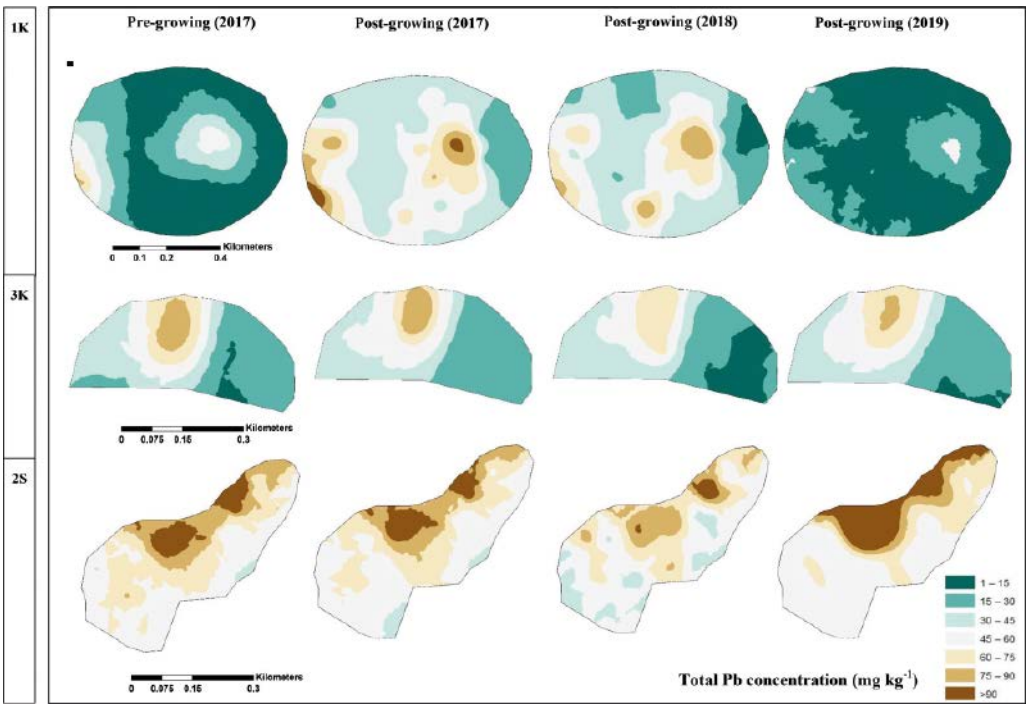

Figure 3: Spatial variability interpolation maps of total Pb concentration in three agricultural fields under irrigated conditions for four sampling dates from 2017 to 2019.

that all three fields were below the risk assessment guidelines. This study is important in environmental monitoring of agricultural soils after the GKM spill of 2015 to help farmers and consumers make informed decisions of the field soils used for growing important crops like alfalfa, corn, and pumpkin in northwestern New Mexico.

REFERENCES:

[1] *New Mexico Environment Department (NMED). (2015). Gold King Mine wastewater spill of Wednesday, August 5, 2015: Timeline and archive updates. https://www.env.nm.gov/animas-river-timeline.*

[2] *Chief, K., Artiola, J. F., Wilkinson, S. T., Beamer, P., & Maier, R. M. (2015). Understanding the Gold King Mine spill (Fact Sheet). University of Arizona.*

[3] *USEPA. (2015). Gold King Mine - watershed fact sheet. https:// www.epa.gov/sites/production/ files/2015-08/documents/ goldkingminewatershed-factsheetbackground.pdf.*

[4] *Brevik, E. C., & Burgess, L. C. (2013). Soils and human health. CRC Press.*

[5] *Soil Survey Staff. (2006). Land resource regions and major land resource areas of the United States, the Caribbean, and the Pacific Basin. https://www.nrcs.usda.gov/wps/portal/nrcs/detail/soils/ survey/cid=nrcs142p2_053624.*

[6] *Kottek, M., Grieser, J., Beck, C., Rudolf, B., & Rubel, F. (2006). World map of the Köppen-Geiger climate classification updated. Meteorologische Zeitschrift, 15(3), 259–263. https://doi.org/10.1127/0941- 2948/2006/0130.*

[7] *Weindorf, D. C., & Chakraborty, S. (2016). Portable X-ray fluorescence spectrometry analysis of soils. Soil Science Society of America Journal, 84(5), 1384–1392. https://doi.org/10.1002/saj2.20151.*

[8] *Ritter, A., & Muñoz-Carpena, R. (2013). Performance evaluation of hydrological models: Statistical significance for reducing subjectivity in goodness-of-fit assessments. Journal of Hydrology, 480, 33–45. https://doi.org/10.1016/j.jhydrol.2012.12.004.*

[9] *New Mexico Environment Department (NMED). (2017). Risk assessment guidance for site investigations and remediation. Volume I: Soil screening guidance for human health risk assessments. https://www.env.nm.gov/wp-content/uploads/ sites/12/2016/11/ Final-NMED.*

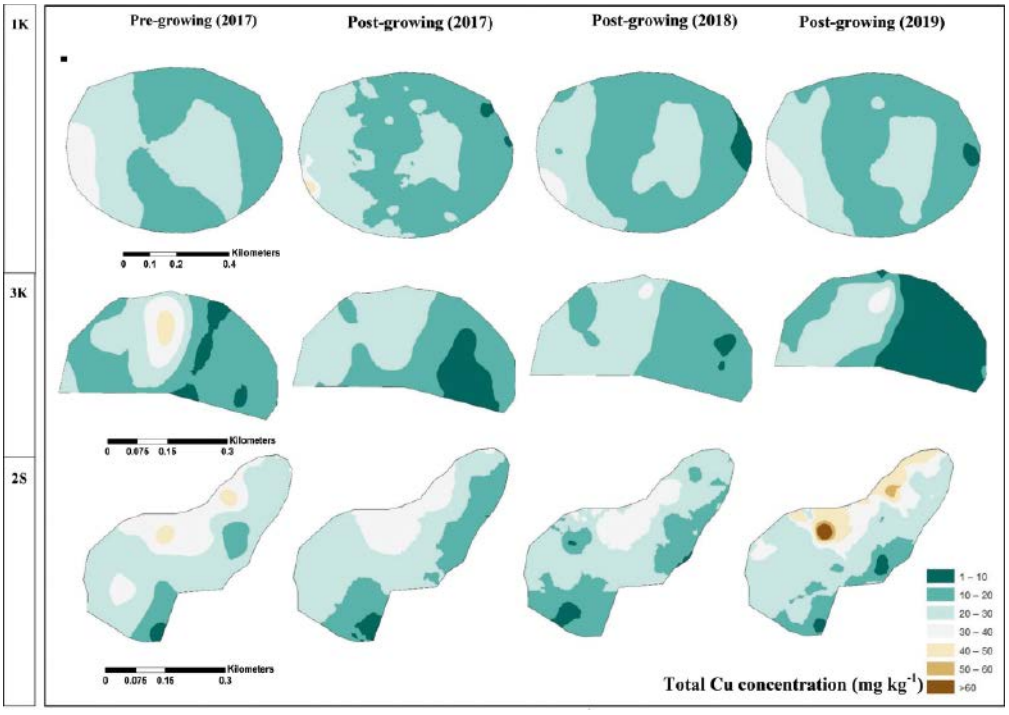

Figure 4: Spatial variability interpolation maps of total Cu concentration in three agricultural fields under irrigated conditions for four sampling dates from 2017 to 2019.

[10] *Chakraborty, S., Man, T., Paulette, L., Deb, S., Li, B., Weindorf, D. C., & Frazier, M. (2017). Rapid assessment of smelter/mining soil contamination via portable X-ray fluorescence spectrometry and indicator kriging. Geoderma, 306, 108–119. https://doi.o.*

[11] *Paulette, L., Man, T.,Weindorf, D. C.,&Person, T. (2015). Rapid assessment of soil and contaminant variability via portable X-ray fluorescence spectroscopy: Copşa Mică, Romania. Geoderma, 243, 130–140. https://doi.org/10.1016/j.geoderma.2014.12.025.*

[12] *Rodriguez-Freire, L., Avasarala, S., Ali, A. M. S., Agnew, D., Hoover, J. H., Artyushkova, K., Latta, D. E., Peterson, E. J., Lewis, J., Crossey, L. J., Brearley,A. J., Cerrato, J.M.,&Brearley,A. J. (2016). Post-Gold King Mine spill investigation of metal .*

[13] *Sharma, P., & Dubey, R. S. (2005). Lead toxicity in plants. Brazilian Journal of Plant Physiology,.*

[14] *Cambardella, C. A., Moorman, T. B., Novak, J. M., Parkin, T. B., Karlen, D. L., Turco, R. F., & Konopka, A. E. (1994). Field-scale variability of soil properties in central Iowa soils. Soil Science Society of America Journal, 58(5), 1501–1511. https://doi.*

Advanced Optical Metrology

Part V

Corrosion

Introduction

Corrosion is a natural process consisting of the chemical, biochemical, or electrochemical reaction between a given material and its environment, producing a deterioration of the material and its functional properties. Because of this, corrosion is one of the most common ways that a material fails. Today, the demands on materials' corrosion resistance are increasing to improve operational reliability and extend product life.

Corrosion is an important industrial problem with an estimated global cost equal to approximately 3.4% of the worldwide gross domestic product in 2013.[1] Besides the enormous economic implications, corrosion in structures, critical pieces, and equipment can cause severe accidents, putting people at risk. For example, corrosion fatigue led to the sudden collapse of the Silver Bridge (Point Pleasant, OH) in 1967, which resulted in the loss of 46 lives and cost millions of dollars.[2] Moreover, corrosion can affect health due to pollution from corrosion products, cause the depletion of natural resources, and negatively impact the appearance of materials.

The majority of corrosion processes involve electrochemical redox reaction; however, the corrosion type depends on the environmental conditions and the material's characteristics. One common way to distinguish corrosion is between generalized and localized. The former occurs homogeneously over the entire surface of the material and causes almost total deterioration, making it the most damaging corrosion and, at the same time, the most easy to identify. It is a common problem in the construction industry, affecting ferrous materials that are not alloyed with other stainless materials.

On the other hand, localized corrosion is more difficult to detect, making it a greater risk than **generalized** corrosion. **Localized** corrosion occurs at specific points in a material, depending on its geometry and the environmental conditions. Among the several forms of localized corrosion, *pitting* and *intergranular* corrosion are the most critical. Pitting corrosion[3] occurs mainly in passivated materials. When oxidizing agents accumulate and the pH of the medium increases, the passiva-

tion layer deteriorates, generating corrosion in localized areas. It develops mainly in the direction of maximum deformation and is accompanied by peeling of individual metal particles so that it can be detected visually without the use of instruments. On the other hand, intergranular corrosion[4] is caused by the segregation of impurities at the grain boundaries or by the enrichment/depletion of one or more alloy elements in the areas surrounding the grain boundary. This type of corrosion cannot be detected by the naked eye, so nondestructive control methods must be used.

Another important type of localized corrosion is *stress corrosion cracking*[5] (SCC), which is caused by the synergistic effect of a susceptible material, a corrosive environment, and a minimum stress. SCC results in rapid, catastrophic failure via cracking, which originates in the material surface and propagates as a response to the applied stress.

Corrosion wear (or tribo-corrosion)[6] is the result of a chemical reaction accelerated by temperature. It is usually caused by moisture or other corrosive liquid or gas. In addition, wear can result from the dynamic contact between two surfaces, such as abrasion and erosion. Corrosive wear is defined as the damage caused by the synergistic attack of wear and corrosion when wear occurs in a corrosive environment. Rust, or oxidation, is the best-known form of corrosive wear.

Microbiologically induced corrosion[7] (MIC) is another relevant corrosive route, where an electrochemical process produces the deterioration of a metallic material where microorganisms (bacteria, fungi, or algae) are involved, either initiating, facilitating, or accelerating the corrosive attack mechanism.

Two critical tools to detect and classify corrosion types are optical and electronic microscopes. Samples are treated using standardized processes to reveal the material's microstructure (metals in particular), which are affected by composition, processing conditions, and post-processing variables. The use of microscopy is a key element in failure investigations and usually provides the necessary information to determine the cause of failure. However, the analysis of micrographs is not straightforward. For example, the cracks caused by SCC are very narrow and closed, making visual identification of this type of cracking before a failure difficult. Therefore, the use of instruments that provide high resolution is critical to assess the state of a given material sample.

REFERENCES:

[1] *Bowman, E. et al. International Measures of Prevention, Application, and Economics of Corrosion Technologies Study. NACE Int. 1–216 (2016).*

[2] *Davis, J. R. Corrosion: Understanding the Basics. (ASM International, 2000).*

[3] *Vargel, C. Pitting corrosion. in Corrosion of Aluminium 163–183 (Elsevier, 2020). doi:10.1016/B978-0-08-099925-8.00014-4.*

[4] *Vargel, C. Intergranular corrosion. in Corrosion of Aluminium 185–197 (Elsevier, 2020). doi:10.1016/B978-0-08-099925-8.00015-6.*

[5] *Raja, V. S. & Shoji, T. Stress Corrosion Cracking: Theory and Practice. (Elsevier Science, 2011).*

[6] *Li, D. Y. Corrosive Wear. in Encyclopedia of Tribology (eds. Wang, Q. J. & Chung, Y.-W.) 590–596 (Springer US, 2013). doi:10.1007/978-0-387-92897-5_866.*

[7] *Telegdi, J., Shaban, A. & Trif, L. Microbiologically influenced corrosion (MIC). in Trends in Oil and Gas Corrosion Research and Technologies 191–214 (Elsevier, 2017). doi:10.1016/B978-0-08-101105-8.00008-5.*

[8] *Was, G. S. Corrosion and Stress Corrosion Cracking Fundamentals. in Fundamentals of Radiation Materials Science 857–949 (Springer New York, 2017). doi:10.1007/978-1-4939-3438-6_15.*

01 Effect of Different Amounts of Graphene on Metal Friction and Wear During the Mixing Process

D. Han, K. Wang, H. Bian, *et al.*

ABSTRACT

An internal mixer is one the most common types of rubber-mixing equipment. This device can operate continuously for a long time, and often develops wear on its end face. The end face wear increases the gap between the mixing chamber and the end face, resulting in material leakage, which reduces the mixing effect and impacts the properties of the compound. Therefore, it is important to study the friction and wear of the mixing compound to the metal during the mixing process. In the present study, the influence of the mixing compound with different amounts of graphene (GE) on the friction and wear of the metal end face was analyzed, and the ratio of the corrosion wear to abrasive wear was calculated for the first time.

INTRODUCTION

Rubber has an undeniable role in the economy since it has been widely applied to numerous high-tech and modern technologies. However, raw rubber has low strength, low modulus, poor wear resistance, and fatigue resistance so that it cannot be used in most engineering applications. Accordingly, it is necessary to fill and reinforce the vast majority of rubbers with, for example, carbon black (CB) and silica (SiO_2). However, macromolecular chains form in the packing due to the sticky nature of rubber materials and elastic hysteresis loss inside the rubber packing, thereby producing friction loss and generating considerable heat. Efficiently dissipating the generated heat to the outside leads to internal spirals in the rubber and degrades its performance. Therefore, it is important to improve the thermal conductivity of rubber products to improve their performance and service life under dynamic use. With the diversification of rubber products, many applications need rubber products with antistatic properties, reasonable electrical conductivity, or a gas barrier. Recent investigations have revealed that adding small amounts of nanofillers, such as clay, carbon nanotubes (CNTs), and graphene to the rubber composite can improve the thermal con-

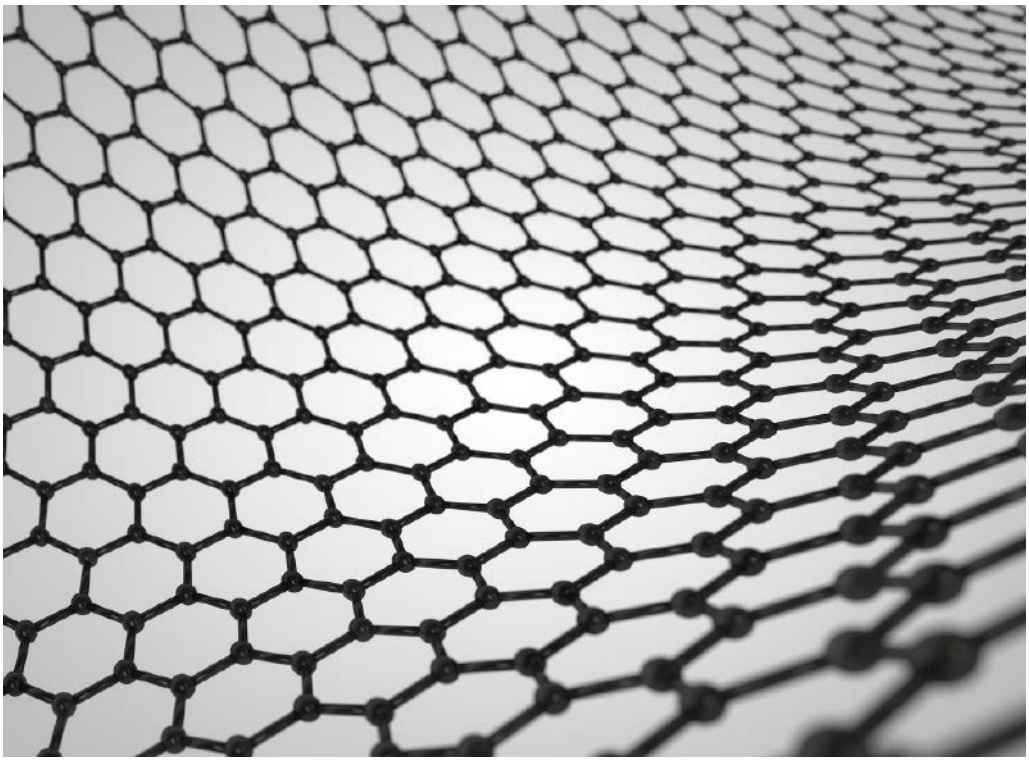

Figure 1: Schematic structure of graphene

ductivity, enhance the heat dissipation capacity, and improve the reinforcement efficiency and functional properties of the final product.

Graphene (GE) is a two-dimensional (2D) crystal with a single atomic layer formed by sp2 hybridization of carbon atoms arranged neatly in cellular lattice structural units. GE is one of the strongest substances known so far, and it is highly ductile and flexible. **Figure 1** shows the schematic structure of GE.

Yong Lin[1] studied the filler–rubber interface interaction in GE/silicon dioxide hybrid styrene–butadiene rubber composites and quantified the number of confinement regions. It was found that the larger the volume fraction of the constraint region, the stronger the interfacial interaction. Moreover, experiments and numerical simulations showed that the higher the volume fraction of the confinement zone, the better the mechanical properties of the composites.

Xumin Zhang[2] studied the thermal conductivity, expansion, and mechanical properties of PrGO/natural rubber (NR) nanocomposites. It was found that as the amount of PrGO in the composite increases, the thermal conductivity and energy storage modulus of PrGO/NR nanocomposite increases, while solvent absorption decreases. Moreover, adding 3 phr of PrGO increases the tensile strength and tear strength of nano-NR composites by 23% and 150%, respectively.

Hong Zhu[3] studied the effect of GE/silicon dioxide nanocomposites on the properties of SSBR/BR. It was found that adding reduced graphene oxide (rGO) improves the mechanical properties of SSBR/BR.

Yanping Wu[4] studied the mechanical and tribological properties of GE-reinforced rubber composites. The results showed that the mechanical properties of SSBR–BR composite filled with FGS were substantially better than those of the unfilled and equivalent filler-loaded graphene oxide (GO) and rGO-filled SSBR–BR composites. Moreover, it was found that the addition of GO, rGO, and FGS decreases the wear resistance of SSBR-BR composites.

GE/rubber composites have become a hot topic in the rubber field in recent years.[5–11] In this article, the effect of adding different amounts of GE on the friction and wear of the end face metal during the mixing process was studied.

EXPERIMENTS

Instruments

Hake internal mixer, BL-6157 Double Roll Mill, ZT-2588S steam generator, RPA 2000 Rubber Processing Performance Analyzer, Disper-GRADER Dispersion Meter, LEXT™ OLS5000 3D laser measuring microscope (Olympus® Japan), CSM-Friction and Wear Tester.

Formula

The formula is shown in **Table 1**.

Mixing process

In order to ensure the accuracy of the experiment, the test sample was made by pressing through a double-roller mill. To ensure the smoothness of rubber samples, samples pressurized by the double roller mill were put into the grinding tool to obtain a smooth surface and reduce the influence of surface roughness on the friction coefficient.

Test methods

1. The Panye effect[12-13] refers to the phenomenon that the dynamic modulus of filled rubber decreases sharply with the increase of strain. This phenomenon is usually used to reflect the dispersion of packing. The deformation of six rubber compounds was scanned by a rubber analyzer, and the distribution of dynamic modulus G0 changing against strain was obtained.
2. The Silanization reaction index is an important to measure the degree of silane modification of silica. A rubber processing analyzer was used to test the silylation reaction index. The greater the silanization reaction index, the higher the degree of silanization reaction, and the better the overall properties of the rubber compound.
3. Friction and wear testing was carried out using a CSM. To this end, the experimental pressure, rotational speed, and the test time were set to 5 N, 70 rpm, and 120 min, respectively. In order to study the wear condition of the internal mixer end face, the same metal grinding head material and end face material were used in the experiment. To ensure complete silanization, the mixing temperature was kept at 145–155 °C (293–311 °F) for 1 min. The temperature of CSM was set to 150 °C (302 °F) to ensure the reliability of the experiment. CSM is shown in **Figure 3**.
4. 3D morphology observation: The metal surface morphology was observed by using a 3D laser measuring microscope (OLS5000, LEXT, Olympus), where the wear amount was obtained by measuring the volume reduction of the metal grinding head.
5. Dispersion test: A carbon black dispersion tester was used to test the degree of disper-

Substance	C1	C2	C3	C4	C5	C6
NR	100	100	100	100	100	100
Nanosilicon dioxide	30	30	30	30	30	30
GE	0	0	1	2	3	4
ZnO	2	2	2	2	2	2
Anti-aging agent 4020	2	2	2	2	2	2
SAD	2	2	2	2	2	2
TESPT	0	5	5	5	5	5
DPG	1.3	1.3	1.3	1.3	1.3	1.3
S	1.3	1.3	1.3	1.3	1.3	1.3
CZ	1.8	1.8	1.8	1.8	1.8	1.8

Table 1: Chemical composition of GE/natural rubber composites

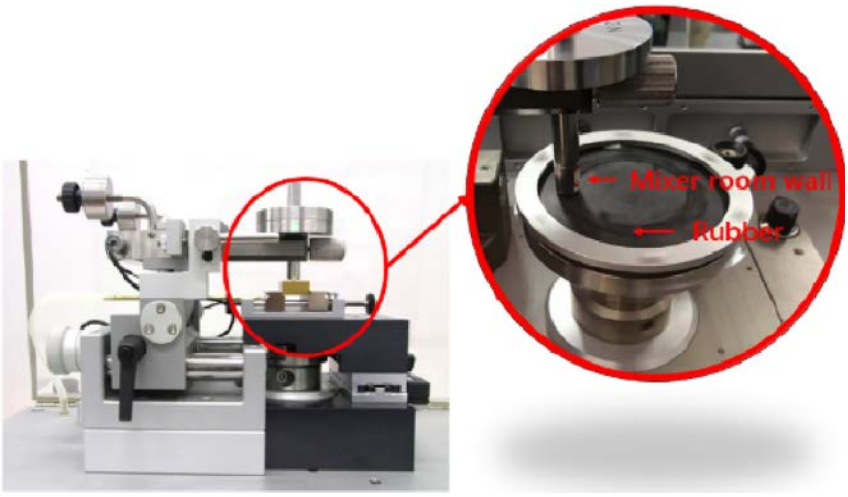

Figure 2: Configuration of the CSM wear test device

sion and obtain the dispersion value based on the ASTM D7723 standard (**Figure 2**).

SILANIZATION REACTION MECHANISM

Bis(3-triethoxysilylpropyl)tetrasulfide (TESPT) is a bifunctional silane coupling agent. Arkles[14] proposed a four-step reaction model based on the coupling process of TESPT:

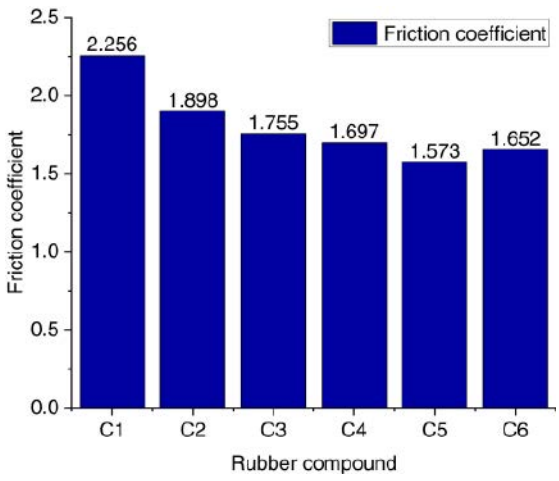

Figure 3: Average friction coefficient in different compounds

1. Three Si-OR groups connected with silicon are hydrolyzed to Si OH;

2. Si-OH is dehydrated and condensed into oligosiloxane containing Si OH;

3. Si-OH in the oligomer forms a hydrogen bond with OH on the substrate surface;

4. A covalent bond is formed with the substrate along the dehydration reaction in the heating curing process, but only one of the silicon hydroxyl groups of silane is bonded with the substrate surface at the interface, leaving two Si-OHs and condensation with Si-OHs in other silanes or free states. Therefore, the two materials with different properties can be coupled interfacially by using a silane-coupling agent, improving the composite properties, increasing the bonding strength, and obtaining a new composite with excellent performance and reliability.

Most wear occurs in the final mixing process, where the temperature is high and the mixer is in a closed state. In this high-temperature environment, ethanol vapor could not overflow the mixer, thereby resulting in corrosion wear. Accordingly, high-temperature, vapor-induced corrosion should be considered in investigating the friction and wear of the end face of the mixer. However, it is an enormous challenge to disassemble the end face of the internal mixer during the actual process and measure the quality of ethanol vapor. During the experiment on the CSM friction and wear testing machine, high-temperature ethanol vapor is sprayed on the surface of the mixing glue and metal in proportion to the degree of silylation reaction to simulate the mixing situation of the internal mixer.

RESULTS

Dispersion analysis of the packing

Payne effect

The rubber compounds without GE and TESPT could not have a silanization reaction. Consequently, a chemical connection does not form between the silica and rubber, resulting in a poor silica dispersion. With the increase of the amount of GE, the Payne effect of the rubber compound increases gradually. The GE could intercalate between silica particles, isolate silica particles, and prevent silica agglomeration. Moreover, GE-intercalated silica affects the silica dispersion. Additionally, as the GE continuously increases,

the agglomeration of GE became intensified, thereby increasing the Payne effect.

Dispersion comparison

The worst silica dispersion in the rubber compound belongs to the case without TESPT, which also has the highest silica aggregates. It is observed that as the amount of GE in the compound increases, the aggregate of GE increases, while the dispersion of the rubber compound decreases. The GE has a 2D crystal with a single atomic layer, which is composed of carbon atoms connected by sp2 hybridization. Therefore, GE intercalates silica particles, and its planar structure can hinder the silanization reaction.

Silanization reaction index

For the rubber compound of the silica formula system, the greater the silanization reaction index, the higher the degree of the silanization reaction, the more the overall dispersion of silica and rubber molecules and the better the silica dispersion. For the same formula system, the proportion of silanization reaction index reflects the proportion of silanization reaction product ethanol. In this regard, RPA 2000 was used, and the silanization reaction indices of five rubber compounds are evaluated.

The silylation reaction index of the mixers decreases gradually with the increase of the amount of GE. The products of the silanization reaction are ethanol and water. The wear of metal caused by water vapor has been studied, so the effect of produced ethanol from the silanization reaction was studied in this experiment. In the actual production process, it is a challenge to disassemble the internal mixer and measure the wear of the internal mixer face in real time, and it is not feasible to measure the quality of the produced ethanol vapor in the mixing process. In this experiment, when the wear test was carried out on the CSM, high-temperature ethanol vapor was sprayed on the surface of the rubber compound in proportion to the degree of the silylation reaction to simulate the real mixing process.

Effect of adding different amounts of GE on metal friction and wear

The coefficient of friction

Figure 3 reveals that the largest friction coefficient can be achieved in the rubber compound without TESPT and GE. This is because the silanization reaction of silica could not occur without adding TESPT in the mixing process. Accordingly, silica aggregates do not form easily among silica molecules. After adding TESPT, a silanization reaction occurs in the mixing process and a chemical bond establishes between silica and rubber. Accordingly, the silica dispersion increases and the aggregate of silica decreases. As a result, the friction coefficient of the C2 compound is significantly reduced compared to that of the C1 compound.

Three-dimensional morphology of metals

Comparing A1 and B1 in **Figure 4**, a large number of scratches appear on the metal surface after friction. Moreover, comparing A2 and B2, more pits appear on the height contour of the metal surface after friction, and the original height contour peaks mostly flatten. A large amount of silica aggregates in the rubber compound. Since silica has high hardness, the metal surface is worn so that many scratches appear on the metal surface after friction.

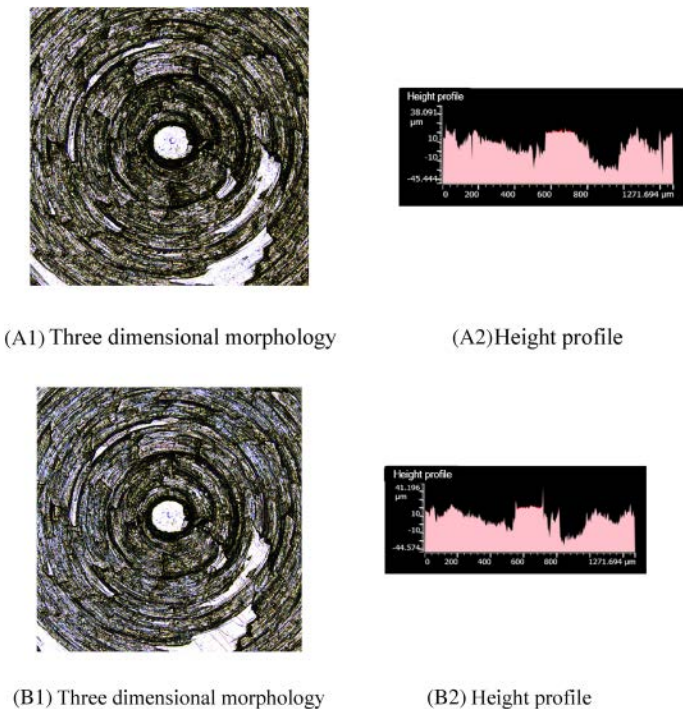

Figure 4: The surface morphology of the metal before and after the friction of the rubber compound without GE and TESPT (A1 and A2 are before friction; B1 and B2 are after friction). GE, graphene; TESPT, bis(3-triethoxysilylpropyl) tetrasulfide.

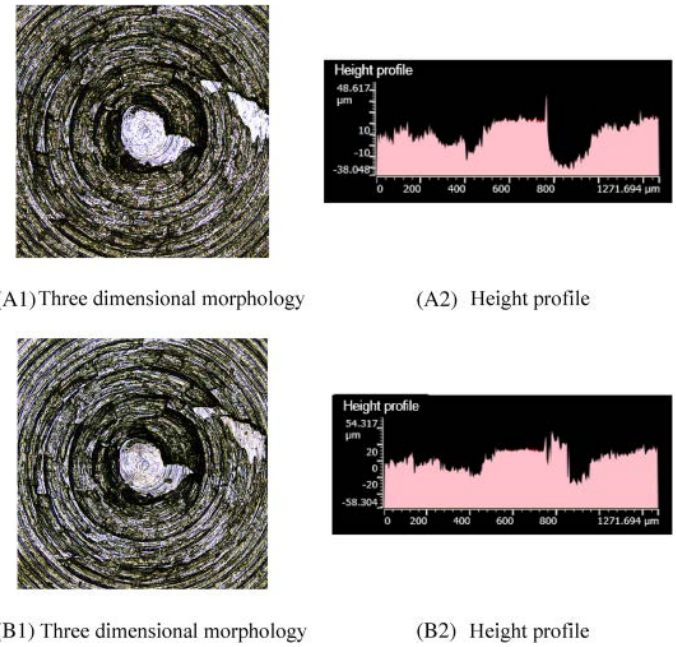

Figure 5: The surface morphology of the metal before and after the friction of the rubber compound without GE (A1 and A2 are before friction; B1 and B2 are after friction).

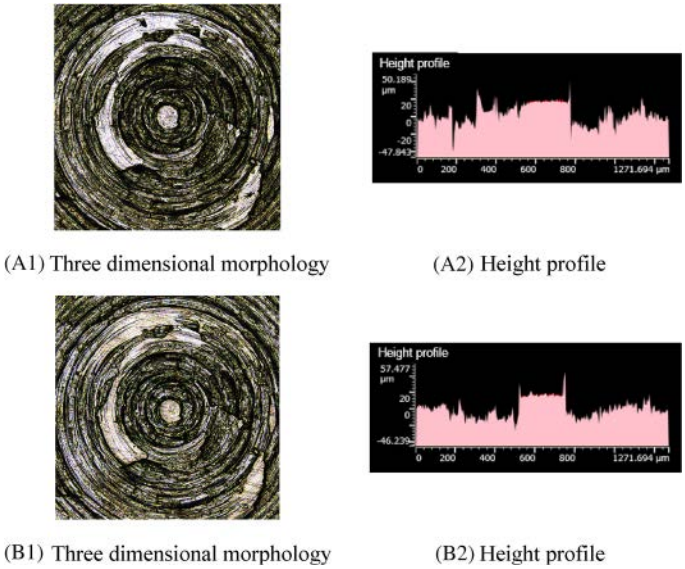

Figure 6: Surface morphology of the metal before and after friction with 1 phr of GE.

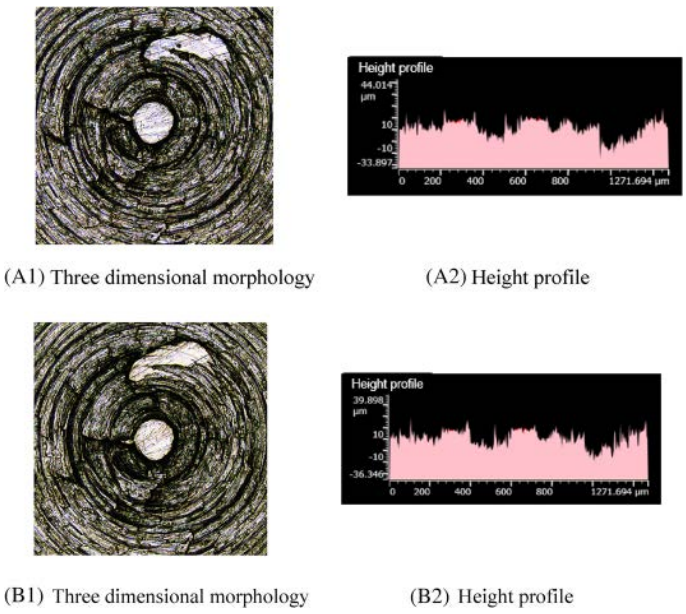

Figure 7: Surface morphology of the metal before and after friction with 2 phr of GE (A1 and A2 are before friction; B1 and B2 are after friction).

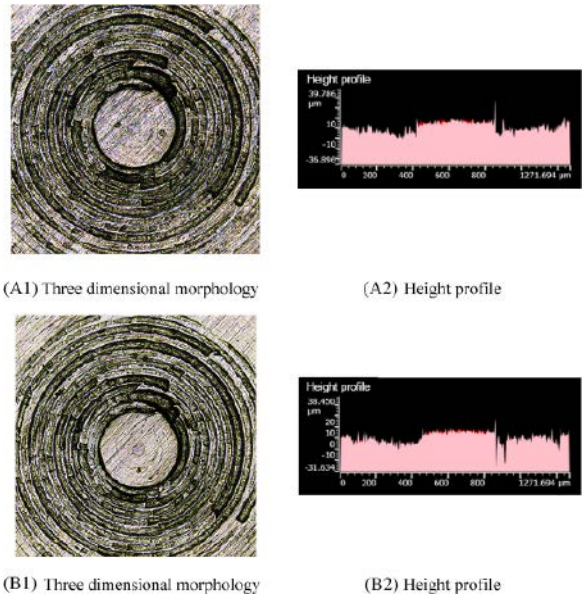

Figure 8: The surface morphology of the metal before and after friction of the rubber compound with 3 phr of GE (A1 and A2 are before friction; B1 and B2 are after friction).

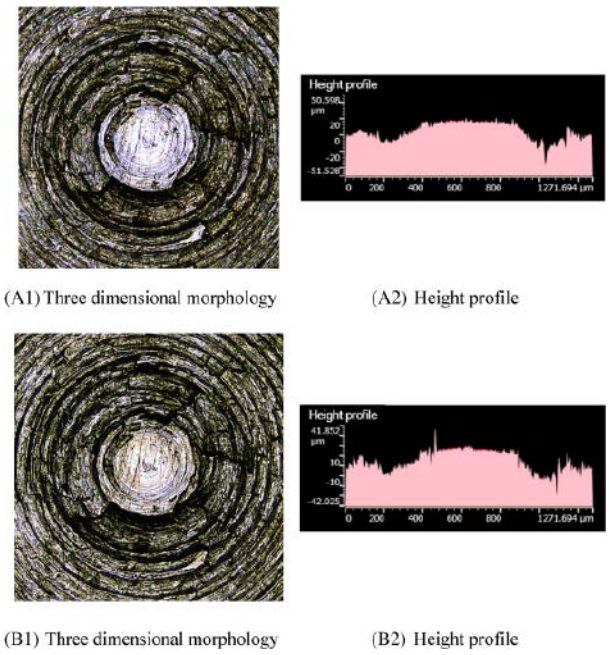

Figure 9: The surface morphology of the metal before and after friction of the rubber compound with 4 phr of GE (A1 and A2 are before friction; B1 and B2 are after friction).

Comparing A1 and B1 in **Figure 5**, there are fewer scratches on the metal surface after friction. Furthermore, **Figure 5** A2, B2 indicates that the height profile of the metal surface partially flattens after friction so that the peak of the height profile changed greatly. When TESPT is added to the compound mixture, the number of silica aggregates is lower. As a result, scratches on the metal surface reduce. However, with the progress of the silanization reaction, the temperature of ethanol vapor gradually increases and has a corrosive effect on metal. Considering the friction of the mixing adhesive on metal, this phenomenon results in the production of highly corrosive wear. Therefore, although there were few scratches on the metal surface, the height profile of the metal surface changed greatly, and the wear vapor-induced corrosion becomes the worst case.

Comparing A1 and B1 in **Figure 6**, more scratches appear on the metal surface after friction. Furthermore, **Figure 6** A2, B2 indicates that a large part of the height contour peaks of the metal surface flatten and pits appear in the height contour. GE intercalates silica particles, and its planar structure hinders the silylation reaction. Therefore, with the addition of 1 phr GE, the silanization reaction index and the amount of high-temperature ethanol vapor decrease, and the amount of corrosive wear decreases. Since GE has reasonable toughness and the intercalation of GE between silica particles hinders the contact between silica aggregates and metals, the amount of abrasive wear reduces.

Figure 7 A1, B1 shows that there are fewer scratches on the metal surface after friction. **Figure 7** A2, B2 illustrates that a small number of height peaks on the metal surface flatten after friction, and the overall change of height contour peaks is negligible. This phenomenon mainly originates from GE intercalation between silica particles, which further hinders the contact between silica aggregates and the base metal. It is observed that as the GE content increases, the corrosion wear decreases significantly.

Similar to previous parts, **Figure 8** A1, B1 shows that there are fewer scratches on the metal surface after friction. Moreover, **Figure 8** A2, B2 indicates that the height profile of the metal surface slightly changes after friction. This phenomenon may be attributed to the GE lamellae further hindering the contact between silica aggregates and metals. In this case, the metal contacts with the silica aggregate only when a piece of GE was worn completely, and then another GE layer appears. As the GE content increases, the silylation reaction index further decreases and the high-temperature steam decreases, thereby reducing the corrosion wear.

Figure 9 A1, B1 shows that there are more scratches on the metal surface after friction. **Figure 9** A2, B2 shows that after friction, part of the height contour peak of the metal surface flattens, pits appear in the height contour, and the overall height contour changes greatly. When 4 phr GE is added to the compound, a large amount of agglomeration between GE and TESPT is wrapped by GE, which hinders the silanization reaction, thereby producing a small amount of high-temperature ethanol vapor and a low amount of corrosive wear. Meanwhile, the hindrance of silica particles by GE sheets reduces, and a large number of silica aggregates appear. Consequently, the rubber compound with 4 phr GE has the largest abrasive wear on the metal.

Metal wear volume
TESPT has the largest wear on the metal. It is observed that with the gradual increase of the GE content, the wear of the rubber compound on the metal decreases first and then increases. The minimum wear can be achieved when 3 phr GE was added. When the amount of GE exceeds 3 phr, the wear amount of the rubber compound on the metal increases.

TESPT was an important raw material for silanization reaction. There is no TESPT in compound C1, so a silanization reaction cannot occur. Therefore, silica dispersion in this compound is very poor so that more and large silica aggregates appear. The friction of silica aggregates on the metal is the most important source of abrasive wear. Accordingly, the rubber compound C1 has great abrasive wear on the metal. After adding TESPT, the silica dispersion increases so that the silica aggregate decreases. More specifically, the metal wear of C2 rubber compound reduces by 7.22% compared with that of the C1 rubber compound.

As the amount of GE further increases, the GE lamellae further hinder the contact between silica aggregates and metals, and the wear of the rubber compound on the metal decreases. However, when the amount of GE exceeded 3 phr, a large number of GE agglomerates and GE encapsulated TESPT, which hindered the silanization reaction. Accordingly, small amounts of high-temperature steam and corrosive wear are produced. With a large number of GE aggregates, the blocking effect of GE sheets on silica particles is reduced, and a large number of silica aggregates appear in the rubber compound. Among the studied compounds, the rubber compound with 4 phr GE has the largest wear capacity on the metal.

Proportion of corrosive and abrasive wear
The CSM friction and wear tests were carried out on the rubber compound without spraying high-temperature ethanol vapor, so there is no corrosive wear so that abrasive wear is the only wear mechanism.

It was found that GE intercalates silica particles, hinders the movement of silica particles, and reduces the silica dispersion. Moreover, GE laminate could wrap TESPT and reduce the occurrence of silylation reaction. Therefore, as the GE content increases, the degree of the silanization reaction decreases. Meanwhile, the production of high-temperature steam decreases, thereby reducing the proportion of corrosion wear to abrasive wear.

Roughness changes before and after friction
The largest surface roughness can be achieved for the compound with no TESPT. This may be attributed to the absence of silanization reaction so that the silica aggregates. On the other hand, with the increase of the amount of GE, the silanization reaction decreases so that silica aggregates. Therefore, with the increase of the amount of GE, the surface roughness gradually increases after the metal friction was rubbed by the rubber compound.

CONCLUSION

Based on the results, it was found that as the amount of GE in the rubber compound increases, the proportion of abrasive wear on the metal increases, the proportion of corrosive wear on the metal decreases, and the metal wear decreases first and then increases. With the increase of the GE content, the production of high-temperature steam and the proportion of corrosive wear decreases.

The lowest metal wear can be achieved when the GE amount is 3 phr. However, when the GE amount exceeds 3 phr, a large number of GE agglomerates and GE encapsulated TESPT, which hinders the silanization reaction, resulting in a small amount of high-temperature steam production and a low amount of corrosion wear. However, with a large number of GE aggregated, the blocking effect of GE sheets on silica particles reduces, and a large number of silica aggregates appear in the rubber compound. Therefore, the mixing compound with 4 phr GE has greater wear on the metal.

ACKNOWLEDGMENTS

This research was funded by Key Technology and Equipment for Intelligent Green Manufacturing of Rubber Products, grant number ZR2016XJ003; Natural Science Foundation of Shandong Province, grant number ZR2019BEE056; Polymer Material Intelligent Manufacturing Innovation Team, grant number 2019KJB007; Key R & D Plan of Shandong Province, grant number 2019GGX102018; Shandong Provincial Natural Science Foundation, grant number ZR2020QE207;and also funded by Hunan Province 121 innovative talents project. The funders contributed to the work. The authors would like to thank the Shandong Provincial Key Laboratory of Polymer Material Advanced Manufacturing Technology for their support in this experiment.

REFERENCES:

[1] *Y. Lin, S. Liu, J. Peng, L. Liu, Appl. Sci. Manuf. 2016, 86, 19.*

[2] *X. Zhang, J. Wang, H. Jia, S. You, X. Xiong, L. Ding, Z. Xu, Compos. Part B 2016, 84, 121.*

[3] *H. Zhu, Z. Wang, X. Huang, F. Wang, L. Kong, B. Guo, T. Ding, Compos. Part B 2019, 175, 107027.*

[4] *Y. Wu, L. Chen, S. Qin, J. Li, H. Zhou, J. Chen, J. Appl. Polym. Sci. 2017, 134, 44970.*

[5] *D. S. Han, S. Zhang, K. Wang, Y. Pan, D. Zhu, J. Appl. Polym. Sci. 2021, 138, e50761.*

[6] *S. Geng, P. Wang, T. Ding, Compos. Sci. Technol. 2011, 72, 36.*

[7] *M. A. Tarawneh, S. H. Ahmad, S. Y. Yahya, R. Rasid, S. Y.,Noum, J. Reinf. Plast. Compos. 2011, 30, 363.*

[8] *P. M. Ajayan, O. Stephan, C. Colliex, D. Trauth, Science 1994, 256, 1212.*

[9] *L. Shen, X. Zhang, Y. Lei, M. Liang, Y. Chen, W. Chen, H. Zou, Polym. Compos. 2021, 1. https://doi.org/10.1002/pc.26165.*

[10] *H. Yan, T. Yuanzheng, J. Theor. Comput. Chem. 2013, 12, 1.*

[11] *X. Li, Y. Xia, Acta Mater. Compos. Sin. 2015, 32, 1007.*

[12] *Z. Xu, Y. Song, Q. Zheng, Polymer 2019, 185, 121953.*

[13] *J. Flambard, F. Carrette, C. Monchy-Leroy, E. Andrieu, L. Laffont, J. Nucl. Mater. 2021, 543, 152562.*

[14] *B. Arkles, J. R. Steinmetz, J. Zazyczny, P. Mehta, J. Adhes. Sci. Technol. 1992, 6, 193.*

02 The Effect of Cathodic Polarization on the Corrosion Behavior of X65 Steel in Seawater Containing Sulfate-Reducing Bacteria

M. Lv, X. Li, M. Du

ABSTRACT

Sulfate-reducing bacteria (SRB) are one of the main reasons for the accelerated corrosion of steel. Cathodic polarization is an effective and economic method against marine corrosion, including microbiologically induced corrosion. However, the interaction between cathodic polarization and microbial activity has not been well defined. In this study, a fluorine-doped tin oxide electrode is used to study the effect of cathodic current on SRB cells. The results clearly show that the attachment degree of SRB is dependent on the electric quantity and current intensity. The large electric quantity and high cathodic current can effectively inhibit bacterial attachment and subsequent biofilm formation. Furthermore, the effect of cathodic potential on the corrosion behavior of X65 steel in the presence of SRB is systematically investigated. Results show that the impressed charges, the increase of pH, and the formation of calcareous deposits on the electrode surface at the cathodic potential of –1,050 mV/SCE inhibit the attachment of SRB. In turn, the presence of SRB also interferes with the electrochemical reactions that occur during the polarization process, thus increasing the cathodic current. The interaction between SRB-induced corrosion and the process of preventing corrosion by various cathodic potentials is discussed.

INTRODUCTION

Cathodic polarization is an effective and common method to prevent corrosion of metallic structures and marine facilities.[1] The protection potential of –770 mV/SCE at room temperature can resist the naturally occurring corrosion current and prevent the steel from corrosion risk.[2]

However, there have been some unaccountably external corrosion problems, and in many cases, the presence of microorganisms (e.g., sulfatereducing bacteria [SRB]) is associated with these problems.[3] Microbiologically induced corrosion (MIC) is a bioelectrochemical process that initiates or accelerates the corrosion reaction by microbial activity.[4,5] MIC induced by SRB has been extensively investigated in the literature. Zhu *et al.*[8] found that the corrosion rate of X56 steel in the sea mud containing SRB was 10-fold higher than in the sea mud without SRB. SRB can reduce sulfate (SO_4^{2-}) to sulfide (H_2S, HS^-), which may indirectly contribute to the accumulation of corrosive sulfide and organic acid end products, causing localized pitting of metals.[9] Several mechanisms have been proposed to explain the role of SRB in MIC,[10-15] including cathodic depolarization, local corrosive cell, and metabolite-induced corrosion. Cathodic depolarization accelerates the cathodic reaction due to the consumption of cathode hydrogen via hydrogenase biocatalysis by SRB, which increases the electron demand of the anode and associated corrosion.[16,17] Metal sulfides produced by SRB metabolism are electrically conductive and cathodic with respect to steel, forming aggressive corrosion cells.[14] Recently, it has been suggested that SRB can acquire the energy needed by obtaining electrons via direct or indirect contact with the steel substrate, leading to more severe corrosion.[18]

Studies have shown that the electrochemical changes at the metal–solution interface during cathodic polarization influence the composition and concentration of chemical species and the attachment of microorganisms. [19-21]. Sun *et al.*[22] studied the effects of SRB on cathodic polarization of Q235 steel in the soils and showed that the number of SRB in soils decreased, and the protection efficiency increased with the shift of applied potential to a negative direction. Saravia *et al.*[23] stated that there was a decrease in the number of attached cells when the cathodic potential was applied in the initial stages of biofilm formation. Olivares *et al.*[24] , however, presented opposite findings. They found that the SRB population on polarization potential-applied pipeline steel (–850mV vs. Cu/CuSO4) was twice that of without cathodic polarization. Liu *et al.*[25] confirmed that the application of cathodic polarization did not affect the growth of planktonic bacteria, but it was beneficial to the adhesion of SRB cells to steel in the extracted soil solution.

To date, the interaction between cathodic polarization and microbial activity has not been well clarified due to the complicated processes occurring at the cathodically polarized surface. The objective of this study was to investigate the effect of cathodic polarization on microbial attachment and the effect of various cathodic potentials on the corrosion of X65 steel in sea water containing SRB.

MATERIALS AND METHODS

Materials

Fluorine-doped tin oxide (FTO) conducting glass (10 × 20 mm) was used for fluorescent confocal imaging to study the effect of cathodic current on SRB cells. Another specimen was X65 pipeline steel, which was used to study the effect of cathodic potential on corrosion in the presence of SRB. The X65 specimen (10 × 10 × 3 mm) was machined and embedded in epoxy resin, leaving a work area of 1 cm^2 for electrochemical measurement. The work face of the specimen was mechanically abraded with silicon carbide metallurgical papers sequentially, degreased by anhydrous ethanol, and then dried in high-purity nitrogen. All the prepared specimens were sanitized for 30 min using an ultraviolet lamp before use to ensure that there was no contamination by other bacteria.

SRB strain and its inoculation process

In this study, SRB (i.e., *Desulfovibrio caledoniensis*) were isolated from the rust layers of carbon steel immersed in seawater (Qingdao, China) and identified by polymerase chain reaction (PCR) amplification of 16S ribosomal DNA. SRB strains were cultivated in a constant-temperature incubator at 30 °C (86 °F) for 5 days. Then, 5 ml of SRB strains were transferred into 500 ml seawater (containing the whole culture medium) to prepare the test solution. Before inoculation, the medium was deoxygenated with high-purity nitrogen for 30 min and then sterilized by autoclaving at 121 °C (249.8 °F) for 20 min. The living cell num-

ber of SRB was calculated by the most probable number ASTM standard D4412-84.

Surface analysis

Bacterial attachment on the FTO glass electrode surface in situ was characterized using a confocal laser scanning microscope (FLUOVIEW™ FV1000; Olympus®). Before observation, the electrodes were soaked in sterile phosphate-buffered saline solution containing 5% (v/v) glutaraldehyde for 30 min and then stained with a fluorescent dye (DAPI) for 30 min in darkness.

The surface morphologies of X65 steel were observed using a scanning electron microscope (SEM; JSM-6700F; JEOL). The elemental composition and valence of the corrosion products were measured by energy-dispersive X-ray spectroscopy (EDS; JSM-6700F; JEOL) and X-ray photoelectron spectroscopy (XPS; ESCALAB 250Xi; Thermo Fisher Scientific).

A three-dimensional measuring laser microscope (LEXT™ OLS4000; Olympus, Tokyo, Japan) was used to characterize the surface morphology of the corroded steel specimens after the removal of corrosion products. Before the corroded surface examination, the specimens were taken from the test solution and subsequently immersed in a pickling solution containing corrosion inhibitor (hexamethylenetetramine) for 5 min, then rinsed with distilled water, cleaned with absolute ethanol, and finally dried with a nitrogen gas stream.

Electrochemical measurements

All the electrochemical measurements were performed using a Gamry electrochemical workstation. A saturated calomel electrode and a platinum plate were used as the reference and counter electrode, respectively. X65 steel was cathodically polarized for 14 days at the potentials of –800 and –1,050 mV/SCE, respectively. In addition, the cathodic potentials of –1,050 mV/SCE (the first 7 days) to –800 mV/SCE (the last 7 days) and –800 mV/SCE (the first 7 days) to –1,050 mV/SCE (the last 7 days) were also applied. Electrochemical impedance spectroscopy (EIS) was performed when the open circuit potential (OCP) reached a steady state. The applied polarization potential was switched off for a certain period to allow the potential to return to OCP, and then the EIS measurement was performed. After the EIS test was completed, the applied polarization potential was again switched on. EIS was obtained in the frequency range of 105–10–2 Hz, and the amplitude of the sinusoidal voltage signal was 10 mV. The EIS data were analyzed using Zview2 software with a suitable equivalent circuit model. All electrochemical experiments were carried out at 25 °C (77 °F) in an airtight system and repeated at least three times to check the reproducibility.

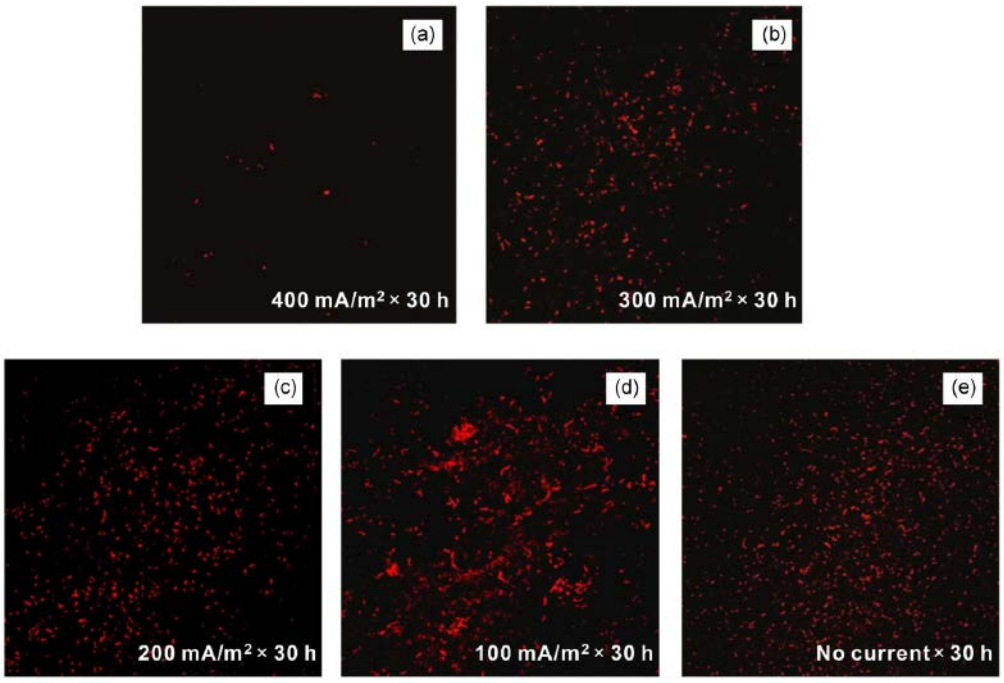

Figure 1: Fluorescent images of sulfate-reducing bacteria cells attached to the surface of the fluorine-doped tin oxide electrode after applying different cathodic current for 30 hr: (a) 400 mA/m^2, (b) 300 mA/m^2, (c) 200 mA/m^2, (d) 100 mA/m^2, (e) no current.

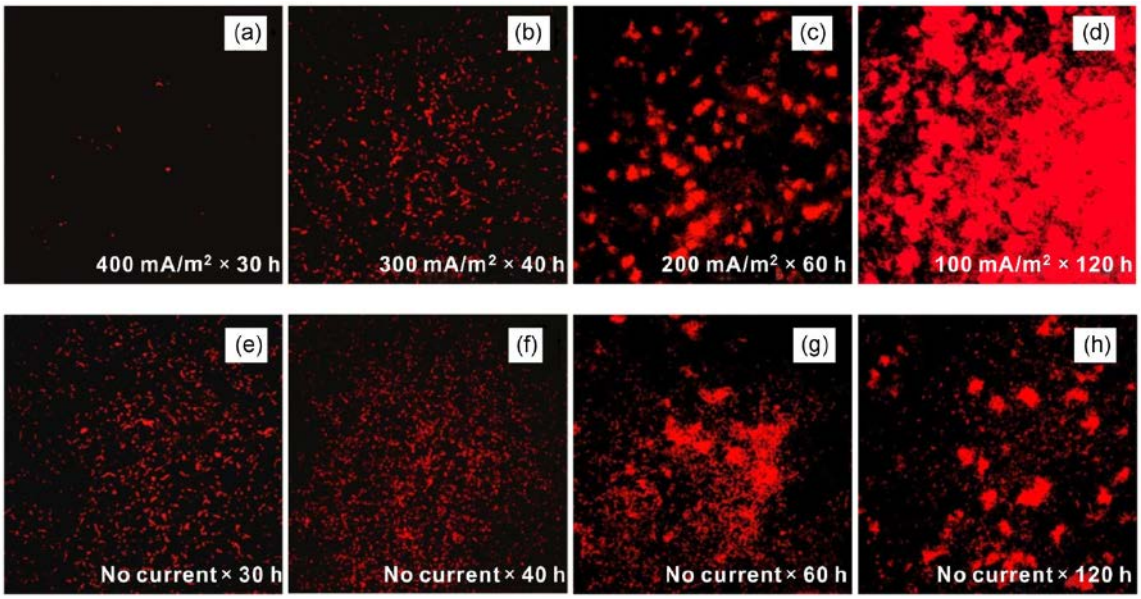

Figure 2: Fluorescent images of sulfate-reducing bacteria cells attached to the surface of the fluorine-doped tin oxide electrode after applying the same quantity of electric charge: (a) 400 mA/m²× 30 hr, (b) 300 mA/m²× 40 hr, (c) 200 mA/m² × 60 hr, (d) 100 mA/m² × 120 hr, and the control system: (e) No current × 30 hr, (f) No current × 40 hr, (g) No current × 60 hr, and (h) No current × 120 hr.

RESULTS AND DISCUSSION

The growth curve of SRB

The growth curve of SRB displayed a typical three-stage growth cycle. The first stage, which lasted for 1–4 days, is the exponential growth phase. During this stage, the number of active SRB increased rapidly. The growth stage from 5–10 days is the stationary phase. During this stage, the number of SRB increased and decreased equally, so the total number of SRB was large and stable. After 10 days, the growth process reached the death phase, during which the number of SRB decreased dramatically due to the lack of essential nutriments.

The effect of cathodic current on bacterial attachment

After applying different cathodic current for 30 hr, the effect of electric quantity on the attachment of SRB to the FTO electrode was studied, as given in **Figure 1**. The results showed that when more negative charges were applied, less SRB cells were attached. When the electric quantity of 400 mA/m² ×30 hr) was applied, the attachment of SRB on the electrode surface was significantly less than that of the control system (no current). The electric quantities of 300 mA/m²×30 hr and 200 mA/m²×30 hr had a little influence on the adhesion degree of SRB. Wilson *et al.*[26] have reported that cell surface was negatively charged by ionized phosphoryl and carboxylate substituents under normal conditions. Therefore, SRB cells may be repelled by a large build-up of negative charges on the surface of cathodically polarized electrode.[27] When the electric quantity applied to the FTO increased, there was an increase in the electrostatic repulsion. Consequently, the attachment of SRB was inhibited by the large electric quantity (400 mA/m²×30 hr). Interestingly, when a relatively small electric quantity was applied to the surface of the FTO electrode (**Figure 1d**), the number of attached SRB was more than that of the control system.

These results indicated that electric quantity was an important factor affecting the attachment of SRB. However, when the same electric quantity was applied, was microbial attachment related to current intensity? **Figure 2** shows the attachment of SRB on the surface of FTO electrode at the same electric quantity, but at various current densities. As shown in **Figure 2a–d**, the number of attached SRB cells markedly decreased with the increase of current density. The high cathodic current of 400 mA/m² effectively inhibited bacterial attachment and subsequent biofilm formation. It was further demonstrated that although the same quantity of electric charge was applied, a low current of 100 mA/m² pro-

moted bacterial attachment. When the electrostatic force between FTO and SRB was insufficient, cathodic polarization promoted the evolution of hydrogen, which contributed to the growth of hydrogenase-positive SRB.[28] Thus, there was an increase in SRB cells attached to the FTO at 100 mA/m^2. Given the above analysis, the attachment of SRB can be properly controlled by adjusting the electric quantity in combination with a high current.

The effect of cathodic potential on the corrosion of X65 steel in SRB-containing seawater

Most microorganisms tend to colonize, proliferate, and form a biofilm on metal surfaces, resulting in MIC. The initial attachment of bacteria is a crucial step, which lays the foundation for the formation of biofilm. Therefore, it is important to prevent or delay bacterial attachment and growth for corrosion control. In marine engineering, the commonly used criterion for the effectiveness of cathodic protection is the polarization potential. Therefore, –800 and –1,050 mV/SCE were selected as the applied potentials for this study. In addition, the cathodic potential ranging from –1,050 to –800 mV/SCE was impressed to X65 steel, that is, the negative potential of –1,050 mV/SCE was used to inhibit bacterial attachment in the rapid growth phase of SRB, and the inhibition effect of –800 mV/SCE on corrosion in the later stage was studied. The cathodic potential shifted negatively from –800 to –1,050 mV/SCE.

OCP monitoring

The different OCP variations in both systems, SRB-inoculated medium and sterile medium, indicated that the activity of SRB affected the corrosion process of X65 steel. The OCP of X65 steel in the sterile system remained stable at around –670 mV/SCE. In contrast, the OCP values in the SRB system fluctuated significantly and moved negatively to –718 mV/SCE after 5 days. It was possible that the activity of SRB changed the electrochemical process, providing a high driving force for the corrosion of X65 steel. Subsequently, the OCP moved to a positive direction and stabilized at the potential of around –640 mV/SCE.

EIS measurements

For specimens in the SRB-containing medium at OCP, the diameter of the Nyquist plot increased from 1 to 4 days, then decreased with time gradually, and afterward increased again after 14 days. The increase of the Nyquist plot diameter was attributed to the formed biofilm and corrosion products providing some protection to the steel in the initial incubation time, which hindered the charge transfer process. The decrease of the Nyquist plot diameter indicated that the high SRB activity accelerated the corrosion of X65 steel. Meanwhile, the production of corrosive agents such as sulfide, organic acids, and/or inorganic acids by SRB promoted the anode dissolution of metal.[7,15] After 14 days, the Nyquist plot diameter increased again due to the decline in the SRB activity. The peak of the phase angle shifted to a high frequency before 4 days and then to a low frequency. This situation indicated the formation of a protective corrosion product film, followed by the breakdown of the film. In the presence of SRB at cathodic potential of –800 mV/SCE, the diameter of the Nyquist plot was several times smaller than that at OCP, indicating that this cathodic potential had no protective effect on SRB-induced corrosion. When the potential of –1,050 mV/SCE was applied on the electrode, the diameter of Nyquist plot increased gradually. The impedance values were larger than that at OCP, which indicated that this potential effectively slowed down the corrosion in the presence of SRB. The potential ranging from –1,050 to –800 mV/SCE also offered some protection to the specimen toward further corrosion. The Nyquist plot for –800 to –1,050 mV/SCE was relatively volatile, and there may be a slight anodic dissolution.

The time-dependent changes of R_{ct} fitted from the EIS data at various cathodic potentials was studied. Generally, a higher R_{ct} indicates a lower corrosion rate of steel. At OCP, the R_{ct} increased and reached the maximum value after 4 days, and then decreased gradually. The initial increase of R_{ct} can be attributed to the production of biofilm and corrosion products that formed a protective film on the specimen surface. After 4 days, the number of active SRB increased rapidly and reached the maximum value at 7 days, which accelerated the corrosion of X65 steel. In addition, the integrity of the protective film may be degraded, thereby forming an active corrosion cell between the FeS film (cathode) and the nearby metal substrate (anode), which resulted in a rapid decrease of R_{ct}. However, in the case of the cathodic polarization, R_{ct} was increased when the polarization potential shifted negatively. The results were well matched with the cathodic protection theory mentioned in Evan's diagram; that is, the increase of protective potential increased the corrosion resistance. The R_{ct} with the highest increase was observed at –1,050 mV/SCE. It revealed that

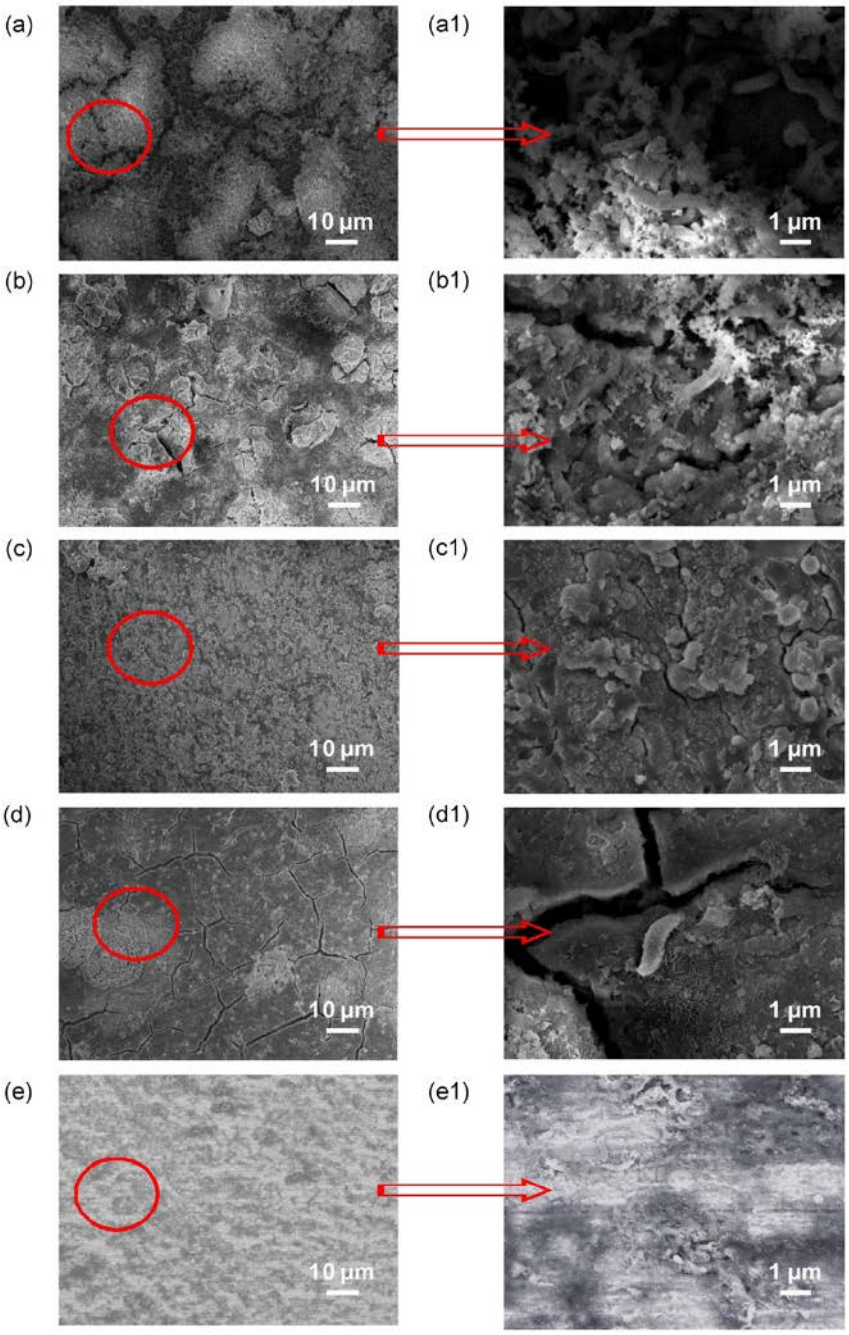

Figure 3: SEM images of X65 steel at various potentials: (a,a1) OCP; (b,b1) –800 mV/SCE; (c,c1) –1,050 mV/SCE; (d,d1) –1,050 to –800 mV/SCE, and (e,e1) –800 to –1,050 mV/SCE after 14 days of exposure in the SRB-containing medium. OCP, open circuit potential; SCE, saturated calomel electrode; SEM, scanning electron microscope; SRB, sulfate-reducing bacteria.

anodic dissolution was almost inhibited at the cathodic potential of –1,050 mV/SCE.

Current densities' recording

It was observed that the current density decreased rapidly within a few hours and reached a steady state. Additionally, the cathodic current increased after a few days. This increase was suggested to result from the following factors: (a) cathodically produced hydrogen promoted an SRB activity and (b) iron sulfides produced by SRB were cathodic, relative to X65 steel, which may form a corrosion cell, resulting in a higher cathodic current.[29]

pH variation

The pH values decreased abruptly in the SRB-containing culture solution with bacterial growth and then increased. The initial drop in pH values can be attributed to the generation of organic acids. SRB consumed cathodic hydrogen through a hydrogen intermediate (i.e., hydrogenase) for the reduction of SO_4^{2-}, as given below:

$$SO_4^{2-} + 8H^+ + 8e^- \rightarrow HS^- + 3H_2O + OH^- \quad (1)$$

The reaction increased the concentration of OH^- because it consumed H^+, increasing, the pH of the solution. Although the changes in pH for all systems exhibited a similar pattern, the pH values at various polarization potentials were higher than that at OCP. This indicated that the alkalinity generated by cathodic polarization was higher than that by microbiological activity.

Surface analysis

Figure 3 shows the SEM images of X65 specimens at various polarization potentials after 14 days of exposure in SRB-containing seawater. A large number of loosely discrete products were attached to the surface at OCP (**Figure 3a**). Numerous SRB cells were embedded in the corrosion products and biofilm matrix. The EDS results showed that the elements of corrosion products were mostly Fe, C, O, and S. Thus, the corrosion products were principally iron oxides, sulfides, as well as carbon-based compounds that accumulated from the culture medium. When the cathodic potential of –800 mV/SCE was applied on the electrode, the corrosion product layer was more compact (**Figure 3b**). It is observed that SRB cells still existed among the corrosion products. At –1,050 mV/SCE, dense deposits were formed on the X65 steel surface (**Figure 3c**) and no bacteria were observed on the surface. The EDS analysis indicated the presence of calcareous deposits and

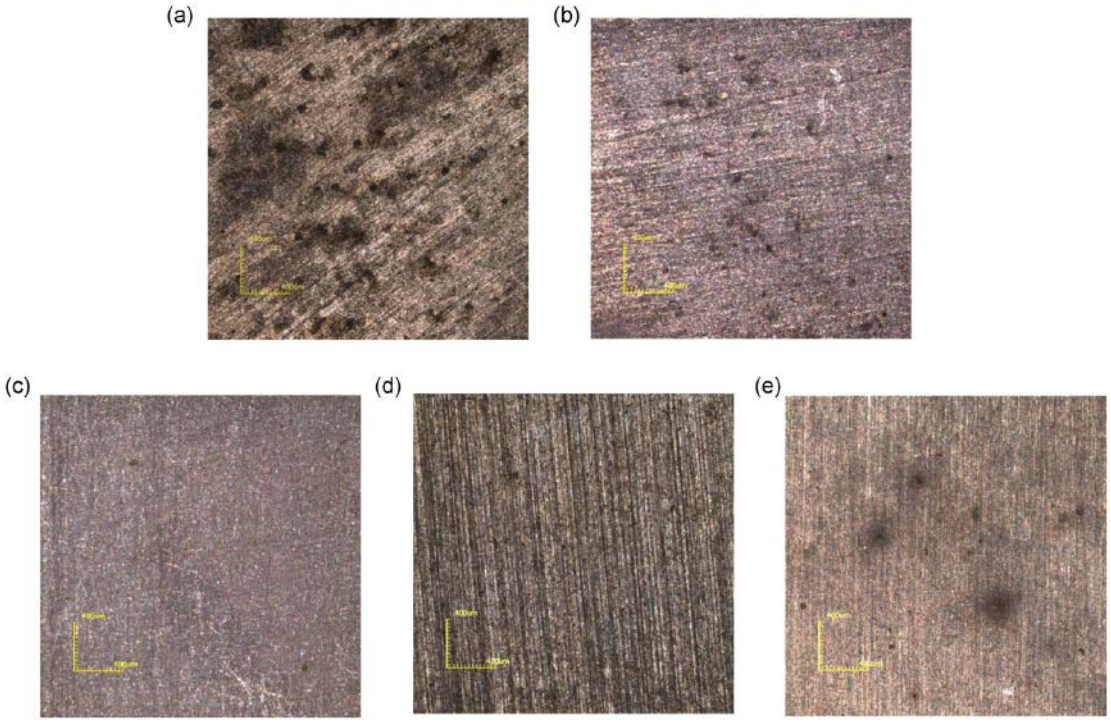

Figure 4: Corrosion morphologies of X65 steel after removing corrosion products at various potentials: (a) OCP; (b) –800 mV/SCE; (c) –1,050 mV/SCE; (d) –1,050 to –800 mV/SCE, and (e) –800 to –1,050 mV/SCE. OCP, open circuit potential; SCE, saturated calomel electrode.

a low amount of iron sulfides. The formation of calcareous deposits on the electrode surface was the result of negative protection potential producing high pH value, which was beneficial to the deposition of calcium ions. At –1,050 to –800 mV/SCE, there were obvious corrosion cracks on the surface, which were caused by drying during specimen preparation (**Figure 3d**). At –800 to –1,050mV/SCE, the steel electrode contained a layer of corrosion products (**Figure 3e**) with extensive SRB cells.

Corrosion morphologies of X65 steel after removing corrosion products are shown in **Figure 4**. Some big and deep pits were observed at OCP (**Figure 10a**), which was attributed to anodic dissolution occurring on the steel surface and SRB-induced pitting. At cathodic potential of –800 mV/SCE (**Figure 10b**), pitting corrosion still occurred. By contrast, the surface morphology of the specimen at –1,050 mV/SCE was, in general, smooth with no apparent pitting corrosion (**Figure 10c**). It was consistent with the electrochemical result that corrosion was prevented by a cathodic potential of –1,050 mV/SCE. At –1,050 to –800 mV/SCE (**Figure 4d**), the general corrosion of X65 steel was effectively controlled, except for a few small pits. When the cathodic potential shifted negatively from –800 to –1,050 mV/SCE, these pits seemed to be wider but not deeper than that at –800 mV/SCE (**Figure 4e**).

XPS analysis

XPS spectra were employed to qualitatively and quantitatively determinate the corrosion products of the X65 specimen. For the Fe spectrum of corrosion products, $FeSO_4$, Fe_2O_3, FeOOH, FeS, and FeS_2 were detected in almost all specimens. Interestingly, some iron sulfides were also found at the cathodic potential of –1,050 mV/SCE. It can be hypothesized that a negative potential of –1,050 mV/SCE can play a better protective effect, but it cannot completely eliminate the occurrence of MIC.

The influence of cathodic potential on SRB-induced corrosion

The SEM micrographs in this study showed a significant reduction of the bacterial number on the cathodic surface polarized to –1,050 mV/SCE. For most cathodic surfaces in the anaerobic condition, an impressed cathodic potential forced the following reactions:

$2H_2O + 2e^- \rightarrow H^+ + 2OH^-$. (2)

In this case, the production of OH^- caused an increase of interfacial pH, which seemed high enough to inhibit the initial attachment of SRB. Furthermore, the surface charge on bacteria cells depended on interfacial pH, which determined the degree of protonation of ionogenic groups associated with the cell wall to be negatively charged. The microbial cell produced a negatively charged polysaccharide, glycocalyx; thus, its attachment to the polarized surface was electrostatically repelled when a cathodic potential of –1,050 mV/SCE was applied.[30,31]

Calcareous deposits were formed on the surface of the cathodically polarized electrode. The increase in local pH, in turn, forced a shift in the equilibria of all chemical reactions involving calcium, magnesium, and carbonate:

$HCO^- + OH– \rightarrow H_2O + CO_3^{2-}$ (3)

$Mg^{2+} + 2OH^- \rightarrow Mg(OH)$ (4)

$Ca^{2+} + CO_3^{2-} \rightarrow CaCO_3$ (5)

Cations such as Ca^{2+} and Mg^{2+} are required for bacterial adhesion as a "bridge."[32] The precipitation of Ca and Mg ions caused a decrease in their local concentration due to the generation of OH^-, thereby inhibiting the attachment of SRB to the surface of cathodically polarized X65 steel. These calcareous deposits also provided a physical barrier to general corrosion attack. At the cathodic potential of –1,050 mV/SCE, the formation of calcareous deposits and the alkaline environment on the surface of the polarized electrode was not suitable for SRB to obtain electrons from the overly negative polarized X65 steel and grow. According to the corrosion morphology of X65 steel after removing corrosion products (**Figure 4c**), the protection potential of –1,050 mV/SCE was sufficient to control the corrosion induced by SRB.

The bacterial activity was not affected by the protection potential of –800 mV/SCE applied to the X65 steel. Besides the general corrosion observed on the metal surface, a type of localized corrosion was developed when the potential of –800 mV/SCE was applied to the SRB system (**Figure 4b**). Thus, –800 mV/SCE was not sufficient to inhibit SRB-induced corrosion. Some works have found that cathodic hydrogen generation at the cathodically protected surface promoted the growth of hydrogenase-containing SRB.[32] Chemical species (including H^+ ions) were reduced at the metal surface:

$H^+ + e^- \rightarrow {}^{[H]}$. (6)

The generated atoms $^{[H]}$ were transported to the biofilm and then oxidized by hydrogenase enzyme to reduce SO_4^{2-}. Further, H^+ protons were adsorbed on the metal surface and reduced again. It was apparent that the cathodic potential changed the bacterial metabolism and consequently affected the current demand.

However, several studies indicated that SRB can also obtain electrons from metallic iron directly via membrane-associated proteins (e.g., cytochromes) to reduce SO_4^{2-}.[33-35] Therefore, the cathodic polarization potential must be lower than the optimal protection criterion for steel due to the presence of SRB.

In the experiment conducted at the cathodic potential ranging from –800 to –1,050 mV/SCE, the SEM observation (**Figure 3e**) indicated that SRB strongly attached to the electrode surface, despite the fact that potential negatively shifted to –1,050 mV/SCE after 7 days. The reason was suggested that cathodic polarization was not sufficient to remove bacteria from the pre-existing biofilm.[29] When a potential of –1,050 to –800 mV/SCE was applied, the protective effect was similar to that at –1,050 mV/ SCE. It indicated that the changes in the metal interface caused by –1,050 mV/SCE were sufficient to suppress SRB-induced corrosion for a period of time after the potential shifted to –800 mV/SCE. However, long-term predictions require further research in SRB-containing seawater.

CONCLUSIONS

In this study, it was demonstrated that the degree of SRB attachment on the electrode surface was associated with the electric quantity and the intensity of the cathodic current. Due to the build-up of negative charges on the electrode surface, the cathodic current of 400mA/m2×30 hr effectively inhibited bacterial attachment. In contrast, when a low cathodic current of 100mA/m2 was applied, bacterial attachment and growth were promoted. Also, the attachment of SRB on the electrode surface was not inhibited by the potential of –800mV/SCE. The generated atoms [H] on the polarized surface contributed to the metabolic activity of SRB. A further negative shift

of the protection potential to –1,050mV/SCE exhibited an effective inhibitory effect on SRB-induced pitting corrosion. The impressed charges, the increase of pH, and the formation of calcareous deposits on the electrode surface were the driving forces to inhibit the attachment of SRB. The cathodic potential ranging from –1,050 to –800mV/SCE also provided effective protection for X65 steel due to the interfacial changes caused by potential of –1,050mV/SCE in the first 7 days. However, at the potential ranging from –800 to –1,050mV/SCE, pitting corrosion still existed on the electrode surface, indicating that the applied potential of –1,050mV/SCE could inhibit SRB attachment, but it was not sufficient to remove SRB from the pre-existing biofilm.

REFERENCES:

[1] *Y. S. Kim, S. K. Lee, H. J. Chung, J. G. Kim, Ocean Eng. 2018, 148, 223.*

[2] *J. H. Kim, Y. S. Kim, J. G. Kim, Ocean Eng. 2016, 115, 149.*

[3] *R. G. Esquivel, G. Z. Olivares, M. J. H. Gayosso, A. G. Trejo, Mater. Corros. 2011, 62, 61.*

[4] *C. H. Williamson, L. A. Jain, B. Mishra, D. L. Olson, J. R. Spear, Appl. Microbiol. Biotechnol. 2015, 99, 6945.*

[5] *R. Javaherdashti, Appl. Microbiol. Biotechnol. 2011, 91, 1507.*

[6] *K. M. Moon, H. R. Cho, M. H. Lee, S. K. Shin, S. C. Koh, Met. Mater. Int. 2007, 13, 211.*

[7] *F. M. AlAbbas, R. Bhola, J. R. Spear, D. L. Olson, B. Mishra, Int. J. Electrochem. Sci. 2013, 8, 859.*

[8] *Y. Zhu, Y. Huang, C. Zheng, Q. Yu, Mater. Corros. 2007, 58, 447.*

[9] *S. Y. Li, K. S. Jeon, T. Y. Kang, Y. T. Kho, Y. G. Kim, Corrosion 2001, 57, 815.*

[10] *V. W. Kuehr, V. D. Vlugt, Water (den Haag) 1934, 18, 147.*

[11] *S. Daumas, M. Magot, J. L. Crolet, Res. Microbiol. 1993, 144, 327.*

[12] *D. Thierry, W. Sand Corrosion Mechanisms in Theory and Practice (Eds: P. Marcus, J. Oudar), Marcel Dekker, New York, NY 1995.*

[13] *D. Thierry, W. Sand Corrosion Mechanisms in Theory and Practice, 2nd ed. (Ed: P. Marcus), Marcel Dekker, New York, NY 2002.*

[14] *W. A. Hamilton, Biofouling 2003, 19, 65.*

[15] *R. Jia, J. L. Tan, P. Jin, D. J. Blackwood, D. Xu, T. Gu, Corros. Sci. 2018, 130, 1.*

[16] *T. Q. Wu, M. C. Yan, D. C. Zeng, J. Xu, C. K. Yu, C. Sun, W. Ke, Acta Metall. Sin. 2014, 28, 93.*

[17] *H. A. Videla, Biofouling 2009, 15, 37.*

[18] *P. Zhang, D. Xu, Y. Li, K. Yang, T. Gu, Bioelectrochemistry 2015, 101, 14.*

[19] *S. H. Hong, J. Jeong, S. Shim, H. Kang, S. Kwon, K. H. Ahn, J. Yoon, Biotechnol. Bioeng. 2008, 100, 379.*

[20] *O. Istanbullu, J. Babauta, H. Duc Nguyen, H. Beyenal, Biofouling 2012, 28, 769.*

[21] *S. Shim, S. H. Hong, Y. Tak, J. Yoon, Biofouling 2011, 27, 217.*

[22] *C. Sun, J. Xu, F. H. Wang, C. K. Yu, Mater. Corros. 2010, 61, 762.*

[23] *S. G. G. de Saravia, M. F. L. de Mele, H. A. Videla, R. G. J. Edyvean, Biofouling 1997, 11, 1.*

[24] *G. Olivares, G. Mejia, G. Caloca, I. Lopez, F. Dabur, C. Ulloa-Ochoa, R. Esquivel, Corrosion 2003.*

[25] *T. Liu, Y. F. Cheng, J. Alloy. Compd. 2017, 729, 180.*

[26] *W. W. Wilson, M. M. Wade, S. C. Holman, F. R. Champlin, J. Microbiol. Methods 2001, 43, 153.*

[27] *A. T. Poortinga, J. Smit, H. C. V. D. Mei, H. J. Busscher, Biotechnol. Bioeng. 2001, 76, 395.*

[28] *F. Guan, X. Zhai, J. Duan, M. Zhang, B. Hou, PLOS One 2016, 11, e0162315.*

[29] *J. G. Guezennec, Int. Biodeterior. Biodegrad. 1994, 34, 275.*

[30] *B. Little, P. Wagner, D. Duquette, Corrosion 1988, 44, 270.*

[31] *R. G. J. Edyvean, A. D. Maines, C. J. Hutchinson, N. J. Silk, L. V. Evans, Int. Biodeterior. Biodegrad. 1992, 29, 251.*

[32] *J. Guezennec, Biofouling 1991, 3, 339.*

[33] *J. Duan, S. Wu, X. Zhang, G. Huang, M. Du, B. Hou, Electrochim. Acta 2008, 54, 22.*

[34] *H. Venzlaff, D. Enning, J. Srinivasan, K. J. J. Mayrhofer, A. W. Hassel, F. Widdel, M. Stratmann, Corros. Sci. 2013, 66, 88.*

[35] *H. T. Dinh, J. Kuever, M. Mußmann, A. W. Hassel, M. Stratmann, F. Widdel, Nature 2004, 427, 829.*

03 Comparison of Test Methods Used to Analyze Stress Corrosion Cracking of Differently Tempered 7xxx Alloys

N. Magaji, R. Mayrhofer, B. Krger, *et al.*

ABSTRACT

This paper compares and critically analyzes various test methods used to assess stress corrosion cracking (SCC) susceptibility of the alloy EN AW-7075 (Al-Zn-Mg-Cu) in various temper conditions. Constant load test in an alternating immersion environment was used as the standard reference test. Constant displacement tests in the form of U-bend specimens and four-point loaded bend specimens was conducted in a neutral and acidic salt-spray fog test environment, an alternating salt spray fog environment, and alternating immersion environment. A novel incremental step load test was also carried out in a continuous immersion environment. It was shown that the neutral salt-spray fog test environments could potentially substitute the alternating immersion test for testing SCC susceptibility.

INTRODUCTION

The high-strength Al-Zn-Mg-Cu alloys (7xxx series) have drawn considerable attention in the automobile industry in the past few years. This is due to their high strength (up to 600 MPa), light weight, and high resistance to corrosion.[1] However, one of the main problems is their high risk of susceptibility to stress corrosion cracking (SCC), which can lead to catastrophic failures in service.[2] Due to the complex nature of SCC, there is currently no common consensus on possible mechanisms.[3,4] SCC is highly influenced by the nature and magnitude of stress. Consequently, the choice of loading systems for testing SCC can have a substantial impact on the test results.[5] The three commonly used stressing modes involve the application of a constant total strain, a constant load, and the use of a constant strain rate.

The aim of this work is to compare and critically analyze the advantages and disadvantages of the most common SCC test methods for the assessment of SCC in high-strength Al-Mg-

Zn-Cu alloys. This work aims to understand the practicality of each test method with respect to automotive applications and analyze the influencing parameters that need to be considered when choosing an appropriate test method.

MATERIALS AND METHODS

Materials

The material, whose composition is given in **Table 1**, was received in 300 × 300 $mm^{[2]}$ sheets of 1.5 mm thickness in three heat treatment conditions (**Table 2**).

Corrosion testing

Constant load test

The constant load test was carried out according to ASTM G47-98.[6] Standard A80 samples according to DIN EN ISO-6892-1:2017–02 were prepared by punching,[7] and they were uniaxially stressed to maintain a constant load corresponding to 75% of their yield strength.[6] Each stressed sample was subjected to alternating immersion testing in an aqueous NaCl solution according to ASTM G44-99 for a total duration of 30 days. A minimum of three trials were carried out for each material. The main analysis parameter considered was the time to failure. Fracture surfaces were analyzed using a scanning electron microscope to determine the nature of fracture. In addition, optical microscopy was carried out on fractured and unfractured samples.

U-bend test

The U-bend sample preparation was performed according to ASTM G30-97.[8] U-bending samples were punched with an impact cutter and holes were drilled on either side. Spacers were used to ensure that bending did not exceed the final bend that was fastened. Once the samples were prepared, they were exposed to five environments for a definite period, or until failure of the sample. See **Table 3** for details.

Four-point loaded bend test

The four-point loaded specimens were prepared according to ASTM G39-99.[9] Four-point bending specimen holders support the specimen at the ends and bend the specimens by forcing two inner supports against it. Once the samples were prepared, a minimum of three samples were exposed to two test environments, namely DIN EN ISO 11997- 1 Cycle B and ASTM G44-99 (Alternating immersion test).[10,11] The main analysis parameter considered was the time to failure. SEM fractographic analysis of the failed samples was carried out to determine the nature of the fracture.

Incremental step load test

In this test, specimens were subjected to an increasing step load cycle while being exposed to a test environment. The maximum load reached was used to compare the susceptibility of different alloys. One of the principal advantages of this test is that it always ends with a failure and does not need to be stopped after a specific duration. The setup of this experiment is similar to that of a constant load test, wherein an A80 sample is covered by a solution holder and uniaxially stressed. The test starts with a pre-load time of 96 h, in which the load is set to 50% of maximum load (load to failure). Thereafter, the load is increased every hour in steps of 5% of maximum force until the specimens fail. Throughout this load cycle, the sample is exposed to a test solution of 5% NaCl with an initial pH of 4, achieved by adding HCl to the solution. The minimum load to failure was compared to determine the SCC susceptibility ranking. SEM investigations as well as optical microscopy were carried out to determine the nature of the fracture surface.

Table 1: Composition of the test material (wt%)

Si	Mg	Mn	Cu	Fe	Zn	Cr	Ni	Zr	Al
0.07	2.43	0.05	1.58	0.16	5.94	0.21	0.01	0.02	Bal.

Table 2: Temper treatment cycles

Temper treatment	Tempering process
T4	As delivered
T6	T4+ 130 °C for 13 h
T7	T4 + 115 °C for 6 h + 168 °C for 16 h

Environment	Temperature	Description	Solution concentration	pH	Maximum exposure duration
DIN EN ISO 11997–1:2016-5	Cyclic as shown in Fig.	Cyclic Humidity	5 wt% NaCl	6.5–7.2	42 days
DIN EN ISO 9227:2012 NSS	35 ± 2 °C	Continuous spray	5 wt% NaCl	6.5–7.2	30 days
DIN EN ISO 9227:2012 CASS	50 ± 2 °C	Continuous spray	5 wt% NaCl + 0.26 g L^{-1} of ($CuCl_2.2H_2O$)	3.1–3.3	14 days
ASTM G44-99	Solution:23 ± 2 °C	Alternating immersion	3.5% NaCl	6.5–7.5	30 days
	Air: 23 ± 2 °C (anomaly from the norm which states 27 ± 2 °C)				
DIN 55665:2007–01 (Outdoor Exposure Test)	Natural weather conditions	Weekly spray	3% NaCl solution	6.5–7.5	1 year

Table 3: Description of environments used in this study

Analytical methods

Optical microscopy

After the test exposure duration, the samples were cleaned, and cross-sections of each specimen type were prepared. These micro-sections were observed to determine the nature of the crack, the influence of other corrosion forms, and crack initiation sites. The microscopy was done using an Olympus® LEXT™ OLS4100 laser scanning digital microscope. The samples for each microstructural analysis were hot mounted under pressure with an epoxide resin. Subsequently, they were ground to 1200 level grit and then polished. The etching of the samples was carried out by dipping the specimen in 10% phosphoric acid for 30 min.

Scanning electron microscopy

Fracture analysis of failed specimens was performed using a scanning electron microscope (SEM) to determine the mode of failure and the nature of the fracture surface. The electron microscopy was performed with the MIRA Scan 3, from Tescan. A 10 V accelerating voltage was used for secondary electrons imaging.

RESULTS AND DISCUSSION

Characterization of materials

As expected, the T6 tempered alloy had the highest ultimate tensile strength and hardness. The electrical conductivity was seen to increase with annealing duration.

Constant load test

The constant load test was used as a standard reference for this study due to the experience and knowledge base in this test.

The results of the minimum time to failure for the constant load test, showed a clear influence of the temper treatment on the SCC susceptibility, with 7075-T4 being the most susceptible material, since it showed the fastest failure within 2 days of testing, followed by 7075-T6, which failed after 5 days of testing. The 7075-T7 alloy passed the 30-day test limit without failure.

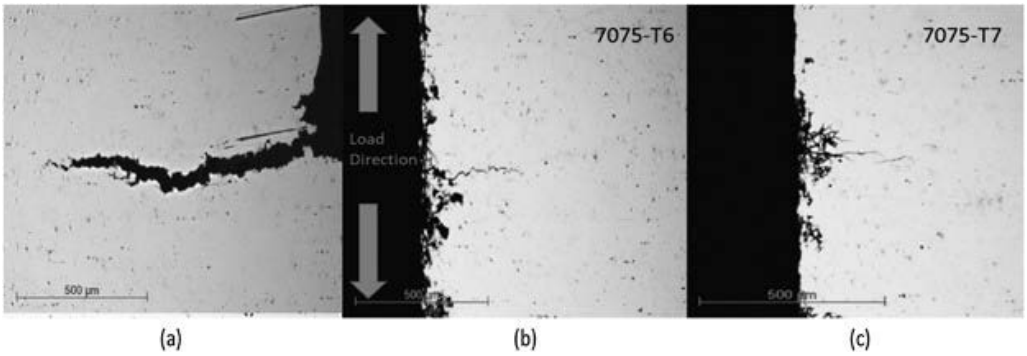

Figure 1: Cross-sections of the constant load specimens observed under optical microscopy. (a) 7075-T4, (b)7075-T6, and (c) 7075-T7

The metallographic examination of failed specimens revealed that the nature of the cracks was intergranular and multiple cracks were observed near the surface of the failure. **Figure 1** shows the cross-section of the tested specimen. While 7075-T4 and 7075-T6 show localized corrosion influence, the 7075-T7 alloy shows crack initiation from an intergranular corrosion site.

Moreover, the SEM fractography of tensile tested samples in air revealed a ductile fracture surface with a typical honey-comb structure. In comparison, the fracture surface of the sample that failed during the SCC test showed an intergranular fracture surface, which is mostly brittle in nature. Primary cracks along with secondary branching are also visible on the surface. The failed sample of 7075-T6 alloy also showed a similar fracture surface, with a brittle quasi cleavage structure with primarily intergranular fracture surface.

These results indicate that the failure mechanism is intergranular in nature and correlate well with investigations by Schnatterer and Zander,[12] who got the same ranking of susceptibility using the SSRT test. They attributed the higher SCC susceptibility of 7075-T4 to the substantial IGC influence, due to anodic dissolution of the MgZn2 precipitates and lower SCC susceptibility of the over-aged alloy to incorporation of Cu to the grain boundary precipitates, resulting in an increase of their potential. Speidel *et al*.[5] also observed that over-aging (T7) greatly decreases the SCC susceptibility of high copper containing alloy, attributing it to formation of nobler Cu containing precipitates and, therefore, reducing anodic dissolution. However, a deeper understanding of this mechanism can only be obtained through TEM observations and grain boundary studies of the materials and the effect of tempering.

U-bend test

The 7075-T4 alloy underwent the earliest failure in all the corrosive environments as in the constant load test. It failed within a span of two days in all the considered environments. The failures of 7075-T6 were slightly delayed compared to the T4-treated samples in all the environments. The longest time observed for failure of this material was found for the alternating immersion test of 15 days. The 7075-T7 alloy showed no complete failure after the maximum duration of tests. However, it must be noted that samples of this temper from the alternating immersion test and the CASS test showed micro-cracks in optical microscopy.

The output of these results has direct correlation with the standard reference test. Comparing the time to failure of alloys in the different environments, the ranking of susceptibility is the same in all the environments. Interestingly, the correlation of the ranking produced by the fog tests, to the outdoor exposure test is also substantial. This good correlation of the climate tests to the outdoor exposure test shows a potential for the use of climate-chamber tests, which are a common practice test in automotive corrosion testing. The salt spray tests could be further developed to test SCC and potentially replace the alternating immersion test.

The DIN EN ISO 9227–2012 CASS test shows the highest corrosion influence of the four environments tested. This could be due to its acidic nature, higher temperature, the presence of higher chloride ions (due to presence

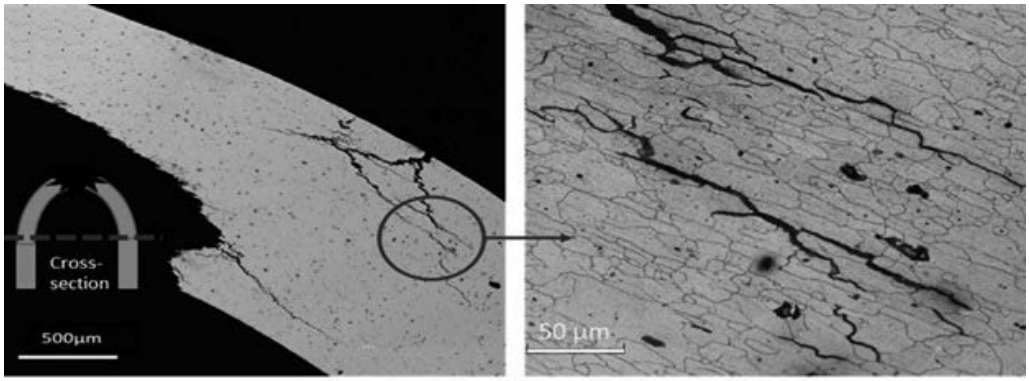

Figure 2: (a) Failed 7075-T4 sample after 1 day of exposure to the DIN EN ISO 9227:2012 NSS environment and (b) etched and magnified image showing intergranular fracture.

of copper chloride), and due to the localized galvanic corrosion by copper ions. However, it is noticed in the micrographs and SEM fractographs that stress corrosion cracking, in this environment, is accompanied by severe forms of corrosion, especially intergranular corrosion. This makes it difficult to determine the exact cause of failure, deeming this environment inappropriate to test SCC.

Figure 2a shows the crack surface of the 7075-T4 alloy after 2 days of exposure to the neutral salt spray environment (DIN EN ISO 9227-2012 NSS). It represents the typical crack propagation direction observed in all the failed samples. Branching of the crack surface and multiple cracks are visible.

These cracks could also possibly be initiated before the cracks that led to failure. Hence, multiple cracks could lead to a significant relaxation of stress as compared to one propagating crack, leading to slower crack propagation and crack arrest. It can also be seen from the etched sample (**Figure 2b**) that the crack propagation is intergranular in nature. This factor could influence the results, while considering time to failure as primary criteria to qualify materials.

It is also observed that the crack initiates perpendicular to the surface and on further propagation changes its direction to parallel to the upper surface and arrests within the sample before failure. The U-bend sample has uneven stress distributions within the sample due to its high plasticity. Once a crack initiates in these regions, the stress distribution in the U-bend sample changes. The stress direction could also change, hence changing the crack path as well. This uneven change in stress distribution is an important factor to be considered in SCC testing.

Four-point loaded bend specimen

A comparison of the results of this test with the reference test, both in an alternating immersion environment, gives a clear difference in the effect of loading mode, since they were both stressed to 75% of the yield strength and exposed to the same environmental condition. The 7075-T6 alloy, in the constant load test, showed earliest failure after 5 days of exposure, whereas the same alloy in the four-point load bending test did not fail within 30 days of exposure. This could be attributed to the stress relaxation that occurs in the four-point load test on the initiation of the crack on the edges. On the other hand, crack initiation in the constant load test leads to the increase of stress on the remaining sample, leading to faster propagation of cracks and faster failure. This result agrees with the results of Brenner et. al. who also attributed the faster failure of the constant load test to stress concentration.[13]

During the four-point bending test, we observed that the failure crack was in the contact region of the roller and the specimen, rather than the expected region of the sample between the contact rollers where the stress is distributed. There are two possible factors for this behavior or the combination of both, that results in this cracking. The first factor is the frictional stress at the point of contact of the roller and the specimen as explained by Turnbull *et al*.[14] This failure adds unknown stresses to the induced stresses in the specimen. This error on the stress invalidates the advantage of knowing the exact stress to fail-

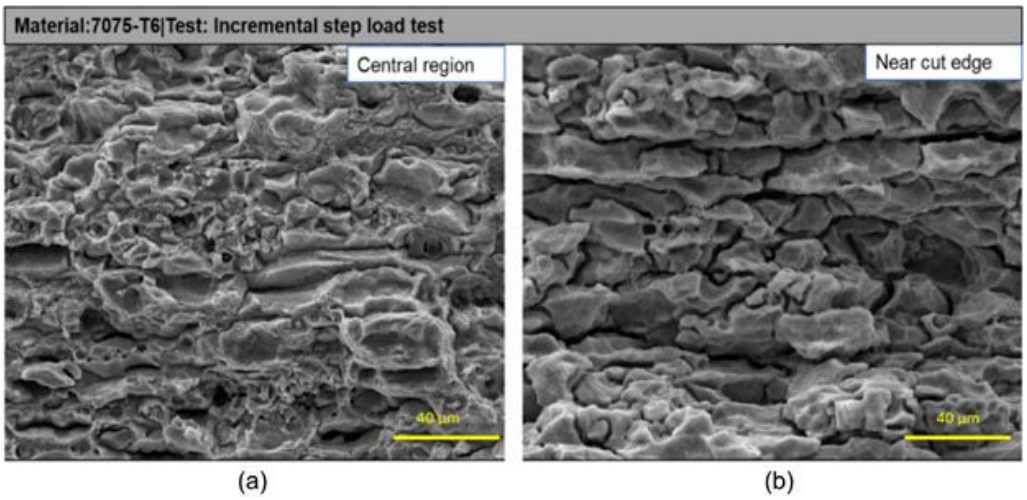

Figure 3: 7075-T6 fracture surface after failure at 55% Fmk in the incremental step load test. (a) Center of the cross section and (b) near the cut edge of specimen.

ure in this type of specimen. The second factor is the crevice corrosion that could take place at the contact point as mentioned in ASTM G39-99.[9] This crevice corrosion near the contact point is accompanied by an increase in hydrogen contents possibly leading to hydrogen included failure in this region. Since this is an uncontrolled process, it could lead to hindrance of the testing of SCC, and it becomes difficult to ascertain the parameters to failure.

Incremental step load test

The incremental step-load test is a novel test used in this study for testing the susceptibility of stress corrosion cracking of aluminum 7xxx alloys. The advantages of this test include the shorter timespan of the experiment of a maximum of 106 h, as compared to the other tests that ran up to 30 days or more. Another huge advantage of this test, as with the slow strain rate test, is that the test ends with failure for all the samples and does not need to be stopped at any arbitrary time, eliminating the uncertainty of whether the time ascertained for the test is appropriate. Although a practical application of incremental loading of stress may not be reasonable in real-world conditions, this test could be suitable for qualitative comparison of susceptibility of alloys by two factors, namely time to failure and maximum stress withstood. This gives a good qualitative ranking capability when alloys are to be compared. In this work, the results of the incremental step load test showed good agreement with the standard reference test.

The proposed mechanism taking place in this test is comparable to that of SSRT. Since SCC is a time dependent process, the aim of the preload time, in which the sample is exposed to the corrosive 5% NaCl solution and stressed at a load of 50% of the ultimate tensile strength, is to initiate stress corrosion cracking in the material, assuming that the stress is sufficient to do so. Once the crack is initiated after the pre-load time, the stress is increased and held in that stress state for a given time. The aim of this hold time is to induce SCC within the opened regions of crack, as in the slow strain rate test, producing then a complete brittle fracture. Since this is a load-driven test, the initiation of a crack would result in the increase of stress in the remaining specimen. This could lead to plasticity in the remaining region, hence, leading to a higher probability of stress corrosion cracking to occur. If the hydrogen induction mechanism is taken into consideration, the hydrogen atoms have time to be adsorbed into the open crack surface, and an increase of stress could increase the movement of hydrogen within the material by movement of dislocations. This induction of SCC would then differ with difference in susceptibility of materials, leading to failure of more susceptible alloys at lower stresses and vice versa, thus creating a ranking of the alloys.

The incremental step-load test considers two parameters to determine susceptibility of the alloy, namely the maximum stress withstood for the step loading and the time to failure. The 7075-T4 did not withstand the preexposure duration and failed after 48 h of expo-

sure to 5% NaCl with a stress of 50% of the maximum load to failure (Fmk) followed by the failure of 7075-T6 at 63 h. The minimum load to failure ranged from 50% to 85%. The over-aged alloy did not show any susceptibility and passed the maximum load step of 95% Fmk. It is interesting to note, the correlation between these results to the other tests and the similarity of the ranking of the materials.

Figure 3 shows the fracture surface of 7075-T6 which failed at a stress of 55% Fmk, where Fmk stands for maximum load to failure. Two regions, one at the center of the specimen cross-section and another near the cut edge, show very different morphologies. The former shows both brittle and ductile areas. The region near the cut edge, however, shows a complete brittle intergranular cracking with branching. This difference in morphology could be attributed to the stresses present at the edges due to cutting. This could also explain the difference in failure stresses ranging from 50% Fmk to 85% Fmk. The embrittlement near the edges could be due to the effect of the plastic deformation of the edges due to punching, which causes substantial residual stresses on the specimen. The initiation of cracks due to this, could be uneven depending on the cut edges and these cracks could result in an overload on the rest of the material, once the crack is initiated from the edge. This explains the ductile regions visible in the center of the fracture specimen. In order to reduce the effect of cut edges, it is proposed that the test be optimized by use of milled or lasered specimens.

Critical analysis of the test methods

This work demonstrates the importance of loading mode and magnitude during SCC testing. Two specimens in constant total strain mode were examined: U-bend and 4-point loaded bend specimen. It was seen that the plastically strained U-bend test showed fast results as compared to the elastically 4-point bend test, due to a higher magnitude of stresses. However, the disadvantage of plastic straining is the complex calculation of stresses within the sample and uneven distribution of stresses. This inhomogeneous stress distribution does not allow for a quantitative determination of threshold stresses for SCC failure. It must also be considered that elastically strained specimens undergo stress relaxation once the crack initiates. The extent of this relaxation is dependent on the sample holder and the specimen size.[15]

On comparison of constant load and constant strain mode, the stress concentration increases, in a constant load mode, once the crack initiates. This makes the constant load test a more severe test. Multiple cracks were also observed in failed specimens, which could lead to inhomogeneous stress relaxation.[16] All the environments tested in this work were found to be sufficiently aggressive to cause SCC. The same susceptibility ranking was obtained in all the environments and the outdoor exposure test. However, each environment had different speeds of failure. The slowest was the alternating immersion test, which could be explained by absence of free atmospheric hydrogen ions present in the test, as compared to the salt spray fog test. The severest test was the CASS test, which could be attributed to its low pH, high temperature, higher chloride ions, and presence of Cu2+ ions, which could lead to localized galvanic corrosion. However, optical microscopy showed, that this test was highly influenced by other corrosion forms, such as intergranular and pitting corrosion. These other corrosion forms could have a substantial influence on the time to failure as well, making it an inappropriate test method to test SCC. A detailed analysis of the influence of pH, salt-content, temperature, and other environmental factors needs to be carried out in order to develop an appropriate SCC testing environment.

CONCLUSIONS

Four tests were conducted, compared, and critically analyzed to determine an SCC susceptibility ranking for differently tempered 7075 alloys. The following is a summary of the important observations and results obtained in this work.

1. Comparison of various environments used in this thesis showed that the acidic DIN EN ISO 9227:2012 CASS environment had the strongest corrosion influence on the tested materials. However, the SCC was also accompanied by other forms of corrosion, which could possibly affect the test results. The results of salt-spray tests, DIN EN ISO 9227:2012 NSS and DIN EN ISO 11997-1(B), showed that these tests can be appropriate substitutes for the standard alternating immersion environment. Since these test environments are well established in the automotive application, they have the potential to be further used for testing SCC susceptibility of 7xxx alloys for automotive application.

2. The U-bend test was easy to execute and economically viable. It also exhibited a good qualitative differentiability of SCC susceptibility of the 7075 alloy to SCC, which was confirmed by the correlation to the reference test as well as the outdoor exposure test.

3. The U-bend test showed fast results due to the large plastic strains on the specimen, hence, it is appropriate for an accelerated qualitative test. However, influence of stress relaxation and stress-redistribution due to crack formation must be thoroughly analyzed to use this test for commercial applications.

4. The U-bend test also shows a large dependence on sample preparation.

5. The four-point loaded bend samples did not produce a good differentiability of SCC susceptibility within the timeframe of the test. This was attributed to stress relaxation of the specimen on crack formation. Moreover, the failure of specimens was partly associated with crevice corrosion and frictional stress at the point of contact of the metal and stressing frame. These factors must be taken into consideration for further application of this test method. Possible improvements in this test could include concentration of the stress in the center of the specimen by means of notching or punching.

6. With the present parameters of the incremental step load test, it was seen that it was difficult to determine the cause of failure in this test. The test parameters were seen to have a substantial influence on the result. The optimization of the parameters, such as pre-load timing, step duration, different environmental parameters, and mill finished edges, could be beneficial for the future use of this method as an accelerated test for SCC susceptibility of 7xxx alloys.

7. The naturally aged 7075-T4 alloy showed the highest susceptibility in all the tests, followed by the peak-aged 7075-T6 alloy. The over-aged 7075-T7 alloy showed reduced susceptibility.

REFERENCES:

[1] *Davis, J. R. Corrosion of Aluminum and Aluminum Alloys. (ASM International, 1999).*

[2] *Raja, V. S. & Shoji, T. Stress Corrosion Cracking: Theory and Practice. (Elsevier Science, 2011).*

[3] *Marichev, V. A. The mechanisms of crack growth in stress corrosion cracking of aluminium alloys. Mater. Corros. und Korrosion 34, 300–309 (1983).*

[4] *Burleigh, T. D. The Postulated Mechanisms for Stress Corrosion Cracking of Aluminum Alloys: A Review of the Literature 1980-1989. CORROSION 47, 89–98 (1991).*

[5] *Speidel, M. O. Stress corrosion cracking of aluminum alloys. Metall. Trans. A 6, 631–651 (1975).*

[6] *ASTM G47-98(2011). Standard Test Method for Determining Susceptibility to Stress Corrosion Cracking of 2xxx and 7xxx Aluminium Alloy Products. (1998) doi:10.1520/G0047-20.*

[7] *DIN EN ISO 6892–1:2017–02. Metallische Werkstoffe- Zugversuch- Teil 1. Prüfverfahren bei Raumtemperatur. (2017).*

[8] *ASTM G30-97(2016). Standard Practice for Making and Using Ubend Stress-Corrosion Test Specimens. (1997).*

[9] *ASTM G39-99 (Reapproved 2016). Standard Practice for Preparation and Use of Bent-Beam Stress-Corrosion Test Specimens. (1999).*

[10] *ASTM G44-99 (Reapproved 2013). Standard Practice for Exposure of Metals and Alloys by Alternate Immersion in Neutral 3.5% Sodium Chloride Solution. (1999).*

[11] *DIN EN ISO 11997-1:2016-05. Beschichtungsstoffe-Bestimmung der Beständigkeit (Salzsprühnebel)/trocken/feuchte. (2016).*

[12] *Schnatterer, C. & Zander, D. Influence of heat treatments on the stress corrosion cracking susceptibility of 7075 aluminum wires in NaCl solutions. Mater. Corros. 67, 1164–1172 (2016).*

[13] *Brenner, P. & Gruhl, W. No Title. Z. Met. 52, 599 (1961).*

[14] *Turnbull, A. & Crocker, L. E. Four point bend testing - finite element analysis of the stress and strain distribution. http://eprintspublications.npl.co.uk/6097/ (2014).*

[15] *Turnbull, A. Test methods for environment assisted cracking. Br. Corros. J. 27, 271–289 (1992).*

[16] *Richardson, T. J. A. Shreir's Corrosion. (Elsevier Science, 2009).*

04 Microstructure Analysis of Corrosion Resistance of Cast AlCu4Mg1 Alloy

I. Hren, S. Kusmierczak, K. Kurajdov

ABSTRACT

In the automotive industry, the demand for aluminium alloys is growing every year and the requirements for these alloys are also increasing. This article discusses the evaluation of corrosion resistance of cast rods from alloy EN AW 2024. Experimental samples were laboratory subjected to a standard corrosion test according to CSN ISO 4287. Corrosive behavior was evaluated using light and electron microscopy. Furthermore, an analysis of the hardness of the material and the chemical composition was carried out. A map of corrosion-affected phases of the microstructure was also created, depending on time. This, together with the course of hardness, provides a comprehensive overview of the corrosion behavior of cast rods, which will serve as a starting point for further research in the field of barrier protection.

INTRODUCTION

The use of aluminum alloys in aerospace and automotive engineering products places increased demands on the corrosion resistance of materials to improve operational reliability and extend product life. The exclusion of possible causes of accidents and failures of automotive equipment (AE) due to the corrosion of aluminum alloys is based on comprehensive studies of climatic resistance of materials in their development and certification phase, rational design of AE products, excluding stagnant zones, as well as controlled operation, accompanied by timely identification and elimination of emerging corrosion damage.

Commonly used methods for assessing the corrosion status of an AE product are visual inspection and nondestructive testing. For aluminum alloys, the formation of pitting (PC) and intergranular corrosion (IC) is the most critical. Pitting corrosion develops mainly in the direction of maximum deformation and is accompanied by peeling of individual metal particles so that it can be detected visually without the use of instrumental research methods. On the other hand, IC, in which destruction

occurs along the grain boundaries deep into the semi-finished product, cannot be detected by the naked eye, so nondestructive methods are required. Not much work has been done to study the effect of the degree of sensitivity of alloys on MCC and the change in their mechanical properties after casting.

There is a need to study the influence of IC in climatic tests of structural aluminum alloys operating in conditions of increased aggressiveness of the atmosphere to change mechanical properties, which is necessary for the development of preventive measures aimed at improving reliable car operation. The aim of the article is to investigate the corrosion behavior of aluminum alloy 2024 in a salt environment with respect to the surface condition of the corrosion product in the alloy.

RESEARCH MATERIAL AND METHODS

The composition of the alloy 2024[1] is given in **Table 1**. Macro-photographies of obtained samples were registered using a Canon EOS 1200D camera. Metallographic specimens were prepared by grinding on waterproof abrasive papers (P180, P320, P600, P1200, and P2000) and polishing using water suspensions of polycrystalline diamond with grain size of 3 and 1 µm. Microstructural investigation was performed by means of light microscopy (Olympus® LEXT™ OLS5000 3D measuring laser microscope with 4K scanning technology and Olympus MXU software). A Tescan VEGA3 electron microscope was used to examine the microstructure of the alloy by SEM. The chemical composition of selected phases precipitated in the microstructure was analyzed by energy dispersive X-ray spectroscopy (EDX) using an analyzer and SW Esprit 1.9. The Vickers hardness of the material according to the standard ČSN 42 0374 was measured at a load of 0.025 kgf.

Si	Fe	Cu	Mn	Mg	Cr	Zn	Ti	Al
0.54	0.4	3.75	0.6	0.5	0.05	0.11	0.028	rest

Table 1: Chemical composition of EN AW 2024 alloy

RESULTS AND DISCUSSION

Microstructure analysis

The microstructure of the cast material (**Fig. 1**) consists of dendrites, which have a uniform distribution and comparable size. There is a clear occurrence of interdendritic porosity, which is typical for this type of Al alloy.[1–5] The microstructure of the experimental alloy EN AW 2024 in the cast state consists mainly of binary eutectic $\alpha + CuAl_2$ and a small amount of ternary eutectic $\alpha + CuAl_2 + Cu_2Mg_2Al_5$.

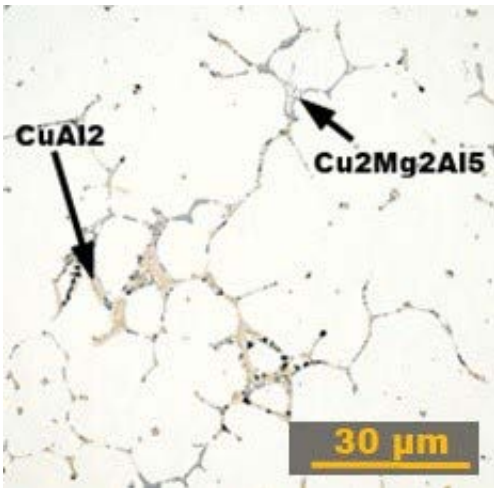

Figure 1: Microstructure of alloy AA 2024 with identified phase; mag. 500x.

MICROSCOPIC EVALUATION OF CORROSION ATTACK ON THE ALLOY

A salt spray test was performed according to CSN 038137. The samples were exposed to corrosion in a Liebisch S400 MTR corrosion chamber for the time specified in CSN ISO 8407.[6] The test was graded with exposure times of 168, 240, 480, and 720 hours. The individual cycles were performed in a test medium of 5% NaCl, concentration 50 g / l, at a temperature of 35 ± 20 °C (95 + 68 °F), and the pH of the solution was 6.5 to 7.2. The exposure time and labeling of the samples are given in **Table 2**.

At the end of the test, the samples were removed for corrosion, cleaned, dried, and metallographically prepared. Evaluation of corrosion attack was performed using a light microscope.

Corrosion load time	168 hours	240 hours	480 hours	720 hours
Sample identification	A	B	C	D

Table 2: Marking of EN AW 2024 alloy samples after corrosion test

After 168 hours of exposure in a corrosive environment (**Fig. 2**), uneven local areas of corrosion attack were visible in cross section. The microscope images indicated it was pitting corrosion. The pits were relatively large, such as the documented corrosion degradation: length 16.44 µm and depth of the pit 6.22 µm. The detail documents the state of grain boundaries in the subsurface layers of the experimental sample.

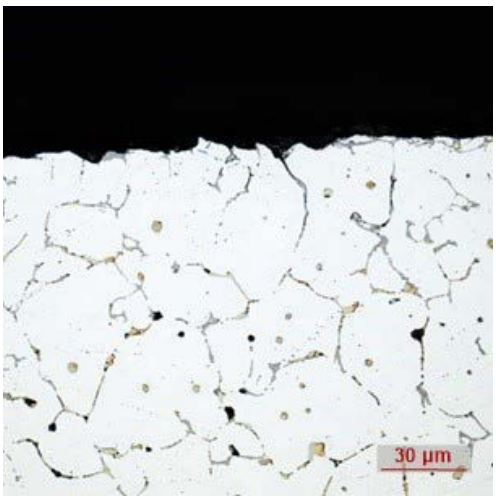

Figure 2: Corrosion attack, exposure in a corrosive environment; 168 h.

After 240 hours of exposure in a corrosive environment (**Fig. 3**), significant pitting corrosion in the sample can be seen, while with the time of exposure in the corrosive environment, the pitting grows unevenly (e.g., width 21.083 µm and depth 8.19 µm). There is also a significant weakening of grain boundaries by corrosion products in subsurface layers.

After longer exposure times, the corrosion attack spread in all directions. For clarity, **Figure 4** shows examples of pitting corrosion and the formation and spread of IC after only 480 hours of exposure in a corrosive environment. **Figure 4** shows the exclusion of phases along grain boundaries and interdendritic porosity at grain boundaries. In this case, the corrosion products penetrate to a depth of 75 µm from the sample surface. The detail documents the violation of the cohesion of the material.

After 720 h of exposure of the sample to a corrosive environment, intergranular corrosion spreads in all directions, which is shown in **Fig. 5**. The exclusion of Al_2Cu phases along grain boundaries is evident here. Intergranular corrosion penetrates up to 95 µm below the alloy surface.

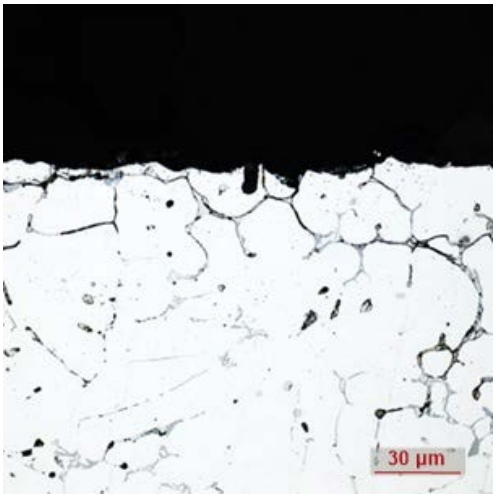

Figure 3: Corrosion attack, exposure in a corrosive environment; 240 h.

Figure 4: Microstructure of the sample after 480 h in a corrosive environment.

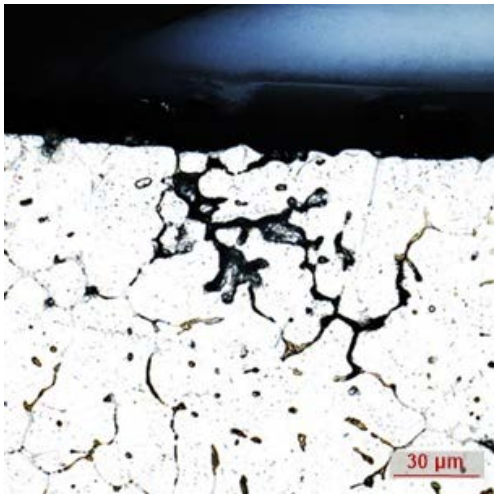

Figure 5: Microstructure of the sample after 720 h in a corrosive environment.

EDX ANALYSIS OF SAMPLE MORPHOLOGY

The study of the surface morphology of the samples was performed using electron microscopy. In all cases, a TESCAN VEGA 3 electron scanning microscope was used for imaging, while the samples were always studied at a magnification of 1,000x, 2,500x, and then 4,000x.

Figure 6 shows that in an area where IC occurs, corrosion products have penetrated into the α-matrix that surrounds them. An increased distribution of O was observed. This confirms the recording of the area EDX analysis and the quantification of the results of the area EDX analysis in both areas (**Figs. 6 and 7**), where the oxygen content was measured up to about 23% wt.

EVALUATION OF THE COURSE OF HARDNESS

Another evaluation of the experimental samples was to examine the course of hardness depending on the depth of occurrence of corrosion products, which are essentially intermetallic phases. The hardness of the sample without corrosion was 80 HV. The hardness decreases toward the core of the sample, as the amount of corrosion products decreases from the surface to the core of the sample.

CONCLUSION

Based on the performed experiments, five samples were made from EN AW 2024 alloy, which were subsequently subjected to a detailed examination, during which the influence of the corrosion environment on the structure of the material and its properties (hardness) was studied. Based on the performed analyses, the following conclusions were reached:

- After 168 to 240 hours of exposure to salt spray, an uneven distribution of pitting corrosion was found with a penetration of 16 mm below the surface of the material
- After 480 hours of exposure to salt spray, an uneven distribution of pitting and intergranular corrosion was found, which occurs in dendritic cores as these areas are depleted of Cu in the micro-segregation, and penetrates to a depth of 50 mm

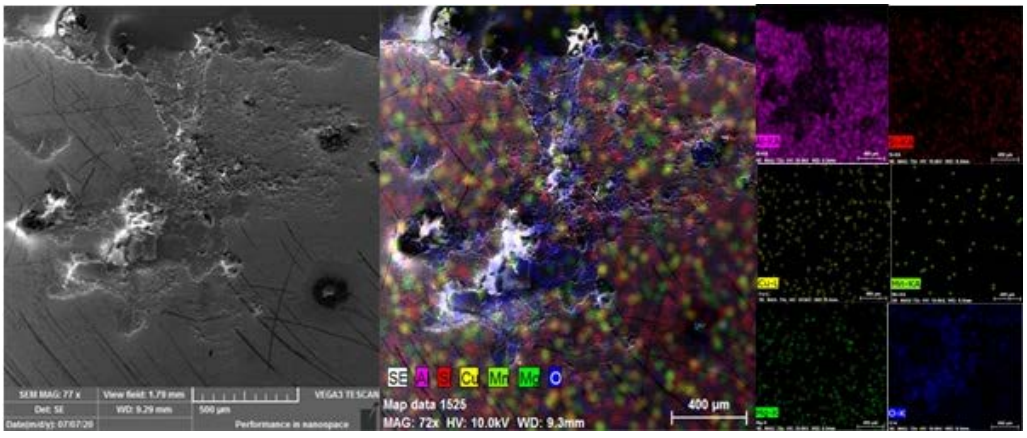

Figure 6: Microstructure of Sample C, elemental cross-sectional maps of the sample.

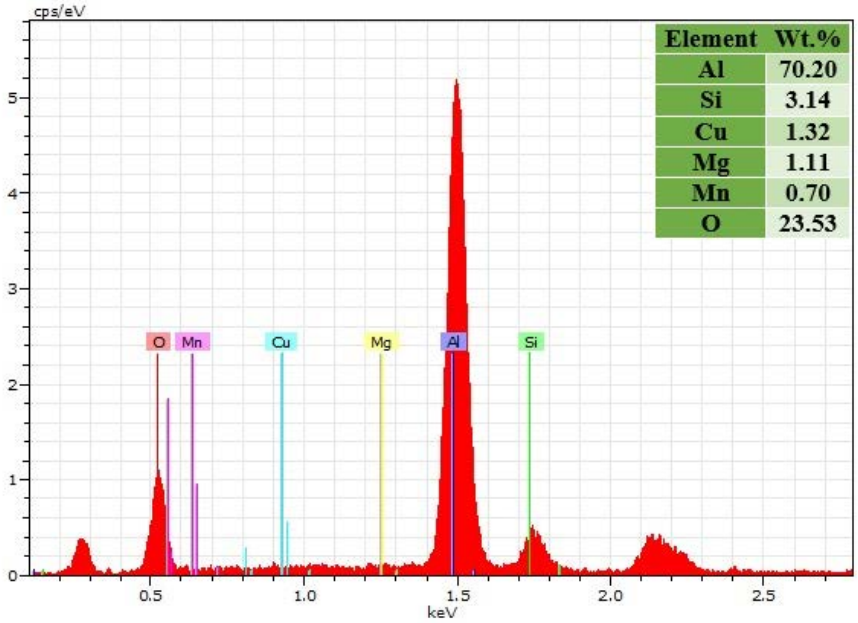

Figure 7: Area EDX analysis of a selected area from sample C and quantification of the results of area EDX analysis.

- For a sample after 720 hours of salt spray exposure, the microstructure shows an uneven distribution of pitting and intergranular corrosion closely associated with interdendritic phases, with penetration up to 95 μm below the alloy surface
- Samples after 480 and 720 hours show intergranular corrosion, which begins to act at grain boundaries that are rich in Al_2Cu and continues in areas of α-phase depleted by Cu; area EDX analysis confirmed areas of intergranular corrosion in the α-matrix, and an increased distribution of O was observed
- From the performed hardness analysis, it can be seen that the reduction of the hardness of the material is associated with the reduction of the number of Cu in the α-phase regions, which was consumed for the formation of corrosion products in the form of intergranular corrosion

REFERENCES:

[1] *Lin, Y. C. et al. Effects of creep-aging processing on the corrosion resistance and mechanical properties of an Al–Cu–Mg alloy. Mater. Sci. Eng. A 605, 192–202 (2014).*

[2] *McNaughtan, D., Worsfold, M. & Robinson, M. J. Corrosion product force measurements in the study of exfoliation and stress corrosion cracking in high strength aluminium alloys. Corros. Sci. 45, 2377–2389 (2003).*

[3] *Eivani, A. R., Zhou, J. & Duszczyk, J. Mechanism of the formation of peripheral coarse grain structure in hot extrusion of Al-4.5Zn-1Mg. Philos. Mag. 96, 1188–1196 (2016).*

[4] *ČSN ISO 9227. Corrosion tests in artificial atmospheres - Salt spray tests. Eur. Stand. EN ISO 92272006 3, (2007).*

[5] *Kusmierczak, S. & Hren, I. Influence of Al-Si7Mg0.3 Alloy Modification on Corrosion Behaviour in the Salt Environment. Manuf. Technol. 19, 802–806 (2019).*

[6] *Zhou, C., Yang, X. & Luan, G. Effect of root flaws on the fatigue property of friction stir welds in 2024-T3 aluminum alloys. Mater. Sci. Eng. A 418, 155–160 (2006).*

Advanced Optical Metrology

Part VI

Particles

Introduction

The term particle is derived from Latin, where the prefix "part" means a portion of something, and the suffix "–icle" is equivalent to small. Its meaning depends on the subject but is generally used to name a portion of matter with reduced dimensions. There is a whole field called particle physics that studies the elemental particles that form matter. However, elemental particles like electrons, protons, quarks, etc., are not what chemists and materials scientists mean when they refer to particles. For them, a particle is the smallest fragment of matter that maintains the chemical properties of a body. In this sense, atoms and molecules are particles, but most of the time, the term particle is used to refer to micro and nanoparticles.

A nanoparticle is a particle with a size between 1 and 100 nm, although the term is used for particles up to 500 nm and for fibers, tubes, or rods that are less than 100 nm in at least one dimension.[1] Metal particles smaller than 1 nm are referred to as "atom clusters." Other classes include microparticles (1–1000 µm), fine particles (100–2500 nm), and coarse particles (2500–10000 nm).

UNIQUE PROPERTIES

Nano and microparticles are distinctive materials that have enormous technological and scientific value. They are used in many applications, including energy, medical, and environmental. Even though nano and microparticles have the same composition as analogous bulk material, they display very interesting optical, electrical, thermal, and magnetic properties. Materials science has developed several methods to tune these properties for specific applications.

Nano and microscale particles have two technologically relevant features. First, particulate systems have a very high surface-to-weight ratio. As a result, surface energies are large with respect to volumes, and, therefore, the energetics of reactions (and rates) are different. This characteristic makes them valuable for a wide range of applications such as coatings, catalysts, adsorbents, and more. On the other hand, when the scale is about a few nanometers, new properties and new striking phenomena take place.

Properties such as melting point, fluorescence, electrical conductivity, magnetic permeability, and chemical reactivity change as a function of the particle's size.[2] For example, at the nanoscale, quantum effects are dominant, which is why semiconductor quantum dots emit different wavelengths of light depending on their nano-size.[3] Another example is magnesium (Mg), where the number of atoms and the size of the cluster/particle, determines the electronic band gap of the material. The electronic proper-

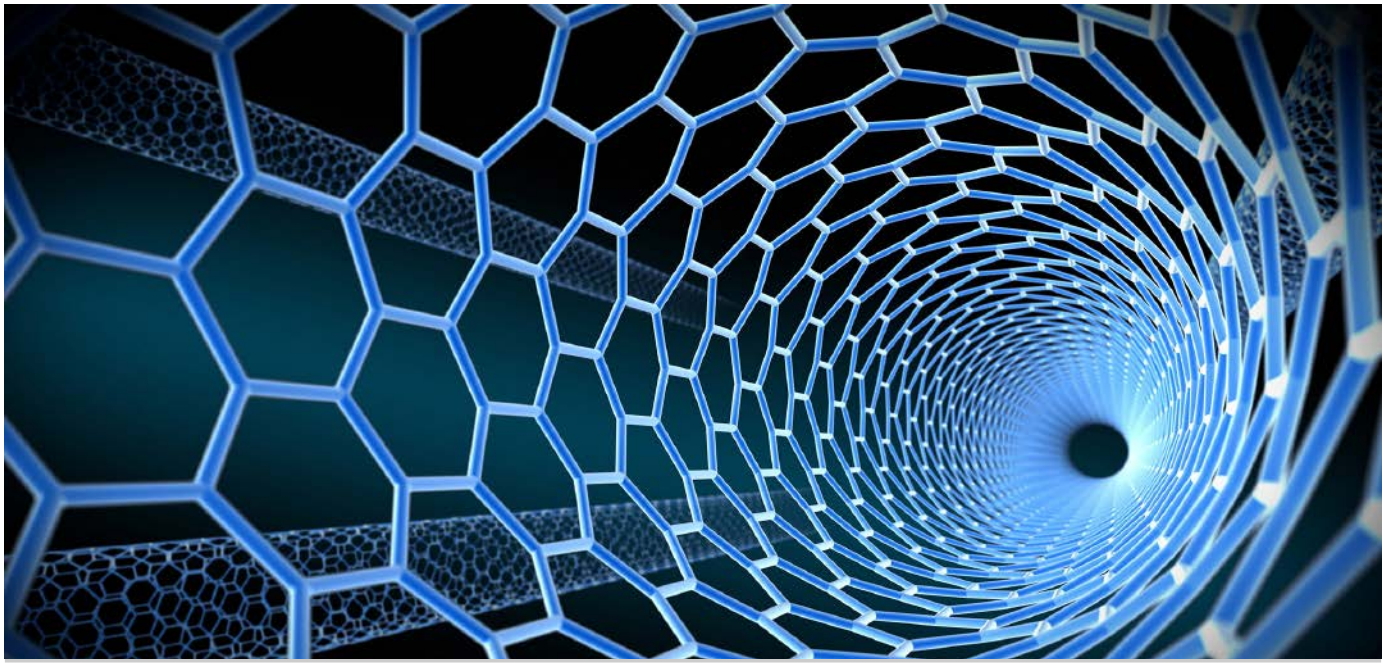

Figure 1

ties of the clusters or particles change from a semi-conductor (<18 atoms) to metallic.[4]

Nanoparticles made of gold and silver exhibit size-dependence in their optical properties. [6] For example, Figure 2 shows where different shapes and sizes determine a material's optical properties. Gold and silver nanoparticles absorb and scatter light very efficiently. They interact strongly with light because the conductive electrons on the metal surface undergo a collective oscillation when they are excited by light at specific wavelengths; this is known as surface plasmon resonance (SPR). The absorption and scattering properties of these nanoparticles can be tuned by controlling the particle size, shape, and the local refractive index near the particle surface.[6]

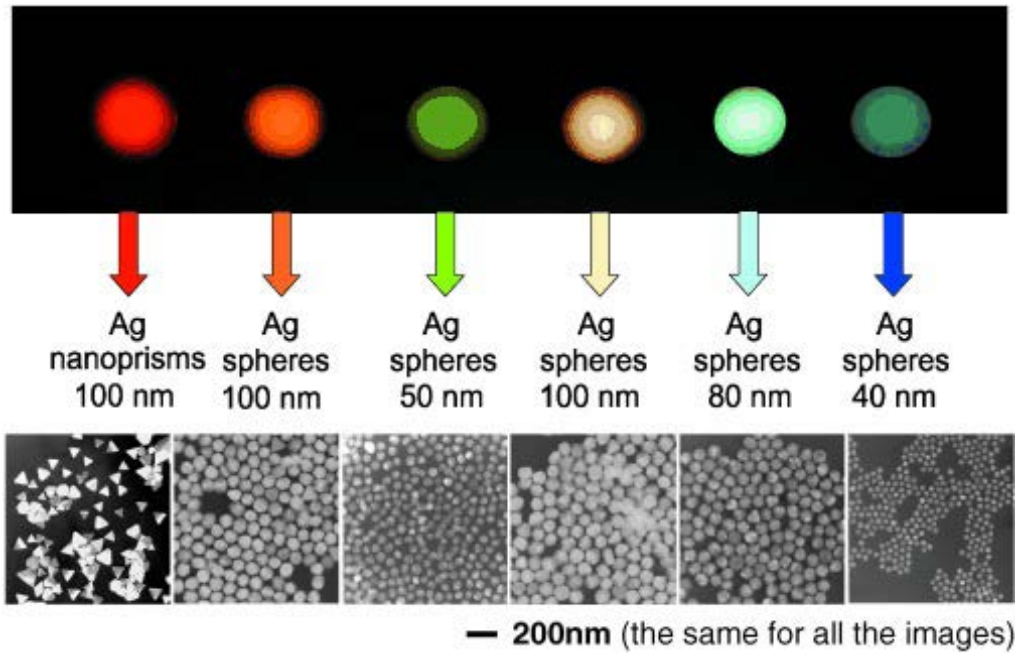

Figure 2: Size, shape, and composition determines the Rayleigh light-scattering properties of various nanoparticles.[8]

Gold and silver nanoparticles have diverse applications in drug delivery, such as determining and sensing drugs in pharmaceuticals.[7]

DIVERSE SHAPES AND SYNTHESIS PATHS

Based on their shape, nanoparticles can occur as nanosheets or nanofilms, which have at least one dimension in this size range; and nanorods and nanoparticles, which have two and three dimensions in this size range, respectively. There are also nanotubes, which are nanoscale materials that have a tube-like structure (e.g., carbon nanotubes).

Nano and microparticles are usually synthesized using physical and chemical methods. In physical methods, particles are generated by decreasing the size of the source material (top-down approach). Physical techniques include milling, gas condensation, electro-spraying, lithography, and thermal decomposition. On the other hand, in chemical methods, particles are created by nucleating and growing particles from atomic or molecular precursors in the liquid or vapor phase of a chemical reaction (bottom-up approach). Chemical methods include microemulsion, emulsion polymerization, hydrothermal, microfluidic, chemical vapor, pyrolysis, and sol-gel processes. Chemical methods generate nanostructures with fewer defects, enable more complex and homogeneous compositions, and are easily scalable for low-cost and rapid fabrication.

UNCOUNTABLE APPLICATIONS

Several industries benefit from nano and microparticles. The microelectronics industry—one of the first to use nanoparticles—supplies an annual market of 500,000 million dollars (2016).[9] Today, medicine is one of the most promising areas for the application of microparticles to treat specific diseases, as drug delivery systems and/or nano/micro-actuators.[10] Moreover, in the field of energy, microparticles are being used to develop systems with greater energy storage capacity, as in the case of carbon nano tubes in modern batteries.[9] Likewise, energy capture capacity can lead to the development of devices that produce their own energy with a significant advantage over wiring or batteries. The food industry also sees advantages in the use of nanoparticles, since they can be used to detect changes in food at early stages, helping avoid contamination prior to consumption.[9]

As our understanding of how we can develop and improve the synthesis and characterization methods of nano and microparticles, we will continue to find new applications that help solve global challenges in applications like energy, health, and food, positively impacting our daily lives thanks to their fascinating and tunable properties.

REFERENCES:

[1] *A.C. Grimsdale, K. Müllen, The Chemistry of Organic Nanomaterials, Angew. Chemie Int. Ed. 44 (2005) 5592–5629. https://doi.org/10.1002/anie.200500805.*

[2] *K. Yoshihara, M. Sakamoto, H. Tamamitsu, M. Arakawa, K. Saitow, Extraordinary Field Enhancement of TiO 2 Porous Layer up to 500-Fold, Adv. Opt. Mater. 6 (2018) 1800462. https://doi.org/10.1002/adom.201800462.*

[3] *D. Ren, B. Wang, C. Hu, Z. You, Quantum dot probes for cellular analysis, Anal. Methods. 9 (2017) 2621–2632. https://doi.org/10.1039/C7AY00018A.*

[4] *O.C. Thomas, W. Zheng, S. Xu, K.H. Bowen, Onset of Metallic Behavior in Magnesium Clusters, Phys. Rev. Lett. 89 (2002) 213403. https://doi.org/10.1103/PhysRevLett.89.213403.*

[5] *Introduction to Nanoscience: Some Basics, (n.d.). https://serc.carleton.edu/msu_nanotech/nano_intro.html.*

[6] *A.J. Haes, C.L. Haynes, A.D. McFarland, G.C. Schatz, R.P. Van Duyne, S. Zou, Plasmonic Materials for Surface-Enhanced Sensing and Spectroscopy, MRS Bull. 30 (2005) 368–375. https://doi.org/10.1557/mrs2005.100.*

[7] *K. Alaqad, T.A. Saleh, Gold and Silver Nanoparticles: Synthesis Methods, Characterization Routes and Applications towards Drugs, J. Environ. Anal. Toxicol. 6 (2016). https://doi.org/10.4172/2161-0525.1000384.*

[8] *C.A. Mirkin, The Beginning of a Small Revolution, Small. 1 (2004) 14–16. https://doi.org/10.1002/smll.200400092.*

[9] *C.R. Kagan, L.E. Fernandez, Y. Gogotsi, P.T. Hammond, M.C. Hersam, A.E. Nel, R.M. Penner, C.G. Willson, P.S. Weiss, Nano Day: Celebrating the Next Decade of Nanoscience and Nanotechnology, ACS Nano. 10 (2016) 9093–9103. https://doi.org/10.1021/acsnano.6b06655.*

[10] *D. Ditter, P. Blümler, B. Klöckner, J. Hilgert, R. Zentel, Microfluidic Synthesis of Liquid Crystalline Elastomer Particle Transport Systems which Can Be Remote-Controlled Magnetically, Adv. Funct. Mater. 29 (2019) 1902454. https://doi.org/10.1002/adfm.201902454.*

01 Microfluidic Synthesis of Liquid Crystalline Elastomer Particle Transport Systems that Can Be Remote-Controlled Magnetically

D. Ditter, P. Blümler, B. Klöckner, *et al.*

ABSTRACT

The synthesis of liquid crystalline elastomer (LCE) particles, which can be remote-controlled magnetically and used as transport systems, is presented for the first time. Ferri-magnetic, rod-shaped Fe_3O_4 nanoparticles are functionalized to make them compatible with organic LCE precursor compounds. Their influence on the LCE precursor alignment is studied and thermoresponsive as well as photoresponsive LCE microparticles are synthesized with a microfluidic device. The potential of synthesized LCE particles as transport systems is demonstrated by the transport of plastic, textiles, or copper, which can be pushed just due to magnetic forces or transported in general by taking advantage of the phase-dependent "stickiness" of LCEs. These studies open doors to novel applications of LCEs as microrobots using magnetism as a control.

INTRODUCTION

The interest for microactuators grow constantly.[1–4] Recently, a transition from hard and rigid to soft and flexible microactuators took place, probably because of the easy corrosion and low biocompatibility of hard actuators.[5,6] An emerging smart soft actuator material is liquid crystalline elastomers (LCEs), which can be triggered with diverse stimuli fields like heat, light, or electric.[7,8] They consist of mesogenic groups, which are incorporated in an elastomer network and thus combine the orientational order of the LC phase with rubber elasticity.[9,10]

To move LCEs magnetically, they have to be made magnetic. An approach to realize this is the integration of magnetic components like ferri-magnetic Fe_3O_4 nanoparticles. For this purpose, such inorganic nanoparticles can be functionalized with polymers to make them compatible with the organic LC matrix.[11] So far, LCEs containing magnetic nanoparticles were mainly synthesized to trig-

ger their phase transition/actuation through heating with AC electromagnetic fields.[8,11,12] However, to the best of our knowledge, no attempts were made to use magnetism for a controlled movement of LCE particles in space.

In this publication we present a route to synthesize a large amount of thermo- and photoresponsive LCE microparticles with a microfluidic setup. They can be moved in magnetic fields with high precision and are suitable as transport systems.

MATERIALS AND METHODS

Materials and Reagents

The liquid crystalline monomers, crosslinker, the dye for the initiator, the Fe_3O_4 nanorods were synthesized as described in the literature (see doi.org/ 10.1002/adfm.201902454 for references). 1,6-Hexanediol diacrylate was purchased from Alfa Aesar. The photoalignment material ROP-108 EXP001 was purchased from Rolic Technologies Ltd. 4-Cyano-4-(thiobenzoylthio)pentanoic acid and the silicone oils (100 cSt and 1000 cSt) were purchased from Sigma Aldrich. Hydrofluoroether Novec HFE-7300 was purchased from 3M. Microscope slides (size: 76 × 26 mm, thickness: 1 mm) were purchased from CARL ROTH. Tetrahydrofuran was purchased from Fisher Scientific. Ethanol and Hellmanex III concentrate were purchased from VWR Chemicals. Butyryl choline butyltriphenylborate (Borat V) was purchased from Spectra group limited.

PTFE tubings for the microfluidic device were purchased from WICOM. Fused silica capillary, T-junction, nuts and ferrules for the microfluidic device were purchased from Postnova Analytics GmbH. The coldlight source KL 1600 was purchased from Schott. The red light HighPower LED (623 nm) was purchased from Conrad.

Characterization of Polymers

^{1}H-NMRs and ^{19}F-NMRs were measured using a 300 MHz spectrometer (model: Avance III HD 300) from Bruker. GPC was measured in THF with polystyrene as an external and toluene as an internal standard. A refractive index detector (G 1362 RID) and a UV/vis detector (UV-2075 Plus) from Jasco were used to detect the polymers. IR spectroscopy was performed using a FT/IR-4100 from Jasco. Spectra were analyzed with a Spectra Manager 2.0 from Jasco. UV/vis spectra were measured with a Jasco spectrophotometer V-630. Spectra were analyzed using Spectra Manager 2 from Jasco. TGA measurements were performed with a Perkin Elmer Pyris 6 under nitrogen flow using a heating rate of 10 °C (50 °F) min−1 (50–700 °C or 122–1292 °F). TEM measurements were performed on a Tecnai G2 Spirit (FEI) at 120 kV using a 2_2k camera.

LC Phase Analysis of Fe_3O_4 Containing LCE Precursors

Microscope slides were cut into 25 × 25 mm pieces, rinsed with a Hellmanex III solution, deionized water, and ethanol for 3 min respectively, dried with a nitrogen stream, and treated with oxygen plasma in a plasma oven (model: PlasmaPrep5) from Gala Instrumente GmbH for 5 min with a power of 100 W.

40 µL photoalignment layer solution ROP-108 EXP001 was spin-coated dynamically at 2000 rounds per minute (rpm) for 60 s on top of the microscope slides, dried at 150 °C (302 °F) for 10 min on a hot plate, allowed to cool down to room temperature, and irradiated with linear polarized UV-light (UV source: Oriel LSH302 (500 W lamp)) with an angle of incidence of 90° through a polarizer from Olympus® U-POT Japan (>300 nm) for 10 min. 10 mg of the particular LCE precursor (formulation 1a without or including 45 mol% comonomer 3 and formulation 1b) containing 0, 5, and 10 wt% (wt% referred to the monomer(s)/crosslinker mixture) Fe_3O_4 was dissolved in 100 µL THF and spin-coated dynamically with 3000 rpm on top of the alignment layer.

LCE precursor films were heated in their LC phase with a hot stage (model: Linkam TMS 94) and investigated via polarized optical microscopy (model: Olympus BX51 microscope). Images were taken with a microscope camera (model: Olympus DP22 camera) and analyzed using the imaging software Cell^D.

Analysis of LCE Actuations

Thermal and photochemical actuations of all LCE particles were investigated using a light microscope (model: Olympus BX51 microscope) equipped with a microscope camera (model: Olympus DP22 camera) and a hot stage (model: Linkam TMS 94) to set the desired temperature. The LCE particles were heated from the LC to the isotropic phase (80 to 130 °C or 176 ° to 266 °F) for thermoresponsive LCEs synthesized out of formulation 1a without comonomer 3; 50 to 100 °C (122 to 212 °F) for thermoresponsive LCEs synthesized out of formulation 1a including 45 mol% comonomer 3; 40 to 110 °C (104 to 230 °F) for photoresponsive LCEs synthesized out of formulation 1b)

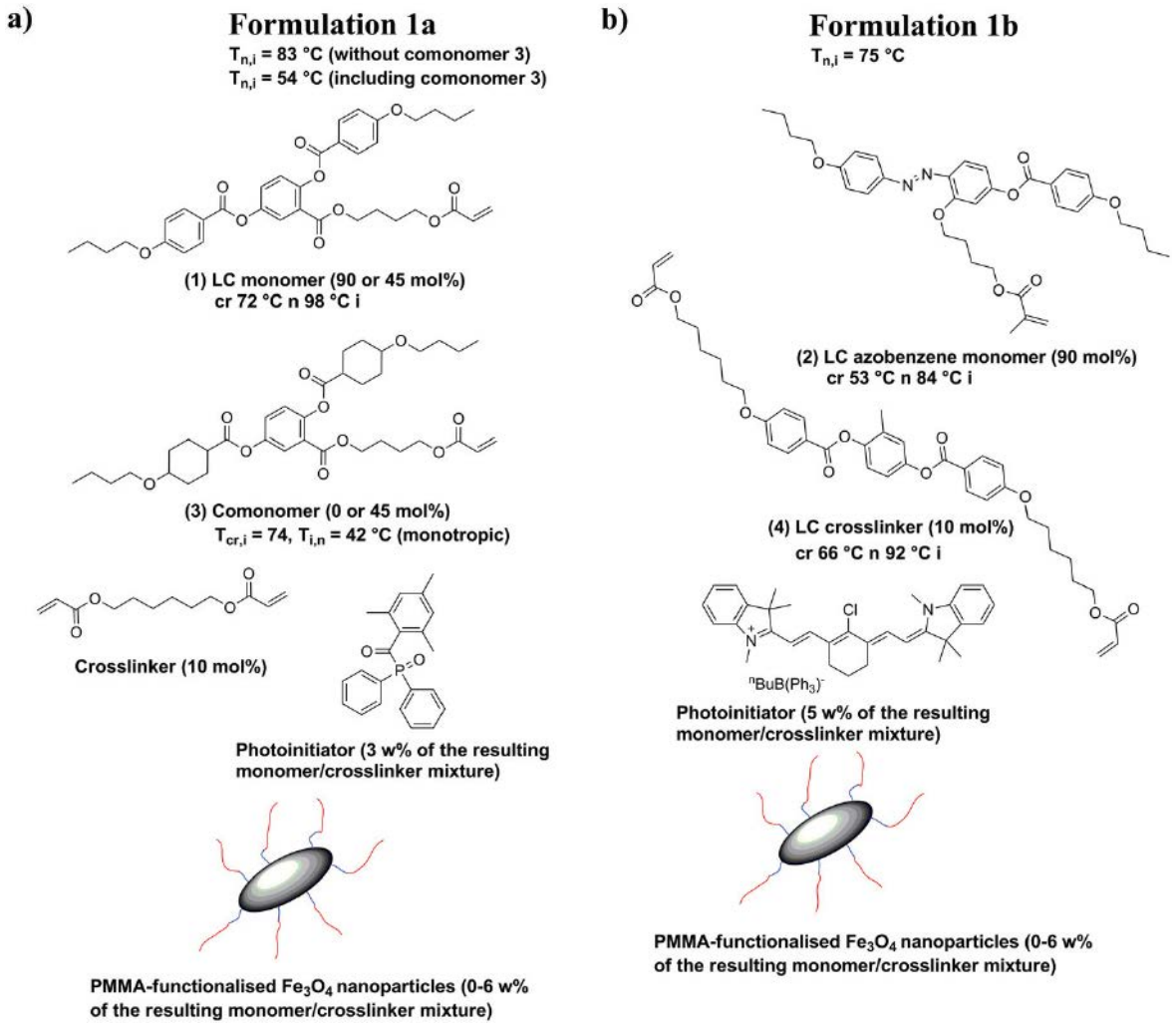

Figure 1: a) Thermoresponsive LCE precursor consisting of LC monomer 1 (4′-acryloyloxybutyl 2,5-(4′-butyloxybenzoyloxy)benzoate) (90 mol%) or a mixture of LC monomer 1 (45 mol%) and comonomer 3 (4′-acryloyloxybutyl 2,5-di(4′-pentylcyclohexyloyloxy)benzoate) (45 mol%), a crosslinker (1,6-hexandioldiacrylate) (10 mol%), a UV-initiator (diphenylphosphine oxide or TPO) (3 wt% referred to the monomer/crosslinker mixture), and PMMA functionalized Fe_3O_4 nanorods (0–6 wt% referred to the monomer/crosslinker mixture). b) Photoresponsive LCE precursor consisting of LC azobenzene monomer 2 (4-butoxy-2′-(4-methacryloyloxybutoxy)-4′-(4-butoxybenzoyloxy)azobenzene) (90 mol%), LC crosslinker 4 (2-methyl-1,4-phenylene bis(4-((6-(acryloyloxy)hexyl)oxy)benzoate)) (10 mol%), a NIR initiator (1,3,3,1′,3′,3′-hexamethyl-11-chloro-10,12-propylene-tricarbocyanine triphenylbutyl borate or CBC) (5 wt% referred to the monomer/crosslinker mixture), and PMMA functionalized Fe_3O_4 nanorods (0–6 wt% referred to the monomer/crosslinker mixture).

and their sizes were analyzed using the imaging software Cell^D. Irradiation of the photoresponsive samples were performed at 70 °C (158 °F) with the coldlight source KL 1600 using light guides to focus the light on samples. Irradiation with red light was performed with the help of a red-light filter from Schott (>500 nm), which was held in the light beam.

See the original article and supporting information for all experimental procedures (doi.org/ 10.1002/adfm.201902454).

RESULTS AND DISCUSSION

Synthesis of PMMA Functionalized Anisotropic Fe_3O_4 Nanoparticles

Rod-shaped, ferri-magnetic Fe_3O_4 nanoparticles were made compatible with organic LCE precursors through functionalization with poly(methyl methacrylate) (PMMA). Hereby, stable suspensions could be obtained, especially when the LC precursor monomers are heated into their isotropic phase. The reaction scheme to obtain PMMA functional-

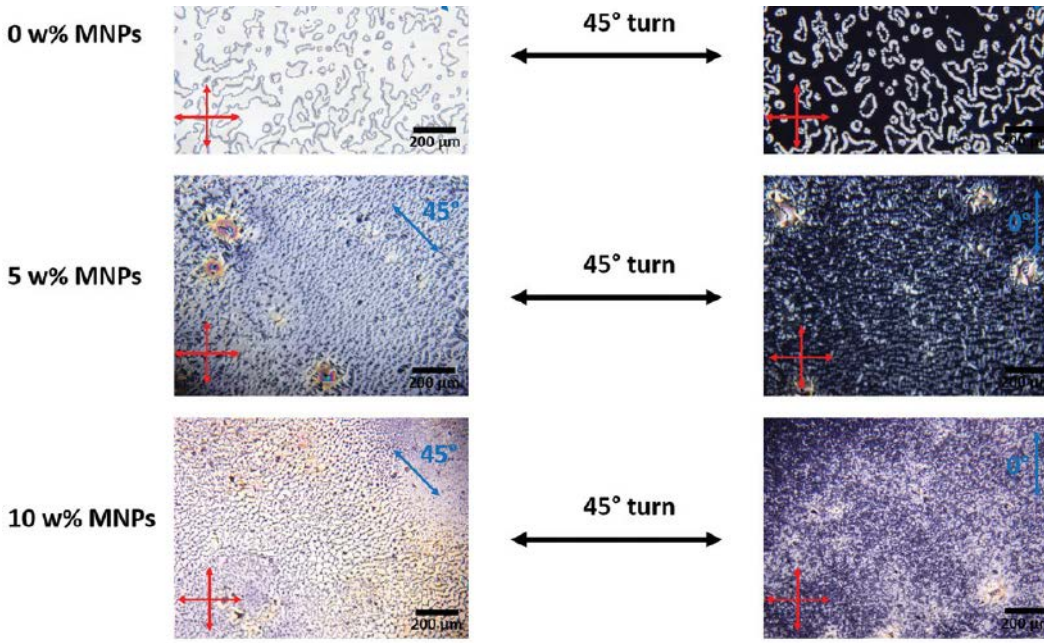

Figure 2: POM images of thermoresponsive LCE precursor mixtures 1a which are spin coated on top of a photoalignment layer and heated into the LC phase (70 °C or 158 °F). It is shown that the contrast of dark and bright states–when the director lies parallel or at a 45° angle regarding to the crossed polarizers–decrease with increasing amounts of MNPs. Thus, it can be concluded that MNPs disturb the alignment. The red arrows indicate the position of the crossed polarizers, and the blue arrows indicate the director's alignment (scale bar: 200 µm).

ized magnetic nanoparticles (MNPs) follows a previously described procedure[13].

Anisotropic, magnetic Fe_3O_4 nanoparticles were synthesized through reduction of Fe_3O_4 particles under a hydrogen/ nitrogen atmosphere. Functionalized Fe_3O_4 nanorods had a length of about 340 nm and a length to width ratio of 4.4 to 1, which was proofed via transmission electron microscopy.

Functionalization of magnetic nanoparticles (MNPs) was done via a grafting-to process with poly(methyl methacrylate-b-dopamine acryl amide) (P(MMA-b-DOPA)). The ratio between the PMMA block and the DOPA block was determined to be 10:1 (by 1H-NMR spectroscopy).

Integration of MNPs into LCE Precursors and their Influence on LC Alignment

The functionalized nanoparticles should be integrable homogeneously into organic thermoresponsive and photoresponsive LCE precursor mixtures. To demonstrate this, two LCE precursor systems were chosen. Their ingredients, including functionalized nanoparticles, are shown in **Figure 1a, b.**

To show the solubility of MNPs in LCE precursors, the ingredients of formulation 1a and 1b were dissolved in tetrahydrofuran, mixed, and the solvent was evaporated afterward. The amount of MNPs was varied between 0 and 10 wt%. While formulations without MNPs were colorless (formulation 1a) or showed an orange color (formulation 1b), the brown color of functionalized Fe_3O_4 particles was adopted with increasing MNP amount. This homogeneous color change of the LCE precursors without observing any aggregates by bare eye is a first proof of compatibility.

To take a closer look, we spin-coated thin films of formulations 1a and 1b containing different amounts of MNPs on a photoalignment layer. Afterward we annealed the films in their LC phase. Thereafter, the dispersions were investigated with polarized optical microscopy (POM). POM images of films of the thermoresponsive system 1a (without comonomer 3) including 0, 5, and 10 wt% MNPs are presented in **Figure 2.**

All films (this was also found for the other mixtures) showed dark and bright states when the director was oriented parallel or at a 45° angle regarding to the crossed polarizers. The contrast between dark and bright states indicates the quality of alignment. It can be observed that with increasing amount of MNPs the contrast and thus the director alignment decreases or is partially not present anymore. The reason for this is probably that the surface of the MNPs disturbs the director field of the LC phase. This observation already allows predicting that the magnitude of actuation of the LCEs should decrease with increasing

Fe_3O_4 nanoparticle amount since the MNPs reduce the homogeneity of the director field.

Microfluidic Synthesis and Actuation Properties of Magnetic Thermoresponsive and Photoresponsive LCE Particles

To synthesize LCE particles with a microfluidic setup, precursors were dissolved in THF, stirred to ensure homogeneous dispersions, and the THF was evaporated under reduced pressure. Precursors were then inserted in the microfluidic device. The mixtures were pumped through the device by a low viscous silicon oil at 90 °C (194 °F) (isotropic phase of the LC monomers) to melt them and to obtain the nanoparticles homogeneously dispersed in the isotropic phase. Precursor droplets were formed at the end of a glass capillary. The droplets were then guided over a precision hot plate and polymerized and crosslinked in their LC phase. Alignment was obtained through shear forces. In this way photoresponsive as well as thermoresponsive LCEs containing 0–6 wt% MNPs regarding to the respective monomer/crosslinker mixture were prepared. Thermoresponsive LCEs containing 45 mol% comonomer 3 were synthesized with MNP amounts of 3 and 6 wt%.

Thermal and photochemical actuations were analyzed with an optical microscope by heating them from their LC to their isotropic state. Examples of actuations of a thermoresponsive and a photoresponsive micron-sized LCE particle, including 3 wt% MNPs, are shown in **Figure 3.** The actuations are reversible at least up to 10 actuation cycles. This proves that well crosslinked LCEs are obtained under these conditions.

In **Figure 3,** the thermal and photochemical LCE actuation properties in dependence of their amount of MNPs of the different systems are presented. In general, actuation decreases with increasing amounts of nanoparticles, thus confirming that MNPs disturb the director orientation (see Section 2.2). Particles without MNPs showed thermal actuations of about 40%, which is typical for this kind of LCEs.[14–16] When increasing the Fe_3O_4 amount from 0 to 6 wt%, thermal actuations decrease from about 40% to 30% (ther-

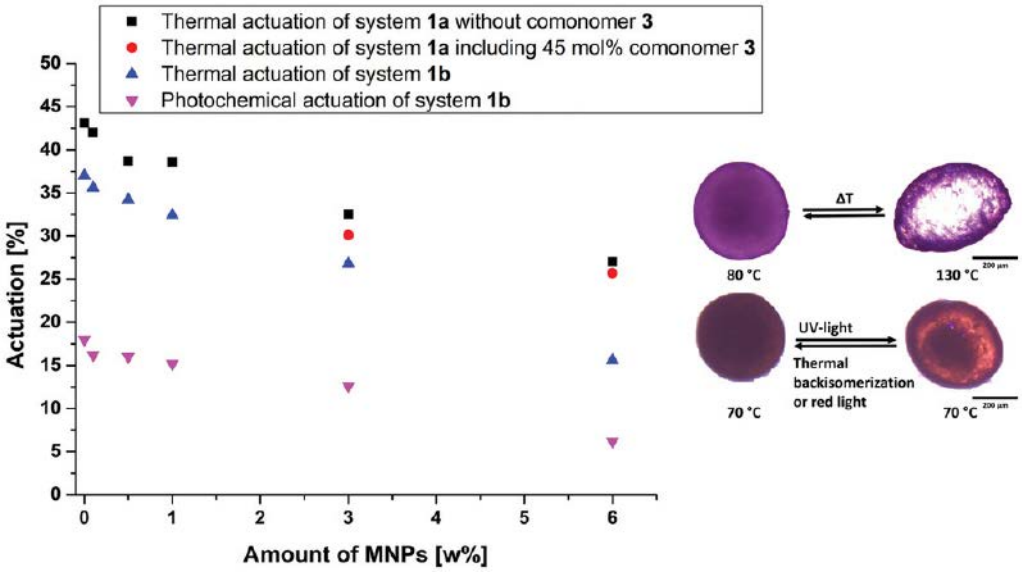

Figure 3: Thermal actuations of the thermoresponsive LCE systems synthesized out of precursor 1a without and including 45 mol% comonomer 3 as well as thermal and photochemical actuations of the photoresponsive LCE system synthesized out of precursor 1b in dependence of their amount of MNPs. On the right side, examples of thermal and photochemical actuations of magnetic LCE microparticles are shown. Upper actuation: Thermal actuation between 80 and 130 °C (176 and 266 °F) of a LCE particle (synthesized out of formulation 1a without comonomer 3) containing 3 wt% Fe_3O_4 particles. Lower actuation: Photochemical actuation of a LCE particle (synthesized out of formulation 1b) containing 3 wt% Fe_3O_4 particles (scale bar: 200 µm).

moresponsive system 1a without comonomer 3) or 15% (photoresponsive system 1b). Photochemical actuations of LCEs synthesized out of formulation 1b decrease from 18% to 6%. Comonomer containing LCEs showed thermal actuations of about 30%, which is slightly below the values of LCEs without comonomer 3, while the actuation temperature decreased from 90–130 to 50–90 °C (194–266 to 122–194 °F). We defined thereby the actuation as the difference of particle length before and after actuation divided by the shorter length (always the dimension in which the particle length increases during heating or UV-irradiation has been regarded).

Guiding of LCE Particles with Magnetic Forces

For the experiments, particles were placed on the surfaces of different fluids that were filled in a glass vial, and a bar magnet was brought in their proximity. Thermo- as well as photoresponsive particles containing 0.5 to 6.0 wt% MNPs followed the magnetic field of the bar magnet on the surfaces whereby the speed increased with increasing amount of MNPs. This trend is not surprising since a higher amount of MNPs increases their magnetism. However, LCE particles containing less than 0.5 wt% MNPs did not follow the bar magnet because they are not or insufficiently magnetizable.

A magnetic setup[17] was used to move particles in the centimeter range with a precision in the submillimeter range. The permanent magnetic device consists of a coaxial arrangement of two Halbach cylinders. The setup was placed under a microscope, and particles inside a glass vial were placed in the middle of the setup on top of a copper block that was heated with a hot plate below to guide particles at different temperatures. To demonstrate magnetic guiding with this device, magnetic LCE particles were moved along a rectangular path. This is presented in **Figure 4a.** We show two particles at once to demonstrate that a collective movement is possible too. Here, it has to be mentioned that those particles tend to stick together in the magnetic setup due to their magnetic dipoles. Additionally, particles can be rotated around themselves through a magnetic stirrer that is shown in **Figure 4b.** To demonstrate that, in general, all kinds of desired movements are possible, we used the two particles shown in **Figure 4a** to "write" LCE on a DMSO layer. It has to be considered that the magnetic force of

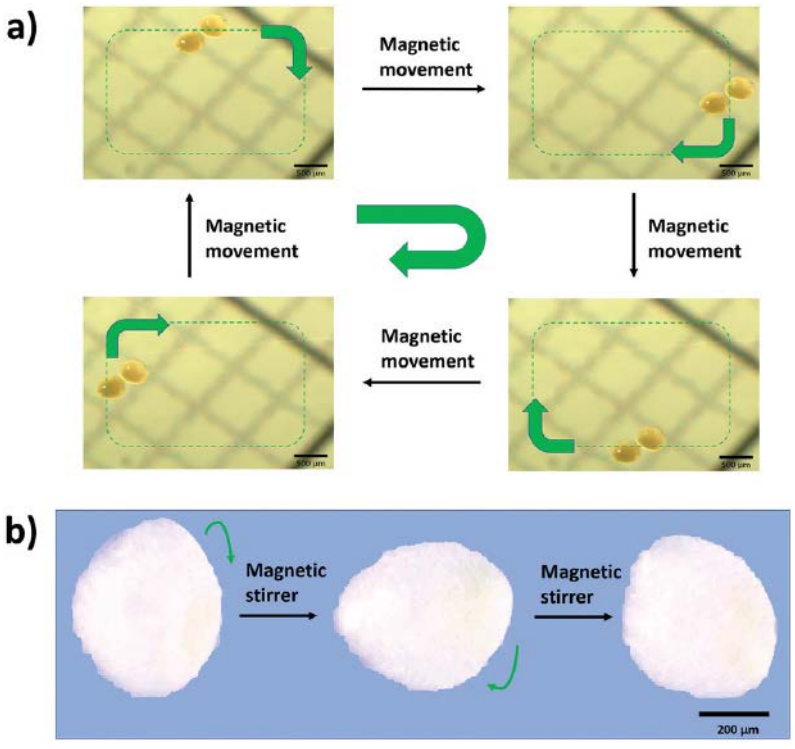

Figure 4: Movements of magnetic LCE particles with magnetic forces. a) Rectangular-like movement of two thermoresponsive magnetic LCE particles (synthesized out of formulation 1a without comonomer 3) containing 6 wt% ferri-magnetic Fe_3O_4 particles caused by the magnetic fields generated by the device shown in **Figure 4e.** The direction of movement is changed by varying the angle between the dipole and quadrupole. The desired moving path is indicated by a dashed green rectangle. The moving direction is indicated by green arrows (scale bar: 500 µm). b) Rotation of a thermoresponsive magnetic LCE particle (synthesized out of formulation 1a without comonomer 3) containing 3 wt% ferri-magnetic Fe_3O_4 particles. The rotation is caused by a magnetic stirrer (scale bar: 200 µm).

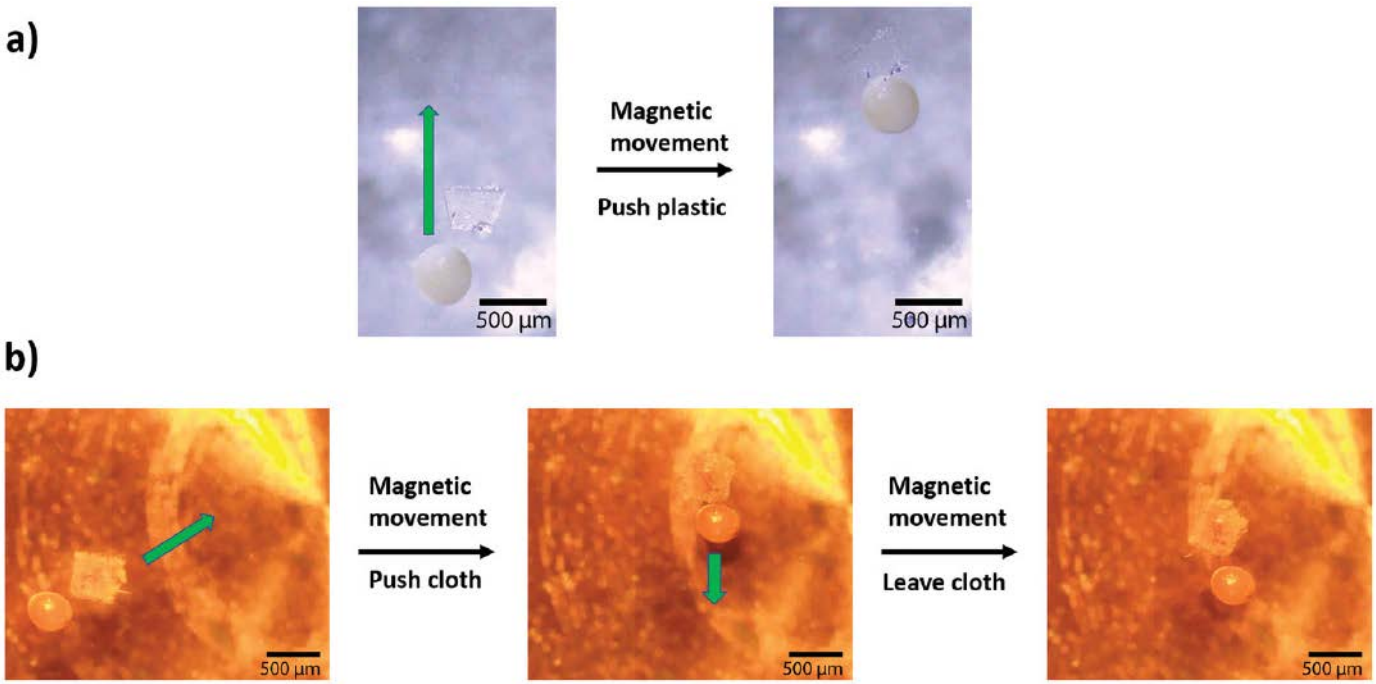

Figure 5: Pushing of a piece of a) plastic with a thermoresponsive LCE particle (synthesized out of formulation 1a without comonomer 3) containing 6 wt% ferri-magnetic Fe_3O_4 or b) textile with a photoresponsive magnetic LCE particle (synthesized out of formulation 1b) containing 6 wt% ferromagnetic Fe_3O_4 on top of a DMSO surface. Pushing is caused exclusively through magnetic forces caused by the magnetic setup shown in **Figure 4e.** The direction of movement is indicated by green arrows. The direction of movement is changed by varying the angle between the dipole and quadrupole (scale bar: 500 µm).

this setup is weaker in comparison to the bar magnet. Thus, magnetic particles including at least 3 wt% MNPs were necessary to observe a movement in the middle of the device.

Combination of Guiding and Actuation of LCE Particles in Magnetic Fields

To demonstrate the combination of guidance and actuation, we moved a photoresponsive LCE particle (synthesized out of formulation 1b) in a circle-like form on a DMSO surface at 70 °C (158 °F) and irradiated it with UV-light, which caused an actuation of 12.6% at a desired position. Generally, the thermoresponsive systems could be actuated by temperature variations. Since heating of the liquids takes, however, much time and as the particles can rotate (tumble around) on the surface it is not so easy to perform a well-controlled actuation just by heating. Nevertheless, reversible actuations were observed proving that the used fluids do not affect LCEs—for example—through swelling.

Magnetic LCE Particles as Transport Systems

The potential of the magnetic LCE particles as transport systems was investigated. For this, nonmagnetic materials like textiles, copper, or plastic were used as transport goods. There are two possibilities for transportation. First, the pure magnetic forces can be used to guide the LCE particles to other microparticles and push them ahead of themselves in the desired directions. This is shown in **Figure 5** where pieces of plastic and textiles are transported. However, with this approach it is just possible to push something and thus, if the direction of transportation needs to be changed, it is necessary that LCE particles leave the materials first and have to be brought to them from another direction again. To avoid this and to open the possibility to pull something, it is, however, possible to use the different stickiness of LCEs in their LC and isotropic phase.

During our experiments we recognized that nonmagnetic particles tend to stick to LCEs in their LC phase and leave the LCEs when they are brought in their isotropic phase. The reason for this is probably that LCEs become softer in the isotropic phase and thus it is easier for other micro-objects to leave the particles when they were tacked before.

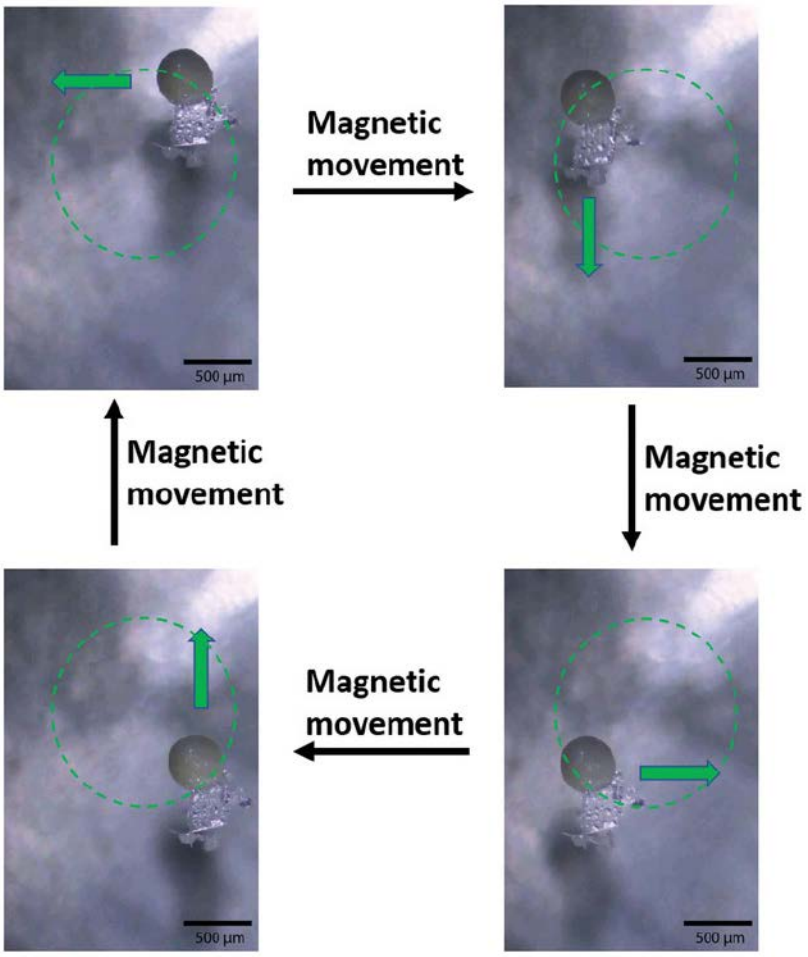

Figure 6: Circle-like transportation of a piece of plastic of a thermoresponsive magnetic LCE particle (synthesized out of formulation 1a without comonomer 3) containing 6 wt% ferri-magnetic Fe_3O_4 on top of a DMSO surface caused by the magnetic setup shown in **Figure 4e.** The desired movement path is indicated by the dashed green circle. The moving direction is indicated by green arrows. The direction of transportation is changed by varying the angle between the dipole and quadrupole (scale bar: 500 µm).

The trend of other objects to stick to the LCE particles was strongest if they got in contact with them in the isotropic phase and cooled down into the LC phase afterward. The reason for this might be that the objects are pushed easily into the soft isotropic LCE particles so that a large connecting interface is created. After cooling the LCE particles down, the objects cannot escape as the particles are in their tougher LC phase. As a result, they work like grippers. Hereby, objects can be transported (pushed and pulled) with the used magnetic setup what is demonstrated as a circle-like transportation of plastic in **Figure 6.**

CONCLUSION

Photoresponsive and thermoresponsive LCE microparticles, which can be moved magnetically and serve as actuators and transport systems, could be synthesized with a microfluidic device for the first time. Fe_3O_4 MNPs were integrated in these particles through functionalization with PMMA. The particles could be remote controlled magnetically on fluidic surfaces either with a bar magnet or a more sophisticated magnetic device. Light- and temperature-induced actuations of the LCE particles in dependence of their MNP contents were investigated and combined with magnetic movements. It was shown that MNPs lead to a disturbance of the director alignment of the used LCE precursors and thus, LCE actuations decrease with increasing amounts of Fe_3O_4. Here, a compromise needs to be found between actuation properties (degree of actuation) and magnetic addressability (speed of guiding) in dependence of the desired application. The guidance of LCEs in magnetic fields, and the use of their different stickiness to other materials in the LC and isotropic phase allowed their usage as transport systems. Our studies show that it is possible to synthesize a huge amount of such LCE transport systems and show their potential to use them as microrobots to transport micro-objects. Admittedly, their usage to complete tasks in the human body is still a dream but it demonstrates a possible next step to reach this goal.

REFERENCES:

[1] *A. Buguin, M.-H. Li, P. Silberzan, B. Ladoux, P. Keller, Micro-Actuators: When Artificial Muscles Made of Nematic Liquid Crystal Elastomers Meet Soft Lithography, J. Am. Chem. Soc. 128 (2006) 1088–1089. https://doi.org/10.1021/ja0575070.*

[2] *C. Ohm, C. Serra, R. Zentel, A Continuous Flow Synthesis of Micrometer-Sized Actuators from Liquid Crystalline Elastomers, Adv. Mater. 21 (2009) 4859–4862. https://doi.org/10.1002/adma.200901522.*

[3] *H. Yang, G. Ye, X. Wang, P. Keller, Micron-sized liquid crystalline elastomer actuators, Soft Matter. 7 (2011) 815–823. https://doi.org/10.1039/C0SM00734J.*

[4] *D.L. Polla, A.G. Erdman, W.P. Robbins, D.T. Markus, J. Diaz-Diaz, R. Rizq, Y. Nam, H.T. Brickner, A. Wang, P. Krulevitch, Microdevices in Medicine, Annu. Rev. Biomed. Eng. 2 (2000) 551–576. https://doi.org/10.1146/annurev.bioeng.2.1.551.*

[5] *C. Hu, S. Pané, B.J. Nelson, Soft Micro- and Nanorobotics, Annu. Rev. Control. Robot. Auton. Syst. 1 (2018) 53–75. https://doi.org/10.1146/annurev-control-060117-104947.*

[6] *F. Cheng, R. Yin, Y. Zhang, C.-C. Yen, Y. Yu, Fully plastic microrobots which manipulate objects using only visible light, Soft Matter. 6 (2010) 3447. https://doi.org/10.1039/c0sm00012d.*

[7] *C. Ohm, M. Brehmer, R. Zentel, Liquid Crystalline Elastomers as Actuators and Sensors, Adv. Mater. 22 (2010) 3366–3387. https://doi.org/10.1002/adma.200904059.*

[8] *A. Kaiser, M. Winkler, S. Krause, H. Finkelmann, A.M. Schmidt, Magnetoactive liquid crystal elastomer nanocomposites, J. Mater. Chem. 19 (2009) 538–543. https://doi.org/10.1039/B813120C.*

[9] *M. Warner, E.M. Terentjev, Liquid crystal elastomers, Oxford university press, 2007.*

[10] *H. Wermter, H. Finkelmann, Liquid crystalline elastomers as artificial muscles, E-Polymers. 1 (2001). https://doi.org/10.1515/epoly.2001.1.1.111.*

[11] *A.M. Schmidt, Electromagnetic Activation of Shape Memory Polymer Networks Containing Magnetic Nanoparticles, Macromol. Rapid Commun. 27 (2006) 1168–1172. https://doi.org/10.1002/marc.200600225.*

[12] *M. Winkler, A. Kaiser, S. Krause, H. Finkelmann, A.M. Schmidt, Liquid Crystal Elastomers with Magnetic Actuation, Macromol. Symp. 291–292 (2010) 186–192. https://doi.org/10.1002/masy.201050522.*

[13] *B. Klöckner, P. Daniel, M. Brehmer, W. Tremel, R. Zentel, Liquid crystalline phases from polymer functionalized ferri-magnetic Fe 3 O 4 nanorods, J. Mater. Chem. C. 5 (2017) 6688–6696. https://doi.org/10.1039/C7TC01106G.*

[14] *L.B. Braun, T. Hessberger, R. Zentel, Microfluidic synthesis of micrometer-sized photoresponsive actuators based on liquid crystalline elastomers, J. Mater. Chem. C. 4 (2016) 8670–8678. https://doi.org/10.1039/C6TC02587K.*

[15] *M.-H. Li, P. Keller, Artificial muscles based on liquid crystal elastomers, Philos. Trans. R. Soc. A Math. Phys. Eng. Sci. 364 (2006) 2763–2777. https://doi.org/10.1098/rsta.2006.1853.*

[16] *D.L. Thomsen, P. Keller, J. Naciri, R. Pink, H. Jeon, D. Shenoy, B.R. Ratna, Liquid Crystal Elastomers with Mechanical Properties of a Muscle, Macromolecules. 34 (2001) 5868–5875. https://doi.org/10.1021/ma001639q.*

[17] *O. Baun, P. Blümler, Permanent magnet system to guide superparamagnetic particles, J. Magn. Magn. Mater. 439 (2017) 294–304. https://doi.org/10.1016/j.jmmm.2017.05.001.*

02 Extraordinary Field Enhancement of TiO_2 Porous Layer up to 500-Fold

K. Yoshihara, M. Sakamoto, H. Tamamitsu, *et al.*

ABSTRACT

Titanium dioxide (TiO_2) is known as a very important material for photocatalysts, the photoelectrode for hydrogen evolution reaction, and the porous layer of perovskite solar cells. Here, extraordinary field enhancement of a porous TiO_2 layer, mesoscopic film is shown. The field enhancement is investigated with respect to the fluorescence intensity of a dye molecule and an enhancement factor (EF) of up to 500 is achieved, which corresponds to the largest EF for a semiconductor. Furthermore, EF is up to 30000 after numerical corrections. The large EF is realized for a porous TiO_2 layer composed of a specific particle size of 550 nm, which is consistent with the results of fluorescence intensity, scattering intensity, and two different theoretical calculations based on Mie scattering theory, with respect to particle size.

INTRODUCTION

When a noble metal with nanostructure is irradiated with light, localized surface plasmons are resonantly generated, which enhance various physical and chemical processes near the surface, like Raman scattering or fluorescence intensities of molecules,[1,2] also known as surface-enhanced fluorescence (SEF). The enhancement factor (EF) of SEF is much lower than that of surface-enhanced Raman scattering (SERS) due to fluorescence quenching via energy transfer from an excited dye molecule to the noble metal substrate with a high density of states. To solve this problem, cost-effective dielectric materials with opposite characteristics to noble metals are potential candidates as enhancement materials. For example, an electronically forbidden transition material, i.e., indirect transition in the bandgap of a semiconductor, can suppress energy transfer from an excited molecule to a substrate material that has the nature of an indirect-transition semiconductor as a forbidden transition.

In the present study, titanium dioxide (TiO_2) was investigated as a SEF material. TiO_2 has been an important material for photocata-

lysts,[3] the porous layer used as the scaffold to obtain good perovskite crystal as well as charge transport of perovskite solar cells,[4,5] and as the photoelectrode for the hydrogen evolution reaction[6]. As for the field enhancement of TiO_2, two studies were reported on finite-difference time-domain calculations, i.e., spherical particle[7] and nanodisk,[8] but there has been no report on porous TiO_2 layers yet so far.

Here, we demonstrate the field enhancement of a porous TiO_2 layer by measuring the SEF of dye molecules. The porous TiO_2 layer preparation consists of mechanochemical ball milling and drop casting of a TiO_2 solution.

MATERIALS AND METHODS

Preparation of TiO_2 Solution and Enhanced Substrate Using Drop Casting

TiO_2 particles were processed by a mechanical wet-process ball-milling method using a commercial planetary ball-milling apparatus (Premium line P-7, Fritsch Co., Ltd.). TiO_2 anatase powder (1 g), zirconia (ZrO2) milling balls (1 mm diameter, 40 g), and methanol (6 g) were placed in a ZrO2 milling vessel (45 mL) and ball-milled at 600 rpm for 3 h. The size of the TiO_2 particles in the solution was measured by dynamic light scattering. Solutions of the TiO_2 particles after milling were prepared by diluting with either water or methanol. The enhanced substrate was prepared by drop casting the diluted TiO_2 solution onto an indium tin oxide (ITO) glass substrate, which was cleaned with a sonicator and dried in advance. The ITO glass was used for observation of the TiO_2 layer with a scanning electron microscope (SEM). Then, the TiO_2 layer covered the ITO layer to an area that was 50 times greater than that of the focal point of light used for fluorescence measurements.

Measurements of Enhancement Spectra and Estimation of Enhancement Factor

The fluorescence spectrum of the CV dye molecule was measured with a confocal microscope spectrometer (HR800, Horiba Jobin Yvon) at an excitation wavelength of 632.8 nm using a He–Ne laser. An objective lens (SMLPLN, 100×, Olympus®) with a superlong working distance (7.6 mm) was used to measure the fluorescence spectra of the sample solution under a cover glass. The optical cell for measurement of the fluorescence spectrum was designed to give a solution layer between the cover glass and the TiO_2 layer, and was described elsewhere (see original work for references[9]). The dye solution used was CV dissolved in methanol to a concentration of 3.6×10^{-5} m. A fluorescence spectrum was obtained as the average of the number of fluorescence spectra of 10 different positions of TiO_2: a spectrum at a position was measured with 10 accumulations of the data collection time of spectrum as 1 s. The EF of fluorescence intensity was obtained by measuring four spectra: 1) the fluorescence spectrum of the CV solution with the TiO_2 layer (I1), 2) the fluorescence spectrum of the CV solution without the TiO_2 layer (I2), 3) the background spectrum of 1 with methanol as the solvent and with the TiO_2 layer (I3), and 4) the background spectrum of 2 with methanol as the solvent and without the TiO_2 layer (I4). The EF of fluorescence intensity was then obtained using these four spectra, according to EF = (I1 – I3)/(I2 – I4). EF values were obtained from the averages of 10 spectra for the I1 and the I2 and 5 spectra for the I3 and the I4, and all error bars denote to 2σ, where σ is a standard deviation from EF average. The EF was also evaluated by taking account of the penetration depth of laser light into TiO_2 layer under the condition of the same volumes probed by the laser and at the same number of CV molecules.

Evaluation and Calculation of the TiO_2 Layer

The scattering spectrum of the TiO_2 layer was measured in the darkfield using the same fluorescence microscope spectrometer. A ring-shaped halogen lamp (KL1500LCD, Carl Zeiss) equipped with an objective lens was used as the light source for the scattering measurement under darkfield conditions. To compensate for the operation of the instrumentation on the scattering spectrum, the scattering spectrum of a commercial diffuse reflector was measured as a standard spectrum. The absorption spectrum of TiO_2 layer was measured by a JASCO V-660 spectrophotometer. The obtained absorption coefficient, α, was used to calculate the penetration depth, $1/\alpha$, of the laser light into TiO_2 layer. The surface of the TiO_2 layer was analyzed by measuring height images with a laser microscope (LEXT™ OLS4000 microscope, Olympus). The height data were then used for the FDTD calculation. The electric field distribution on the surface of the TiO_2 layer was calculated using the DTD method with the FullWAVE commercial software (Cybernet Systems Co., Ltd.). The scattering efficiency Qsca, was calculated using the Mieplot software (version 4.05.02, Philip Laven). For these calculations, the refractive index of TiO_2 (anatase) at an excitation wavelength of 632.8 nm was used; n = 2.33 as the

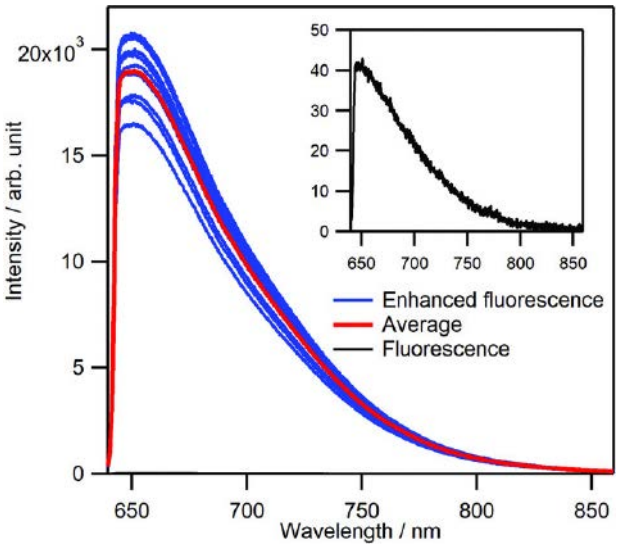

Figure 1: Fluorescence spectra of CV solution measured with (blue and red) and without (black) the TiO_2 layer. The red spectrum shows the average of the blue spectra.

real part and $\kappa = 1.6 \times 10^{-3}$ as the imaginary part, of which the values were obtained from an average of reported values. The refractive indices for gold (Au), silver (Ag), and silicon (Si) at an excitation wavelength of 632.8 nm were used as values in the software. The extinction efficiency Qext, Qext = Qabs + Qsca, was also calculated for TiO_2, Au, Ag, and Si.

See the original work and its supporting information for more experimental details[9].

RESULTS AND DISCUSSIONS

Figure 1 shows the fluorescence spectra of a crystal violet (CV) solution with (blue curve) and without (black curve) the TiO_2 layer. These data were obtained using a TiO_2 layer prepared from a solution composed of a volume ratio of water/methanol = 27. The fluorescence intensity of CV was significantly increased in the presence of the TiO_2 layer. The average and maximum EF values were estimated to be 480 and 526, respectively. Compared with EFs published for various materials and semiconductors, the EF for TiO_2 is significantly large.

Next, the TiO_2 layer was analyzed by measuring surface height images with a laser microscope. **Figure 2a, b** shows typical height images for TiO_2 layers prepared by drop casting aqueous-methanol and methanol solutions, respectively. These images reveal that the former layer has a higher surface roughness. The surface roughness was quantified by estimation of the mean height, S_a. As a result, S_a for the layer prepared from aqueous-methanol solution was 2.9 times greater than that prepared from methanol solution. In addition, S_a was also changed by the concentration of TiO_2 in a solution. Therefore, S_a can be controlled according to either the solvent or the concentration.

EFs were investigated as a function of S_a, as shown in **Figure 3a.** The results indicate that the EF increases with the surface roughness, whereas it decreases over the peak position of Sa. The maximum EF of 480 was located around S_a=0.55 µm; therefore, there is a specific size to obtain a significantly large EF (S_a

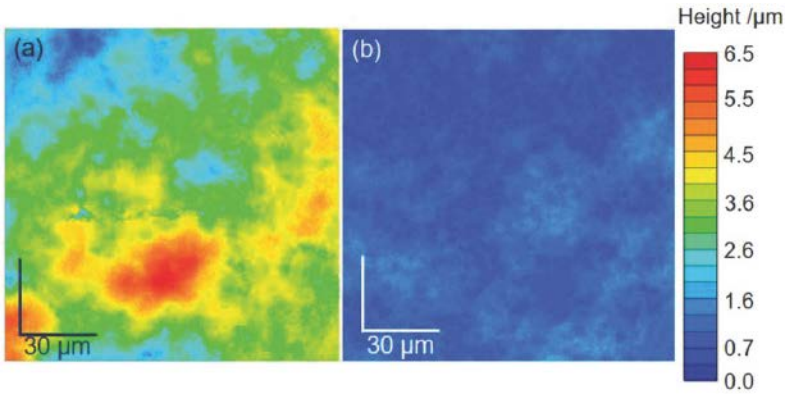

Figure 2: Laser microscope images of the surface of TiO_2 layers prepared by drop casting of TiO_2 particles from a) aqueous-methanol solution and b) methanol solution. A pixel resolution of the laser microscope is set as 126 nm × 126 nm at the x–y region.

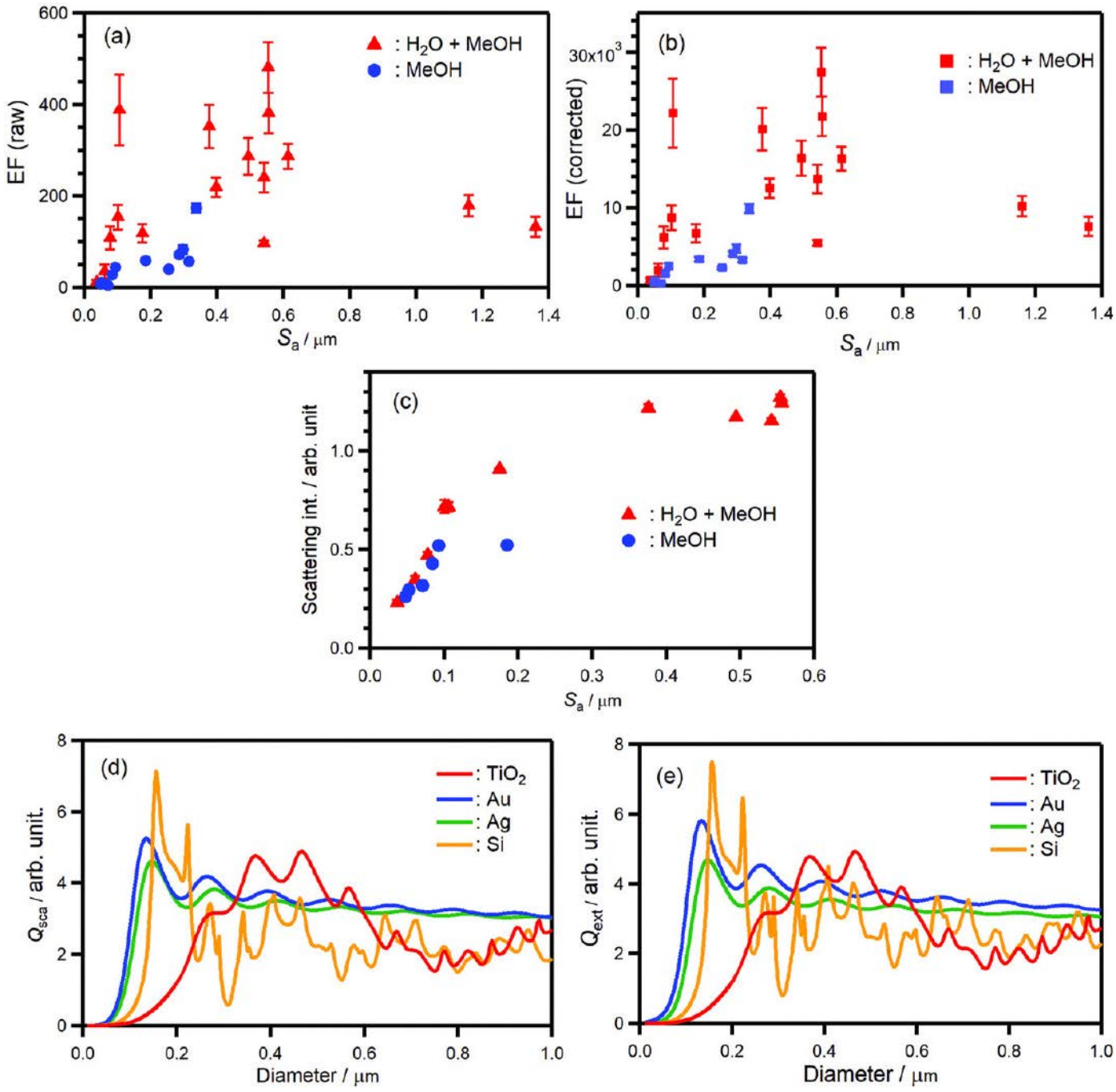

Figure 3: a) EF of TiO_2 layers prepared from drop casting aqueous-methanol and methanol solutions as a function of surface roughness. The EF values are obtained as raw data without corrections for the volumes probed by the laser and the number of CV molecules. b) EF of TiO_2 layers prepared from drop-casting aqueous-methanol and methanol solutions as a function of surface roughness. This EF indicates "EF per a CV molecule." Namely, the EF values are obtained as corrected ones using the data (a) and the solution volumes probed by laser and the number of CV molecules, i.e., the same volumes of bulk solution and solution in TiO_2 porous layer as well as the same number of molecules there. c) Scattering intensity as a function of surface roughness for TiO_2 layers prepared from drop-casting aqueous-methanol and methanol solutions. d) Qsca for particles of four materials immersed in methanol are calculated as a function of particle size (diameter). e) Q_{ext}, $Q_{ext} = Q_{sca} + Q_{abs}$, for particles of four materials immersed in methanol are calculated as a function of particle size (diameter).

is averaged height of TiO_2 particle in the z-direction. Since the TiO_2 layer is isotropic structure, the value of Sa corresponds to the size in x–y-direction and results in the size of particle). The EFs in **Figure 3a** are carefully obtained by measuring various background signals, while the EFs are treated as raw data without the corrections of solution volumes probed by the laser and the number of CV molecules. In order to analyze the EFs furthermore, we evaluated solution volumes in a bulk solution and in voids of a porous TiO_2 layer probed by the laser, both of which are estimated as 54 and 0.92 μm^3, respectively. According to the volume ratio 54/0.92 μm^3, there is 57 times difference in between the volumes as well as the number of CV molecules. **Figure 3b** shows corrected EFs under the same solution volume and the same number of CV molecules. Note that the maximum EF is up to 30,000 at around the particle size with 550 nm. Namely, this EF indicates "EF per a CV molecule."

Figure 3d shows the calculated results for the scattering efficiency Q_{sca} of a TiO_2 spherical particle dispersed in methanol as a function of the particle diameter. To compare the results for TiO_2 with those for other materials, Q_{sca} was also calculated for Ag and Au particles under the same condition. Note that Q_{sca} for TiO_2 is larger than those for Au, Ag, and Si in a specific size, and is the largest for the particle size range of 0.35–0.6 μm. Furthermore, we examined extinction efficiency Q_{ext}, $Q_{ext} = Q_{sca} + Q_{abs}$, for these materials. As a result, the value of TiO_2 is the highest at around 500 nm, as shown in **Figure 3e.** Thus, the present TiO_2 particles have a significantly high EF, which to the best of our knowledge is the largest obtained in studies on SEF using semiconductors. Moreover, we investigated field enhancements by changing particle sizes of TiO_2, Si, Au, and Ag using FDTD calculations. Namely, the EFs of these four materials were calculated on a single spherical particle, immersed in methanol, with diameters of 300, 400, 500, and 600 nm. The TiO_2 particle gives the highest EF in four materials at the diameter of 500–600 nm, whereas smaller particles of 300 nm show that Ag and Au particles give higher EFs than that of TiO_2.

To evaluate the relation between the EF and the surface structure, the electric field of the TiO_2 layer was calculated using the FDTD method. It was found that the EF is large at the surface of TiO_2 with a surface roughness of several hundred nanometers. This trend is in good agreement with the experimental data, i.e., the EF became a maximum at a surface roughness of 550 nm, as shown in **Figures 5a,** b. Therefore, according to both experimental and theoretical evidence, TiO_2 with a size of ≈500 nm results in extraordinary EF.

CONCLUSION

In summary, ball-milled TiO_2 particles were mechanically prepared and were dispersed in a solution and drop-cast to produce a TiO_2 porous layer on a glass substrate. The TiO_2 porous layer composed of particles with sizes in the range of 0.3–0.6 μm resulted in significant field enhancement, which was in good agreement with the scattering spectra and calculations using the FDTD method and Mie theory. Such a large field enhancement as EF = 500 is ascribed to the properties of TiO_2 particles with specific size (0.3–0.6 μm), such as a high refractive index, indirect transitions, hot spot, and many edges. In addition, the EF corrected, under the same solution volume probed by the laser and the same number of CV molecules, was up to 30000 at around the particle size with 550 nm. Special advantages of the present system for accomplishing such extraordinary EF are principally the following three, i) porous TiO_2 layer gives many hot spots among particles, ii) a component of porous layer is particles with the size of around 500 nm that can give the maximum field enhancement, iii) particles with many edges giving higher electric field.

REFERENCES:

[1] *S.A. Maier, Plasmonics: fundamentals and applications, Springer Science \& Business Media, 2007.*

[2] *K. Aslan, C.D. Geddes, Metal-enhanced fluorescence: progress towards a unified plasmon-fluorophore description, John Wiley \& Sons, Inc: Hoboken, NJ, 2010.*

[3] *U.I. Gaya, A.H. Abdullah, Heterogeneous photocatalytic degradation of organic contaminants over titanium dioxide: A review of fundamentals, progress and problems, J. Photochem. Photobiol. C Photochem. Rev. 9 (2008) 1–12. https://doi.org/10.1016/j.jphotochemrev.2007.12.003.*

[4] *G. Kakavelakis, K. Petridis, E. Kymakis, Recent advances in plasmonic metal and rare-earth-element upconversion nanoparticle doped perovskite solar cells, J. Mater. Chem. A. 5 (2017) 21604–21624. https://doi.org/10.1039/C7TA05428A.*

[5] *T. Miyasaka, Toward Printable Sensitized Mesoscopic Solar Cells: Light-Harvesting Management with Thin TiO 2 Films, J. Phys. Chem. Lett. 2 (2011) 262–269. https://doi.org/10.1021/jz101424p.*

[6] *R. Abe, Recent progress on photocatalytic and photoelectrochemical water splitting under visible light irradiation, J. Photochem. Photobiol. C Photochem. Rev. 11 (2010) 179–209. https://doi.org/10.1016/j.jphotochemrev.2011.02.003.*

[7] *Y. Tanaka, G. Obara, A. Zenidaka, N.N. Nedyalkov, M. Terakawa, M. Obara, Near-field interaction of two-dimensional high-permittivity spherical particle arrays on substrate in the Mie resonance scattering domain, Opt. Express. 18 (2010) 27226. https://doi.org/10.1364/OE.18.027226.*

[8] *H.-J. Lin, K. de Oliveira Lima, P. Gredin, M. Mortier, L. Billot, Z. Chen, L. Aigouy, Fluorescence enhancement near single TiO 2 nanodisks, Appl. Phys. Lett. 111 (2017) 251109. https://doi.org/10.1063/1.4994311.*

[9] *K. Yoshihara, M. Sakamoto, H. Tamamitsu, M. Arakawa, K. Saitow, Extraordinary Field Enhancement of TiO 2 Porous Layer up to 500–Fold, Adv. Opt. Mater. 6 (2018) 1800462. https://doi.org/10.1002/adom.201800462.*

03 $NaMgF_3:Tb^{3+}@NaMgF_3$ Nanoparticles Containing Deep Traps for Optical Information Storage

Y. Wang, D. Chen, Y. Zhuang, *et al.*

ABSTRACT

Persistent luminescence materials containing deep traps have attracted attention in the field of optical information storage. However, the lack of nanomaterials with satisfactory light storage ability has become one of the main obstacles to practical applications. In this work, $NaMgF_3:Tb^{3+}@NaMgF_3:Tb^{3+}$ nanoparticles are reported that exhibit excellent light storage ability into deep traps upon X-ray irradiation and controllable photon emissions under thermal stimulation. A surface passivation strategy by constructing a core–shell structure is adopted, which is proved valid to greatly enhance the PersL efficiency. Due to the excellent dispersibility and stability in water, luminescent inks containing the nanoparticles are successfully prepared and the applications to inkjet printing optical information storage and information decryption are demonstrated.

INTRODUCTION

Magnetic storage, semiconductor memory, and optical information storage are the three main storage technologies in the information age.[1,2] Among them, optical information storage shows the advantages of low production cost, low energy consumption, excellent resistance to external interference, and long storage life; thus it is widely used in the long-term storage of large amounts of data that are not modified frequently.[3,4] However, due to the diffraction limit, the storage capacity of the traditional 2D optical information storage technology (such as Blu-ray discs) has been difficult to make a big breakthrough.[5]

Persistent luminescence (PersL) materials are a kind of phosphor with light storage ability and delayed photon emissions under thermal or photostimulation.[6-8] When the trap depths of the PersL materials are sufficiently deep, the charge carriers could be frozen in the traps at room temperature (RT) for a long duration, thus enabling long-term optical information storage. In the past few years,

a lot of work has been done on developing new materials and exploring their applications in multifunctional optical information storage.[9,10] Designing new PersL materials with nanoscale and deep traps is of great significance for the development of high-capacity optical information storage technology. At present, there are few reports on the nanoparticles with excellent PersL performance. One of the main reasons could be serious PersL quenching and structural instability when the particle size is decreased to nanoscale.

It has been reported that $NaMgF_3$ is a kind of material with good X-ray absorption ability.[11,12] Besides, the emission spectra of the NaMgF3 matrix could be tailored with considerable flexibility, and the application scenarios of this material are accordingly further expanded. However, the energy storage capacity of lanthanide-doped $NaMgF_3$ nanoparticles under X-ray irradiation has not been thoroughly reported, although many important applications such as photobiomedical detection and high-throughput optical information storage may emerge. In this work, we reported fluoride nanoparticles $NaMgF_3:Tb^{3+}$ containing deep traps for light storage and demonstrated their applications to optical information storage by using an inkjet printing technology.

MATERIALS AND METHODS

Raw Materials and Chemicals

$Mg(NO_3)_2{\cdot}6H_2O$ (99.9%), $Tb(NO_3)3{\cdot}5H_2O$ (99.9%,), and oleic acid (OA, A.R.) were purchased from Aladdin Corporation. NaF (99.99%) was purchased from Macklin Corporation. All the materials were directly used without further purification. Synthesis of $NaMgF_3:Tb^{3+}$ Nanoparticles: $NaMg^{1-x}F_3:xTb^{3+}$ (x = 0.06–0.3, with a concentration gradient of 0.03) nanoparticles were synthesized by using a hydrothermal reported in the literature with some modifications (see original work and its supporting information for references) 1, 1.5, and 2 times of the original reactant concentrations were compared, and 1.5 times was chosen as the optimal condition as the composition plan in this work. Briefly, stoichiometric $Mg(NO_3)_2{\cdot}6H_2O$ and $Tb(NO_3)_3{\cdot}5H_2O$ (the total amount of Mg and Tb cations was 5 mmol) were dissolved into 5 mL deionized water. 4.5 mL oleic acid was added dropwise into the cationic solution and kept stirring for 10 min to produce oleic-acid-based complex compounds. Another anion solution containing 15 mmol NaF and 5 mL deionized water was added dropwise into the above solution, stirred at 600 rpm for 1 h to form a milky colloidal solution. The solution was transferred to a 40 mL Teflon-lined autoclave, sealed, and kept at 160 °C (320 °F) for 12 h. After cooling to RT, white products were collected by centrifugation. To remove remaining organic ligands, first, the products were washed with deionized water/ethanol for three times and dispersed with 6 mL acetone, respectively. Then, add 250 µL hydrochloric acid (0.1 mol L–1) into each solution followed with an ultrasonic oscillation for 2 h at RT. Lastly, the products were washed again with deionized water/ethanol three times. The final products of $NaMgF_3:Tb^{3+}$ nanoparticles (≈521 mg) were dispersed into 12 mL ethanol for further use.

Synthesis of $NaMgF_3:Tb^{3+}@NaMgF_3$ Core–Shell Nanoparticles

The synthesized $NaMgF_3:Tb^3$ nanoparticles in ethanol (12 mL) was mixed with 0.5 mmol $Mg(NO_3)_2{\cdot}6H_2O$, 1.5 mmol NaF, and 4.5 mL OA. The mixture was transferred into a 40 mL Teflon-lined autoclave and stirred for 10 min. The autoclave was sealed and kept at 160 °C (320 °F) for 12 h. After cooling to RT, white products were collected by centrifugation. The products were washed with deionized water/ethanol for three times, treated with hydrochloric acid (0.1 mol L–1) to remove remaining organic ligands, and washed again with deionized water/ethanol for three times. The final products of $NaMgF_3:Tb^{3+}@NaMgF_3$ core–shell nanoparticles were obtained by drying in an oven at 60 °C (140 °F) overnight.

Preparation of Luminescent Inks Containing Nanoparticles and Setup for Inkjet Printing

The synthesized $NaMgF_3:Tb^{3+}@NaMgF_3$ nanoparticles (100 mg) were dispersed into 5 mL deionized water and stirred thoroughly to prepare a luminescent ink. The aqueous ink could be kept at RT for 14 d without obvious precipitation. The ink was then loaded into an inkjet printing system (MicroFab, Jetlab@4). A 50 µm diameter piezoelectric-type nozzle was selected. The driving voltage waveforms and negative pressure values of the inkjet printer were adjusted to generate stable and continuous droplets. The spatial accuracy of the inkjet printing system was ≈5 µm. A sapphire single crystal sheet (ϕ30 mm × 1 mm) was placed under the printing nozzle. The temperature of the substrate was set to 40 °C (104 °F). Typically, a customer-designed pattern was inkjet-printed on the sapphire substrate. The printed pat-

tern was irradiated by an X-ray source (average dose rate ≈2.58 μSv s–1) or 5 min and kept in the dark at RT for further use. Finally, a PersL image was reproduced by heating to 400 K and recorded with a digital camera.

Structural and Optical Characterizations

Powder XRD patterns of the nanoparticles were recorded by using an X-ray diffractometer (Bruker, D8 Advance) with Cu Kα radiation at an interval of 0.02° with a scanning speed of 10° min^{-1}. The particle morphology and microstructure were observed using a field-emission transmission electron microscope (Talos F200s). PL and PLE spectra were measured with a spectrophotometer (Edinburgh Instrument, FLS980); all samples were tested in dry powders. The RL spectra were recorded with a fiber spectrophotometer (Ocean Optics, QE Pro). The PersL decay curves and PersL spectra were recorded with a home-built measurement system driven by a LabVIEW-based program. In this system, a portable X-ray tube (Amptek, Mini-X2) with a maximum output of 10 W (typical voltage 50 kV, tube current 0.2 mA, and average dose rate ≈2.58 μSv s–1) was used as the excitation source to generate PersL. A filter-attached photomultiplier tube (PMT, Hamamatsu, R928P) and a fiber spectrophotometer (Ocean Optics, QE Pro) were applied to record the PersL intensity and spectra, respectively. The TL glow curves were recorded using another LabVIEW program driven measurement system. Briefly, the sample was irradiated by the X-ray source for 5 min (total dose ≈774 μSv) at 250 K. After removing the excitation source, the TL signals were recorded by the PMT detector from 250 to 550 K. The temperature of the sample was controlled by using a cooling/heating stage (Linkam, THMS600E). The TL spectra at different temperature were monitored by the above fiber spectrophotometer. Fluorescence microscopic images were taken by a fluorescent microscope (Olympus®, BX53M microscope). Photographic images of the samples under daylight or the PersL images were taken with a digital camera (Canon, EOS 5D Mark II) in all-manual modes.

RESULTS AND DISCUSSION

Phase Analysis and Optical Characterization of $NaMgF_3$:Tb^{3+} Nanoparticles

The X-ray diffraction patterns of the $NaMgF_3$:Tb^{3+} nanoparticles with 24% Tb^{3+} concentration were in good agreement with the standard diffraction patterns of $NaMgF_3$. A slight diffraction shift observed suggest unit cell expansion due to the substitution of larger Tb^{3+} ions. The $NaMgF_3$ crystal belongs to an orthorhombic perovskite structure with a space group of *Pbnm*.[13] The crystal is composed of corner-connected MgF_6 octahedrons and NaF_8 polyhedrons. Moreover, the consistency between X-ray-excited luminescence (RL) and photoluminescence (PL) spectra verified that X-ray was an efficient excitation source to give green emissions for $NaMgF_3$:Tb^{3+}. The transmission electron microscopy (TEM) images of the $NaMgF_3$:Tb^{3+} nanoparticles showed uniform and cubic morphology with an average size of ≈18.0 nm. The energy dispersive spectroscopy analysis of elemental mapping showed the measured compositions of 21.9% (Na), 17.5% (Mg), 55.7% (F), and 4.9% (Tb).

Optimizing the Doping Concentration of Tb^{3+}

Several $NaMgF_3$:Tb^{3+} nanoparticles with different Tb^{3+} concentrations were synthesized. With the increase of the Tb^{3+} concentration, the cell lattice expanded, resulting in a gradual shift of the XRD peaks toward the small-angle direction. Also, the PL intensity was enhanced with increasing the Tb^{3+} concentration and reached the maximum at 24%. The highest thermoluminescence (TL) intensity was found in the nanoparticles with 21% of Tb^{3+} doping. With the increasing of Tb^{3+} concentration, the average distance between the luminescent centers and emission quenchers could be reduced and energy transfer rate was increased, which resulted in the concentration quenching of PL intensity and TL intensity. The $NaMgF_3$:Tb^{3+} nanoparticles with 24% Tb^{3+} were used in the following sections.

Constructing a Core–Shell Structure in Nanoparticles

In this section, we adopted a surface passivation strategy by constructing a core–shell structure in nanoparticles. Specifically, the synthesized $NaMgF_3$:Tb^{3+} nanoparticles were used as the cores to grow a nonadoped $NaMgF_3$ shell (**Figure 1a**).

The TEM examinations indicated that the average size of the nanoparticles was increased from 18.0 (cores) to 19.2 (1/50), 20.0 nm (1/10), and 20.4 nm (**Figure 1b**). Accordingly, the thickness of the $NaMgF_3$ passivation shell was determined as 1.2 nm (1/50), 2.0 nm (1/10), and 2.4 nm (1/5), respectively. Also, the XRD patterns confirmed that pure phase of $NaMgF_3$ was remained in the core–shell nanoparticles (**Figure 1c**).

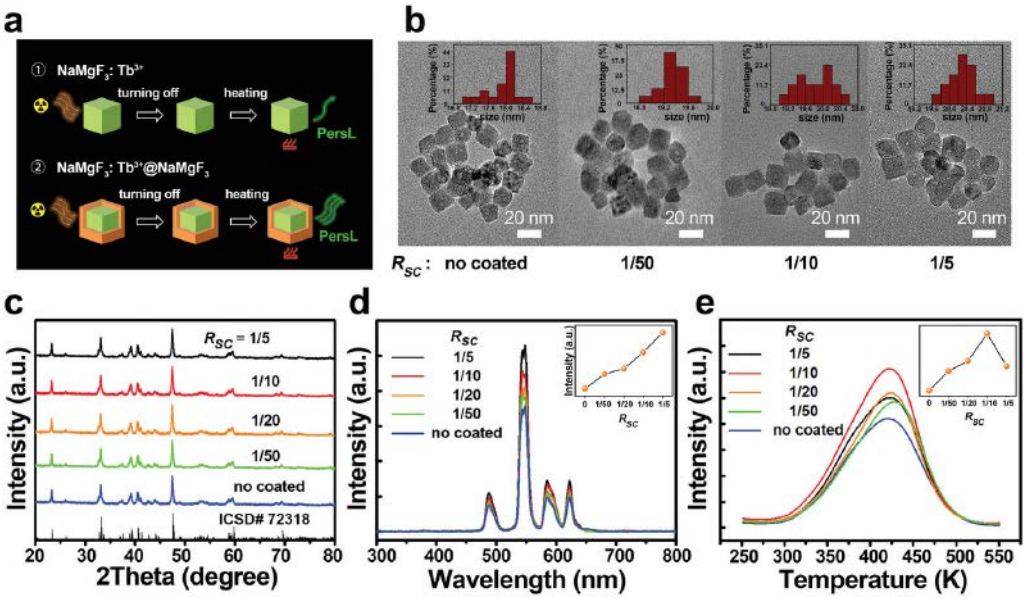

Figure 1: $NaMgF_3:Tb^{3+}@NaMgF_3$ nanoparticles with a core–shell structure. a) Schematic illustration of the core–shell structure and the PersL improvement. Surface quenchers on the shells were separated from the Tb^{3+} emitters inside the cores. b) TEM images of the $NaMgF_3:Tb^{3+}@NaMgF_3$ nanoparticles. The insets show the particle size distribution of the nanoparticles. c) XRD patterns, d) PL spectra, and e) TL glow curves of the nanoparticles with different *RSC*.

Figure 1d shows that the PL intensity of the nanoparticles under excitation of 297 nm was clearly enhanced after coating the shells. Also, the shape of the TL glow curves was independent on the shell thickness, suggesting that no new trap was introduced by the shell layer (**Figure 1e**). On the other hand, the TL intensity was also improved with increasing the shell thickness. Based on the above results, we consider that the improvement of TL should be similar to the PL enhancement due to the inhibition of energy transfer to surface quenchers.

Optical Information Storage Applications

Figure 2a shows the photographic images of the luminescent ink containing the $NaMgF_3:Tb^{3+}@NaMgF_3$ nanoparticles. The ink had been left standing for 7 d before use, and no obvious stratification was observed. Under X-ray irradiation, the ink gave bright green emission. Furthermore, the ink was loaded into an inkjet printing system. A pattern of the Xiamen University logo with a size of Ø10 mm was printed on a sapphire substrate (information writing, **Figure 2b**). Under the fluorescence microscope (under excitation at 405 nm), one could see that the printed pattern was composed of small dots in an orthogonal array. The dots showed a regular circular morphology and a diameter of ≈100 μm (**Figure 2c**).

The sapphire substrate was placed under X-ray irradiation for energy charging (5 min). As shown in **Figure 2d,** a luminescent pattern was clearly observed under X-ray irradiation, and it quickly faded once the excitation source was turned off. The X-ray-charged pattern was kept in the dark at RT for 10 min and moved to a heater preset at 400 K. After taking several seconds for heat conduction, the stored pattern on the sapphire substrate was reproduced and recorded by a digital camera (information readout, **Figure 2d**).

Furthermore, the delayed emission of the PersL nanoparticles could be used in information encryption and decryption. As schematically illustrated in **Figure 2e,** a specific pattern made of inkjet-printed $NaMgF_3:Tb^{3+}@NaMgF_3$ nanoparticles was written on the substrate. The pattern was then covered with a full layer of CdSe quantum dots. Since the CdSe and $NaMgF_3:Tb^{3+}@NaMgF_3$ both gave green emission under UV and X-ray irradiation, the pattern was well hidden (being an unreadable state, **Figure 2f**). On the other hand, only the $NaMgF_3:Tb^{3+}@NaMgF_3$ nanopar-

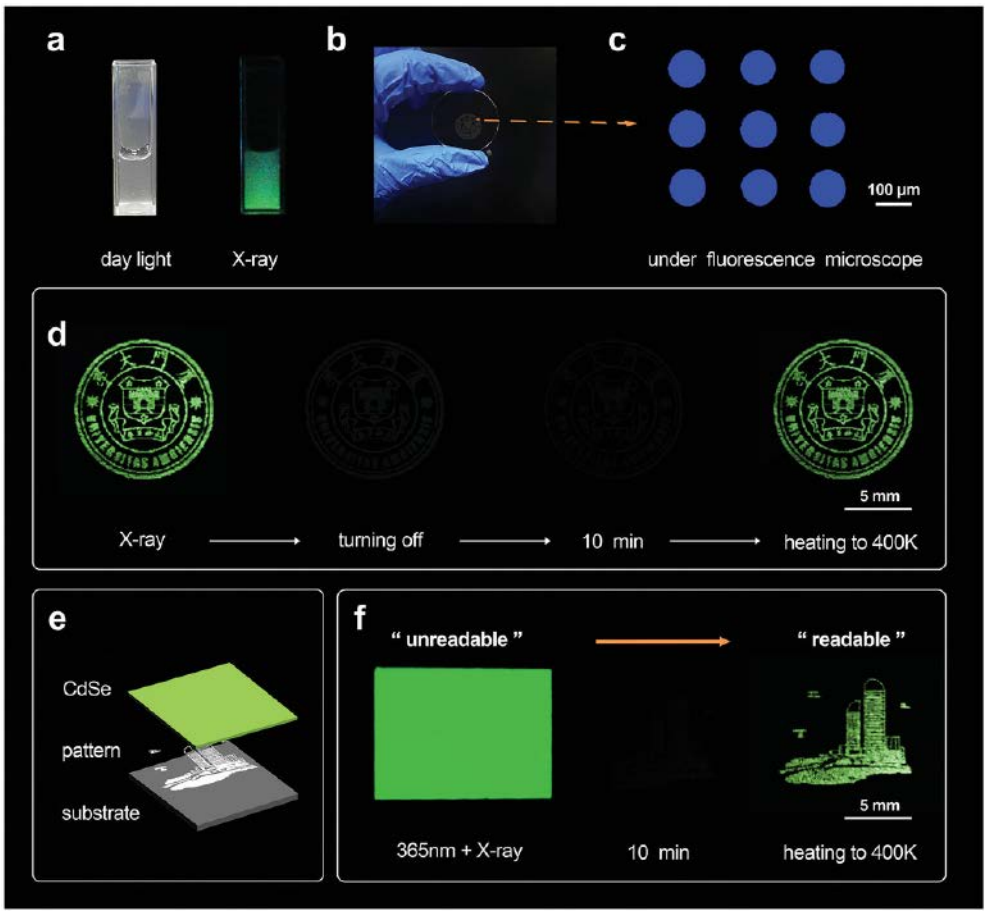

Figure 2: Applications of the $NaMgF_3:Tb^{3+}@NaMgF_3$ nanoparticles to optical information storage and information encryption. a) Photographs of the luminescent ink under day light and X-ray irradiation. The ink was left standing for 7 d before use. b) Photograph of a sapphire substrate after printing with a Xiamen University logo. c) Image of the printed pixels under fluorescence microscope. d) Photographs of the emission images during X-ray irradiation, at the moment of turning off, with a delay time of 10 min, and heated to 400 K. e) Schematic illustration of the optical information encryption and decryption. f) Photographs of the emission images during UV (365 nm) + X-ray irradiation, turning off with a delay time of 10 min, and heated to 400 K. The encrypted information was unreadable during irradiation and turned into readable after heating. Exposure time for (d: X-ray), (d: heating), (f: 365 nm + X-ray), (f: heating) was 3 s, respectively.

ticles were able to store irradiation energy. When the substrate was heated to 400 K consequently, the $NaMgF_3:Tb^{3+}@NaMgF_3$ gave PersL and decrypt the recorded information (tuning to a readable state, **Figure 2f**).

CONCLUSION

In this work, we reported a new type of PersL nanoparticles $NaMgF_3:Tb^{3+}$, which exhibited nanocubic morphology, excellent aqueous dispersibility, and light storage ability in deep traps under X-ray irradiation. These outstanding features enabled the developed nanoparticles to be applied to inkjet printing technology. Due to the light storage ability and delayed photon emissions, the $NaMgF_3:Tb^{3+}@NaMgF_3$ nanoparticles exhibited a broad prospect in the optical information storage and information encryption applications. The developed $NaMgF_3:Tb^{3+}@NaMgF_3$ nanoparticles with nanoscale size and deep traps for energy storage may open up new opportunities for advanced optical materials for the applications of information technology.

REFERENCES:

[1] *M. Gu, Q. Zhang, S. Lamon, Nanomaterials for optical data storage, Nat. Rev. Mater. 1 (2016) 16070. https://doi.org/10.1038/natrevmats.2016.70.*

[2] *M. Gu, X. Li, Y. Cao, Optical storage arrays: a perspective for future big data storage, Light Sci. Appl. 3 (2014) e177–e177. https://doi.org/10.1038/lsa.2014.58.*

[3] *S. Kawata, Y. Kawata, Three-Dimensional Optical Data Storage Using Photochromic Materials, Chem. Rev. 100 (2000) 1777–1788. https://doi.org/10.1021/cr980073p.*

[4] *Y. Katsurada, S. Hirata, K. Totani, T. Watanabe, M. Vacha, Phosphorescence: Photoreversible On-Off Recording of Persistent Room-Temperature Phosphorescence, Adv. Opt. Mater. 3 (2015) 1802–1802. https://doi.org/10.1002/adom.201570080.*

[5] *Y. Zhou, Y. Chen, H. He, J. Liao, H.T.T. Duong, M. Parviz, D. Jin, A homogeneous DNA assay by recovering inhibited emission of rare earth ions-doped upconversion nanoparticles, J. Rare Earths. 37 (2019) 11–18. https://doi.org/10.1016/j.jre.2018.05.008.*

[6] *V. Boiko, J. Zeler, M. Markowska, Z. Dai, A. Gerus, P. Bolek, E. Zych, D. Hreniak, Persistent luminescence from Y3Al2Ga3O12 doped with Ce3+ and Cr3+ after X-ray and blue light irradiation, J. Rare Earths. 37 (2019) 1200–1205. https://doi.org/10.1016/j.jre.2019.03.010.*

[7] *J. Xu, S. Tanabe, Persistent luminescence instead of phosphorescence: History, mechanism, and perspective, J. Lumin. 205 (2019) 581–620. https://doi.org/10.1016/j.jlumin.2018.09.047.*

[8] *X. Zhang, Z. Quan, J. Yang, P. Yang, H. Lian, J. Lin, Solvothermal synthesis of well-dispersed NaMgF3 nanocrystals and their optical properties, J. Colloid Interface Sci. 329 (2009) 103–106. https://doi.org/10.1016/j.jcis.2008.09.076.*

[9] *Y. Zhuang, L. Wang, Y. Lv, T.-L. Zhou, R.-J. Xie, Optical Data Storage and Multicolor Emission Readout on Flexible Films Using Deep-Trap Persistent Luminescence Materials, Adv. Funct. Mater. 28 (2018) 1705769. https://doi.org/10.1002/adfm.201705769.*

[10] *Z. Long, Y. Wen, J. Zhou, J. Qiu, H. Wu, X. Xu, X. Yu, D. Zhou, J. Yu, Q. Wang, No-Interference Reading for Optical Information Storage and Ultra-Multiple Anti-Counterfeiting Applications by Designing Targeted Recombination in Charge Carrier Trapping Phosphors, Adv. Opt. Mater. 7 (2019) 1900006. https://doi.org/10.1002/adom.201900006.*

[11] *G.V.M. Williams, S. Janssens, C. Gaedtke, S.G. Raymond, D. Clarke, Observation of photoluminescence and radioluminescence in Eu and Mn doped NaMgF3 nanoparticles, J. Lumin. 143 (2013) 219–225. https://doi.org/10.1016/j.jlumin.2013.05.016.*

[12] *J.J. Schuyt, G.V.M. Williams, Photoluminescence of Dy3+ and Dy2+ in NaMgF3:Dy: A potential infrared radiophotoluminescence dosimeter, Radiat. Meas. 134 (2020) 106326. https://doi.org/10.1016/j.radmeas.2020.106326.*

[13] *X. Peng, M.C. Schlamp, A. V. Kadavanich, A.P. Alivisatos, Epitaxial Growth of Highly Luminescent CdSe/CdS Core/Shell Nanocrystals with Photostability and Electronic Accessibility, J. Am. Chem. Soc. 119 (1997) 7019–7029. https://doi.org/10.1021/ja970754m.*

Industrial Microscope Solutions

Industrial microscopes are a vital tool used for measuring, quality control, inspection, and in soldering and manufacturing. Each industrial microscope we offer uses complex designs that provide unique solutions for the inspection process and aim to improve resolution and sample contrast. Olympus industrial inspection microscopes are suited to a wide variety of analysis applications, from routine inspection to sophisticated analysis, using superb optics for industry-leading performance. We have digital microscopes and software for streamlined workflows and flexible image acquisition solutions.

CLEANLINESS INSPECTOR: OLYMPUS CIX100

Olympus' expertise in imaging and metrology systems provides today's manufacturers with solutions for particle counting, sizing and classification.

The OLYMPUS CIX100 inspection system is a dedicated, turnkey solution for manufacturers who maintain the high quality standards for the cleanliness of manufactured components. Quickly acquire, process, and document technical cleanliness inspection data to comply with company and international standards. The system's intuitive software guides users through each step of the process so even novice operators can acquire cleanliness data quickly and easily.

LEXT™ OLS5100 3D LASER SCANNING MICROSCOPE

Olympus laser confocal microscopes offer superb image quality and accurate 3D measurement by non destructive observation method with advanced optical system. Its operation preparation is easy and no pre-process is necessary with your samples.

Built for failure analysis and material engineering research, the OLS5100 laser microscope combines exceptional measurement accuracy and optical performance with smart tools that make the microscope easy to use. Precisely measure shape and surface roughness at the submicron level quickly and efficiently to simplify your workflow with data you can trust.

The Impact of Particles on Biological Systems and the Environment

Particles with their unique properties are used in numerous applications, such as for electronic devices, pharmaceuticals, and energy materials, just to name a few. In addition, in the "Advanced Optical Metrology: Particles I" eBook, it is described how liquid crystalline elastomer (LCE) particles can be magnetically remote controlled and used as transport systems. When combined with Fe_3O_4, these nanoparticles have the potential to transport plastic, textiles, and copper, enabling novel LCE applications, such as microrobots controlled by magnetism.

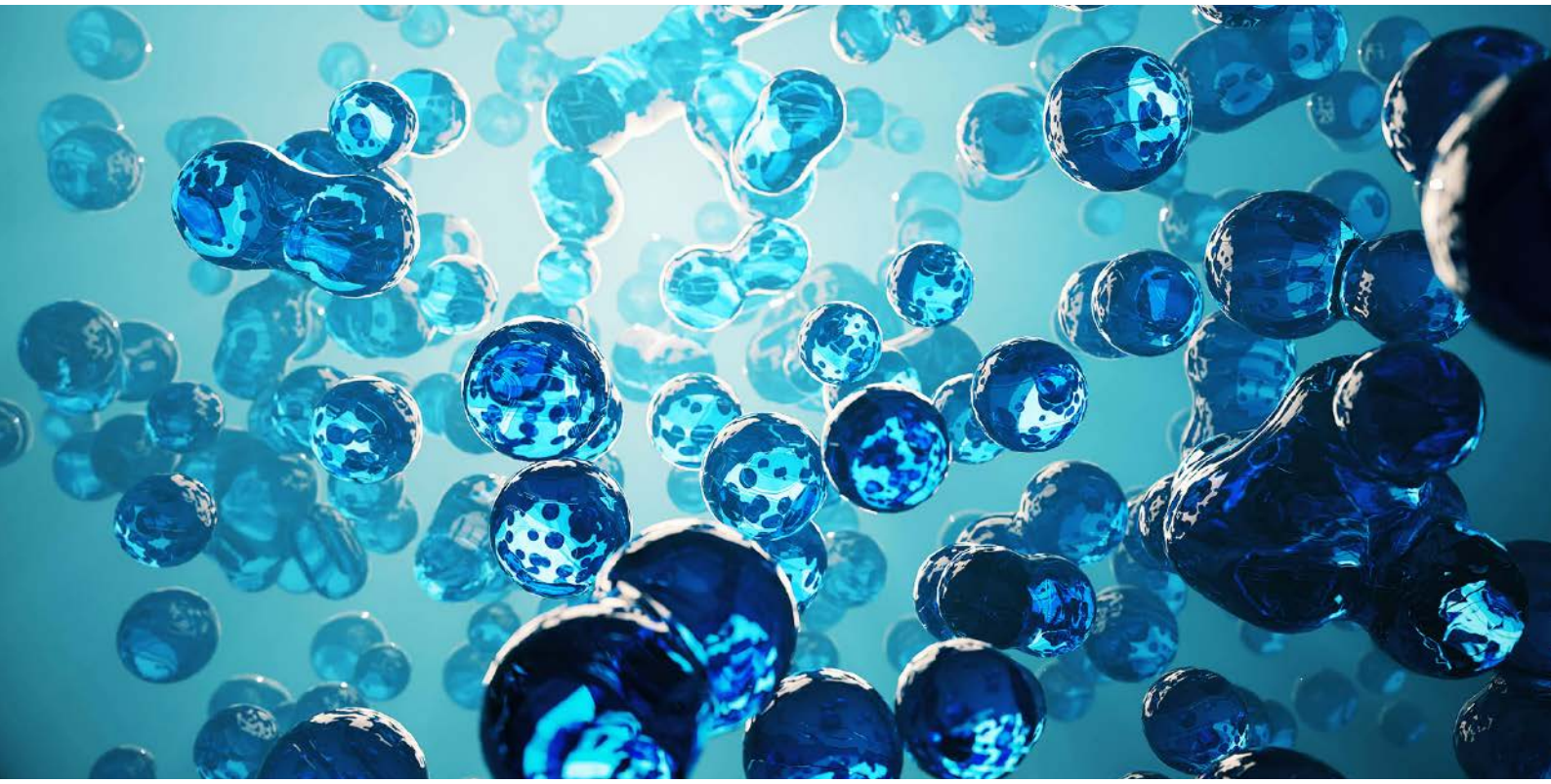

Figure 1: Nano- and microparticles are distinctive materials with enormous technological and scientific value.

The benefits of micro- and nanoparticles are extensive, ranging from treating new diseases to increasing storage energy capacity in batteries. Particle research is generating millions of dollars of revenue, especially in the fields of medicine, energy, and food safety. However, one disadvantage of these particles is their often poor degradability, making them a potential problem for humans, animals, and the environment. This eBook is dedicated to the research of David Wertheim, Professor at Kingston University London; in collaboration with different groups, Prof. Wertheim is using confocal microscopy to analyze the impact of different types of particles on human health and the environment. Herein, the focus lies on his research on particles hazardous to human health detected with solid-state nuclear track detectors (SSNTD).

INTERACTION OF PARTICLES WITH BIOLOGICAL SYSTEMS

Numerous research groups around the world are investigating the impact of micro- and nanoparticles on biological and ecological systems. Both synthetic micro- and nanoparticles, as well as particles resulting from the degradation of waste or emissions, are studied. Some of the results are so shocking that even the daily press reports on them. For example, researchers found that plastic particles can be found everywhere in the world, from Mount Everest[1] to the Mariana Trench[2]. Recently, microplastics were even detected in human blood[3].

At the nanoscale, nanoparticles can physicochemically interact with organic chemicals or metals present in the environment; this interaction may alter their bioavailability and result in mixture effects, such as synergism, antagonism, and addition. The different effects are not only dependent on the properties of individual components but also on environmental conditions and biological systems[4].

One of the main mechanisms of interaction between inorganic nanoparticles and environmental components is adsorption[5–7]. The adsorption of contaminants onto nanoparticles can occur in two ways: as a facilitator in delivering contaminants, where the nanoparticles act as a carrier increasing the uptake by the organisms[8] — a process known as the "trojan horse effect" — and as a reducer of the concentration of contaminants in the environment, either by strong absorption or aggregation/sedimentation, decreasing the co-contaminant mobility and bioavailability[9].

Learn more about the application of confocal microscopy for 3D imaging of particulate matter in a recent presentation by **Prof. David Wertheim** and **Dr. Gavin Gillmore.**

Figure 2: Microplastics are a major problem for the aquatic ecosystem.

AIR POLLUTION PARTICULATE MATTER

Exhaust fumes caused by traffic are a major health concern, especially in densely populated areas. In many countries, there are upper limits for fine dust values that are regularly exceeded despite stricter regulations for particulate filters in diesel vehicles. To understand how diesel particulates enter the body and interact with cells, a detailed understanding of the properties of the particles is necessary.

Air pollution particulate matter is the subject of Prof. David Wertheim's current work, which he is conducting in collaboration with researchers at Queen Mary University of London, UK. In a study published in 2021, they used a new color confocal microscope imaging method to study the 3D shape of diesel particulate matter[10]. They found that the particles adhere to human lung epithelial cells, which is in line

Figure 3: Fine dust pollution in cities harms people and the environment.

with their findings that they can have sharp jagged appearing edges. With the new findings of this study, the researchers are helping to explain why air pollution particulate matter can enter cells of the human respiratory tract, causing various health problems, including neurological and cardiovascular diseases.

SOLID-STATE NUCLEAR TRACK DETECTORS

Small etched plastic detectors, so-called solid-state nuclear track detectors (SSNTD), can be used to monitor radon levels. This is important for the safety of workers exposed to radon at their workplace, as inhalation of radon gas has been linked to the development of lung cancer. In several studies presented in this eBook, Prof. David Wertheim and colleagues have been working to further develop this method using confocal microscopy.

DAVID WERTHEIM

David Wertheim is a Professor in the School of Computer Science and Mathematics at Kingston University London, UK. The main focus of his research is developing methods for analysis and visualization of medical, biological, and material image and signal data; a key area of his current research is the acquisition and analysis of confocal microscope images of particulate matter.

REFERENCES:

[1] *I. E. Napper et al., One Earth (2020) 3, 621–630.*

[2] *X. Peng et al., Geochem. Persp. Let. (2018) 9, 1–5.*

[3] *H. A. Leslie et al., Environment International (2022) 163, 107199.*

[4] *Y. Liu, Y. Nie, J. Wang, J. Wang, X. Wang, S. Chen, G. Zhao, L. Wu, A. Xu, Mechanisms involved in the impact of engineered nanomaterials on the joint toxicity with environmental pollutants, Ecotoxicol. Environ. Saf. 162 (2018) 92–102, https://doi.org/10.1016/j.ecoenv.2018.06.079.*

[5] *Krzyżewska, Iwona, et al. "Inorganic nanomaterials in the aquatic environment: behavior, toxicity, and interaction with environmental elements." Archives of Environmental Protection 42.1 (2016).*

[6] *Li, Mengting, Wei Liu, and Vera I. Slaveykova. "Effects of mixtures of engineered nanoparticles and metallic pollutants on aquatic organisms." Environments 7.4 (2020): 27.*

[7] *Bushra, Rani, Anees Ahmed, and Mohammad Shahadat. "Mechanism of adsorption on nanomaterials." Advanced Environmental Analysis. 2016. 90–111.*

[8] *K.A. Heys, R.F. Shore, M.G. Pereira, K.C. Jones, F.L. Martin, Risk assessment of environmental mixture effects, RSC Adv. 6 (2016) 47844–47857, https://doi. org/10.1039/c6ra05406d.*

[9] *M. Li, W. Liu, V.I. Slaveykova, Effects of mixtures of engineered nanoparticles and metallic pollutants on aquatic organisms, Environments 7 (2020) 1–20.*

[10] *Miyashita, Lisa, Foley, Gary, Gill, Ian, Gillmore, Gavin, Grigg, Jonathan and Wertheim, David (2021) Confocal microscopy 3D imaging of diesel particulate matter. Environmental Science and Pollution Research, 28, pp. 30384–30389.*

04 A New Method of Imaging Particle Tracks in Solid-State Nuclear Track Detectors

D. Wertheim, G. Gillmore, L. Brown, *et al.*

SUMMARY

Solid-state nuclear track detectors are used to determine the concentration of α particles in the environment. The standard method for assessing exposed detectors involves 2D image analysis. However, 3D imaging has the potential to provide additional information relating to angle as well as to differentiate clustered hit sequences and possibly energy of α particles, but this could be time-consuming. Here, we describe a new method for rapid, high-resolution 3D imaging of solid-state nuclear track detectors. A LEXT™ OLS3100 confocal laser scanning microscope (Olympus Corporation, Tokyo, Japan) was used in confocal mode to successfully obtain 3D image data on four CR-39 plastic detectors. Three-dimensional visualization and image analysis enabled the characterization of track features. This method may provide a means of rapid and detailed 3D analysis of solid-state nuclear track detectors.

INTRODUCTION

Inhalation of radon gas (^{222}Rn) and associated ionizing decay products is known to cause lung cancer in humans[1,2]. In the United Kingdom, it has been suggested that 3–5% of total lung cancer deaths can be linked to elevated radon concentrations in the home and/or workplace. Radon monitoring in buildings is therefore routinely undertaken in areas of known risk. Indeed, some organizations such as the Radon Council in the United Kingdom and the Environmental Protection Agency in the United States, advocate a 'to test is best' policy[3]. Radon gas occurs naturally, emanating from the decay of ^{238}U in rock and soils. Measurement of radon in the environment is important in order to give appropriate warning of potential risks, for example in mines and homes, as well as to establish where remedial action is required[4,5,6,7].

Radon gas concentration can be measured using CR-39 plastic detectors[7], which conventionally are assessed by 2D image analysis of the surfaces. It is important to note that there can be some variation in reported results, even in closely spaced detectors[8], due in part to error margins in measurement equipment or techniques. We have previously observed that radon tracks in CR-39 detectors can be visualized using confo-

cal microscopy and hence information about 3D track geometry can be obtained[9].

A number of radon measurement methods are currently in use (e.g., activated carbon and electrets) but the most widely used are CR-39 solid-state nuclear track-etch detectors. In this technique, heavily ionizing α particles leave tracks in the form of radiation damage (via interaction between α particles and the atoms making up the CR-39 polymer). Typically, two CR-39 plastic detectors are installed in a building over a 3-month period, one in the lounge and one in the bedroom of a domestic property, following Health Protection Agency (HPA) protocols[7]. After exposure, in the United Kingdom, the detectors are then sent to an HPA-accredited laboratory for processing. As the latent tracks are not visible under an optical microscope, chemical etching must be performed. This is usually done by etching the detector in a caustic soda (NaOH) bath for 4 hours, after which time the surface pitting made by α particles is revealed. The etch pits can then be counted using a microscope, allowing the radon concentration to be computed (based on the number of tracks for a given area on the detector surface). Where the Radon Metrology Laboratory is concerned at Kingston University (an HPA-accredited laboratory and the source of our detectors in this study), this is carried out by an automated RadoSys microscope/computer system. A number of internationally regulated counting methods have been set up for analyzing radon exposure using passive detectors[10]. The majority use a combination of optical microscopes, spark counters, and computer-based image scanning and processing systems. The etching characteristics of solid-state nuclear track-etch detectors, in particular CR-39-type plastics, are well known from experimental studies, where track evolution with etching follows a well-defined geometry[11].

Some tracks may be at an angle, resulting in variation in gray levels seen in microscopy[12]. Our study extends earlier work[9], which was aimed at classifying and quantifying the shape, size, area, and angular distribution of nuclear tracks in solid-state detectors. Such analysis forms the basis of the fission track dating method[13]. It has been highlighted that it is necessary to count the number of naturally occurring and induced tracks in order to determine the uranium content of the material, to produce fission track-based ages[14]. Induced tracks are formed by irradiating the sample in contact with an external detector, generally a low- uranium mica or a CR-39-type plastic, where induced fission of ^{235}U produces tracks in the detector that can be revealed subsequently by chemical etching.

The track structure of α particles in CR-39 is different from that in crystals[9]. However, there are similarities to radon monitoring in that detectors are chemically etched to reveal and count fission tracks under an optical microscope. Where fission track dating is concerned, it is possible to incorrectly estimate the age of a sample through track loss. For example, shallow angle tracks may not be fully revealed by chemical etching and/or may not be counted correctly. It has been suggested that confocal microscopy may provide a way of quantifying this track loss[9].

AIM

The aim of this study was to acquire and analyze high-resolution 2D and 3D image data of etched radon tracks in CR-39 detectors.

MATERIAL AND METHODS

A LEXT™ OLS3100 confocal laser scanning microscope (Olympus Corporation, Japan) with a 408 nm laser was used in order to acquire images of four etched CR-39 radon detectors. In this study, two objective lenses (50X and 100X) were used for the collection of 3D data, both having a numerical aperture of 0.95. The manufacturer's user manual (version 5) indicates that the microscope has a planar resolution of up to 0.12 µm (using the 100X objective) and a height resolution of up to 0.01 µm. The detectors from the Radon Metrology Laboratory at Kingston University were put on a glass slide, which was then placed on the microscope stage.

Acquisition and analysis of 2D surface images

In this study, 2D surface images of the detectors, obtained with a 10X objective, were analyzed. With the 10X objective lens, each pixel corresponded to 1.25 µm. A charge-coupled device is used to acquire 2D color images from reflected light. The maximum number of pixels per field of view using the charge-coupled device camera (optical) is 1024 x 768. Images of the central portion of the detectors were processed using software we developed at Kingston University using MATLAB (The MathWorks, Inc., Natick, MA, U.S.A.).

The color images (.bmp files) were converted to gray scale and then binary following manual entry of an appropriate threshold value; using the software small objects in the resultant binary image were removed and a 3 x 3 median filter was applied. Appropriate detection of the radon tracks could be checked from an image obtained by superimposing a contour of the detected tracks onto the gray scale or color image, and hence, the suitability of the threshold could be visually assessed. Tracks near the edge of the image were not included in case they were not complete. The detected objects were then analyzed using the 'regionprops' function in MATLAB; this method is similar to that previously described[9]. The area, perimeter, and shape of the tracks were assessed. In addition, the images were visually examined in order to investigate the possible occurrence of closely spaced tracks. Tracks were identified visually on the light white background as dark round or elliptically shaped objects that may have a pale center.

Acquisition and analysis of 3D images

The LEXT microscope was used in confocal mode in order to acquire 3D image data of more than 60 tracks of which 51 were single tracks. The height of the top surface and the deepest track were manually determined in order to allow the image data to be acquired over an appropriate depth range.

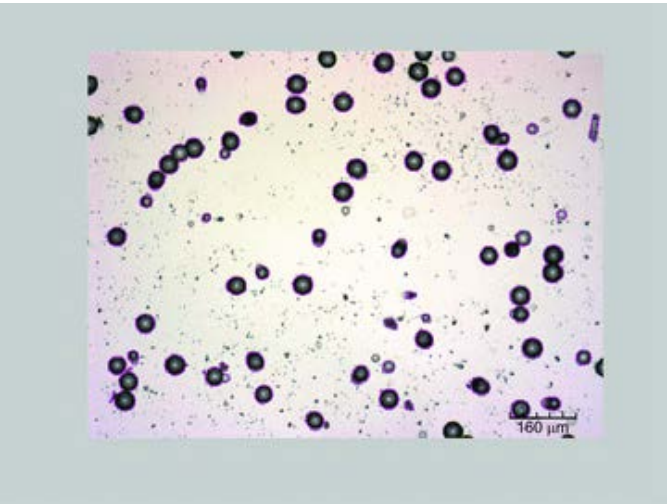

Figure 1: Image showing segmentation of tracks (shown in purple) on an image using a 10X objective. The tracks are seen as darker elliptical or circular areas. A range of track sizes and gray levels is seen as well as some overlapping tracks. The long rectangular object on the upper right is assumed to be an artifact and was thus not included in the analysis.

For this study, a 50X objective was used for the initial 3D examination of the detectors as this appeared to give an appropriate level of detail for the tracks while allowing several tracks to be imaged. The movement between each step in the z-direction was 180 nm for the 50X objective and 50 nm for the 100X objective. For the 50X objective lens, each pixel corresponds to 0.25 µm. In order to view further surrounding tracks, the tiling feature was used to acquire a series of adjacent images which were then stitched together; the stitching involves a 15% overlap of the adjacent tiled images. The 3D visualizations were compared with 2D surface images.

The 3D data, including height information, was visualized and analyzed using the LEXT system. Hence the depth profile and changes in gray level were examined in tracks that appeared to be inclined, as identified by an elliptical cross-section, by manually selecting cross-sections through the visualization of the tracks. We also investigated possible connections between tracks when there were closely spaced multiple events. Data with height information was also exported to a spreadsheet-compatible file so that it could be visualized with additional software we developed using MATLAB.

RESULTS

A total of 229 single tracks or clusters of multiple tracks (range 53 to 63 per detector) were seen in the images of the four detectors. An example of an image of tracks and their detection is shown in **Figure 1.** There were 182 clear single tracks, 25 double adjacent tracks, and 7 regions of apparently more than 2 adjacent tracks; there were a further 15 single or double tracks where there appeared to be some artifacts and hence were not included in the following analysis. The area data for the single tracks was not consistent with a normal distribution using the Ryan–Joiner test in MINITAB v. 15 (Minitab, Inc. State College, PA, U.S.A.), and hence median, quartiles, and range are used for the descriptive statistics. The area, perimeter, equivalent diameter, roundness, and eccentricity of the single and double radon tracks are shown in **Table 1**.

Eccentricity is the ratio of the distance between the foci of the ellipse divided by the length of the major axis; thus, for a circle the value is 0. The eccentricity values suggest that most of the single tracks are elliptical, which

Single tracks	Minimum	Q 1	Median	Q 3	Maximum
Area (µm²)	315.63	1228.13	1668.75	1898.13	3062.50
Equivalent diameter (µm)	20.05	39.54	46.10	49.16	62.44
Perimeter (µm)	64.63	128.89	152.05	161.31	213.56
Major axis length (µm)	21.44	43.45	48.78	51.00	75.79
Minor axis length (µm)	14.33	35.75	43.99	48.35	54.59
Roundness	0.97	1.06	1.09	1.13	1.70
Eccentricity	0.04	0.24	0.37	0.57	0.89

Double tracks	Minimum	Q 1	Median	Q 3	Maximum
Area (µm²)	1067.19	2348.44	3078.13	3448.44	4384.38
Equivalent diameter (µm)	36.86	54.69	62.60	66.26	74.71
Perimeter (µm)	124.98	200.31	241.24	265.24	356.78
Major axis length (µm)	47.09	68.01	86.09	98.83	126.94
Minor axis length (µm)	29.26	43.81	47.83	50.72	55.15
Roundness	1.15	1.28	1.41	1.66	2.31
Eccentricity	0.61	0.78	0.83	0.87	0.92

Table 1: Minimum, Q1, median, Q3, and maximum values of area, perimeter, roundness, and other measures for single and double tracks.

is consistent with visual observation. Using Spearman's rank correlation there is a significant negative correlation between area and eccentricity ($r=0.541$, $n=182$, $P < 0.001$), although there was wide variation when examining the data with a scatter plot.

Compactness is defined as the ratio of perimeter squared divided by area[15] and roundness is that ratio divided by 4π[16]. Thus, a circle has the lowest roundness of 1. In this data, all the objects had a roundness of 1 or more except for one very small object (222 pixels in area) with a measured roundness value of 0.97. The median roundness of the single tracks of 1.09 is also consistent with many tracks not being exactly circular in cross-section.

Three-dimensional visualization helps in investigating variation in area and depth as well as identifying coalescing tracks as seen in **Figure 2** where a 50X objective was used. The

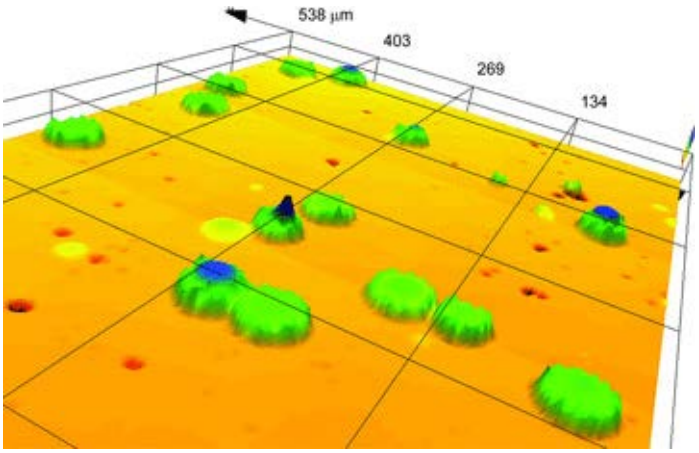

Figure 2: Example of 3D visualization of tracks from data obtained with a 50X objective showing the distribution of tracks in the 3 × 3 stitched area; some adjoining tracks can be seen. The color coding shows the height: red being the top, through yellow, blue, green, and to purple being the deepest.

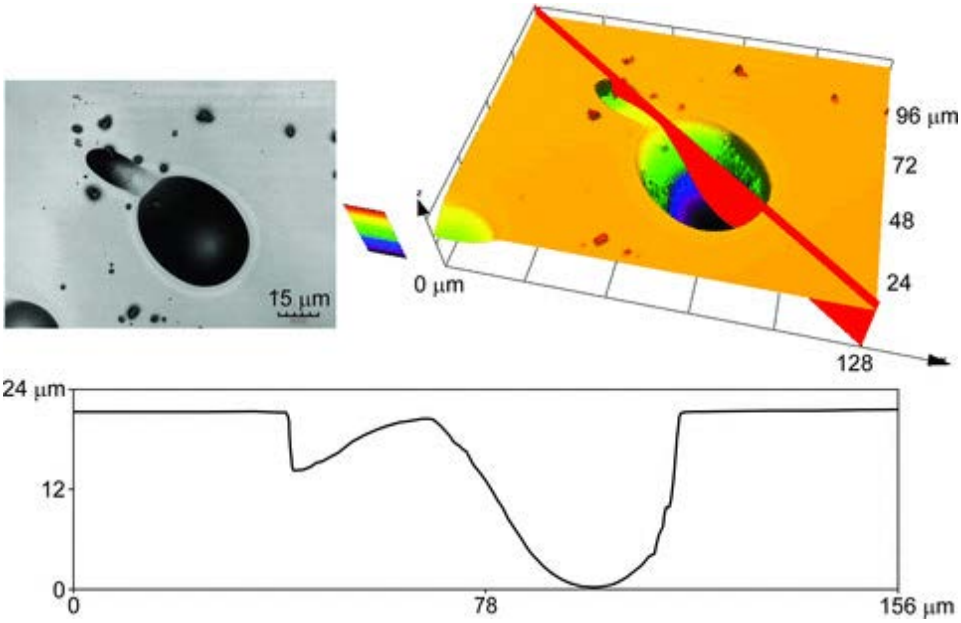

Figure 3: An example showing two tracks in 2D together with a depth-encoded color image and the profile through the tracks that were taken with a 100X objective. As in **Figure 2,** the color coding shows the height: red being the top, through yellow, blue, green, and to purple being the deepest. The gradient profile suggests that the left track was formed by an α particle coming from the right side, whereas the larger right-hand track appears to have been formed by a particle from the left-hand side as the slope is seen to be less steep.

examples in **Figures 2** and **3** show that track areas appear to be highest at the surface and become smaller going deeper into the detector. The 3D image data in **Figure 2** was exported to a spreadsheet file in order to enable the analysis of the track area using additional software developed using MATLAB (The MathWorks, Inc.) at Kingston University. The software detects the surface layer and hence can identify tracks emanating down from the top surface. From the 3D image data, the area of nine single tracks at the detector surface was analyzed and compared with a corresponding 2D image acquired with a 10X objective. The mean (standard deviation) difference in the track area, (3D – 2D measurements) divided by the mean of the 2D and 3D area, was 5.1% (4.2%); this data was consistent with a normal distribution using the Ryan–Joiner test in MINITAB v. 15 (Minitab, Inc.) and using a one-sample t-test were significantly different from 0 (P = 0.008).

Acquisition of each 3D dataset (without tiling) takes typically about 5 minutes depending on settings; 130 steps can be scanned per minute in the z-direction when using any of the objectives. Visualization and basic analysis of the 3D track data typically takes less than 10 minutes, depending on the size of the image and the type of analyses performed. Some of the observed elliptical shape tracks were associated with different gradients on either side of the corresponding depth profile of the 3D data. From the profile graph in **Figure 3,** the deeper track can be seen to have a depth of about 22 µm whereas the shallow track has a depth of about 10 µm. An indication of the track angle can be derived from the depth and spatial position data. The gradient of the profile is likely to indicate the angle at which the α particle hit the detector; two examples of this are seen in **Figures 3** and **4**, which also show that 3D visualization and depth profiles can help in understanding the relative size and angles of a sequence of multiple hits from the way in which the tracks are formed (**Figure 4**). The profile graph in **Figure 4** shows clearly the depths of the two tracks on the right are about 18 and 22 µm. In addition, in the example in **Figure 4**, the outline 2D shape suggests there may be two tracks, whereas the greater detail from 3D visualization shows that there are three tracks.

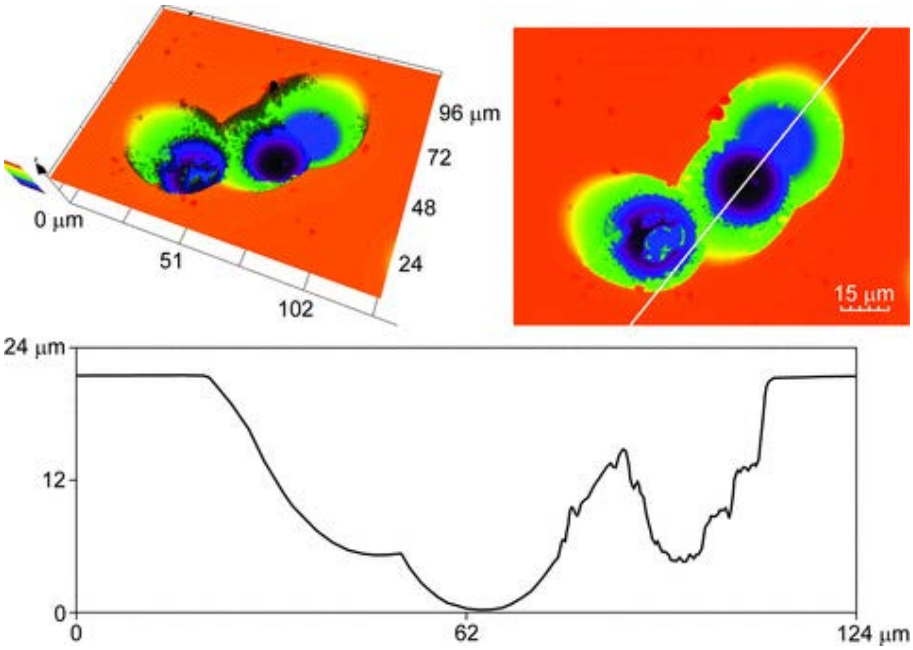

Figure 4: An example of multiple coalescing tracks obtained with a 100X objective. The profile of this image is shown just below and confirms that the tracks are individual overlapping tracks with the middle track being the deepest. The height color coding is as in **Figures 2** and **3**. The white line through the image shows where the profile map has been taken.

DISCUSSION

In this study, clear visualizations of surface and 3D tracks were obtained and a number of patterns such as single, double, and multiple hits as well as angled hits were observed. Further to our earlier paper[9], in this investigation, 3D images of the full depth of tracks together with greater detail were obtained. The lower wavelength laser as well as the 50X and 100X objective lenses used here for 3D microscopy contribute to the improved resolution. Hence, it was possible to visualize in detail the occurrence of angled tracks in 3D and to quantify the angle along different profile lines; such visualization allows assessment of the direction in which the α particles collide with the detector. From the 2D image data, the area of tracks shows marked variation, and preliminary results suggest that this may be inversely related to the eccentricity, which is consistent with visual observations that lower area tracks appeared to be more elliptical in shape. It would be interesting to investigate if area is related to the angle of inclination. The 50X objective used for 3D dataset collection enables higher spatial resolution images than the 10X objective and hence correspondingly influences track area measurement accuracy. Measurements of surface track area obtained from a 3D image using the 50X objective were found to be similar to corresponding area measurements from a 2D image using the 10X objective; the mean difference observed was 5.1% which, albeit small, was significantly different from 0 ($P = 0.008$). The higher track area, observed using 3D imaging, is likely to be due to the decrease in the area seen going deeper into the detector. For 2D imaging, this may result in less contrast around the circumference of the track, which thus could affect the area detected when applying the thresholding algorithm.

The variability of radon track measurements from 2D measurements may in part be due to the difficulty of selecting true tracks from an artifact. It was observed that high-resolution 3D visualization can help in accurately identifying tracks and quantification of their geometry. Although collecting 3D datasets takes more time than conventional 2D imaging, the 3D data enables further analysis of tracks than from 2D data alone; this should help in better understanding track formation and more

precise determination of the number of radon tracks. For example, multiple closely spaced tracks could be due to hits from multiple particles or possibly bouncing of particles on the detector surface; 3D imaging should enable the distinction of particle bouncing from multiple particle hits by assessment of the depth and angle data. The occurrence of areas of adjacent multiple hit tracks was observed; the reason for α particles appearing to impinge on the detector more often in certain areas is unclear, but it is possible that the process of track formation causes a change in surface charge. In summary, high-resolution 3D images of radon tracks in CR-39 plastic detectors obtained using confocal microscopy in combination with 2D microscope images enable detailed analysis of their physical dimensions and shape; the full depth of tracks and their angle with respect to the surface could be quantified. The techniques described in this study allow detection of tracks of different sizes and may thus help to improve the accuracy and repeatability of radon measurements as well as gain a better understanding of track formation.

REFERENCES:

[1] *Darby, S., Hill, D., Auvinen, A., et al. (2005) Radon in homes and risk of lung cancer: collaborative analysis of individual data from 13 European case-control studies. BMJ. 330, 223–226.*

[2] *ICRP (International Commission on Radiological Protection) (2007) Recommendations of the International Commission on Radiological Protection. ICRP publication 103. Ann. ICRP. 37(2–4), 1–332.*

[3] *Papworth, D.S. (1997) A need to reduce the radon gas hazard in the UK. J. R. Soc. Health. 117, 75–80.*

[4] *Coskeran, T., Denman, A., Phillips, P., Gillmore, G. & Tornberg, R. (2006) A new methodology for cost-effectiveness studies of domestic radon remediation programmes: quality-adjusted life-years gained within primary care trusts in Central England. Sci. Total Environ. 366, 32– 46.*

[5] *Gillmore, G.K., Phillips, P., Denman, A., Sperrin, M. & Pearce, G. (2001) Radon levels in abandoned metalliferous mines, devon, Southwest England, Ecotoxicol. Environ. Saf. 49, 281–292.*

[6] *Gillmore, G., Gilbertson, D., Grattan, J. et al. (2005) The potential risk from radon222 posed to archaeologists and earth scientists: reconnaissance study of radon concentrations, excavations and archaeological shelters in the Great Cave of Niah, Sarawak, Malaysia. Ecotoxicol. Environ. Saf. 60, 213–227.*

[7] *Phillips, P.S., Denman, A.R., Crockett, R.G.M., Gillmore, G., Groves- Kirkby, C.J. & Woolridge, A. (2004) Comparative Analysis of Weekly vs. Three Monthly Radon Measurements in Dwellings. DEFRA Report No., DEFRA/RAS/03.006. DEFRA, London.*

[8] *Cliff, K. & Gillmore, G.K. (eds.) (2001) The radon manual: a guide to the requirements for the detection and measurement of natural radon levels. Associated Remedial Measures and Subsequent Monitoring of Results, 3rd edn. The Radon Council, Shepperton, Middlesex, U.K.*

[9] *Petford, N., Wertheim, D. & Miller J.A. (2005) Radon track imaging in CR-39 plastic detectors using confocal scanning laser microscopy. J. Microsc. 217, 179–183.*

[10] *Naismith, S.P., Howarth, C.B. & Miles, J.H.C. (1998) Results of the 1997 European Commission Intercomparison of Passive Detectors. EUR 18035 EN. European Commission, Brussels.*

[11] *Henshaw, D.L., Allen, J.E., Keitch, P.A. & Randle, P.H. (1994) Spatial distribution of naturally occurring 210Po and 226Ra in children's teeth. Int. J. Radiat Biol. 66, 815–826.*

[12] *Nikezic, D. & Yu K.N. (2008) Computer program TRACK_VISION for simulating optical appearance of etched tracks in CR-39 nuclear track detectors. Comput. Phys. Comm. 178, 591–595.*

[13] *Wagner, W. & Van Der Haute, P. (1992) Fission Track Dating. Kluwer Academic Publishers, Dordecht.*

[14] *Fleischer, R.L., Price, P.B. & Walker, R.M. (1975) Nuclear Tracks in Solids: Principles and Applications. University of California Press, Berkley, California.*

[15] *Gonzalez, R.C. & Woods, R.E. (2002) Digital Image Processing, Second edn, Prentice Hall, New Jersey.*

[16] *Kanthathas, K., Willmot, D.R. & Benson, P.E. (2005) Differentiation of developmental and post-orthodontic white lesions using image analysis. Eur. J. Orthod. 27, 167–172.*

05 Application of Confocal Microscopy for Surface and Volume Imaging of Solid-State Nuclear Track Detectors

D. Wertheim, G. Gillmore

SUMMARY

Inhalation of radon gas is considered a risk factor in the development of lung cancer. Solid-state nuclear track detectors (SSNTDs) are often used for monitoring radon levels. We have previously shown that 3D imaging can help distinguish real tracks from artifacts. In this study, we investigated particle tracks in nine SSNTDs using surface and volume visualization from confocal microscope imaging. An Olympus LEXT™ OLS4000 confocal microscope equipped with the Olympus LEXT Remote Development Kit was used to acquire z-stack images and surface data from the SSNTDs. Surface and volume visualization analysis methods were developed and applied to examine the data. The mean (standard deviation) depth of 45 tracks from the nine detectors was 9.5 (4.6) µm. The mean difference in track depth using the two analysis techniques was 0.08 µm, thus showing good agreement. Furthermore, volume visualization should enable assessment of the structure of tracks deep in the detector.

BACKGROUND

As outlined on pp. 6–7 of this eBook, the inhalation of radon gas has been shown to be a risk factor in the development of lung cancer[1]. It is estimated that there are 1,100 home radon-related lung cancer deaths annually in the United Kingdom alone[2]. Radon levels can be measured using small etched plastic detectors called solid-state nuclear track detectors (SSNTDs); the detectors are often based on poly-allyl-diglycol carbonate or PADC, commercially known as CR-39.

CR-39 detectors

SSNTDs are more similar to human tissue than other passive detectors[3]. They are extensively used in dosimetry because of their low linear energy transfer (LET) threshold for detection of charged particles[4], hence their use

in measuring radon and its decay products in buildings. SSNTDs are also used in neutron dosimetry and the neutron response of such detectors has relied on the simulation of the formation/development of etched tracks as a function of energy and etching time[5]. Some authors have undertaken simulated 3D computation of track shape in order to better understand the potential effect of incidence direction of charged particles and SSNTD track development[6,7]. The measurement of track parameters then can provide data on the energy deposition of the incident particle[3], and analysis of tracks produced by α particles, protons, or nuclear fission fragments is a very valuable tool[8]. The geometry of α-track cone formation in SS- NTDs can provide information on energy and charge and direct measurements of track lengths are sometimes required[8]. The α-track etch-pit diameters can act as a spectrometer in that they can be related to incident α energy[9]. In one study, detectors were broken in order to make direct measurements of the track length[7], while others have utilized atomic force microscopy (AFM), but due to probe geometry the bottom of the track has not been reached[8]; a holographic technique in combination with an interferometer has also been applied to obtain surface views of tracks[8]. Thus, there have been few studies imaging actual track depths using nondestructive techniques.

SSNTD imaging

Conventionally etched SSNTDs are assessed using 2D microscope imaging. Confocal microscopy can be used to obtain 3D image datasets of tracks in SSNTDs[10,11]. Fluorescent confocal microscopy was used to image SSNTDs by treating the detectors with Nile Blue A[10]. We have previously used the LEXT™ OLS3100 confocal microscope to successfully image CR-39 radon track detectors[11-13]. These studies used reflection confocal microscopy to enable 3D visualization and quantification of tracks from surface data without the need for using a fluorescent dye. A recent addition to the LEXT™ OLS4000 microscope enables z-stack images to be stored in addition to the acquisition of surface image data. Hence, this potentially allows examination of 3D material structure around tracks which may help in the interpretation of coalescing and angled tracks.

AIM

The aim of this study was to investigate single and coalescing particle tracks with surface and volume visualization of confocal microscope SSNTD image datasets.

METHOD

Nine CR-39 plastic radon detectors previously exposed in rooms, or a controlled radon chamber were processed by etching for up to 4.5 hours in 6M NaOH solution at 90 °C (194 °F) in the KU (Micro) Radon Laboratory at Kingston University; the etching conditions could potentially affect the microscopic appearance of tracks. The etched SSNTDs were cleaned with distilled water in an ultrasonic bath for 2 minutes. Detectors were individually placed on the microscope stage of an Olympus LEXT™ OLS4000 confocal microscope (Olympus Corporation, Japan). The microscope system was equipped with the Olympus LEXT Remote Development Kit (RDK), thus allowing acquisition of z-stack images as well as surface imaging. The detectors were

initially examined using the LEXT operating in 2D imaging mode using 5X and 10X objective lenses followed by 3D scanning using the standard 'fine' surface scanning mode (with 'Color'); the method is similar to that used in earlier studies with an OLS3100 microscope[12,13]. In confocal mode, 50X or 100X objective lenses were used (NA 0.95), and the microscope has a 405 nm laser. The images were acquired with a size of 1024 × 1024 pixels; using the 50X lens, the *xy* area imaged was 260 × 260 µm, thus giving a lateral spatial resolution of 0.25 µm per pixel. Before scanning, the top (upper detector surface) and bottom levels were determined manually. 2D and 3D screenshots were acquired as single image files. Heightmap data were downloaded in a spreadsheet-compatible file in order to allow subsequent 3D visualization and analysis.

In this study, we examined and compared surface data with z-stack imaging. The surface data were analyzed from the heightmap spreadsheets. Z-stack imaging was obtained using the LEXT RDK, and hence it is possible to enable volume visualization from the confocal slices.

Script files were written for the RDK to run on the controlling PC in order to allow appropriate movement of the objective lens following each z-slice acquisition; in each script file, movement was set such that the objective lens moved up away from the slide in 0.1 µm steps. As the top and bottom posi-

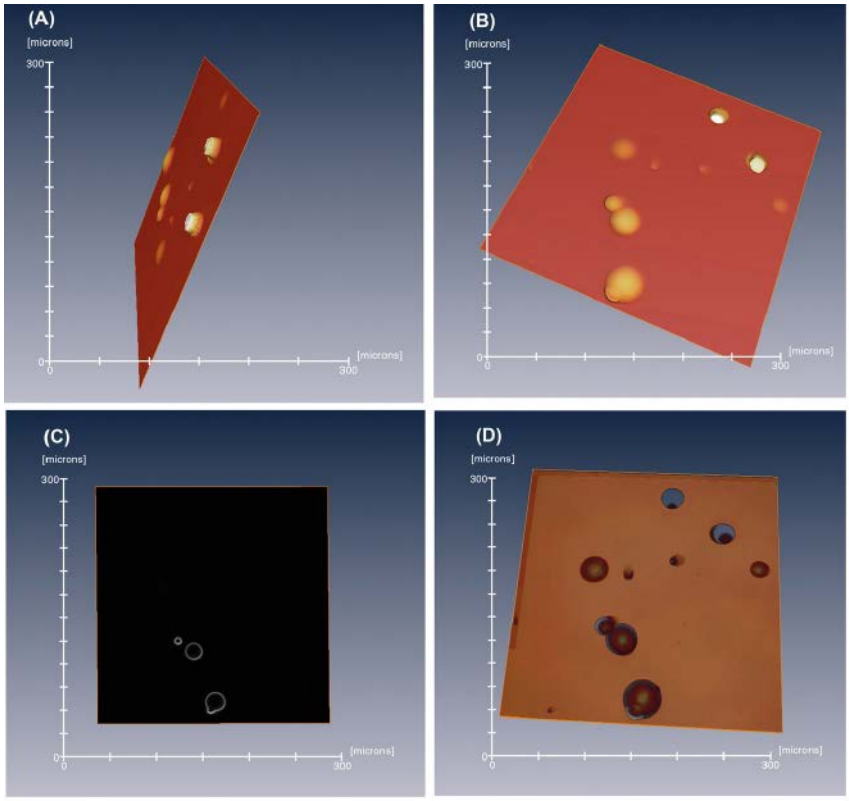

Figure 1: Example showing 3D surface imaging (50X objective) from height data with LEXT microscope; (A) shows a side view from the lower side of the detector, (B) shows 3D surface from top surface, (C) shows an example of a single z-stack intensity image an example of a stack intensity image, and (D) shows 3D volume visualization of tracks from a z-stack dataset. In each image the lengths of the abscissa and ordinate axes are 300 µm.

tions were known, the number of slices to be acquired could be calculated, and hence the number of slices to be collected was set in the script file; the z-stack images were collected.

3D visualization

Software was written in MATLAB (The MathWorks Inc., Natick, MA, U.S.A.) in order to read the height field map spreadsheet files. The mode height was calculated to determine the level of the detector surface. The minimum and maximum heights were computed, and the data was remapped as a gray scale image covering the full range of height values. The resultant images were read into Amira v. 5.4 (VSG, Visualization Sciences Group), and networks were developed to allow examination of the 3D visualization. Further software was developed in MATLAB in order to display surface data and compute the distribution of track depths.

Surface and volume visualizations of the z-stack images were also performed using Amira; isosurface and voltex visualization techniques were applied to examine the image data.

Comparison of track depths

Track depths calculated from the surface spreadsheet files were compared with the stack data for 45 tracks in the nine detectors. In Amira, the depth of the tracks was examined using orthoslice visualization; in this mode, the signal from the confocal microscope imaging can easily be seen in successive z-slice images, and an example can be seen in **Figure 1C**. The track depths were thus calculated from the difference between the detector surface level and the lower surface of each of the tracks as the distance between slices is constant; the lower surface was defined as the lowest position where the track is discernible. Data were tested for consistency with a normal distribution using the Ryan–Joiner test in Minitab v. 16 (Minitab Inc., U.S.A.).

RESULTS

Visualization using 3D surface and volume approaches were compared. **Figure 1** shows an example of surface imaging from depth data in comparison with volume visualization. The Figure shows views from the lower side of the detector and looking from the top surface. This is compared with volume visualization (**Figure 1D**) formed by combining the z-stack of intensity images, one of which is shown in **Figure 1C**. The techniques applied for volume visualization of the stack data did not apply connection of surfaces so that the raw intensity data were used; this can result in apparent gaps but avoids potential difficulties from applying assumptions about surface geometry.

Figure 2 shows an example of zooming in on an angled track as well as two apparently very closely coalescing tracks. The volume visualization technique allows zooming in to examine the surface in more detail, thus identifying the likely closely coalescing tracks and the appearance of an angled track. These examples illustrate that visualization of z-stack data enables structure of the tracks deep in the detector to be seen. An example of the analysis of track depth data using software we developed in MATLAB is shown in **Figure 3**. Using data from another detector, the representation of depth in a gray scale or pseudocolor image helps to assess the depth of each individual track with respect to the detector surface. Tracks 1, 2,

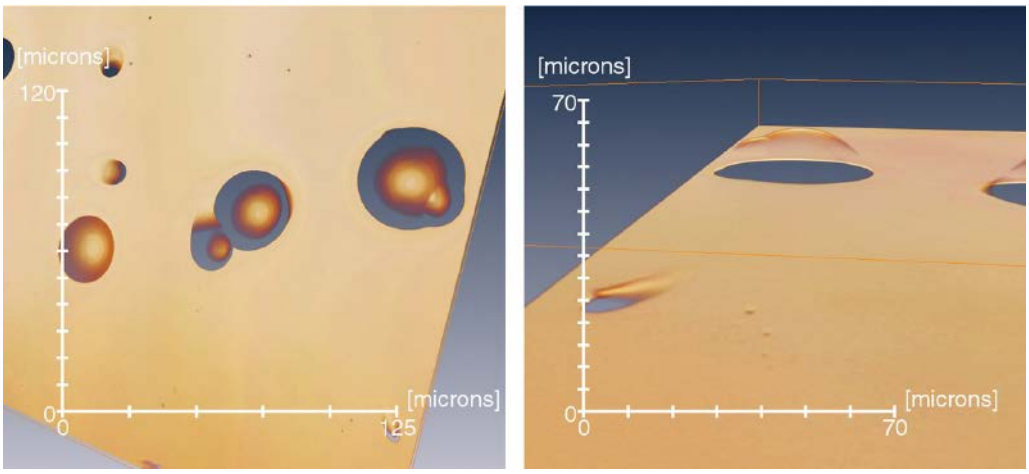

Figure 2: Example showing zoomed visualization of **Figure 1** stack imaging. The left-hand image shows a view of the top surface and the right-hand image shows an image viewed from deep in the detector to the top surface.

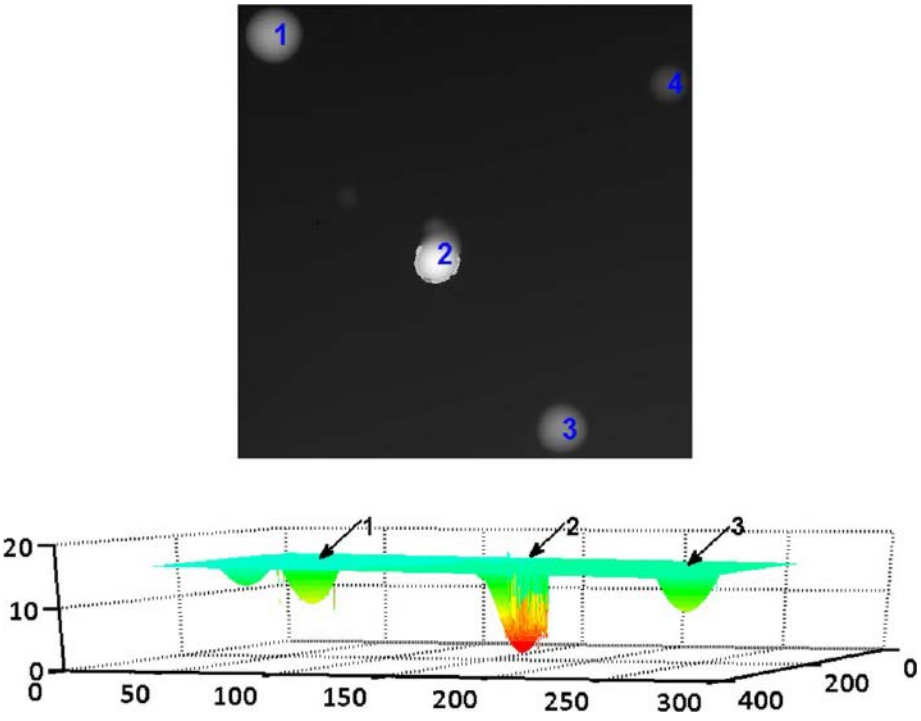

Figure 3: An example of a depiction of track depth data using a greyscale image (upper). The lower part of the figure shows a 3D representation of the data.

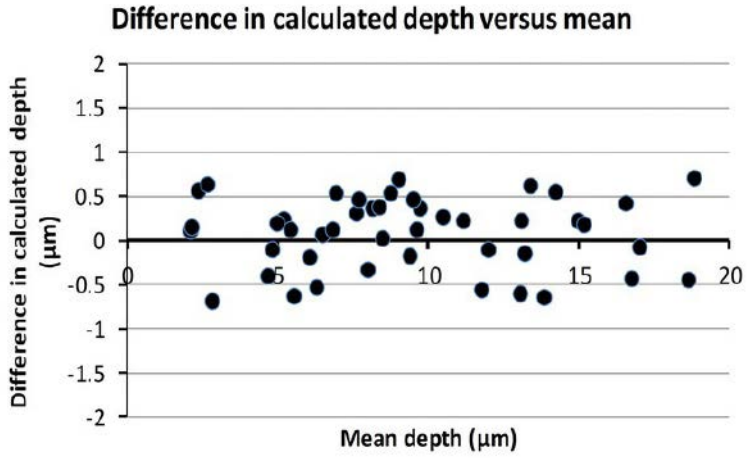

Figure 4: Graph showing the difference in calculated depth (surface measured depth – stack measured depth) plotted against the mean of the two measurements.

and 3 have depths of 7.5, 14.5, and 6.6 µm, respectively, as can be seen in the lower part of the figure with a 3D representation obtained using software we developed in MATLAB.

Comparison of track depths

The mean (standard deviation) depth of the 45 tracks was 9.5 (4.6) µm. **Figure 4** shows a graph of the difference in calculated depth (surface depth minus stack measured depth) against the mean in accordance with a method for comparing measurements[14]. The mean (standard deviation) difference in calculated depths between the two methods was 0.08 (0.40) µm. There was no significant correlation between the difference in the two measurements and the mean (Pearson's correlation coefficient $r = -0.02$, $p = 0.9$). The depths are consistent with previous observations[13].

DISCUSSION

Assessment accuracy is important not only for radon detection and remediation but also for dosimetry. Coalescing tracks may cause problems of interpretation using conventional 2D analysis, these difficulties could be addressed using 3D imaging which also helps to distinguish real tracks from artifacts; artifacts due to dust or similar particles should be evident by protrusion above the top surface. Coalescing tracks are likely to be particularly evident with high track densities associated with high radon concentrations.

Detection of surface features has wide applications in material analysis. In the case of SSNTDs, surface tracking may be difficult for very steep tracks that could occur in some deep and angled tracks. Furthermore, coalescing tracks could be difficult to assess because of the associated complex profile. Z-stack imaging allows the raw data to be displayed, thus avoiding possible artifacts that may be seen in steep, angled tracks; furthermore, the method allows a detailed view of the structure of coalescing tracks. Hence, 3D imaging allows examination of coalescing tracks and helps to discern real tracks from artifacts, both of which potentially could be problematic in 2D analysis. The examples in **Figures 1** and **2** illustrate that visualization of z-stack data images allows examination of the structure of tracks deep in the detector.

Rather than only imaging the surface, in transparent and partially transparent materials, stack imaging should allow examination around the surface into the material. Thus, we have been able to study the structural appearance of tracks. Additional information can possibly be obtained regarding surfaces associated with steep angles with respect to the upper surface. The stack imaging system enables examination of the reflected signal, thus allowing detailed interpretation of the data associated with steep angular features as can be seen, for example, in deep tracks and certain angled tracks. In addition, if 3D surface imaging identifies unexpected surfaces, stack imaging can help in the interpretation of data in order to understand better the resultant visualization. The comparison of calculated depths using the two techniques showed good agreement.

CONCLUSIONS

Series of z-stack images were acquired using the Olympus LEXT™ RDK as well as surface imaging data with the microscope and software was developed to enable 3D visualization and analysis of the data in order to examine radon tracks in CR-39 detectors. Stack imaging can enable visualization that complements conventional 3D surface imaging as it allows examination of the material surrounding the detected surfaces. Comparing the two analysis techniques, there was good agreement in the calculated measurement of track depth. This approach should enable the assessment of the structure of tracks deep in the detector, which could help in the interpretation of images and hence improve SSNTD assessment.

REFERENCES:

[1] *Darby, S., Hill, D., Auvinen, A., et al. (2005) Radon in homes and risk of lung cancer: collaborative analysis of individual data from 13 European case-control studies. Br. Med. J. 330, 223–228.*

[2] *Gray, A., Read, S., McGale, P. & Darby, S. (2009) Lung cancer deaths from indoor radon and the cost effectiveness and potential of policies to reduce them. Br. Med. J. 338, 215–218.*

[3] *Caresana, M., Ferrarini, M., Fuerstner, M. & Mayer S. (2012) Determination of LET in PADC detectors through the measurement of track parameters. Nucl. Instr. Methods Phys. Res. A 683, 8–15.*

[4] *Lounis, Z., Djeffal, S., Morsli, K. & Allab, M. (2001) Track etch parameters in CR-39 detectors for proton and alpha particles in different energies. Nucl. Instr. Methods Phys. Res. B 179, 543–550.*

[5] *Dörschel, B., Bretscheider, R., Hermsdorf, D., Kadner, K. & Kühne, H. (1999) Measurement of the alpha track etch rates along proton and alpha particles trajectories in CR-39 and calculation of detection effi ciency. Rad. Measur. 31, 103–108.*

[6] *Azooz, A.A., Hermsdorf, D. & Al-Jubbori, M.A. (2013) New approach of modeling charged particles track development in CR-39 detectors. Rad. Measur. 58, 94–100.*

[7] *Dörschel, B., Hermsdorf, D., Reichelt, U., Starke, S. & Wang, Y. (2003) 3D computation of the shape of etched tracks in CR-39 for oblique particle incidence and comparison with experimental results. Rad. Measur. 37, 563–571.*

[8] *Palacios, F., Palacios Ferna´ndez, D., Ricardo, J., Palacios, G.F., Sajo-Bohus, L., Goncalves, E., Valin, J.L. & Monroy, F.A. (2011) 3D nuclear track analysis by digital holographic microscopy. Rad. Measur. 46, 98–103*

[9] *Soares, C.J., Alencar, I., Guedes, S., Takizawa, R.H., Smilgys, B. & Hadler, J.C. (2013) Alpha spectrometry study on LR115 and Makrofol through measurements of track diameter. Rad. Measur. 50, 246–248.*

[10] *Hermsdorf, D. & Hunger, M. (2009) Determination of track etch rates from wall profiles of particle tracks etched in direct and reversed direction in PADC CR-39 SSNTDs. Rad. Measur. 44, 766–774.*

[11] *Petford, N., Wertheim, D. & Miller, J. (2005) Radon track imaging in CR-39 plastic detectors using confocal scanning laser microscopy. J. Microsc. 217, 279–283.*

[12] *Wertheim, D., Gillmore, G., Brown, L. & Petford, N. (2010a) A new method of imaging particle tracks in Solid State Nuclear Track Detectors. J. Microsc. 237, 1–6.*

[13] *Wertheim, D., Gillmore, G., Brown, L. & Petford, N. (2010b) 3-D imaging of particle tracks in solid state nuclear track detectors. Nat. Haz. Earth Syst. Sci. 10, 1033–1036.*

[14] *Bland, J.M. & Altman, D.G. (1986) Statistical methods for assessing agreement between two methods of clinical measurement. Lancet 1(8476), 307–310.*

06 Application of Confocal Microscopy for 3D Visualization of Tracks in Solid-State Nuclear Track Detectors

D. Wertheim, G. Gillmore

ABSTRACT

Inhalation of radon gas is considered to be associated with about 1,100 people dying annually from lung cancer in the UK alone. Accurate and timely assessment of radon levels is thus important in areas with known elevated radon level risk in order to be able to institute remedial procedures. A common method for monitoring radon concentration is with small plastic detectors known as solid-state nuclear track detectors (SSNTDs). This paper reviews recent research in 3D imaging of SSNTDs using confocal microscopy.

INTRODUCTION

Inhalation of radon gas, that is ^{222}Rn and its associated radioactive heavy metallic daughter products such as ^{214}Po, is estimated to be associated with about 1,100 lung cancer-related deaths annually in the UK[1–3] and 21,000 in the USA[4]. Furthermore, radon exposure can increase the risk of lung cancer in smokers as well as non-smokers[5]. The gas is a natural hazard that can be found in elevated levels in areas of the UK as well overseas; it is formed as a result of the natural radioactive breakdown of uranium ^{238}U present in rocks and soils. Radon gas is colorless and odorless, so its presence could remain undetected without the use of appropriate sensing technology. It is possible for concentrations to become unsafe, for example in poorly ventilated rooms, mines, and caves[6]. Amelioration in both homes and workplaces by adequate room ventilation measures may thus be required in order to reduce radon levels in affected areas[7]. Hence, monitoring radon concentrations in buildings is routinely undertaken in certain areas with the potential for elevated radon levels.

Measurement of radon levels in buildings is thus an important step toward tackling increased radon gas levels in rooms inhabited by humans. Solid-state nuclear track detectors (SSNTDs) are small passive devices often made of plastic that can be used to measure radon concentrations in the atmosphere. They are commonly placed in an outer enclosure that ensures air passes over the detector. Alpha particles formed by the nuclear breakdown of radon cause tiny sub-microscopic indentations, termed tracks, in the SSNTD. In order to make these visible for a light microscope, the detectors are etched. Radon gas concentration can be measured with CR-39 plastic detectors[8], but even detectors near each other can give differing readings[6]. CR-39 solid-state

nuclear track–etch detectors are the most commonly used for radon gas measurements.

Typically, the detectors are placed in rooms for several weeks. In order to make tracks in the SSNTD from alpha particles visible with a microscope, the tracks are enlarged using a process called etching, but this can vary in time, temperature, and etchant concentration. The standard method of assessing radon concentration involves analysis of 2D microscope images of the SSNTDs; using this approach, tracks often appear circular or elliptical in cross-section. However, distinguishing real tracks from artifacts using 2D imaging and analysis alone can be difficult.

Radon concentrations are derived from counting the number of tracks seen in SSNTDs exposed for a given period. The tracks are conventionally counted by image analysis of 2D microscope images of the detector. The length of time of the etching process can affect the size of the tracks seen[9]. This potentially could affect the counting process as short etching times could result in small tracks that may be difficult to discern, whereas long etching times could result in coalescing tracks from which it could be difficult to discern individual tracks as well as distinguishing real tracks from artifacts. Thus, etching times are important to consider as well as similarly etching temperature and pH.

DEVELOPMENTS IN MICROSCOPE IMAGING OF RADON TRACKS

Confocal microscopy has previously been used to examine fission tracks in mica and apatite[10]. We have developed and applied methods for 3D image analysis and visualization of radon tracks in SSNTDs using confocal microscopy[9,11-14]. There can be some variation in track diameters; the results from a study indicated that the typical median (range) equivalent track diameter for single tracks is 46.1 (20.05 to 62.44) µm for standard processing[12,13]. In our studies, Olympus LEXT™ confocal microscopes have been used to image tracks, and the results have shown that tracks can have different sizes, shapes, and angles. In addition, we identified that tracks in close proximity can coalesce into a cluster; such clusters could potentially be difficult for 2D image analysis to distinguish from artifacts. 3D imaging allows a clearer distinction of real tracks from artifacts compared with 2D imaging as the full 3D extent can be ascertained from the visualization rather than just a surface image. Thus, we suggest that 3D imaging and analysis may help to improve measurement accuracy.

COMPARISON OF 2D AND 3D IMAGING

In our studies, we have used LEXT™ models OLS3100, OLS4000, and OLS4100 confocal laser scanning microscopes (Olympus Corporation, Tokyo, Japan) to acquire 3D image data on CR-39 plastic detectors as previously described[9,12-14]; the detectors used were from the Radon Metrology Laboratory at Kingston University. The detectors were placed on a glass slide or directly on the microscope stage. Confocal microscope images were obtained primarily using a 50X or 100X objective mostly in fine mode; both lenses had a numerical aperture (NA) of 0.95. Examples comparing 2D imaging with 3D imaging are shown in **Figures 1 to 3. Figure 1** shows an example of an artifact caused by debris on the surface that can be seen to be easily identified with 3D imaging as it lies above the surface, whereas it could potentially be confused with a small track using 2D imaging alone.

Figure 1 shows a 2D image of an SSNTD. From the image one bright area could be a small track or artifact. 3D imaging shows that it is indeed an artifact as seen in **Figures 2** (right-hand image) and 3 since it emanates above the detector surface.

Depending on radon concentration and length of exposure of the detector, tracks can occur in close proximity to other tracks on the SSNTD. If tracks coalesce, it is possible that a basic 2D imaging and analysis system could have a tendency to count such multiple strikes as one or as an artifact if not of circular appearance. With longer exposures or higher radon concentrations, there is an increased likelihood that tracks could overlap or be superimposed on one another. If tracks coalesce it is possible that individual tracks may be difficult to detect using 2D image analysis, and there may thus be the potential for underassessment of track numbers; 3D imaging allows detailed examination of coalescing tracks, which could thus help in situations where SSNTDs are used over long periods or in high radon concentrations.

Our studies with the Olympus LEXT microscope have shown that confocal microscopy can be used to examine SSNTD tracks

EXAMPLE IMAGES

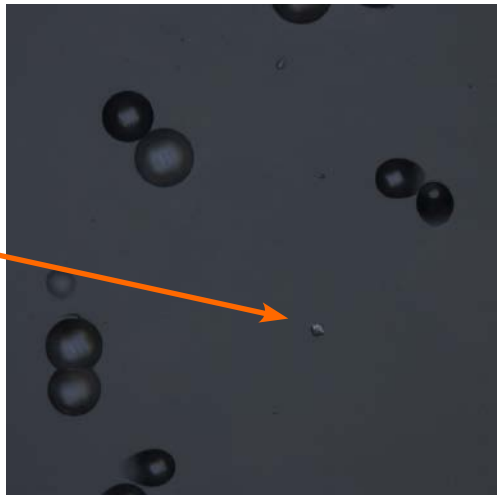

Figure 1: 2D image of an SSNTD using a 50X objective lens. Scale 257 by 257 µm. Blue arrow indicates an area that appears to be an artifact or a small track.

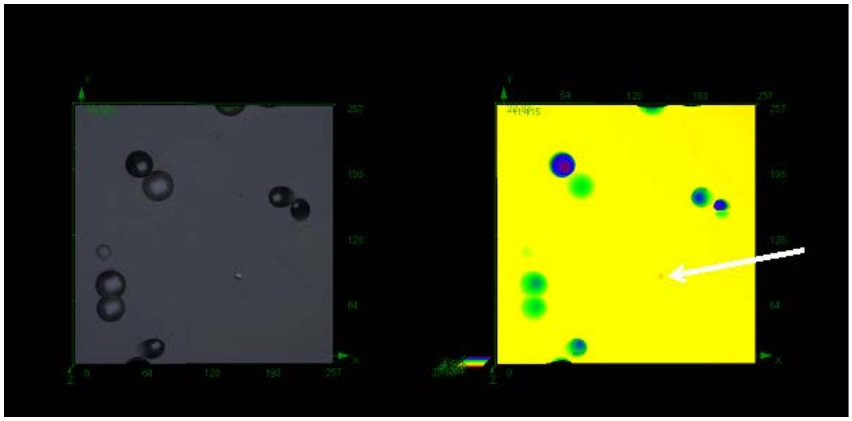

Figure 2: Equivalent 3D images showing detection of an artifact (orange, indicated with white arrow) above the level of the track in yellow. The left image shows a color view with a true color representation, whereas the right-hand image is color encoded for height with blue/violet being the deepest and red the highest level; the surface of the detector is thus in yellow.

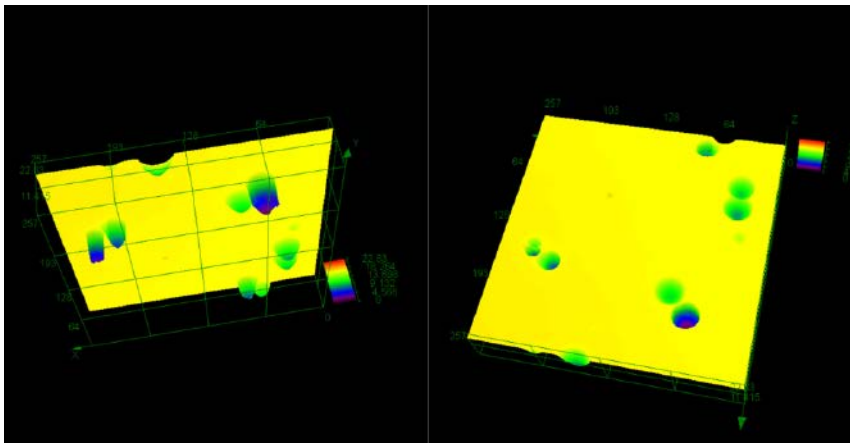

Figure 3: Alternative 3D views of the same detector with color-coded height, i.e., blue/violet being the deepest and red the highest level; the surface of the detector is yellow.

in 3D[9,12]. Suitable specimen and slide preparation are important as had helped in applying the techniques to other fields of study, such as imaging of volcanic ash particles[15].

CONCLUSIONS

Radon measurement is a key step in identifying whether levels of this colorless, odorless, radioactive gas could pose a risk to human health. A number of measurement methods are available, and one of the simplest to use is with SSNTDs. SSNTDs require no power supply and minimal maintenance and so are ideal for use around buildings as well as in remote areas. Part of our current research involves investigating if SSNTD measurement accuracy can be improved using 3D microscopy imaging compared with 2D imaging. Our results suggest that 3D imaging of radon tracks can help to enable distinguishing artifacts from real tracks; in particular 3D imaging helps to clearly identify features on the surface of the detectors that 2D imaging would not be able to easily characterize. Additionally, 3D imaging helps in the identification of multiple coalescing tracks, which are a particular issue in detectors with a high number of tracks and may have complex shapes; if the image detection is based solely on detecting round shapes, there could be a possibility for underassessment of the number of tracks. Confocal imaging enables the number of contributing tracks in coalescence to be examined closely as well as distinguishing real tracks from artifacts. Thus, 3D imaging may help in improving the accuracy of track determination in SSNTDs.

REFERENCES

[1] *Darby S., Hill D., Auvinen A., Barros-Dios JM., et al. Radon in homes and risk of lung cancer: collaborative analysis of individual data from 13 European case-control studies. BMJ. 2005 Jan 29;330(7485):223. doi: 10.1136/bmj.38308.477650.63.*

[2] *Gray A, Read S, McGale P, Darby S. Lung cancer deaths from indoor radon and the cost effectiveness and potential of policies to reduce them. BMJ. 2009 Jan 6;338:a3110. doi: 10.1136/bmj.a3110.*

[3] *ICRP, 2007. The 2007 Recommendations of the International Commission on Radiological Protection. ICRP Publication 103. Ann. ICRP 37 (2-4). https://www.icrp.org/publication.asp?id=ICRP%20Publication%20103 (accessed 31st January 2022).*

[4] *Environmental Protection Agency (EPA), 2003. EPA Assessment of Risks from Radon in Homes. Office of Radiation and Indoor Air, United States Environmental Protection Agency, EPA Report 402-R-03-003, Washington DC, USA. https://www.epa.gov/sites/default/files/2015-05/documents/402-r-03-003.pdf (accessed 31st January 2022).*

[5] *Torres-Durán, M., Ruano-Ravina, A., Parente-Lamelas, I, Leiro-Fernández, V., et al. Lung cancer in never-smokers: a case-control study in a radon-prone area (Galicia, Spain). Eur Respir J. 2014 Oct;44(4):994-1001. doi: 10.1183/09031936.00017114.*

[6] *Cliff K, Gillmore GK. (Eds.), 2001. The Radon Manual: A Guide to the Requirements for the Detection and Measurement of Natural Radon Levels. Associated Remedial Measures and Subsequent Monitoring of Results, 3rd Edition. The Radon Council, Shepperton, Middlesex.*

[7] *Health and Safety Executive, 2010. Radon in the workplace, http://www.hse.gov.uk/radiation/ionising/radon.htm (accessed 31st January 2022).*

[8] *Phillips PS, Denman AR, Crockett RGM, Gillmore G, Groves-Kirkby CJ, Woolridge A, 2004. Comparative Analysis of Weekly vs. three monthly radon measurements in dwellings. DEFRA Report No., DEFRA/RAS/03.006.*

[9] *Gillmore G, Wertheim D, Crust S. Effects of etching time on alpha tracks in solid state nuclear track detectors. Sci Total Environ. 2017 Jan 1;575:905-909. doi: 10.1016/j.scitotenv.2016.09.147.*

[10] *Petford N, Miller JA. The study of fission tracks and other crystalline defects using confocal scanning laser microscopy. Journal of Microscopy. 1993; 170: 201–212.*

[11] *Petford N, Wertheim D, Miller JA. Radon track imaging in CR-39 plastic detectors using confocal scanning laser microscopy. J Microsc. 2005 Mar;217(Pt 3):179-83. doi: 10.1111/j.1365-2818.2005.01444.x.*

[12] *Wertheim D, Gillmore G, Brown L, Petford N. A new method of imaging particle tracks in solid state nuclear track detectors. J Microsc. 2010 Jan;237(1):1-6. doi: 10.1111/j.1365-2818.2009.03314.x.*

[13] *Wertheim D, Gillmore G, Brown L, Petford N. 3-D imaging of particle tracks in solid state nuclear track detectors. Natural Hazards and Earth System Sciences. 2010; 10: 1033–1036. https://doi.org/10.5194/nhess-10-1033-2010.*

[14] *Wertheim D, Gillmore G. Application of confocal microscopy for surface and volume imaging of solid state nuclear track detectors. J Microsc. 2014 Apr;254(1):42-46. doi: 10.1111/jmi.12114.*

[15] *Wertheim D, Gillmore G, Gill I, Petford N. High resolution 3D confocal microscope imaging of volcanic ash particles. Sci Total Environ. 2017 Jul 15;590-591:838-842. doi: 10.1016/j.scitotenv.2017.02.230.*

Advanced Optical Metrology

Part VII

Additive Manufacturing: Metallurgy, Cut Analysis & Porosity

Additive Manufacturing Process Classification, Applications, Trends, Opportunities, and Challenges

Additive manufacturing (AM), also known as 3D printing, is a process of joining materials to make parts based on data coming from digital 3D models. AM is a layer-by-layer manufacturing process, which differentiates it from conventional subtractive and formative manufacturing technologies.

In industry, sector after sector is moving away from conventional production methods to AM, a technology that has been recommended for substantial research investment.[1] The global economic impact of AM is estimated to be around US$550 billion per year by 2030.[2]

Many industries—including aerospace, medical, automotive, tooling, energy, natural resources, consumer, and defense—have started to embrace the benefits of AM. Currently, there is a paradigm shift taking place—for years, AM has been used primarily for customization, prototyping, and low-volume manufacturing. However, in recent years, AM is increasingly being used for mass production and is no longer limited to product prototypes. This advancement from prototyping to serial production has created many research and development opportunities, especially for quality management and certification.

The process starts with a digital model that reflects the desired design. Preprocessing is often needed on the file depending on materials, applications, and AM processes. A proper AM process must be chosen that fulfills the material and application of interest. After the layered manufacturing is completed, post-processing may be needed to eventually reach the physical part. **Figure 1** shows the AM process chain schematically.

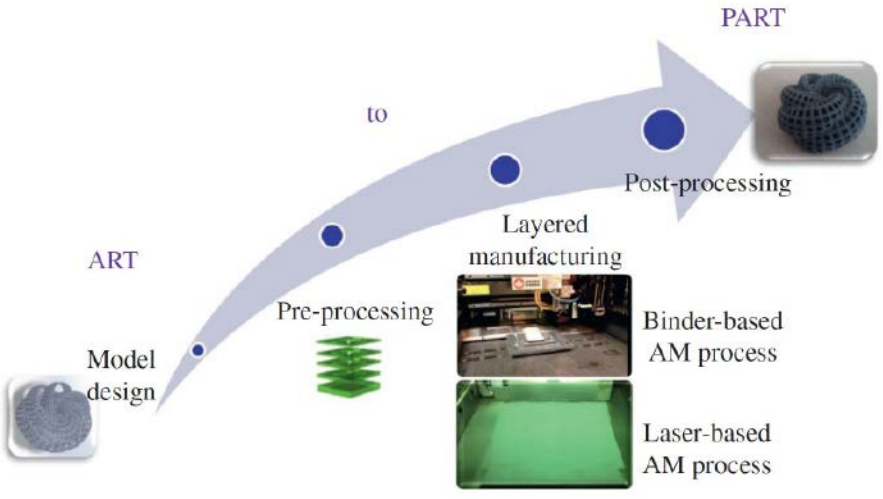

Figure 1: AM chain producing physical parts from a digital design.

Modern AM started in the 1980s with the ideas of Charles Hull, who successfully acquired a patent for his stereolithography apparatus, a process that solidifies thin layers of photopolymer using a laser beam. Following this concept, many new technologies, including direct metal laser sintering, selective laser melting, and binder jetting (BJ), were developed in the 1990s. The cost of AM machines started to decrease in the 2000s, helping make the technology more accessible and widely adopted. Knowledge of AM concepts, technology, and software are crucial elements of this paradigm shift, and efforts are underway to fully integrate them into educational platforms.

AM CLASSIFICATION

According to ASTM ISO/ASTM52900 standards, AM processes are categorized in the following techniques:

a. **Binder jetting (BJ):** a liquid bonding agent is selectively deposited to join powder materials.
b. **Directed energy deposition (DED):** focused thermal energy (e.g., laser, electron beam, or plasma arc) is used to fuse materials by melting while the raw materials are being deposited.
c. **Material extrusion:** material is selectively dispensed through a nozzle or orifice.
d. **Material jetting:** droplets of constitutive material are selectively deposited. Examples of materials include photopolymer and wax.
e. **Powder bed fusion (PBF):** thermal energy selectively fuses regions of a powder bed.
f. **Sheet lamination:** sheets of material are bonded to form a part.
g. **Vat photopolymerization:** a liquid photopolymer in a vat is selectively cured by light-activated polymerization.

The industry has adopted PBF, DED, BJ, material extrusion, material jetting, and sheet lamination as the main AM techniques for metal manufacturing, where the mentioned sequence shows the domination of each process in the market.

Figure 2: Complex parts made by AM. The spherical nest has three spheres inside.

MAIN ADVANTAGES AND CHALLENGES OF AM PROCESSES

One of the major applications of AM is the manufacture of functional prototypes. Such prototyping usually costs a fraction of conventional processes and is much faster. This accelerates the design cycle (design, test, revision, and redesign). Products, such as molds that would require more than 4–6 months to be developed, can be ready for operation in 2–3 months using AM, making AM an **on-demand, low-cost, and rapid prototyping** tool.

Many time-consuming and expensive manufacturing techniques can be superseded by **fast and efficient** metal AM for **low-volume manufacturing**. However, for mass production, AM still lags behind conventional techniques, such as casting and forging.

One of the most attractive features of AM is that it enables the **fabrication of complex shapes** that cannot be produced by any other conventional manufacturing methods (**Figure 2**). Unlike conventional methods, AM offers a platform for "design for use" rather than "design for manufacture." Parts with complex or organic geometry optimized for performance may cost less. However, attention must be given to the fact that not all complex parts and geometrical features are manufacturable by AM. Process constraints in metal AM (e.g., overhanging features) may cause issues in terms of residual stresses and defects.

Due to its topology optimization, AM allows the design and manufacture of **high-strength but lightweight structures,** where conventional manufacturing processes fail to do so. This is a highly desirable characteristic in several industries, especially energy and trans-

portation, because lighter pieces usually mean fewer transport and operating costs.

On the other hand, mechanical assemblies are common in industrial products. Parts consolidation offered by AM provides many advantages due to the reduction of the number of individual parts needed to be designed, manufactured, and assembled to form the final system. AM even removes the need for assembly in some cases. Several applications of AM have obvious benefits for fostering product performance through lightweight/consolidation without compromising high strength, including the optimization of heat sinks to dissipate heat flux better, fluid flow to minimize drag forces, and energy absorption to minimize energy consumption.

The capability to **create multiphase materials** with gradual variations in composition is another important feature of AM. The material composition can gradually be altered to obtain the desired functionality. AM also enables the development of **functionally graded structures** with a single-phase material, where the density gradually changes through the addition of cellular/lattice structures, and embedding objects (e.g., sensors) within structures.

Finally, **prosthetics and implants customized and tailored for specific patients** are already being manufactured using AM. Many developments in the fabrication of soft tissues for the fabrication of organs, as well as a host of other personalized medical items and sensors, are underway. It has been proven that the use of precise AM replicas can significantly reduce surgery time for many patients.

MARKET SIZE AND FORECAST

The worldwide market for AM hardware, software, materials, and services is anticipated to exceed US$40 billion by 2027. Moreover, metal AM is one of the fastest-growing segments in the world. The annual growth in the revenue of metal AM materials has been higher than that of photopolymers, polymer powders, and filaments between 2013 and 2018.[3] The systems that were dominant in the market of metal AM include PBF (mainly with a laser heat source) and powder-fed laser DED as well as new technologies, such as BJ and cold spray. Most material sales include metal powders and wire feedstock.

In terms of market share, the aerospace industry covers the largest share, followed by the medical sector.[4] The aerospace industry profits from turbines, helicopters, and jet-engine component fabrication as well as new space applications such as rocket engines, attracting large venture capital worldwide, especially in the United States.

METAL ADDITIVE MANUFACTURING APPLICATIONS

AM processes began adapting to different sectors as early as 1990, as shown in the timeline in **Figure 3.**

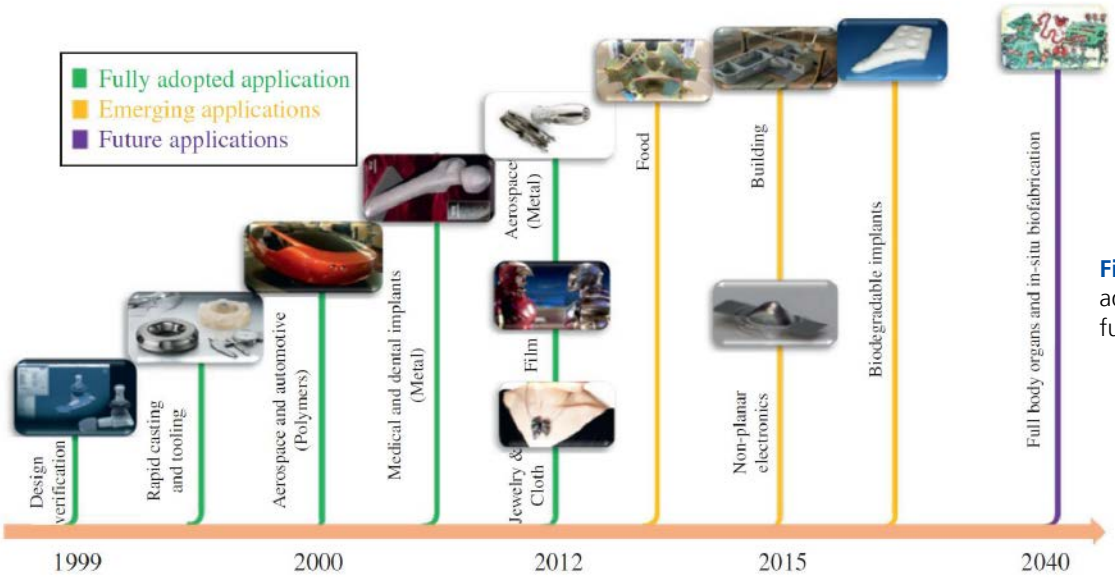

Figure 3: Timeline for adopted, emerging, and future applications of AM.

Figure 4 schematically shows three classes of AM processes (PBF, BJ, and DED) widely employed in metal manufacturing. For large-size components, the powder-fed and wire-fed DED processes are the most applicable, where the printed part may not require high resolution with complex features. In contrast, PBF and BJ can be used for smaller metal parts with higher resolution and complexity. In contrast, the density of parts produced by DED is almost perfect, but in BJ, the density cannot be high. PBF is a middle process that can produce relatively large parts up to 50 cm with high resolution and high complexity using the current state of PBF technology since 2020.

The **medical industry** was one of the early adopters of AM for the fabrication of not only metal parts, but also ceramics, polymers, and functionally graded materials. Metal AM has been used to produce medical devices and tools, surgery guides and prototypes, implants, prosthetics, orthotics, dental implants, crowns, and bridges from biocompatible metals, such as various titanium, tantalum, and nickel alloys. Due to the high precision required to produce medical parts, PBF processes are the dominant AM technique in this sector. In addition, porosity and selective stiffness are of major importance to medical devices. Thus, BJ is playing an important role as it can produce implants with controlled porosity.

AM is also particularly attractive in the **aerospace and defense industries** because the lower material waste, light weight, reduced need for assembly through component consolidation, and the capability to produce highly intricate and complex parts contribute to cost savings and lower fuel consumption thanks to a lower level of certification required for fewer parts.[5]

In space applications, the race is even faster paced. In 2015, the first-ever communications satellite with a design life of 16 years and weight of 4.7 metric tons (named TurkmenAlem52E) with an aluminum 3D printed antenna horn mounting strut was launched by SpaceX. On the rocket engine applications, major activities are underway by SpaceX, NASA, and Aerojet Rocketdyne to adopt AM for rocket engine components because the qualification testing and heritage could be transferrable in many situations.

DED technology is also used in the aerospace and defense industries for repairing and refurbishing parts. It is a particularly important application given the long life cycle of aviation systems and the high cost and long lead-time associated with the replacement of the parts.

Additionally, AM processes can enable the manufacture of complex-shaped metal and plastic antennas from different alloys and dielectrics, opening up tremendous opportunities for the **communication industry.** Advanced AM-made RF antenna structures have the potential to revolutionize the design, supply, and sustainment of such devices. An AM design process can be fully integrated into the antenna design platforms to support not only customization but also antenna performance enhancement in the field.

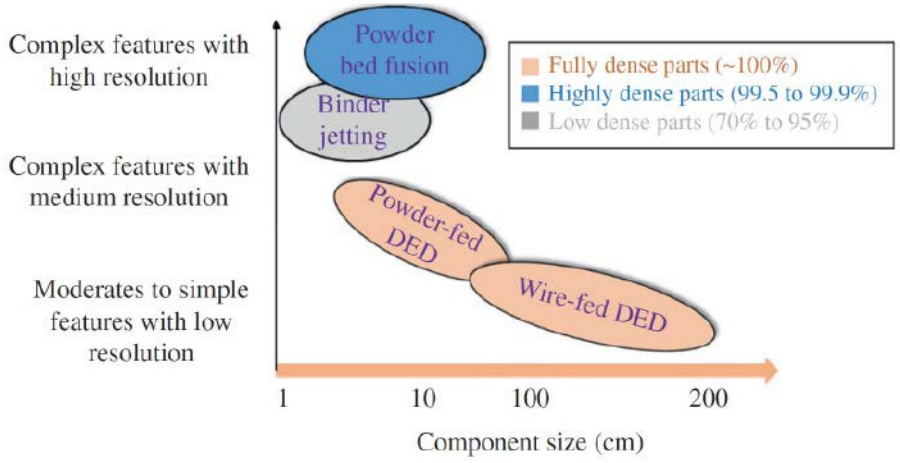

Figure 4: Most important metal AM processes versus part size, complexity, and resolution needed.

The rapid prototyping feature of AM provides a key step in the design verification to attain innovative solutions in the **energy and resources industries.** AM has also become an increasingly mainstream operation to fabricate end-use functional parts at a low-volume level. When AM-made parts need tooling, it can be used to make lightweight structures with complex internal features. Thus, the next generation of energy, oil, and gas components have substantially benefited from AM features, especially parts that need to meet performance and environmental standards. Dense, corrosive-resistant, and high-strength components can be developed using DED for demands in the energy and resources industries. One crucial application of AM in these industries is the development of spare parts.

The application of metal AM in the **automotive industry** has been in the creation of prototypes, heritage parts for obsolete models, and spare parts and tools. Even though the automotive industry is not yet using AM directly for the production of final metal parts in serial production vehicles, a new trend for reaching that goal has already started. Many automotive companies such as Volkswagen, BMW Group, Porsche, General Motors (GM), and Toyota have entered the AM market either through investing in the improvement of their in-house AM capabilities or through making alliances with machine developers, 3D software companies, AM material producers, or research centers to expedite the adoption of metal AM.

Finally, one of the obvious applications of metal AM is in **tooling** and **mold production** for other industries, such as medical, aerospace, and automotive. In the consumer products sector, the promise of mass customization drives the gradually increasing usage of metal AM in various consumer products, such as decorative objects, jewelry, custom sports gear, and structures (bicycle frames). The design freeform, material graded structures, light weight, and fast design-to-market cycle offered by AM are predicted to have revolutionary effects on industrial and personal products.

ECONOMIC AND ENVIRONMENTAL BENEFITS AND SOCIETAL IMPACT

AM technologies are usually greener than conventional methods because there is less material wasted, and there may be up to 50% energy savings during part production.[6]

Moreover, metal-based AM technologies virtually eliminate machining and the subsequent need for toxic cutting fluids as well as costly pollutants that are challenging to dispose of and have a negative environmental impact.[7] In addition, AM parts can reduce weight in the range of 50–100 kg per aircraft, significantly reducing fuel costs; every kilogram removed from a fleet of 400 commercial jet-liners leads to an annual fuel consumption reduction of 60,000 L (15,850 gallons).

When machining a block of material for simple geometries would be preferable, AM will be much more appealing for making parts with hollow shells, lattices, features with complex curvatures, and internal conformal channels. Thus, AM's sustainability is correlating with geometic complexity. It is important to do a thorough analysis of the sustainability of metal AM upfront to understand the benefit of the process for a specific geometry. In addition, life cycle assessment studies are needed to quantify the environmental impact of AM more precisely. The full product life cycle from production to overhaul must be included in the analysis.

AM TRENDS, CHALLENGES, AND OPPORTUNITIES

In addition to new business models being developed by various industries, there are several challenges that the AM community must overcome:

a. **Qualified materials:** one of the major challenges in the field of metals and metal alloys is the number of powders that have been qualified for use with metal AM systems, including laser, electron beam, and binder-based AM processes.
b. **Speed and productivity:** further process development is needed to enhance surface quality during AM processes to improve speed and productivity.
c. **Repeatability and quality assurance:** AM is sensitive to both environmental and process disturbances, from fluctuating temperature and humidity levels to non-uniform powder sizes. Full control of the process and surrounding environment is difficult, so there's a focus on solutions that employ sensors to monitor conditions and quality control algorithms to automatically adjust process parameters—such as laser power and process speed—through closed-loop control systems to compensate for any disturbances.

d. **Industry-wide standards:** the absence of such standards may hinder the continued adoption of AM for industrial applications.
e. **End-to-end workflow, integration, and automation:** many customers are reluctant to accept a new material/process/design or technology that does not have history in their applications. To minimize industry hesitation on AM adoption, an effective end-to-end workflow must be developed that is simple yet integrated and automated. Currently, the lack of digital infrastructure is a major obstacle to creating effective automated workflows for the AM industry. Automated AM is part of the factory of tomorrow, a forefront of the ongoing industrial revolution within the industry 4.0 approach.
f. **Software limitations:** commercially available software for designing AM parts, support structure development, and interfacing with AM machines have limitations in assessing the feasibility of prints and identifying process constraints. The current software and hardware still need more improvements to facilitate timely communication in AM.
g. **Initial financial investments:** the AM ecosystem covers software, materials, experts, post-processing equipment, certifications, as well as training for employees. This investment can be large, hindering companies from embracing this technology effectively.
h. **Security:** AM has promoted globally distributed manufacturing, and the existence of hackers is a reality. They can tweak the AM designs to create intentional defects that are not detectable but may have catastrophic consequences when used in actual systems.
i. **Skillsets gap:** there is a limited workforce of qualified personnel that can develop an entry strategy for companies that want to embrace AM. Overall, learning about the capabilities and limitations of metal AM will aid companies in developing meaningful and successful applications for the technology. Promoting AM consultancies is another way to foster knowledge transfer. In addition, AM conferences and webinars are playing critical roles to fill the skillsets gap.

As these challenges are overcome, AM will transform the entire manufacturing sector over the next 10 to 15 years. With AM, designers do not design for manufacturing anymore—they design for end-users. This is a paradigm shift. Finally, it is reported that AM would be able to reduce the capital required to reach a minimum manufacturing volume.[8]

REFERENCES:

[1] *C. A. D. Competitive, A. In, and A. Manufacturing, "Executive Office of the President President ' s Council of Advisors on Science and Technology," 2012. [Online]. Available: https://www.energy.gov/sites/prod/files/2013/11/f4/pcast_annex1_july2012.pdf*

[2] *J. Bromberger and K. Richard, "Additive manufacturing: A long-term game changer for manufacturers," McKinsey Co., 2017. [Online]. Available: https://www.mckinsey.com/business-functions/operations/our-insights/additive-manufacturing-a-long-term-game-changer-for-manufacturers*

[3] *T. Wohlers, Wohlers Report 2020: 3D printing and additive manufacturing state of the industry, Wohlers As. Wohlers Associates, 2020. [Online]. Available: https://www.wohlersassociates.com/2020report.htm*

[4] *"AMPOIWERreport, 'Metal additive manufacturing suppliers predict a market size growth of 27.9%.'" [Online]. Available: https://additive-manufacturing-report.com/additive-manufacturing-market*

[5] *J. O. Milewski, Additive Manufacturing of Metals, vol. 258. Cham: Springer International Publishing, 2017. doi: 10.1007/978-3-319-58205-4.*

[6] *DOE-ADVANCED MANUFACTURING OFFICE, "Additive Manufacturing : Pursuing the Promise," Doe, p. 2, 2011, [Online]. Available: https://www1.eere.energy.gov/manufacturing/pdfs/additive_manufacturing.pdf*

[7] *N. Diaz, M. Helu, S. Jayanathan, Yifen Chen, A. Horvath, and D. Dornfeld, "Environmental analysis of milling machine tool use in various manufacturing environments," in Proceedings of the 2010 IEEE International Symposium on Sustainable Systems and Technology, May 2010, pp. 1–6. doi: 10.1109/ISSST.2010.5507763.*

[8] *B. Mcgrath, "3D opportunity for life cycle assessments. Additive manufacturing branches out," Deloitte Univ. Press, p. 20, 2015, [Online]. Available: https://www2.deloitte.com/content/dam/insights/us/articles/additive-manufacturing-in-lca-analysis/DUP_719-3D-opportunity-life-cycle_MASTER.pdf*

01 Microstructural Porosity in Metal Parts Fabricated by Powder Bed Fusion

A. Sola, A. Nouri

ABSTRACT

Metal additive manufacturing (AM) is a manufacturing technique that can build complex metal parts layer by layer. Powder bed fusion (PBF) is one of the most common AM techniques. However, PBF induces microstructural defects that can adversely affect the performance of the manufactured components. The present article provides an overview of the formation mechanisms of pores in AM metals and some emerging techniques for the detection and quantification of pores.

INTRODUCTION

Additive manufacturing (AM) is the most appropriate definition that reflects the use of the layer-by-layer addition of material to build up 3D objects. The AM fabrication process includes two basic steps: coating and consolidating. The coating step requires applying a new layer of material to the existing working surface. While the consolidating step implies printing the newly applied layer to the underlying layer using sintering, melting, polymerizing, or other processes. The consolidating step is carried out by an energy source, which can be a light beam or an electron beam. The two steps, coating and consolidating, are repeated layer by layer until the full part is produced.[1]

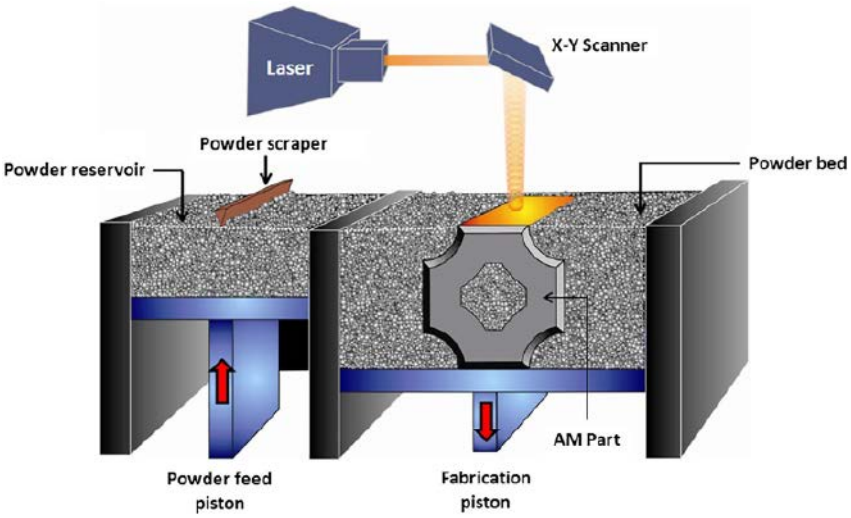

Figure 1: Schematic representation of laser-based powder bed fusion process and equipment.

AM offers unmatched flexibility with respect to the part geometry;[1–5] however, surface roughness and waviness of AM parts are one of the main disadvantages of these methods that must be mitigated through surface finishing technology in order to enhance component performance.

Powder bed fusion (PBF) is one of the most commonly used AM techniques. PBF requires powdered feedstock that is sequentially processed in thin layers and solidified either by a laser beam (L-PBF) or by an electron beam (EBM).[6]

A schematic illustration of an L-PBF instrument setup is shown in **Figure 1.** Upon moving down the build platform, a new layer of powder is deposited on top of the pre-

vious layer, and the procedure is repeated until the complete object is produced. The energy conveyed by the laser beam is high enough to also reach the previously consolidated layers that are partially re-melted or re-sintered together with the new powder. In this way, interlayer bonding is obtained.[7]

With respect to other AM methods, L-PBF takes advantage of processing a wide variety of powder materials.[7,8] Powders that are not likely to melt or sinter can also be processed via L-PBF by adding a sacrificial binder material, typically a polymer binder. The binder is removed afterward using thermal treatment (debinding); however, a further post-processing step is required to reduce the residual porosity, which can be as high as 60%. Thus, almost fully dense parts can be obtained by either post-processing via furnace sintering, hot isostatic pressing (HIP), infiltration with a polymer, or with a low-melting-point metal[7]. On the other hand, EBM is only applicable to conductive materials (i.e., metals) and is used preferentially for titanium alloys[9].

Regarding the disadvantages, pores and voids are reported to be the most frequently occurring defects in selective laser sintering (SLS).[10] In addition, a variety of microstructural inhomogeneities may also be present in PBF parts, including impurities (inclusions, contaminations, and metal oxides), not melted or partially melted particles, and anomalous grain growth and crystallographic textures.

In this article, the term "pore" is used to refer to microstructural pores, defined as residual voids and defects in the microstructure of the built part.[46] They are formed unintentionally and must be avoided or minimized to limit their adverse effect on mechanical properties and to ensure the consistency of AM parts.

FORMATION MECHANISMS OF PORES IN DIFFERENT METAL PARTS

Steel and other ferrous alloys

Khairallah et al.[11,12] proposed a model to simulate the melt-flow mechanisms and their impact on the microstructure of 316L stainless steel processed by L-PBF. According to the model, as the laser scans over the powder bed, an indentation is created and subsequently collapsed due to an abrupt reversal of the melt-flow velocity-vector field. This sudden breakdown of the depression favors the entrapment of gas bubbles at the bottom of the track. The abrupt change in the velocity-vector field also results in the formation of a vortex that further promotes the development of bubbles and the eventual coalescence of such bubbles into a larger pore. In L-PBF, if the balance of the laser power, scan speed, and beam size exceeds a threshold value, the melting mode is controlled by evaporation (keyhole mode). The resulting melt pool is no longer semicircular, and the laser beam can affect the metal down to a deeper depth than in the more-common conduction mode. Due to the repeated formation and collapse of vapor cavities, a sequence of voids is created along the laser beam path.[13,14] This model is able to explain the formation of additional pores other than keyholes. In the transition zone of the melt track, occasionally, the quick movement of the laser beam does not allow for the complete melting of the particles at the rim of the track. Particles that are not properly melted cannot be incorporated into the melt pool and the voids between them cannot be filled.

Choo *et al.*[15] fabricated 316L stainless steel parts by L-PBF under decreasing power levels. As a consequence of decreasing laser power, porosity was initially increased due to an increase in the number of pores, whereas the average pore volume remained unchanged. With a further decrease in laser power, porosity continued to increase due to the increase of the average pore size, whereas the number of pores slightly decreased. In fact, when the energy input became insufficient to enable complete melting of the feedstock or to induce an effective overlap between adjacent scan tracks, the frequency of pores and the lack of fusion defects progressively increased. In the end, pores and defects could link and coalesce, resulting in a reduced number of large and flat pores that were preferentially perpendicular to the growth direction. Moreover, independently of the laser power, large spherical pores with keyhole geometry were preferentially distributed at the edge of the samples, where the scan tracks came to an end or changed direction due to the scanning strategy as previously observed also by Khairallah *et al.*[11,12]

Åsberg *et al.*[16] processed a tool made with steel H13 using L-PBF and investigated the effect of different thermal treatments on residual porosity. The level of porosity was higher near the edges than in the core of the cross-section. Such subsurface porosity could be associated with the change from core scanning strategy to contour scan-

ning strategy, where the speed and direction of the laser beam are changed.[11,12,15] Stress relieving heat treatment alone or combined with standard hardening and tempering treatment did not cause any change in porosity, whereas HIP induced sensible densification by closing the lack of fusion defects and reducing the size of gas pores.[16]

Morrow *et al.*[17] investigated 304L and 316L stainless steel gas atomized powders and underlined the importance of the chemical composition and morphological aspects of feedstock powders. Furthermore, the presence of nanoscale particles that cause submicron precipitates in the finished parts and gas entrapment is likely to outlive L-PBF processing.

Titanium and its alloys

Gu *et al.*[18] analyzed the effect of different scanning speeds on the microstructure and related mechanical properties of commercially pure titanium (cp-Ti) parts produced by SLM. Considering the mechanical behavior, the SLM parts processed at low scan speed exhibited relatively low values of hardness and wear resistance. The limited performance of these samples was related to the presence of thermal cracks, and also to the development of coarsened grains. For a very high scan speed, the formation of a refined martensitic phase was favored, but the mechanical properties were equally diminished due to the presence of balling-induced large defects.

Cunningham *et al.*[19] applied advanced synchrotron-based X-ray microtomography to analyze the presence of pores in EBM Ti-6Al-4V parts both in the as-built and post-processed HIP state. As-built parts were affected by spherical and irregular pores. The presence of pores in the feedstock powder was shown to correspond to the presence of spherical pores in the as-built components. Alternatively, irregular pores were mainly formed due to a lack of fusion. After the HIP treatment, they observed that only the irregular pores caused by lack of fusion were eliminated, while the spherical pores that were initially formed by gas entrapment in the feedstock powder survived.

Thijs *et al.*[4] performed a systematic analysis of the effect of processing parameters and scanning strategy on the microstructure of Ti-6Al-4V parts processed by SLM. When the laser scanning velocity deviated from its optimal value, the part density suddenly dropped due to the formation of large, elongated pores alongside the scanning direction.[4]

Qiu *et al.*[20] reported that when the layer thickness was kept constant with a relatively low value (= 20 µm in their study), the porosity of Ti-6Al-4V parts processed by SLM became lower with increasing laser power and scan speed. However, if the scan speed is excessively increased and the laser power is not adjusted accordingly, the pores are expected to develop due to the low energy density and the resulting lack of fusion. The observed porosity could be closed almost completely by the HIP. However, the complete elimination of porosity after HIP was not the only reason for the improvement in ductility and loss in strength since the martensitic phase originally present in the as-built part was also transformed into α and βphases.[20]

Aluminum alloys

Processing Al alloys pose additional problems with respect to steel and Ti alloys, due to the strong reflectivity of Al-based powder, its high thermal conductivity that quickly disperses heat from the melt pool to the previously consolidated layers, and the possible formation of oxides on top of the melt pool[21]. As a result, even if almost fully dense Al-based parts can be produced by SLM, various mechanisms can induce the formation of voids[2,3,5,21]. Some of these mechanisms are related to the feedstock powder and some are related to the processing conditions.

Weingarten *et al.*[5] found that any attempt to increase the build-up rate by increasing the laser beam diameter or the powder layer thickness can cause a density loss as high as 10%. This is mainly a consequence of the gas porosity that remains entrapped in the metal due to the fast processing condition and rapid cooling.

The importance of surface moisture was also emphasized in A357 parts processed by SLM.[22,23] The existence of very small spherical pores with a diameter smaller than 5 µm was equally attributed to the presence of moisture on the surface of feedstock particles and the reactions with Al. Despite the initial small size of the hydrogen-rich pores, they were sensibly enlarged during high-temperature solution heat treatment.

According to Tang and Pistorius,[24] the fatigue life of AlSi10Mg parts produced by SLM is drastically reduced by pores associated with small oxide fragments that form from the Al oxide film on the feedstock powder. Unlike the Al alloy, the Al oxide film does not melt during SLM processing. Since the wettability of melted Al-Si alloys toward Al oxide is very

low,[25] the melted metal inside the particle separates from the native oxide film on the surface. The oxide film is very thin and brittle and is likely to break and generate submicron fragments.[24] Tang and Pistorius[24] also observed a correlation between large pores and coarse oxide particles and fragments. Since the melted Al-Si alloy is not able to wet oxides, the presence of large oxide particles adversely affects the consolidation mechanisms. Such large defects were concentrated on the upper part of the constructs, suggesting that oxide particles are preferentially developed close to the top surface or are moved up there through vaporization and spatter mechanisms.[24]

Similar to other metal AM parts, in Al alloy components the presence of not melted particles and oxides is also expected to cause porosity with a random geometry.[21] Thijs *et al.*[21] observed large and elongated keyhole pores that were preferentially located near the edge of parts (i.e., at the start/end points of the scan tracks) where heat is likely to accumulate.

Coherent results were presented by Romano *et al.*,[26] who underlined the combined effect of size and location of pores. As a rule, a surface defect is more detrimental to fatigue life than an embedded pore with the same size and shape. In fact, a surface defect was proven to cause a 30% larger stress intensity factor than an embedded defect.

Nickel-chromium (Ni-Cr) superalloys

Sheridan *et al.*[27] analyzed the effect of scan strategy (movement pattern of the laser beam) and processing parameters on the formation of porosity in Inconel 718 parts processed by SLM. The continuous scan strategy (a continuous meandering movement of the laser beam) resulted in a lower average density of pores and a lower size distribution of pore population with respect to the striped and island-based scan strategies. An appropriate setting of the processing parameters, including laser power, scan speed, hatch spacing, and layer thickness allowed to reach fully dense parts. Notably, the potential effect of pores on fatigue life depends on their relative distance from each other, their distance to the surface, and their location with respect to crystallographic features, such as grain boundaries and triple or quadruple joints.[28]

POROSITY DETECTION AND MEASUREMENT

Two different approaches to porosity analysis are proposed in the literature. The first one is a post-processing strategy (detecting, measuring, and possibly analyzing the existing pores in the finished part). Alternatively, the development of pores can be evaluated in situ, directly during manufacturing; in this way, if problems arise during manufacturing, the printing parameters can be corrected at an early stage, typically through closed-loop repairing tactics.[29]

Post-processing detection of porosity

Porosity, P, has often been estimated from the measurement of density, through the equation:

$$P=(1-\frac{\rho\_measured}{\rho\_theoretical})100 \quad (1)$$

Where $\rho_{measured}$ is the measured density of the part and $\rho_{theoretical}$ is the theoretical density of the fully dense material. This technique is not able to account for those cavities that are filled with not melted particles. In addition, if Archimedes' principle is used, the density measurement is significantly affected by the surface roughness.[6, 30] Moreover, unlike conventional wrought materials, $\rho_{theoretical}$ is not certain for powders and parts in AM, since their exact chemical composition can be altered by feedstock recycling and possible preferential evaporation of elements during alloying processing.[31] This method may be used to quantify the volume fraction of pores (within the limits previously discussed), but it is not able to provide any information about the size, morphology, and distribution of pores within the part.

Cut and polished cross-sections can be used for direct observation under optical and electron microscopes. However, the metallographic preparation is likely to introduce artifacts and significant morphological changes. Moreover, the result may be biased by several parameters that are arbitrarily chosen. Automatic image analysis strategies are nowadays the focus of research in order to overcome the arbitrariness associated with human error.[31] Micro-computed tomography (micro-CT) is a nondestructive technique that preserves the integrity of tested samples and enables the repeated execution of the test on the same part at different stages of its processing history, for example, before and after HIP.[15, 32, 33] The main advantage of micro-CT is the possibility of examining the shape of pores and their spatial distribution in three dimensions. However, high-quality images can only be obtained

if two conditions are satisfied. First, the X-ray absorption of the constituent phases in the sample must be different. Next, the transmitted X-rays must preserve at least 10% of their original intensity. To this aim, if necessary, smaller samples are to be cut from the originally built part. In this case, micro-CT can no longer be considered a non-destructive technique.[15,34] Furthermore, the accuracy of pore detection is affected by the resolution limit of the tomography equipment, which depends on the voxel size[31] and on the thresholding strategy applied to separate noise and the objects that should be identified as pores.[33]

In situ monitoring of pore formation

Process signatures (critical quantities that are measured in situ) are dynamic quantities that relate to the powder during heating, melting/sintering, and solidification. They can be grouped into either observable signatures or derived signatures.[12]

Most of the available in situ monitoring systems are based on contactless temperature measurement, imaging in the visible range, and low-coherence interferometric imaging. Sensors can be aligned along the optical path of the laser beam (i.e., coaxial configurations); otherwise, they work at a given angle of view outside the optical path (i.e., off-axial configurations). Coaxial configurations are only compatible with L-PBF because the electron magnetic coils that are necessary to direct the electron beam in EBM do not permit the presence of coaxial sensors.[29]

The progress in sensing equipment must be supported by adequate computational means to store and manage the huge amount of data acquired in situ.[29] Effective feedback and reactive or corrective systems are still the subjects of much scientific research.[29]

DISCUSSION

Recently, Zhang *et al.*[35] reviewed pores and other defects in SLM and classified them into three groups: (a) porosities, which are mainly spherical and less than 100 μm; (b) melting-related defects, which are characterized by irregular shape, and (c) cracks, which are the result of quick cooling, sharp thermal gradients and thermal stresses.[35] A schematic representation of these pores is seen in **Figure 2.**

Defect formation mechanisms can be broadly categorized into equipment-related, powder-related, and processing-related defect formations:

a. Equipment-related defect formation: it is evident that the high scanner deflection angles at the edges of the baseplate induce an elliptical distortion of the laser spot, which may cause porosity and lack of fusion in L-PBF.[29] Ferrar *et al.*[36] also reported on the possible formation of pores associated with the inefficient flow of the inert gas through the build chamber. For example, the equilibrium partial pressure of oxygen at the melting point of Ti should be less than 10^{-16} atm to prevent oxidation, which is infeasible from a practical point of view. As a consequence, a certain degree of defectiveness, which includes balling and lack of interlayer bonding, is inevitable.[25]

b. Powder-related defect formation: the powder flowability affects the feeding efficiency, whereas its compressibility determines the particle density within each newly applied powder layer.[37] Absorbed soluble gasses (especially, hydrogen) are also potentially harmful because they can be released during AM processing. Surface-absorbed moisture is believed to be a potential source for hydrogen-related defects in Al alloy parts. Pores and spatter formation are also facilitated by feedstock powder oxidation because

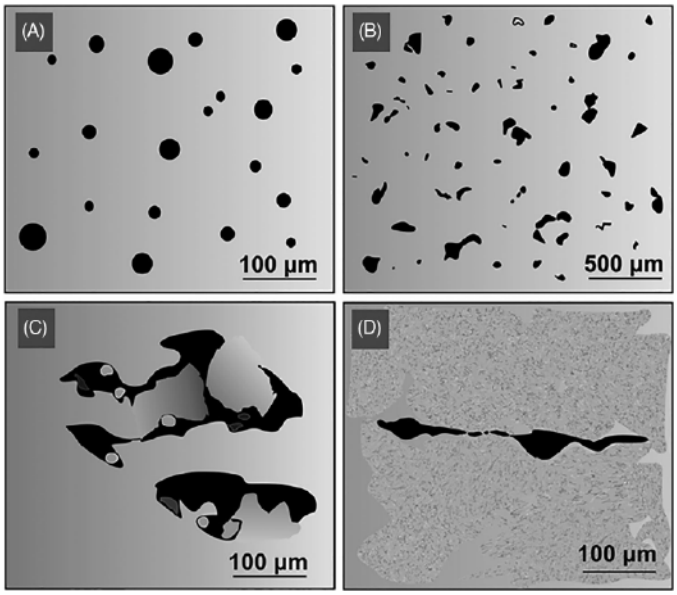

Figure 2: Characteristic pores in laser-based powder bed fusion parts: (A) entrapped gas porosity; (B) incomplete melting-induced porosity; (C) lack of fusion with not melted particles inside large irregular pores and (D) cracks.

of powder handling, reuse, or prolonged storage in an unsuitable environment.[38]

c. Process-related defect formation: if the laser power is too low or if the scan speed is too high, lack of fusion results in not melted particles, and hence the newly added powder layers become increasingly uneven with irregular cavities filled with loose or inadequately fused particles.[9, 39, 40] If the laser power is too high or the scan speed is too low, conversely, keyholing is highly probable.[11, 12] The powder layer thickness is also a key parameter: if the layers are too thin, overheating may occur; on the other hand, if the layers are too thick, interlayer bonding is not effective.[9, 40] Thermal residual stresses are another source of microstructural defects. The thermal mismatch generates residual stresses that cause cracking.[41] Although the appropriate selection of the processing parameters results in almost fully dense parts (with densities exceeding 99.5%), the surviving pores unavoidably impair the mechanical properties of AM parts, especially under tensile and fatigue loading.[41]

Some post-processing treatments have been proposed to reduce the residual porosity in AM parts. While HIP appears to be the most effective treatment, it fails to eliminate trapped gas bubbles.[19] Additionally, the high temperatures reached during HIP may result in some adverse effects, such as grain coarsening or phase transformation.[42, 43] Surface finishing is often applied to reduce surface roughness and possibly to reduce superficial defects that are likely to diminish fatigue resistance. However, in the case of subsurface porosities, surface finishing brings such defects to the surface and these emerged pores become potential crack initiation sites for fatigue failure.[44]

According to the available literature, three main hurdles are yet to be overcome to control and minimize the formation of pores in PBF parts:

1. First, the determination of the pore volume fraction is the minimum requirement. However, the morphology, size, and distribution of pores are also playing an important role in several applications.

2. After identifying the most appropriate characterization technique, the sensitivity of the available instrumentation should be considered with respect to the critical size of the defect for a given application.

3. Additionally, since the unexpected appearance of pores may be a sign of production anomalies, particular attention should be paid to in situ detection systems. The detection of potential anomalies is particularly challenging since AM methods inevitably imply stochastic fluctuations and are often applied to the production of one-of-a-kind parts, which do not have standards for comparison purposes.[6,45]

CONCLUSIONS

Despite the stochastic nature of PBF techniques, a survey of the available literature reveals that some recurrent mechanisms cause the development of microstructural pores. Basically, pores can outlive into the finished parts from the feedstock powder through the gas entrapment during the gas atomization process. Pores may also have originated from the presence of moisture on the surface of the feedstock particles. Alternatively, pores can be originated from an improper setting of the processing parameters.

Moreover, additional process conditions such as the scan strategy may affect the porosity of the finished part. The pre-treatment of the feedstock to remove the surface moisture, as well as the optimization of the process parameters, can be applied to reach density values higher than 99.5%. The residual presence of pores significantly affects the mechanical behavior, especially fatigue life, of the finished parts. As a consequence, the debate is now open in the literature on two basic requirements, namely a further reduction of the residual porosity and the development of appropriate means to detect the formation of pores and microstructural defects in situ. The achievement of these two goals can significantly contribute to the future industrial development and advancement of PBF.

REFERENCES:

[1] *Petrovic, V. et al. Additive layered manufacturing: sectors of industrial application shown through case studies. Int. J. Prod. Res. 49, 1061–1079 (2011).*

[2] *Buchbinder, D., Schleifenbaum, H., Heidrich, S., Meiners, W. & Bültmann, J. High Power Selective Laser Melting (HP SLM) of Aluminum Parts. Phys. Procedia 12, 271–278 (2011).*

[3] *Aboulkhair, N. T., Everitt, N. M., Ashcroft, I. & Tuck, C. Reducing porosity in AlSi10Mg parts processed by selective laser melting. Addit. Manuf. 1–4, 77–86 (2014).*

[4] *Thijs, L., Verhaeghe, F., Craeghs, T., Humbeeck, J. Van & Kruth, J.-P. A study of the microstructural evolution during selective laser melting of Ti–6Al–4V. Acta Mater. 58, 3303–3312 (2010).*

[5] *Weingarten, C. et al. Formation and reduction of hydrogen porosity during selective laser melting of AlSi10Mg. J. Mater. Process. Technol. 221, 112–120 (2015).*

[6] *Gibson, I., Rosen, D. & Stucker, B. Additive Manufacturing Technologies. (Springer New York, 2015). doi:10.1007/978-1-4939-2113-3.*

[7] *Kruth, J. P., Wang, X., Laoui, T. & Froyen, L. Lasers and materials in selective laser sintering. Assem. Autom. 23, 357–371 (2003).*

[8] *Zhang, D. et al. Metal Alloys for Fusion-Based Additive Manufacturing. Adv. Eng. Mater. 20, 1700952 (2018).*

[9] *Gong, H. et al. Influence of defects on mechanical properties of Ti–6Al–4V components produced by selective laser melting and electron beam melting. Mater. Des. 86, 545–554 (2015).*

[10] *Malekipour, E. & El-Mounayri, H. Common defects and contributing parameters in powder bed fusion AM process and their classification for online monitoring and control: a review. Int. J. Adv. Manuf. Technol. 95, 527–550 (2018).*

[11] *Khairallah, S. A., Anderson, A. T., Rubenchik, A. & King, W. E. Laser powder-bed fusion additive manufacturing: Physics of complex melt flow and formation mechanisms of pores, spatter, and denudation zones. Acta Mater. 108, 36–45 (2016).*

[12] *Badiru, A. B., Valencia, V. V & Liu, D. Additive Manufacturing Handbook: Product Development for the Defense Industry. (CRC Press, 2017).*

[13] *King, W. E. et al. Observation of keyhole-mode laser melting in laser powder-bed fusion additive manufacturing. J. Mater. Process. Technol. 214, 2915–2925 (2014).*

[14] *Shrestha, S., Starr, T. & Chou, K. Porosity Analysis in Metal Additive Manufacturing by Micro-CT. in Volume 2: Advanced Manufacturing (American Society of Mechanical Engineers, 2018). doi:10.1115/IMECE2018-87897.*

[15] *Choo, H. et al. Effect of laser power on defect, texture, and microstructure of a laser powder bed fusion processed 316L stainless steel. Mater. Des. 164, 107534 (2019).*

[16] *Åsberg, M., Fredriksson, G., Hatami, S., Fredriksson, W. & Krakhmalev, P. Influence of post treatment on microstructure, porosity and mechanical properties of additive manufactured H13 tool steel. Mater. Sci. Eng. A 742, 584–589 (2019).*

[17] *Morrow, B. M. et al. Impact of Defects in Powder Feedstock Materials on Microstructure of 304L and 316L Stainless Steel Produced by Additive Manufacturing. Metall. Mater. Trans. A 49, 3637–3650 (2018).*

[18] *Gu, D. et al. Densification behavior, microstructure evolution, and wear performance of selective laser melting processed commercially pure titanium. Acta Mater. 60, 3849–3860 (2012).*

[19] *Cunningham, R. et al. Analyzing the effects of powder and post-processing on porosity and properties of electron beam melted Ti-6Al-4V. Mater. Res. Lett. 5, 516–525 (2017).*

[20] *Qiu, C. et al. Influence of processing conditions on strut structure and compressive properties of cellular lattice structures fabricated by selective laser melting. Mater. Sci. Eng. A 628, 188–197 (2015).*

[21] *Thijs, L., Kempen, K., Kruth, J.-P. & Van Humbeeck, J. Fine-structured aluminium products with controllable texture by selective laser melting of pre-alloyed AlSi10Mg powder. Acta Mater. 61, 1809–1819 (2013).*

[22] *Yang, K. V. et al. Porosity formation mechanisms and fatigue response in Al-Si-Mg alloys made by selective laser melting. Mater. Sci. Eng. A 712, 166–174 (2018).*

[23] *Yang, K. V., Rometsch, P., Davies, C. H. J., Huang, A. & Wu, X. Effect of heat treatment on the microstructure and anisotropy in mechanical properties of A357 alloy produced by selective laser melting. Mater. Des. 154, 275–290 (2018).*

[24] *Tang, M. & Pistorius, P. C. Oxides, porosity and fatigue performance of AlSi10Mg parts produced by selective laser melting. Int. J. Fatigue 94, 192–201 (2017).*

[25] *Das, S. Physical Aspects of Process Control in Selective Laser Sintering of Metals. Adv. Eng. Mater. 5, 701–711 (2003).*

[26] *Romano, S., Beretta, S., Brandão, A., Gumpinger, J. & Ghidini, T. HCF resistance of AlSi10Mg produced by SLM in relation to the presence of defects. Procedia Struct. Integr. 7, 101–108 (2017).*

[27] *Sheridan, L., Scott-Emuakpor, O. E., George, T. & Gockel, J. E. Relating porosity to fatigue failure in additively manufactured alloy 718. Mater. Sci. Eng. A 727, 170–176 (2018).*

[28] *Prithivirajan, V. & Sangid, M. D. The role of defects and critical pore size analysis in the fatigue response of additively manufactured IN718 via crystal plasticity. Mater. Des. 150, 139–153 (2018).*

[29] *Grasso, M. & Colosimo, B. M. Process defects and in situ monitoring methods in metal powder bed fusion: a review. Meas. Sci. Technol. 28, 044005 (2017).*

[30] *Bauereiß, A., Scharowsky, T. & Körner, C. Defect generation and propagation mechanism during additive manufacturing by selective beam melting. J. Mater. Process. Technol. 214, 2522–2528 (2014).*

[31] *Wang, P. et al. Scanning optical microscopy for porosity quantification of additively manufactured components. Addit. Manuf. 21, 350–358 (2018).*

[32] *Kim, F. H., Moylan, S. P., Garboczi, E. J. & Slotwinski, J. A. Investigation of pore structure in cobalt chrome additively manufactured parts using X-ray computed tomography and three-dimensional image analysis. Addit. Manuf. 17, 23–38 (2017).*

[33] *Maskery, I. et al. Quantification and characterisation of porosity in selectively laser melted Al–Si10–Mg using X-ray computed tomography. Mater. Charact. 111, 193–204 (2016).*

[34] *Slotwinski, J. A., Garboczi, E. J. & Hebenstreit, K. M. Porosity Measurements and Analysis for Metal Additive Manufacturing Process Control. J. Res. Natl. Inst. Stand. Technol. 119, 494 (2014).*

[35] *Zhang, B., Li, Y. & Bai, Q. Defect Formation Mechanisms in Selective Laser Melting: A Review. Chinese J. Mech. Eng. 30, 515–527 (2017).*

[36] *Ferrar, B., Mullen, L., Jones, E., Stamp, R. & Sutcliffe, C. J. Gas flow effects on selective laser melting (SLM) manufacturing performance. J. Mater. Process. Technol. 212, 355–364 (2012).*

[37] *Nazari, K. A., Nouri, A. & Hilditch, T. Compressibility of a Ti-based alloy with varying amounts of surfactant prepared by high-energy ball milling. Powder Technol. 279, 33–41 (2015).*

[38] *Leung, C. L. A. et al. The effect of powder oxidation on defect formation in laser additive manufacturing. Acta Mater. 166, 294–305 (2019).*

[39] *Milewski, J. O. Additive Manufacturing of Metals: From Fundamental Technology to Rocket Nozzles, Medical Implants, and Custom Jewelry. (Springer International Publishing, 2017).*

[40] *Gong, H., Rafi, K., Gu, H., Starr, T. & Stucker, B. Analysis of defect generation in Ti–6Al–4V parts made using powder bed fusion additive manufacturing processes. Addit. Manuf. 1–4, 87–98 (2014).*

[41] *Iebba, M. et al. Influence of Powder Characteristics on Formation of Porosity in Additive Manufacturing of Ti-6Al-4V Components. J. Mater. Eng. Perform. 26, 4138–4147 (2017).*

[42] *Tong, J., Bowen, C. R., Persson, J. & Plummer, A. Mechanical properties of titanium-based Ti–6Al–4V alloys manufactured by powder bed additive manufacture. Mater. Sci. Technol. 33, 138–148 (2017).*

[43] *Seifi, M., Salem, A., Satko, D., Shaffer, J. & Lewandowski, J. J. Defect distribution and microstructure heterogeneity effects on fracture resistance and fatigue behavior of EBM Ti–6Al–4V. Int. J. Fatigue 94, 263–287 (2017).*

[44] *Mower, T. M. & Long, M. J. Mechanical behavior of additive manufactured, powder-bed laser-fused materials. Mater. Sci. Eng. A 651, 198–213 (2016).*

[45] *Körner, C., Bauereiß, A. & Attar, E. Fundamental consolidation mechanisms during selective beam melting of powders. Model. Simul. Mater. Sci. Eng. 21, 085011 (2013).*

[46] *Sola, A. & Nouri, A. Microstructural porosity in additive manufacturing: The formation and detection of pores in metal parts fabricated by powder bed fusion. J. Adv. Manuf. Process. 1, (2019).*

02 Metal Additive Manufacturing: Design Keys

E. Toyserkani, D. Sarker, O.O. Ibhadode, *et al.*

MATERIALS: STRUCTURE-PROPERTY RELATIONSHIP

In materials science, besides the structure and property of materials, two other major components are processing and performance since the processing route will determine the final material structure.

Material properties are correlated with the microstructure, which can be modified by changing the micro constituents' relative magnitude, known as phases. In the microstructure, phases are categorized according to their distinctive crystal structures, elemental composition, and properties. These properties affect the performance of materials in applications and alter their performance. The modification of microstructure can be done by adding new elements or processing through mechanical and thermal treatments.

Thermomechanical treatments (a combination of mechanical and thermal treatments) are used to yield properties that cannot be achieved using other techniques. Hot isostatic pressing (HIP), which exposes manufactured parts to simultaneously elevated temperature and isostatic gas pressure in a high-pressure containment vessel, may also be used to minimize porosity while changing the phases.

MANUFACTURING OF METALLIC MATERIALS

Distinct from traditional fabrication methods, additive manufacturing (AM) is a technique of producing three-dimensional solid products of any geometry using a digital model. It follows an additive method, where materials are added in consecutive layers and are differentiated from conventional subtractive machining techniques based on the subtraction of materials through cutting or milling.

The manufacture of AM metal powder comprises three stages:[1]

i. Mining and extracting ore to fabricate pure metal or alloy products
ii. Powder production
iii. Powder sorting, classification, and validation

The powder morphology has a substantial effect on bulk packing and flow behaviors. Spherical, regular, and equiaxed powders can organize and pack more competently than irregular powders. However, reports are claiming that irregular powders behave well in terms of flowability in the AM powder bed and powder-fed processes for many applications. The powder morphology can significantly influence the density of final AM components. Very spherical powders are more advantageous to AM processes. On the other hand, this, in fact, reduces the use of possibly cheaper powder manufacturing methods. Recent research outcomes demonstrate that the more irregular the powder shape, the inferior the product density.[2] Powder size distribution is another vital parameter, and it can impact the size of layer thickness and the finest aspect of the AM products.

SOLIDIFICATION IN ADDITIVE MANUFACTURING: NON-EQUILIBRIUM

The laser- or electron-beam (EB)-based AM methods entail a localized moving heat source with a very short interaction time. As the point heat source delivers extremely focused energy, it causes vastly localized heat flux in the melt pool zone, together with a massive temperature gradient in the deposited layers. The temperature gradient at the bottom of the substrate surface is higher compared to the top of the deposited surface. During the solidification process, the alloy partition coefficient drops, which results in the rejection of solute atoms at the solid-liquid boundary. The concentration of solute atoms rises until the solution reaches a steady condition. The solidification temperature at the solid-liquid boundary is influenced by the liquid composition, as well as

the processing speed and angle of this boundary with respect to the heat source centerline.

AM is comparatively a rapid solidification process.[3] There are two main reasons for rapid solidification: (i) enormous undercooling of the melt and (ii) fast-moving temperature fluxes.[4] A common feature of rapid solidification is accompanied by robust liquid flow, such as Marangoni convection, where flow velocities can be as high as 1–4 m/s. In the rapid solidification mode, elemental partitioning is reduced, which extends the solid solubility that may cause the formation of metastable phases. In addition, because of the directional heat conduction, a preferred directionality in grain growth may occur. The combined influence of rapid and directional solidification and phase transformation persuaded by continual thermal cycles has a substantial influence on the deposited parts' microstructure.

Rapid solidification characteristics can be summarized as the refinement of microstructure, an increase of solubility limits, lessening of micro segregation, and non-equilibrium of metastable phase formation.[10] The formation of distinctive microstructural features such as grains, lamellae, and second-phase particles is generally reduced in the fast cooling compared to the standard casting methods.[5] Another possible outcome is the mitigation of dendritic segregation at a point where compositional homogeneity can be attained.[5]

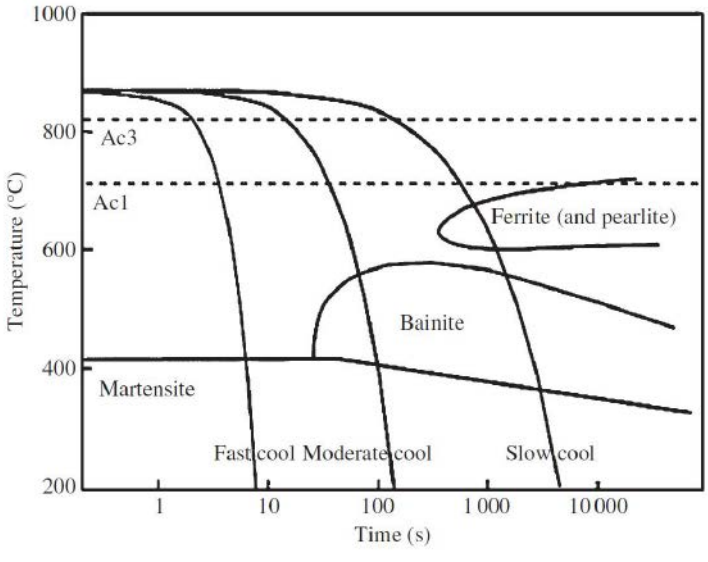

Figure 1: Continuous cooling transformation diagram for steel.
[Source: Openly accessible through creative commons license.]

EQUILIBRIUM SOLIDIFICATION

The structure of a material, which is a function of composition and temperature, can be identified from an equilibrium phase diagram using the assumption of a relatively slow transformation rate or a faster diffusion rate.

Cooling Curve and Phase Diagram

A cooling curve is a graphical presentation of the phase transition temperature with time for pure metals or alloys over a complete temperature range. On the other hand, a phase diagram is a useful tool to understand the formation of phases and their transformation throughout the heating and cooling practice with different alloy compositions. For example, during the manufacturing of stainless steel using laser-based AM technology, it is crucial to optimize the laser input temperature to control the austenite and ferrite phase formation.

Another important tool is the continuous cooling transformation (CCT) diagram, which presents the knowledge of the type of phases that will form in alloys at different cooling rates. It is vital in AM techniques since each deposited layer goes through repeated thermal cycles and eventually has different cooling rates. A CCT diagram for steel is shown in **Figure 1**, where it is evident that a complete martensitic structure forms at fast cooling conditions, whereas bainite, ferrite, and pearlite can occur at relatively slower cooling rates. In the AM process, when the thermal profile of each deposited layer is known, the CCT diagram can be used to estimate the formation of phase types.

NON-EQUILIBRIUM SOLIDIFICATION

The most significant part of the solidification of AM is the heating and cooling cycle, which may cause suppressed phase changes or supersaturated phases. In AM, when every layer passes through a repeated heating and cooling cycle, the temperature in the layer may reach above the phase transformation temperature. This will result in the multiple phase transformation or intricate microstructure, in addition to a residual stress formation.

For better control of microstructure in AM parts, knowledge of the phase transformation during the fast solidification and repeated thermal cycle behaviors is essential. During the rapid cooling, some phases that generally form under equilibrium conditions may not

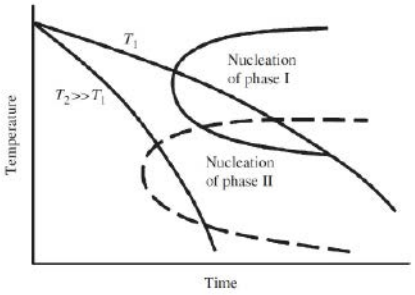

Figure 2: Time-temperature diagram presenting the nucleation onset of two dissimilar theoretical phases with different cooling behaviors.

arise; hence, there would be a chance for the occurrence of metastable phases. The characteristics of the metastable phases are based on the alloy chemical structure and thermal behavior of the cooling method. This aspect is graphically emphasized in **Figure 2**. From the time-temperature diagram, at cooling rate T_1, the primary phase is nucleated as phase I, whenever at a faster cooling rate T_2, ($T_2 \gg T_1$); another phase, phase II is nucleated by detouring phase I. To clarify the phase formation, a phase diagram is shown in **Figure 3,** where phase δ is evident at equilibrium conditions. Due to the rapid cooling process, a metastable phase diagram may be created, which is highlighted by the dashed lines. In this cooling condition, if the delta phase cannot generate, a eutectic system may appear at a lower temperature with different chemical compositions compared to the equilibrium phase diagram.

SOLUTE REDISTRIBUTION AND MICRO SEGREGATION

Micro segregation is defined as the ejection of solute from the freezing material, which afterward distributes heterogeneously and eventually affects the solidification mode. The alloy in liquid form contains a higher solute compared to the solidified condition. Therefore, during the solidification process, there is a chance of the high solute liquid being trapped within the solidified structures. This causes micro segregation or banding of high and low solute alloys and substantial incoherence in material properties.[10]

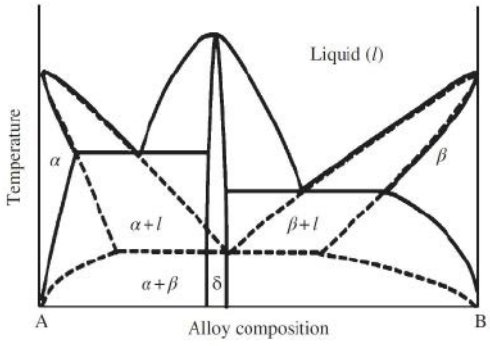

Figure 3: A comparative presentation of the theoretical equilibrium (solid lines) and metastable non-equilibrium phase diagram (dotted lines).

The theory and mechanism of solute redistribution can be expressed using equilibrium and non-equilibrium models, considered in the vigorous conditions of solute redistribution. The factors that are assumed in equilibrium lever laws are (i) complete diffusion in both liquid and solid-state (ii) equilibrium at solid/liquid boundary, and (iii) no undercooling through the growth. Additionally, in the non-equilibrium lever law (Scheil equation), similar assumptions are considered, apart from considering negligible diffusion in the solid. In solidification, these three factors signify the extreme situations of residual micro segregation. According to the equilibrium lever law, there are no concentration gradients in the liquid and solid during solidification and eventually no residual micro segregation in the solidified structure. On the other hand, the non-equilibrium situation possesses residual micro segregation in the solidified structure because of very minor solid diffusivity.

Generally, the solute diffusion coefficient of a solid phase is about four times lower than a liquid phase; therefore, a precise image of plane front solidification is expressed by a hypothesis that no diffusion happens in the solid phase and complete mixing of liquid occurs. However, as the solute is not endorsed to mix in the solid phase, an uneven concentration profile grows behind the progressing interface. The liquid concentration remains consistent with the hypothesis of thorough mixing. An equilibrium solute concentration at the developing solid-liquid interface may be of interest to develop an expression for the shape of the solute concentration in a solid.

Three different categories of solute redistribution are presented in **Figure 4,** which can form with insignificant diffusion in the solid. For type 1, the liquid diffusion or convection-controlled mixing in the liquid is finished or the subsequent solute segregation is vigorous. In contrast, for type 3, liquid diffusion is incomplete without convection-controlled mixing in the liquid and, eventually, the solute segregation is less vigorous. However, type 2 shows intermediate behavior to types 1 and 3, which ensure solute segregation[10]. Therefore, based on the relations between the alloying elements, there

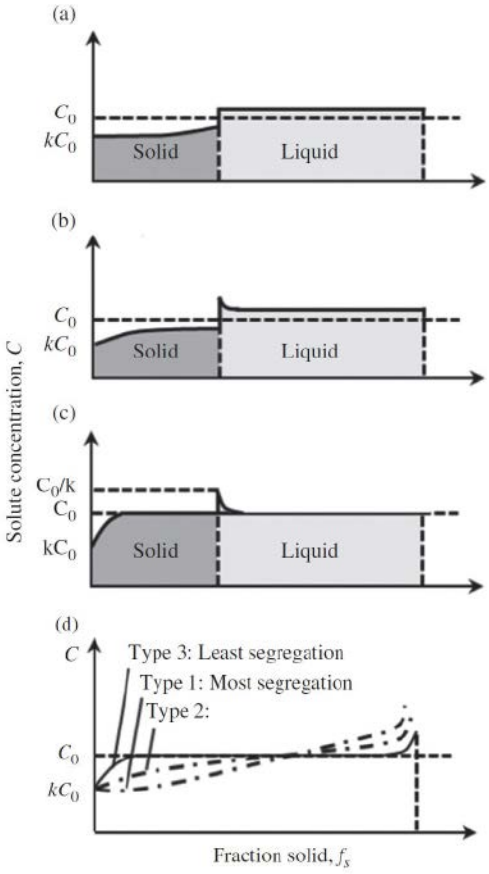

Figure 4: Solute distribution without diffusion in the solid and dissimilar diffusion in the liquid. (a) Type 1: complete liquid diffusion or mixing, (b) Type 2: limited liquid diffusion, some convection, (c) Type 3: limited liquid diffusion, no convection, (d) combination of Type 1, 2, and 3.[10]
[Source: Reproduced with permission from John Wiley & Sons Inc.]

will be remarkable importance on the diffusion rates, temperature, and various concentration profiles at the boundary during solidification.

CONSTITUTIONAL SUPERCOOLING

Usually, in the solidification process, the material in the liquid form first cools at the phase transformation temperature and then starts to solidify with the release of its latent heat.[7] As the cooling progresses, the temperature of the liquid continues to drop. However, the system becomes thermodynamically unstable. Therefore, solidification can be commenced with a small amount of energy accomplished with the latent heat release, which eventually increases the temperature. The real temperature at which the solidification starts is termed "the degree of supercooling." This occurs because of the alloying element segregation at the solid-liquid boundary.[8] The additional concentration of the elements lowers the melting temperature of the liquid. When this reduction is adequate to drop the melting temperature far below the actual temperature, then the liquid will be locally supercooled. Constitutional supercooling considers the interactions between the temperature gradient, interface speed, and the alloying element to develop a simple criterion to forecast the position of the melt, whether it is above or below the liquid. In the former position, the melt remains steady to a lump on the interface that advances shortly into the melt. In the latter position, the melt is supercooled to solidify naturally on any interface lump.[9]

NUCLEATION AND GROWTH KINETICS

In the rapid solidification of a supercooled alloy, the nucleation mechanism is far different from the conventional one. For the highly supercooled pure metals and solid solution alloys, a single nucleation event may be adequate to start and complete the solidification process having a faster crystal growth rate. But the growth of the supercooled material is always diffusion-controlled, which inherently entails a sluggish growth behavior. Therefore, the question is whether a single nucleation matter can lead to the solidification system.

Generally, in most AM techniques, the deposited material in every layer has a similar chemical composition unless a powder-fed directed energy deposition is utilized, in which the powder stream may change from one composition to others on demand. In these circumstances, due to a similar crystal structure, epitaxial growth can eliminate nucleation and let the natural growth happen without activation energy until below the liquidus temperature. On the other hand, when dissimilar materials are deposited during the fabrication of composites, or surface cladding of AM, then the nucleation phenomenon should be considered. In layer-by-layer AM processes, this may also happen when the first layer is deposited on the dissimilar substrate material. When nucleation occurs at the solid/liquid boundary, the newly formed phase needs to conquer an energy obstacle that eventually controls the structure and property of the solidified part.

Nucleation

Nucleation is classified into (i) homogeneous nucleation and (ii) heterogeneous nucleation. Homogeneous nucleation occurs with the formation of uniform nuclei all over the parent phase, while in heterogeneous nucleation, nuclei may advance from the structural discontinuity, such as boundaries of the impurities, foreign particles, dislocations, and so on.

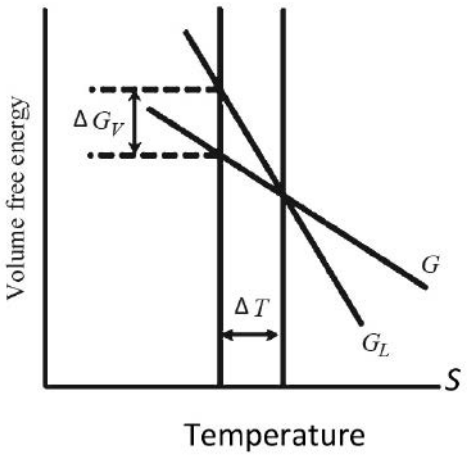

Figure 5: Schematic presentation on the relation between the Gibbs free energy and undercooling temperature.

Considering a relation between the Gibbs free energy and the undercooling temperature shown in **Figure 5,** when a liquid cools far below its melting point (T_m), the Gibbs free energy (G_S) for the solid becomes lower than the liquid (G_L). There would be an undercooling temperature ΔT and a driving force ΔG to result in an impulsive phase transformation.[12] The volume of free energy can be expressed as:

$$\Delta G_V = G_L - G_S \qquad \text{Eq. 1}$$

Briefly, the solidification of pure metal is considered in **Figure 6,** where nuclei of a solid phase (spherical, with a radius r) are formed inside of a liquid-like packing arrangement of clustered atoms.[13] In addition, **Figure 6b** presents two energy sources for the total free energy evolution that conduct a solidification transformation. The first source is the difference between free energy within the solid and liquid, known as the volume free energy, ΔG_V. It becomes negative when the temperature drops down the equilibrium, where it is quantified by the product of nucleus volume (i.e., $4\pi r^3/3$). The second energy source comes from the development of a solid/liquid interface through the solidification process. This is a surface-free energy γ with a positive value, which is quantified by the product of the nucleus surface area (i.e., $4\pi r^2$). Therefore, the complete energy change ΔG is the addition of those two energy sources,

$$\Delta G = \frac{4}{3}\pi r^3 \Delta G_V + 4\pi r^2 \gamma_{sl} \qquad \text{Eq. 2}$$

From a physics point of view, when solid particles in the liquid cluster together to form atoms, their free energy rises. After reaching the size of a critical radius r^*, the growth of the clustered atoms begins with a decline of free energy. In contrast, below the critical size, the cluster will shrink or dissolve. This critical size particle is known as an *embryo,* whereas with greater size, it is called a nucleus. The free energy that arises at the critical radius is the critical free energy ΔG^*, which is the highest of the curve in **Figure 6b.** This is actually an activation of free energy required to form a stable nucleus, or equally as an energy barrier in the nucleation process.

The criterion to begin a nucleation process can be theoretically derived from the condition $d(\Delta G)/dr=0$, and $r^* = 2\gamma_{sl}/\Delta G_V$).

In heterogeneous nucleation or epitaxial growth, a nucleus in a liquid is formed in connection with a substrate. Therefore, the interfacial energies between the liquid, nucleus solid, and substrate metal control the geometry of the nucleus.[14] The total energy can be reduced by assuming the nucleus as the geometry of a spherical cap, as presented in **Figure 7a.** At equilibrium, the interfacial energy is equal to $\gamma_{ML} = \gamma_{SM} + \gamma_{SL} \cos \varnothing$.where γ_{ML} represents the interfacial energy between the substrate and the liquid, γ_{SM} is the interfacial energy within the solid nucleus and substrate, and γ_{SL} is the interfacial energy between the solid nucleus and liquid. In addition, $\varnothing$ is the contact angle of the nucleus. When the chemical composition of the substrate and the nucleus are identical, then the interfacial energy between them is negligible. Moreover, the interfacial energies between the substrate and liquid are similar to the interfacial

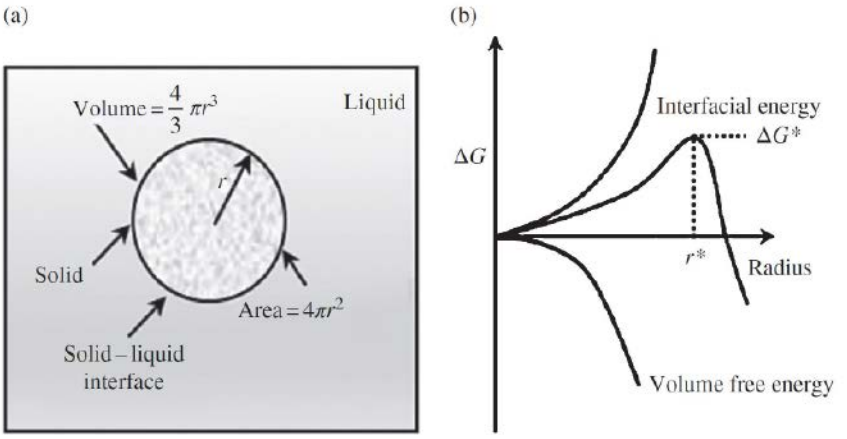

Figure 6: (a) A figure depicting the nucleation of a sphere-shaped particle in a liquid. (b) A plot of free energy against embryo/nucleus radius, where it also presented the critical free energy change (ΔG_v) and the critical nucleus radius (r*).[13]
[Source: Reproduced with permission from John Wiley and Sons.]

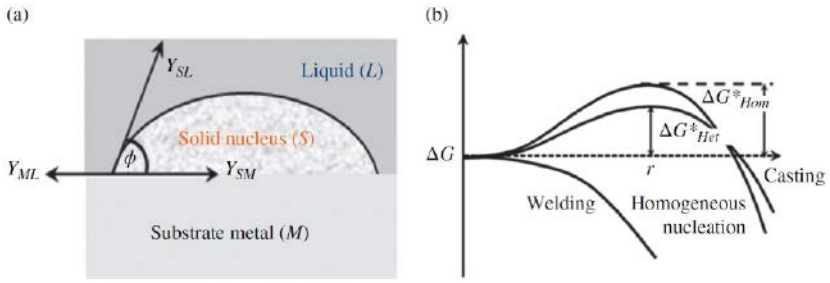

Figure 7: (a) Solid nucleus connected with substrate metal and liquid. (b) Graphic presentation for free energy change related to heterogeneous nucleation observed in casting and welding together with homogeneous nucleation.[14]
[Source: reproduced with permission from John Wiley and Sons.]

energies between the nucleus and liquid. The free energy change related to the creation of a solid spherical cap of radius r is shown by:

$$\Delta G_{het} = -V_S \Delta G_v + A_S \gamma_{SL} \quad \text{Eq. 3}$$

$$\Delta G_{het} = S(\varnothing)\left[-\frac{4}{3}\pi r^3 \Delta G_v + 4\pi r^2 \gamma_{SL}\right] \quad \text{Eq. 4}$$

where ΔG_v is the free energy change per unit volume, accompanying the nucleus development, VS is the volume of the nucleus, AS is the surface area of the interface between the nucleus and the liquid, and $S(\varnothing)$ is the shape factor, which depends on the contact angle. By adopting differentiation of the above equation for r, and considering the result as zero, the critical radius of the heterogeneous nucleation is presented as $r^*_{het} = 2\gamma_{sl}/\Delta G_V$. The energy obstruction for the heterogeneous nucleation is then:

$$\Delta G_{het} = \frac{16\pi\gamma^3_{SL}}{3\Delta G^3_V} S(\varnothing) \quad \text{Eq. 5}$$

In epitaxial solidification, ∅ is zero and so $S(\varnothing)$ approaches zero, which makes ΔG_{het} zero as well. It emphasized that the energy barrier for the epitaxial solidification is negligible contrasted to the casting or other processes, as shown in **Figure 7b.** Because of this small energy barrier, the initiation of nucleation is very fast in epitaxial solidification. Usually, in metal AM, the chemical composition of the solid and liquid is pretty similar, which makes γ_{SL} small, as well as the critical radius. On the other hand, this type of solidification demands incomplete or through melt-back of the substrate to expedite grain evolution from the existing ones. The melt-back of the earlier solidified layer is critical in the context of the continuity of the microstructure through the successively melted and solidified multiple layers.

Growth Behavior

After the initiation of the nucleation, the solid/liquid interface deeds as a growth front. The growth kinetics is dominated by the roughness of the solid/liquid interface on the atomic scale, which may be atomically rough (in metals) or atomically flat (in non-metals). The first one progresses with continuous growth, whereas the second one follows lateral growth, including nucleation and dispersion of ledges.[15]

Growth starts from the previously deposited layers through partial or complete melting, which eventually governs the crystallographic pattern.[11,16] The intensified heat may penetrate further below the deposited layers, enabling the remelting process required to eliminate surface contaminants and the breakdown of oxides, thus offering a clean solid/liquid interface. The microstructure developed close to the melt boundary is controlled by the substrate material, whereas far away from the boundary, it is advanced through competitive growth.[17]

Usually, competitive growth takes place between dendrites with numerous crystallographic orientations and is commonly found in alloys of iron,[18,19] nickel,[20] titanium,[21] and tantalum.[22] Dendrites normally progress by the path of higher heat flow and lead to competitive growth in the structure.

When the solute-rich boundary layer creates a temperature gradient sharper than a critical gradient for constitutional supercooling, a stable planner interface growth is introduced.[15] If constitutional supercooling is encountered, successive lumps at the solidification front may propagate with rapid growth to advance into long arms or cells, approaching parallel to the heat flow and developing a cellular microstructure. However, with a smaller temperature gradient, a broader "mushy zone" is formed, which advances dendritic growth with secondary or tertiary arms.

Combined, the base metal at the boundary line plays as a nucleation site.[10] As the liquid metal within the melt pool is closely touching the thin layer of a substrate while completely splashing them, nucleation progresses without difficulties. During the autogenous joining, nucleation starts with the agglomeration of atoms in the liquid on the previously developed structures continuing with similar crystallographic orientations. This type of growth phenomenon is shown in **Figure 8** and is known as epitaxial nucleation or epitaxial growth. The

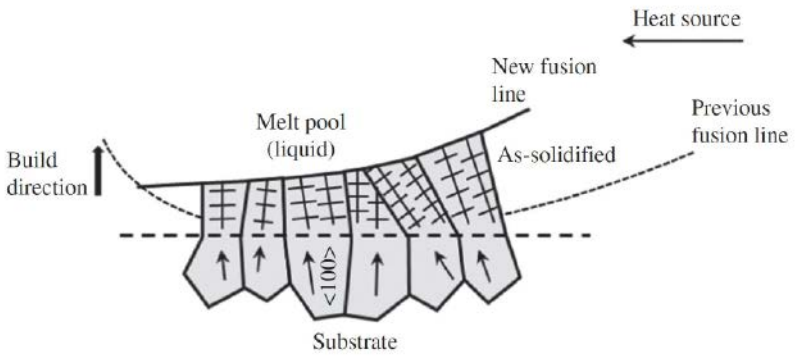

Figure 8: Epitaxial growth of the solidified metal adjacent to the fusion line.[10]
[Source: Reproduced with permission from John Wiley & Sons Inc.]

figure describes the grains' growth with 100 crystallographic orientations, which is common for the face-centered-cubic or body-centered-cubic crystal structures, where columnar grains advance in the 100 direction.

SOLIDIFICATION MICRO-STRUCTURE IN PURE METALS AND ALLOYS

The solidification process may be stable or unstable. Stable solidification is defined as a smoothly growing interface, responsible for the thermal diffusion through the solid phase. In these circumstances, the surface tension and the dynamic movement at the interface are neglected, thus with reduced perturbation. However, unstable solidification occurs when the metastable liquid cools far below the equilibrium temperature. In this situation, thermal diffusion from the interface occurs both in solid and liquid phases when the surface tension and dynamic movement are also considered. The local perturbation on the boundary layer will be enriched, and further protrusion in the liquid will progress with various structural patterns. The formation of grain pattern and the crystallographic texture is controlled by the melting process and the solidification of the liquid melt zone.

The melt area drives away heat through the substrate causing the melt pool to have a curved shape. Depending on the process parameters, the melt pool shape may vary from oval or tear-drop-shaped on the substrate with a semicircular or keyhole cross-section. The geometric profile of the melt pool is significant as it affects the grain structure in the fusion zone. In the keyhole case, the beam goes down the substrate with minimum heat input, which changes the conduction mode at high speeds equally in electron and laser beam techniques. The conduction approach is desired for AM because of the unsteady keyhole that may cause undesired porosity in AM products.

There are four major solidification patterns: (i) planar, (ii) cellular, (iii) columnar, and (iv) equiaxed dendritic **(Figure 9).** The various solidification structures grow depending on the driving force of constitutional supercooling, the distribution of the solute at the boundary, as well as the characteristics of the elements contained in the solidified alloys. Generally, the devastating forces of constitutional supercooling do not exist in pure metal, which will then show a planer solidification approach.[10]

The relation between the different solidification patterns with the degree of constitutional supercooling is shown in **Figure 10.** A planar solidification starts with a greater real temperature in contrast to the equilibrium temperature of the liquid melt.[23] In the planer solidification, a stochastic protuberance may grow into an area of higher temperature and results in the breakdown of the protuberance **(Figure 10a).** Planar solidification is feasible, especially for single crystal growth, where it demands either high purity metal or tremendously high degrees of temperature gradients or solidification rate.

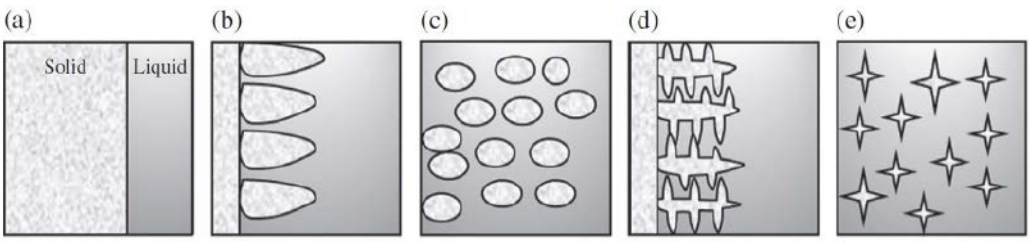

Figure 9: The schematic diagrams illustrate the modes of solidification pattern: (a) planar, (b) and (c) cellular, (d) columnar dendritic, and (e) equiaxed dendritic.

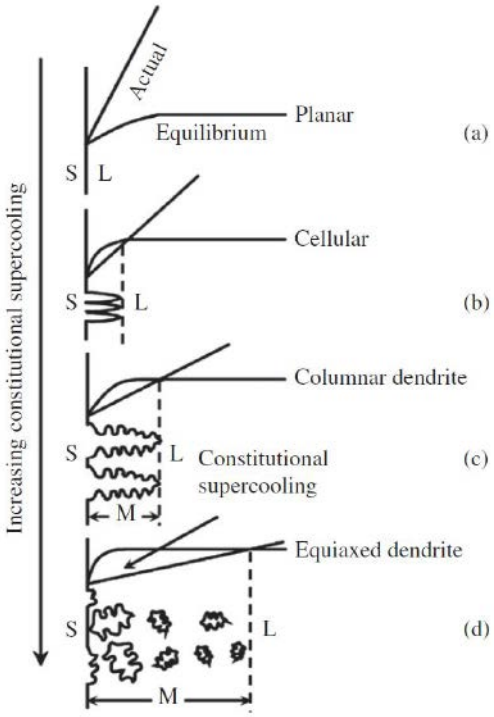

Figure 10: Occurrence of various solidification structures related to constitutional supercooling.[10]
[Source: Reproduced with permission from John Wiley & Sons Inc.]

In constitutional supercooling, the real temperature gradient is lower than the liquid's temperature gradient; a protuberance may mature in the undercooled melt and approach as a cellular or dendritic pattern **(Figure 10b).** When the grain grows like a column without branching the arms, it will form a cellular structure. In contrast, the grains with secondary or tertiary arms will develop a dendritic structure (**Figures 10c** and **10d**). The cellular and dendritic growth are estimated by the degree of constitutional supercooling and the complete stability described by the critical solidification rate. However, planar solidification is independent of the temperature gradient.

Generally, the solidification starts homogeneously after adequate cooling or heterogeneously with the existence of a solid particle in the supercooled melt. Moreover, after nucleation, the consequent growth of the solid from the particle may be unstable, and based on the degree of supercooling, dendritic structures start to form. Dendrites are defined as prototypical structures growing from homogeneous initial states into compound spatio-temporal configurations distinct from equilibrium.

The root of the word "dendrite" originates from the Greek term "dendron," meaning "tree". Similar to a tree, a dendrite shows an extremely branched, arborescent pattern, which is schematically presented in **Figure 11.**

Because of the unsteadiness of the interface, a dendrite structure comprises the primary stem, secondary, or tertiary branches, all advancing in particular crystallographic directions. The dendritic structures in metallurgy form the microstructure of metals or alloys, which heavily controls the mechanical, chemical, and physical characteristics of the material. During the solidification, the growth of the perturbation at the solid/liquid boundary may be inhibited by the surface tension or kinetic phenomenon. The challenge between the steady influence of surface tension and the unsteady influence of supercooling is mainly the cause source for the formation of dendritic compound patterns.

As the grain structure influences the mechanical properties, it is essential to create finer grains in the solidified material to achieve superior properties. However, in laser or EB metal AM, it is crucial to stop grain growth during remelting of the formerly deposited layers, which also brings heterogeneous nucleation and epitaxial grain development either in cellular or dendritic form. When the epitaxial grain growth of the columnar grains is prevented by the development of equiaxed grains close to the melt zone area, and the equiaxed grains are deeper than the remelted penetration depth, then the equiaxed grains govern the average grain size. It is demanded in laser- or EB-based AM that the occurrence of equiaxed grains is estimated by the density of heterogeneous nucleation sites, which may be feasible in the laser powder bed fusion (LPBF) process with a proper powder feed rate.

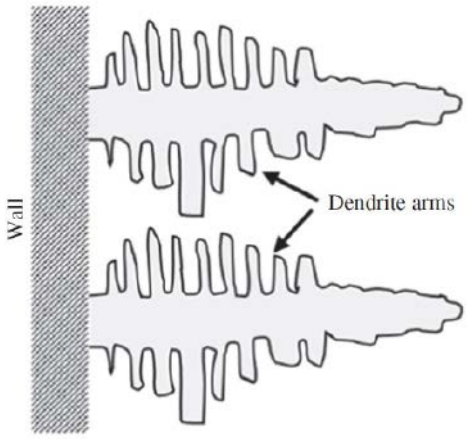

Figure 11: Schematic of the dendrite formation/growth.

DIRECTIONAL SOLIDIFICATION IN AM

The most vital factor in controlling the mechanical properties of AM products is the solidification structure.[6] The connection with higher laser energy provides rapid heating and cooling, resulting in faster solidification during cooling. Moreover, the heat dissipation rate through the substrate is fast enough to develop a rapidly solidified structure. Therefore, grain refinement is usually predicted in the distinctive AM structures because of their inadequate time for grain formation/progression.

The solute intensity or temperature gradients in the melt may produce surface tensions and subsequent Marangoni convection, resulting in an unstable solidification process. Moreover, rapid solidification generally progresses along with the maximum heat flow. The mechanisms of non-equilibrium solidification and the propensity for directional propagation are instantaneous but competitive, which may generate diversity in crystal orientation with limited consistency. As a result, AM-processed metallic products may possess intrinsic anisotropic characteristics.

For a known material composition, the solidification morphology is controlled by parameters such as solidification velocity and temperature gradient. The developed structure may differ from planar to cellular and to dendrites, which normally turn into a finer structure until the regeneration of cellular structures with a growth rate of near-absolute stability. At velocities greater than this range, the banding acts, and finally, the planar interface is completely stabilized. The well-developed cellular structure normally grows without advancing side arms, where their axes are aligned to the heat flux direction without considering any crystal orientation. However, dendrites are regarded as the growth of their arms along crystallographic orientations. Because of the anisotropy in solid/liquid interface energy and growth mechanism, cubic crystal dendrite will propagate along the 001 direction, indicating the heat flow direction.

Throughout the directional solidification and advance of columnar structures, the heat flux follows contrary to the growth direction. This means that the growth rate of the fronts limits the solid/liquid boundary to propagate at this rate. During the alloy solidification, the solute will stack on the boundary, while the distribution coefficient is normally lower than the unity and, eventually, this variation of concentration will impact the equilibrium solidification temperature. The supercooled zone, where equiaxed grains with various volume fractions may take place, depends on the thermal gradient and the solidification rate, and finally directs to the columnar-to-equiaxed transition.

FACTORS AFFECTING SOLIDIFICATION IN AM

Cooling Rate

Generally, solidification/cooling rates are influenced by the heat input, which is manipulated by the laser or EB power, beam scan speed layer thickness, scanning strategies, etc. When the laser power is low and scanning speed is high, this combination normally delivers a smaller heat flux that results in a larger cooling rate. In contrast, with higher laser power and lower scan speed, heat input would be intensified to melt a larger substrate area, which eventually results in a slower cooling rate.

Temperature Gradient and Solidification Rate

Through solidification, columnar grains advance along the path of a higher temperature gradient in the melt pool.[16] The spherical melt pool generates curved and tapered columnar structures because of the deviation in the thermal gradient path from the pool border. However, the comet-featured melt pool creates conventional and wide columnar structures, where the path of the maximum thermal gradient does not shift notably through the process.

If we consider the angle between the direction of grain growth and beam scan speed (SS) is θ, then the constant nominal growth rate R_N would be $R_N = SS \cdot \cos\theta$. In a cubic crystal structure, the ⟨100⟩ direction designates the main dendrite growth direction. This favored growth direction makes the local growth rate R_L greater than the nominal rate R_N. Another angle ϕ is considered between the normal direction of the melt pool border and the ⟨100⟩ direction to link R_L and R_N, which is $R_L = R_N/\cos\phi$. The relationship states that the local growth rate becomes larger with misaligned crystals with respect to the direction of a higher temperature gradient.

Several factors such as moving heating source power (P), beam scan speed, substrate material temperature (T), and beam spot diameter (d) control the G/R_L ratio[11], where G is the local temperature gradient. The value of

G is lower with higher values of *T*. The lower value of *G* must be recompensed by a lower *P-value*. Therefore, *P* must be decreased when *T* is increased to have columnar growth through the solidification. With an increased scan speed, R_L increases without a significant impact on *G*, resulting in a lower value of the G/R_L ratio. However, as the higher scan speed causes a smaller melt area with greater temperature gradients, the increased scan speed may increase the G/R_L ratio. A larger energy intensity or a wider beam diameter is inconvenient to work with because of the promptly decreased beam intensity in the area far from the centerline in a single-mode laser with a Gaussian intensity distribution that restricts uniformity in the microstructure. Therefore, when a larger *d* is unavoidable, *P* needs to be intensified to confirm enough heat flux for the substrate remelting to continue with epitaxial grain growth. Raising the substrate material temperature using a pre-heating procedure somewhat enables the melting with a larger volume but, at the same time, lowers the processing window.

Moreover, the stability of the solid/liquid boundary is dominated by the thermal and supercooling behavior. Considering the constitutional supercooling, the instability at the interface is expressed as:

$$\frac{G}{R} > \frac{\delta T}{D} \qquad \text{Eq. 6}$$

where *G* represents thermal gradient, *R* is the growth rate, δT is the temperature range for solidification, and *D* is the diffusion coefficient of solute material in the melt.

To understand the solidification morphology and their structure, a solidification map is designed with *G* and *R,* in the form of their product as *G.R* and ratio as *G/R*. **Figure 12** describes the influence of *G/R* and *G.R* on the solidification structure, where *G/R* governs the type of solidification pattern and *G.R* controls the size of the structure.[10] The solidification structure may be planar, cellular, columnar dendritic, or equiaxed dendritic. Normally, higher *G/R* ratios result in a planar structure, while lower *G/R* ratios result in an equiaxed structure. Moreover, the size of these four structures decreases with the larger value of *G.R* (cooling rate).

The size of the solidification structure can be estimated using the product *G.R*. Therefore, the arm spacing of columnar or equiaxed grains can be measured using the cooling rate or solidification time, which can be stated as[10]:

$$y = at_f^n = b(\varepsilon_c)^{-n} \qquad \text{Eq. 7}$$

where t_f is the solidification time, ε_c is the cooling rate, and *a, b,* and *n* represent material constants that should be identified based on the experimental data.

The mathematical relation depicts that with the slower cooling rate and the extended growth time, coarser dendritic structures are formed. The surface energy of the solidified material may be lowered with the formation of coarse dendrite arms, as the coarse arms have less surface area per unit volume. This is because the slower cooling allows a longer time for growth and forming coarser dendritic arms. On the other hand, a faster cooling rate does not allow a longer time for growth, producing a finer structure.

The driving force, which is required for dendrites to grow properly, comes from undercooling. There is a difference in temperature between the liquidus and the dendrite slant that makes the undercooling temperature, as stated by:[10]

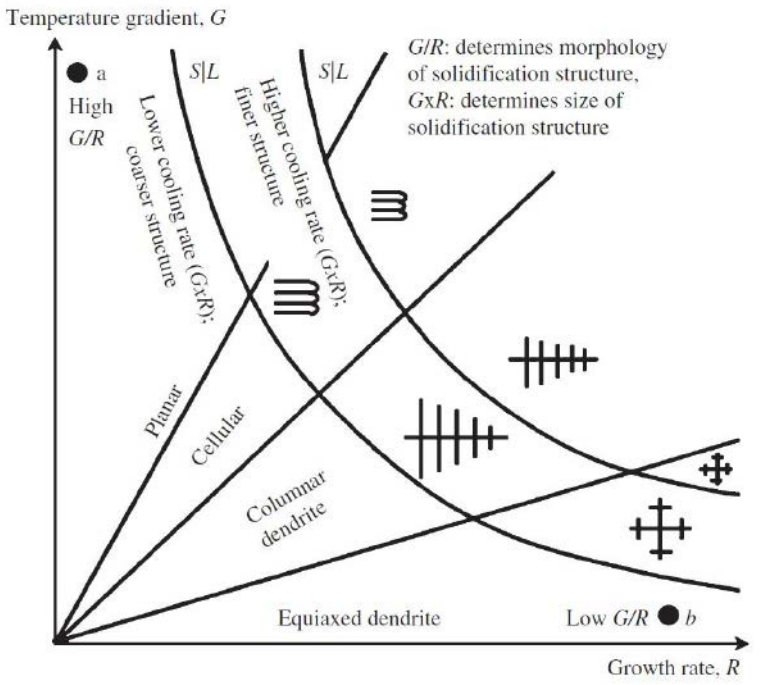

Figure 12: Influence of temperature gradient G and growth rate R on the size and morphology of the solidified structure.[10]
[Source: Reproduced with permission from John Wiley & Sons Inc.]

$$\Delta T_{tot} = \Delta T_c + \Delta T_T + \Delta T_K + \Delta T_R \quad \text{Eq. 8}$$

where ΔT_C, ΔT_T, ΔT_K, and ΔT_R are the undercooling temperatures accompanied by solute diffusion, thermal diffusion, attachment kinetics, and solid/liquid boundary curvature, respectively.

Through the solidification of most metallic materials, ΔT_T, ΔT_K, and ΔT_R are negligible; hence, the solute diffusion undercooling ΔT_C leads the process. Therefore, different solidification structures, from planar to cellular, columnar dendrite, or equiaxed dendrite, are basically formed because of the supercooling at the solid/liquid interface.

Besides the dendritic structure reported in AM, there may be a considerable amount of precipitates in some precipitation strengthened alloys, such as nickel-based superalloys. This happens because of the very fast cooling in the localized melt area, which creates a non-equilibrium condition where diffusion is limited. Another reason is the inadequate time for the alloying constituents to diffuse back into the solidified structure. Therefore, the concentration of the residual melt increases with alloying elements and promotes eutectic solidification to take place at the end of solidification, resulting in precipitates.

Process Parameters
The solidified microstructure and the phase formations are controlled by the input process parameters. Together with the higher specific energy and the faster deposition rate, the liquid melt will be at a higher temperature for an extended time to lower the temperature gradients. Therefore, the grains are allowed to grow coarsened and mainly equiaxed. On the other hand, the minor specific energy is understood by applying a faster scan speed, and hence no adequate time for the grain growth. Moreover, the geometry of the melt pool becomes narrow at a faster scan speed; therefore, the temperature gradients are higher, resulting in the formation of columnar grains. Layer thickness is also another influencing factor, which depends on additional parameters, e.g., power, speed, specific energy, and powder flow rate, to dominate the microstructure in AM products. When the specific energy is brought down, the energy required per unit area to melt down the powder is lowered. This calls for a need to lower the layer thickness. However, the thicker layer causes slower cooling and results in a coarser microstructure. Therefore, the structural development is complex to layer thickness because of the dominance of heat conduction through the substrate, which controls the cooling rate and consequent microstructures.

Solidification Temperature Span
Usually, the broader solidification temperature span creates a greater solid/liquid or mushy zone, which is mostly responsible for the solidification cracking, as the liquid cannot allow load. This temperature range is altered by several factors, such as the existence of impurities and some specific alloying elements. Simultaneously, the nearby grain material will be solidified, which then creates a gap with the grain boundary liquid due to thermal stresses. The eutectic temperature range also enhances the extent of the mushy zone.

Gas Interactions
In AM techniques, argon and nitrogen are generally used to offer an inert atmosphere and satisfy the high tolerance criteria. In the case of EB-PBF, a true vacuum in the chamber is required. Helium is also used for shielding during laser DED to enhance temperature-temporal behavior.

The impact of the shielding gas on the quality of metal powders during laser DED, combined with the AM input parameters, plays a major role in the growth of the final structure and properties of the manufactured products. Although nitrogen is a reactive gas, it can be a suitable shielding gas for those materials, which never react with nitrogen.

SOLIDIFICATION DEFECTS

Porosity
Usually, in AM the pore formations are connected with the process input parameters, such as laser power or beam scan speed. The porosities are categorized as powder and process induced.

Three major mechanisms cause porosity in AM products. First, at very high operating powers, melting may be accomplished throughout a keyhole mode.[11] When the keyholes are not properly developed and stabled, they can turn into an unstable mode, which then frequently forms and collapses, making voids inside the melt. Second, during the atomization of metallic powder, gas can be trapped inside powder particles, creating microscopic gas pores during the process. Consequently, the powder-caring pores can be transferred to the final fabricated parts. Moreover, gas pores can be generated

because of the potential of gas attraction/solution by the alloy melt. Third, the deficiency in fusion imperfections can result from insufficient infiltration of the upper layer melt into the substrate or the formerly solidified layers. This lack of fusion area is detectable by not melted or partially melted powders nearby the pores.

To understand the mechanisms of defect formations during LPBF, the process window for a known and fixed layer thickness and hatch spacing can be classified into four different zones.[24] Zone I is termed a "fully dense zone," which is free from porosity. Zones II and III, which are termed the "over melting zone" and "incomplete melting zone," respectively, have measurable porosities. The porosities introduced by process input parameters in zone II result from the exceeded energy, whereas those of zone III are caused by inadequate energy flux. Finally, Zone IV, the "overheating zone," is generated by a very slow scan speed and higher laser power.

Porosities generated by inadequate melting are typically observed near the boundaries, which are geometrically irregular in shape. Their amounts are greatly persuaded by operating parameters, such as laser power, layer thickness, scanning speed, and hatch spacing. In deficient fusion porosity, the top surface of the earlier layer may not be melted to develop a coherent bond due to the unsatisfactory dissipation of laser energy through the powder layers. Another potential reason for the poor fusion porosity is the entrapment of gas bubbles between the layers during processing. These gas bubbles then result in an unsteady scan track with non-uniform evaporation. The distinctive uncertainty of the scan tracks, therefore, causes intermittent failure of the liquid melt adjacent to the vapor cavity and forms periodic voids.

Similar to the process input parameters, the unsteadiness of the scan track and pore formation can be minimized by the proper adjustment of the beam.[25] There is a chance to release more gas during the slow solidification process, usually at higher energy density or lower scan depth with lower energy densities. Using a pulsed or modulated laser beam, it is possible to regulate the energy indulgence into the powder layer or substrate material, thus manipulating solidified structures, porosity, and other defects. The steadiness of the scan track is significantly impacted by the pulse because the pulse needs to revive the scan track once it fails. The adequate overlapping ratio of the two scan tracks can provide effective removal of porosity formed in early pulse, which eventually minimizes the process-induced cavities. Hence, it is suggested to reduce the lay-off time of the pulse, lower than the solidification time required for the melt. In this situation, it is necessary to use a high duty cycle and a greater extent of overlap area in the melt zone through the pulse transition. During pulsed-wave methods, the consideration of short pulse periods and lower energies is necessary to maintain a small melted area.

Balling

The balling phenomenon is considered the unusual melt pool segregation/breakout that may take place on the surfaces of the laser additive-manufactured parts, especially LPBF. Through the processing, the laser beam scans the surface linearly and the melting occurs along a row of powders, which then creates a constant liquid track similar to a tubular shape. The breakdown of the tube into the spherical-shaped (balling effect) metallic agglomerates drops the surface energy of the melt track until the ultimate equilibrium condition is achieved. The balling effect can result in an intermittent scan track with poor bonding and can be an obstruction to a constant deposition of powder on early-deposited layers. These phenomena can result in porosity or even delamination because of weak interlayers joining together with induced thermal stresses.

In powder-based AM techniques, powder particles absorb energy by the mechanisms of bulk coupling and powder coupling. Initially, a thin layer of distinct powder absorbs energy, influenced by the powder properties. This elevates the temperature on the particle surface, forming a liquid phase through the surface melting of powders. Consequently, the heat flows mostly in the direction of the center of the persisted powders till the steady-state melting temperature is achieved. The volume of liquid formation is influenced by the melting temperature, which is regulated by the laser power and scan speed through line scanning. For example, with a known scan speed and a lower laser power, the solidus temperature drops, forming a smaller volume of liquid melt. This makes a higher viscosity in the liquid-solid mix that, in turn, impends the liquid flow and particle reordering. This eventually drops the general rheological performance of adjacent and contacting liquid and solid particles. Subsequently, the liquid melt in each exposing spot area is able to combine into a discrete coarsened sphere of approximately the

same size as the laser beam's diameter. In these circumstances, no effective bonding occurs between the adjacent balls since inadequate liquid volume stops the satisfactory growth of continuous connecting metal agglomerates. In fact, the result would be multiple irregular shape discrete solidified zones when one looks at the build plate from the top. In addition, lower laser power is responsible for the inadequate undercooling temperature of the liquid melt. Therefore, the formation of coarsened and irregular dendrite structure in solidified balls generates mechanically weak characteristics, thus undermining the part quality.

When a satisfactory volume of the liquid phase is grown with both greater laser power and scan speed, the melt converts into an incessant tubular melted track because of the short exposure time of laser input on every area underneath the moving beam. But the melt pool track would be in an unsteady state; hence, the surface energy will keep dropping to reach an ultimate equilibrium state. When the scan speed increases, the energy intensity by the laser input drops, which then lowers the surrounding temperature and subsequently the diameter of the tubular melt pool track. Therefore, the melt zone's unsteadiness rises considerably. Under these circumstances, the dropped surface energy promotes the spattering of liquid droplets from the melt pool track surface. As a result, many micrometer-sized spherical spatters are solidified near the sintered surface, ensuing in the balling phenomenon. These irregular shape-solidified zones may cause a manufacturing issue by manifesting the potential of recoater jamming during LPBF.

In a multi-layer deposited sample, the balling effect may be excluded by reducing the powder layer thickness. By applying a deoxidizing agent, oxide films can be satisfactorily eliminated from the melt surface, thereby cleaning the balling zone joining system.

Cracking

a. Solidification Cracking

Solidification cracking takes place at the last step of solidification, where dendrites have become complete grains and are detached by a small volume of liquid known as a grain boundary. The possible reasons for solidification cracking in melted metals are depicted as: (a) temperature range of solidification, (b) volume and dispersion of liquid melt at the end of solidification, (c) the early solidification phase, (d) the surface tension at the grain boundary melt, (e) the grain morphology, (f) the ductility of the solidifying metal, and (g) the propensity of the weld metal to contract and the amount of restriction. All these aspects are ultimately connected with the metal composition. Here, the first two aspects are influenced by microsegregation, which is controlled by the cooling rate through solidification like the primary phase formation.

b. Intergranular Cracking

Intergranular cracking arises at the grain boundaries during the last step of the solidification, where solidifying and cooling material possesses higher tensile stresses compared to the strength of the solidified metal. Moreover, the substrate material also passes through a thermal cycle developing expansion and contraction on a small scale. Intergranular cracking is worsened by the intensification of thermal power or thickness of the substrate.

c. Reheat Cracking

Reheat cracking is a common phenomenon in low-grade ferrite steels containing chromium (Cr), molybdenum (Mo), vanadium (V), and tungsten (W). After manufacturing through welding or AM techniques, heat treatment is usually carried out to release stress and minimize the propensity of hydrogen or stress corrosion cracking. However, the major issue is that the cracking may take place in the heat-affected region through reheating.

During AM processes, the temperature in the heat-affected zone close to the fusion line is raised to the austenitizing temperature, where Cr, Mo, and V carbides dissolve into austenite regions. Faster cooling of the heat-affected zone may allow inadequate time to transform carbides, resulting in martensite with supersaturated alloy content. When the reheating is done to release the stress, the alloy content starts to reprecipitate along the high-energy austenite grain boundaries. This stimulates crack formation because of residual thermal stresses.

d. Liquation Cracking

Liquation cracking typically occurs in the mushy zone (MZ) or partially melted zone (PMZ) of the solidified build product, schematically shown in **Figure 13.** The alloy containing low melting temperature carbides results in melting in the PMZ during fast heating, even under the liquidus temperature. When cooling starts to take place, the PMZ undergoes tensile stress because of solidification shrinkage together with the thermal contraction from the solidified layers. In these circumstances, the liquid melt

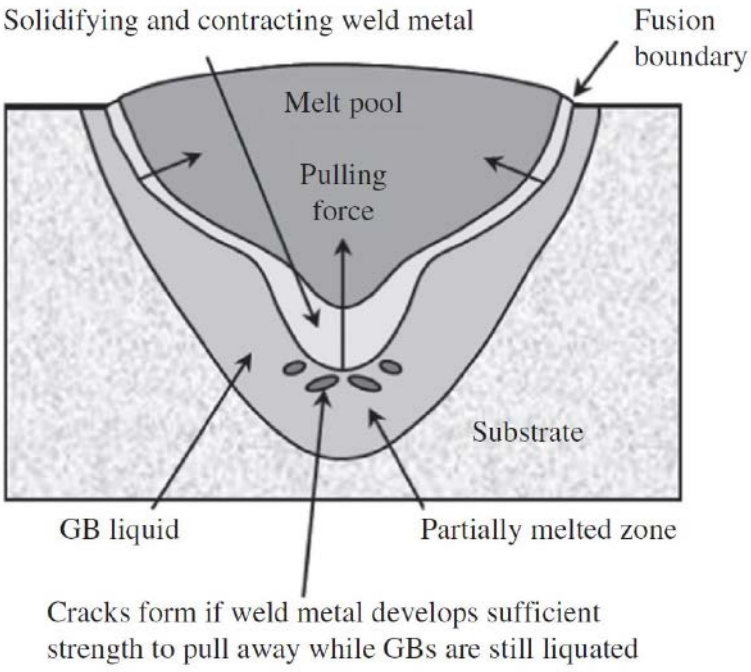

Figure 13: The mechanism of liquation cracking in the melt pool area. Source: Adapted from[10]. [Reproduced with permission from John Wiley & Sons Inc.]

pool around the grain boundaries or carbides may become the crack initiation locations.

Therefore, the possible reasons for liquation cracking are summarized as (i) wider MZ, formed because of a greater difference between liquidus and solidus temperatures, as observed in nickel-based superalloys, (ii) greater solidification shrinkage due to a larger size melt pool such as Ti-6Al-4V alloy, (iii) greater thermal contraction because of a large coefficient of thermal expansion, as observed in aluminum alloys.

Lamellar Tearing

Lamellar tearing is caused because of the combined effect of localized internal stresses and the lower ductility of the substrate material. The substrate material normally reveals nonmetallic inclusions. The tearing is activated by the de-bonding of nonmetallic inclusions such as silicates or sulfides in the substrate metal close to the heat-affected zone, where there is no retrieval of grains or reabsorption of precipitates for the homogenization of microstructure. This region of the substrate also receives greater thermal stresses because of the higher heat input during the AM processes.

POST SOLIDIFICATION PHASE TRANSFORMATION

After completing the solidification and cooling far down the solidus temperature, the metal will continue to cool down to room temperature and then endures the solid-state transformation. Reheating of previously deposited layers can again possess phase transformation. Here, the phase transformation that takes place through AM processing is presented for both cases of heat-treatable and non-heat-treatable alloys.

Ferrous Alloys/Steels

Wide varieties of steels have been manufactured through AM. The very usual microstructure of AM-processed austenitic stainless steels is cellular and columnar dendrites. An equiaxed structure is hardly observed because of the higher temperature gradient during the metal AM. The solidified microstructure is mainly cellular, and its size increases with the increase of deposit depth by accumulating heat through the AM techniques. Austenitic steels regularly have a tiny amount of ferrite distant from austenite.

During solidification, solute rejects at the boundary and enhances the intercellular areas with chromium and molybdenum, resulting in ferrite formation. However, the ferrite content drops at a faster cooling rate due to the inadequate time for solute restructuring at higher rates. Austenitic steels show comparatively higher thermal expansion coefficients, thus being susceptible to solidification cracking. For austenitic steels, the propensity to solidification cracking is reduced with the primary δ-ferrite phase, compared to the austenite phase.

Al Alloys

The most promising aspect of fabricating Al products using AM techniques is their higher thermal conductivity, which minimizes thermally produced stresses, as well as the necessity of support structures. Moreover, higher thermal conductivity permits greater processing speeds. The very familiar Al alloys obtainable in AM are the hardenable AlSi10Mg (EN AC-43000) and the eutectic $AlSi_{12}$ (EN AC-44200). As a high-strength alloy, a hardenable Al–Mg–Sc alloy is recommended by Schmidtke et al.[26] ($AlMg_{4.5}Sc_{0.66}$). Al–Sc alloys have received significant attention from the aerospace industry recently due to their high mechanical strength and attractive elongation rate.

In weldable Al alloys, the finer equiaxed grains are known to be less prone to solidification cracking. The equiaxed grains may have distortion by accommodating contraction strains, which make them ductile. The liquid supply and the remedial of initial cracks can also be an additional efficient approach for fine-grained materials. Moreover, finer grain materials with bigger grain boundaries may have less rigorous segregation of low melting solutes. Therefore, the propensity of the weld metal to contract and the level of restraint are the reasons to influence solidification cracking.

The possibility of AM-processed Al alloy parts exhibiting cracking is very robust. This could have been attributed to (i) greater solidification temperature span, (ii) higher coefficient of thermal expansion, and (iii) larger solidification shrinkage[27]. The laser-processed AM Al alloy also presents liquation and solidification cracks, such as laser-welded Al components. The addition of higher alloying elements in heat-treatable alloys may precipitate lower melting point eutectics, which then create liquation cracks. However, the liquation cracking can be lowered in LPBF manufactured Al alloys by reducing scattered energy concentration from the substrate.

Solidification cracking is barely found in Al alloy manufactured using a continuous-wave Nd:YAG laser; however, the opposite is correct for pulsed-wave Nd:YAG systems. In addition, the heat-treatable 2000 and 6000 Al alloy series are more prone to solidification cracking than the work hardening 5000 alloy series through laser processing.[25] In Al alloys, the solidification cracking is metallurgically guided by the temperature limit of dendrite consistency and the existing liquid level during cooling. The tendency of solidification cracking enhances with a wider solidification temperature range, which is directly correlated with solidification strains.

In the LPBF process, the non-equilibrium and rapid solidification may result in insufficient diffusion that eventually lowers the liquidus and solidus temperatures. Subsequently, a broader temperature range and larger solidification cracking propensity are usually common in the LPBF process of Al alloys, e.g., 0.8% Si in Al–Si; 1–3% Cu in Al–Cu; 1–1.5% Mg in Al–Mg; and 1% Mg_2Si in Al–Mg–Si alloys [27]. However, the addition of some alloying constituents with a focus on narrowing down the solidification temperature limit may change the melt pool composition to minimize cracking.

In laser-processed AM, there is an ideal energy density to develop crack-free, entirely dense products. Therefore, the solidification cracking starts at energy densities larger than the ideal value because of the following: (i) lower liquid viscosity, (ii) lengthy liquid period, and (iii) subsequent higher thermal stresses. On the other hand, with lesser energy densities, a disorganized solidification front and a major balling phenomenon may result in crack formation because of the higher unsteadiness of the liquid due to Marangoni convection, nonlinear capillary forces, and inconsistent wetting angles.

The alloying constituents and impurities are segregated along the grain boundaries during the solidification through the microsegregation process, resulting in the liquation layers that also cause the temperature to further cool down. To reduce the sources of stresses and cracks, adequate liquid is needed to seal the cracks and remove the strain generated through the solidification. Thus, crack admittance by strain development competes with crack remedial through refilling by remaining liquid. Although the crack growth rate rises with strains, the replenishing and remedial approach of the remaining liquid is regulated by its fluidity. The eutectic required to avoid cracking differs with composition and cooling rate.

Nickel Alloys/Superalloys

a. Inconel 625

Inconel 625 (IN625) is a Ni-based solid solution strengthening superalloy and is greatly strengthened by Mo and Nb contents.[28,29] Inconel 625 has applications in aerospace, marine, chemical, and petrochemical industries, possessing superior properties, including strength at elevated temperatures, better creep resistance, excellent fatigue property, resistance to oxidation and corrosion, and accessible processability. However, the microstructure of AM-processed IN625 has austenitic phases, where no carbides and any other phases are recognized. In the laser-processed AM technique, the beam travels very fast (>1,000 mm/s) and makes the solidification time short (<1 ms). The atomic restoration speed ahead of the short period of liquid/solid solidification is greater than the diffusion speed. Therefore, the faster solidification causes the solute atoms to be trapped and creates the well-known "solute trapping."

b. Inconel 718

Inconel 718 (IN718) is a Ni-based superalloy with higher quantities of Nb, Cr, and Fe.[30] It has applications in the aerospace and energy/resources industries because of its good oxidation resistance, creep, and mechanical properties at elevated temperatures. IN718 is reinforced by the precipitation of consistent secondary phases. Knowledge of the solidification phenomenon of IN718 is crucial to be familiar with the phase progression in the AM-processed alloys, and the microstructure of Ni-based alloys is essential to improve compositional variants, process mechanisms, and post-processing techniques to reach similar or superior properties of their equivalents manufactured by conventional methods.

Intermetallic compounds like Laves Ni_3Nb-δ, and Nb-rich MC are usually found in interdendritic areas or grain boundaries of Ni-based alloys, which undesirably affect the mechanical properties. Laves phase, which occurs in Nb-rich melt with a long-chain structure controlled by Nb segregation and liquid melt distribution, is often found to produce hot cracking. In addition to the cooling rate, Laves phase formation is also influenced by the solidification structure reliant on the proportion of temperature gradient and the growth rate. Smaller dendrite arm spacing with a higher cooling rate and lower *G/R* ratio helps result in distinct Laves phase particles. In contrast, the larger dendrite arm spacing with a lower cooling rate and higher *G/R* ratio has a tendency to develop incessantly dispersed larger particles of Laves phase.

c. Stellite

Stellite alloys show better corrosion and wear resistance at a wide variety of interactions and environments in industries, including aerospace, oil and gas, forging, and power production.

The characteristic microstructure of Stellite contains hard carbides distributed through a cobalt-rich solid solution matrix. Stellite 12, which is a hypo-eutectic alloy, forms a solid solution cobalt matrix through solidification. When the temperature drops, the amount of Co in liquid is also lowered and then the eutectic state is attained. The residual liquid reacts with the eutectic structure comprising carbides and a Co-based matrix. Moreover, the alloy possesses blocky eutectic carbides. Laser-processed AM follows faster melting and solidification practice, and the overlapping trends of multiple tracks and layers will result in remelting of the earlier solidified layers, which may cause divergence in microstructure development.

For Co-based superalloys, the major strengthening mechanisms include solid solution strengthening through the dispersion of Cr, W, and other elements in the Co matrix, whereas M_7C_3, $M_{23}C_6$, and other carbides act as a major function in precipitation strengthening between the dendrite regions. Therefore, the higher hardness of the carbides may enrich the hardness value and wear property of the alloys. For AM-processed Stellite 12, M_7C_3 is the primary carbide, which is in a metastable condition and decomposes to discharge Cr, C, and W elements at higher temperatures and facilitates the formation of $M_{23}C_6$ and M_6C carbides.

Titanium Alloys

Titanium alloys have vast applications in aerospace, chemistry, ship manufacturing, and other industrial sectors due to their superior properties, e.g., greater strength-to-weight ratio, high corrosion resistance, and compatibility with composite structure in the application of structural parts[31].

The metallurgy of Ti alloys is directed by the phase transformation that occurs in pure metal at 882 °C (1619 °F). Pure titanium shows an alpha (α) phase (hcp structure) below the temperature and a beta (β) phase (bcc structure) above the temperature.

The primary outcome of alloying additions to titanium is the modification of the conversion temperature and formation of two-phase structures, having both α- and β-phases. Commercially obtainable titanium alloys are categorized based on the impact of α- and β-phases, which consist of (i) α alloys, (ii) near-α, (iii) α–β, (iv) near β, and (v) β alloys. The α alloys are generally not heat treatable and typically weldable; α–β alloys are heat treatable and weldable, with the possibility of losing ductility near the weld area; β alloys are easily heat treatable, mostly weldable, and show higher to medium temperature levels. In a solution-treated state, the alloy possesses superior cold formability. Various types of stabilizing constituents on Ti alloy and their impact on phase transformation are schematically presented in **Figure 14.**

***A* Stabilizers:** These types of components have large solubility in the α-phase, which usually increases the transformation temperature. The effect of α-stabilizing elements on the titanium

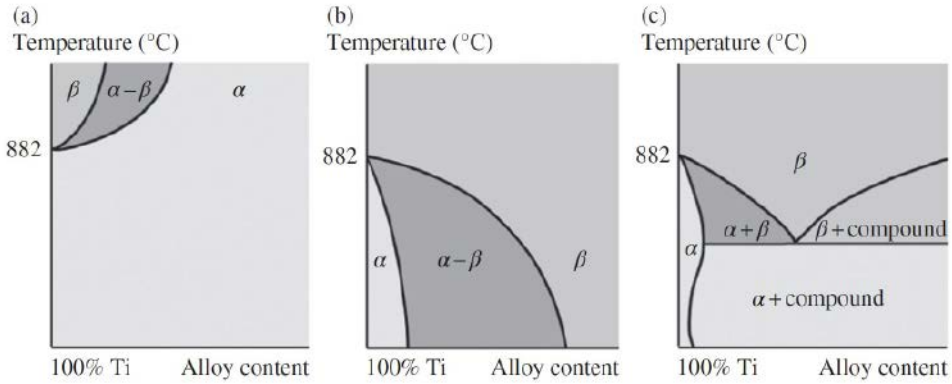

Figure 14: Effect of (a) α-stabilizing, (b) β-isomorphous, and (c) on β-eutectoid elements on the titanium phase diagram.
[Source: openly accessible.]

phase diagram is presented in **Figure 14a.** Very common α stabilizers to Ti alloy are Al, O_2, N_2, or C. The addition of O_2 to pure Ti has the potential to make a variety of grades with higher strength. Al is a commercially used stabilizer, which also acts as the main constituent of many commercial alloys. It can effectively strengthen the α-phase at a higher temperature of about 550 °C (1022 °F). The α-phase can be also reinforced with tin or zirconium, which have substantial solubility equally in the α- and β-phases. They do not prominently affect the transformation temperature and are therefore known as neutral stabilizers.

β **Stabilizers:** Components that reduce the transformation temperature, easily disperse in and reinforce the β-phase, and show lower α phase solubility are termed β stabilizers. They can be classified into two classes based on their constitutional activities with Ti, β-isomorphous elements (Mo, V, Nb, and Ta), and β-eutectoid elements (Fe, Cr, and Mn, where eutectoids are decomposed as titanium–iron, titanium–chromium, and titanium–manganese).

Variation in the phase composition is a significant basis of microstructural heterogeneity in AM-produced metallic products. For example, in α + β titanium alloys (Ti-6Al-4V), usually, three phases are stated, e.g., α phase, β-phase, and α-martensitic phase. Because of the intricate phase transformation methods, it is challenging to precisely calculate the phase composition in AM Ti alloys. The cooling rate and the manufacturing temperature are the two key process parameters to affect the ultimate phase structures in laser or EB-AM-made parts. Therefore, the microstructural differences result from repeated thermal inputs from sequential buildups.

Multiple studies have been conducted to shed some light on the effect of faster cooling on the microstructure development in Ti64 alloy by Ahmed and Rack, where improved Jominy and quench test techniques were adopted[32]. The development of a complete martensitic structure is noticed at cooling rates of 410 and 20 °C/s. This conversion is gradually switched by diffusion-influenced Widmanstätten α-phase at slower cooling rates.

PHASES AFTER POST-PROCESS HEAT TREATMENT

Ferrous Alloys

In laser manufactured 17-4 PH steel, austenite reversion occurs during the aging treatment. The austenite phases in laser-processed AM steel transform to martensite during heat treatment. This is believed to happen due to the stress release, which permits the austenite to transform martensite through post-treatment cooling. Austenite reversion is also common in laser fabricated maraging steel, where during aging, Ni-rich returned austenite shell forms around the retained austenite areas[33].

Al Alloys

The precipitation-hardened AlSi10Mg alloy in the AM process does not show any precipitates because of the rapid solidification, except for some Si segregation near the grain boundaries. After solution treatment, Si starts to form Si particles in the α-Al matrix. The application of water quenching and peak-hardening followed by solution treatment results in globular Si particles with needle-like Mg_2Si precipitates. Therefore, the microstructural anisotropy is diminished through disappearing dendrites, melt pool edges, and heat-affected zones.

Ni Alloys
For IN718, the most commonly applied heat treatments are homogenization or solution aging treatment, which can stimulate the diffusion process through the segregation of some components and dissolve some phases of carbides and Laves in the austenite matrix. Moreover, aging can promote the precipitation of γ′ and γ″ elements. After the heat-treatment process, the plate-like δ-Ni_3Nb precipitates form along the grain boundaries, as well as within the grains. However, γ′ and γ″ precipitates are very fine to determine with precision.

For cobalt-based superalloys, solid solution and precipitation strengthening are the major reinforcing mechanisms. Cr, W, and other components, which disperse on the cobalt matrix, can act as solid solution strengtheners. M7C3 is the major carbides of Stellite 12, which is a metastable phase, fabricated through Laser AM techniques. This carbide phase will decompose to Cr, C, and W components during heat treatment and promote the formation of $M_{23}C_6$ and M_6C carbides.

Ti Alloys
Ti-6Al-4V alloy possesses excellent stability in strength, ductility, fatigue, and fracture properties, except for the creep property at temperatures above 300 °C. The structural development of this alloy is greatly influenced by heat treatment.

In laser-processed AM techniques, the finer acicular α'-phase in the as-manufactured Ti-6Al4V alloy results in an inadequate outcome through a conventional heat-treatment process. The metastable α'-phase is very fine and contains greater densities of dislocations and twins, which impede the grain growth during heat treatment, directing to a finer $\alpha + \beta$ lamellar structure. During the heat treatment (~400 °C), in the first step, the α-phase starts to nucleate along the boundary of the acicular α-phase, which pushes the vanadium into the boundary of the newly formed α grain. After that, the β-phase forms in the area of higher vanadium content among the α-phase laths. Therefore, the heat-treatment temperature is important to retain the refined microstructure. Moreover, the appropriate temperature and the holding time may relieve the residual stress. Consequently, the stress-relief heat treatment may contribute to two major structural modifications decreasing the dislocation density and the breakdown of α'-phases. The lamellar $\alpha + \beta$ structure, which exists as a colony shape, starts to become coarsen α lamellae with increasing the heat-treatment temperature. This way, some α grains become globular and reduce morphological anisotropy.

MECHANICAL PROPERTIES

The defects such as porosity influence crack generation and decline in mechanical properties. Therefore, a higher density above 99.5% is usually the first priority for AM technique optimization. The rationale for optimizing parameters to maximize the density by reducing porosities is the fact that the size and distribution of pores have a major impact on mechanical properties.

Hardness
The hardness depends on the cross-sectional area, where with a larger cross-sectional area, the hardness drops due to microstructure coarsening. The basis of this microstructure coarsening is the greater thermal input in a bigger area, which makes a slower cooling process. Therefore, the heterogeneity in hardness depends on the thermal history of the individual layer. Prospective improvement using different process parameters with respect to the cross-sectional area may improve the heterogeneity in hardness.

a. Hardness of AM-Processed Ferrous Alloys
For multi-layer deposited steels, the micro-hardness value drops from the very initial deposited layers, which afterward enhances along the upper layers. This phenomenon is because of the repeated heating of the former layers and letting the time be annealed to some extent. Additionally, this inconsistency is ascribed to the time dependency of the cooling rate in the liquid melt and comparatively the slow solidification rate in the middle area. Therefore, greater hardness values are typically obtained both at the top and bottom of the AM parts in contrast with the central area.

In low alloy steels (41XX series), the content of alloying components, as well as the amount of carbon, controls the phase formation, which eventually affects the hardness values. In high carbon-containing steel, through the rapid cooling in the AM process, hard martensite phases are developed, which contribute to hardness development.

Austenitic stainless steels such as 316 and 316L have a similar chemical composition with an identical dendritic structure. However, a slight change in carbon content (316L ≤ 0.03 wt.%

C and 316 ≤ 0.08 wt.% C) between 316L and 316 shows a significant change in hardness.

b. Hardness of AM-Manufactured Al Alloys
The most familiar Al alloys fabricated through the AM technique contain greater volumes of Si, which stimulate eutectic solidification. The combined effect of higher cooling rates and alloying elements (e.g., Si) promotes the formation of finer secondary arms spacing, which results in higher hardness in AM-manufactured alloys.

Some post-processing techniques may influence the hardness property in AM-processed Al alloys. Previous research has reported that solutionizing and aging treatment may drop the hardness value, compared to the as-deposited condition. This may occur due to the influence of microstructural change caused by solutionizing and aging treatment, which coarsen the Si particles.

On the other hand, HIP, as a post-process technique, also has an impact on the hardness of AM-manufactured alloys. HIP usually results in microstructural coarsening as well as releasing residual stresses, which drop the hardness of products.

c. Hardness of AM-Manufactured Nickel Alloys
The faster cooling rate in AM-processed Ni alloys leads the strengthening elements such as Mo and Nb to remain in the Ni alloy matrix. Therefore, a greater lattice distortion occurs by these point defects, which also enhances the hardness of the AM-fabricated samples compared to the conventional cast alloys. As IN625 is a solid solution-strengthened superalloy, phase transformation occurs through heat treatment. At low-temperature annealing (e.g., 700 °C (1292 °F)), the release of residual stress lowers the hardness. However, annealing between 800 and 900 °C (1472 and 1652 °F) forms δ (Ni3Nb) precipitate, which improves the hardness. δ is an orthorhombic phase having a greater mismatch with the Ni matrix and thereby develops hardness. However, annealing above 1,000 °C (1832 °F) dissolves δ phases in the Ni matrix and reduces the lattice distortion together with hardness.

d. Hardness of AM-Manufactured Ti Alloys
Generally, the AM-processed Ti-6Al-4V alloy possesses different structural features after various post-processes. For example, LPBF-processed Ti-6Al-4V alloy shows a finer martensitic structure with acicular laths after stress relieving. In contrast, HIP results in a coarser structure of lamellar α and β.

Ti-6Al-4V alloy endures a phase change from body-centered cubic β phase to a structure comprising hexagonal α-phase and few amounts of β-phase when the temperature is about 1,000 °C (1832 °F). The solid-state transformation may result in measurable structures within grains and, based on the cooling behavior during the conversion of temperature, the α-phase may result in diverse morphology.

Some post-processing treatments, such as heat treatment and annealing, may release residual stress with some coarsening effect of α-phases, which eventually raise the ductility and toughness, compromising the strength and hardness of AM-manufactured Ti-6Al-4V alloy. The precipitation hardening and solid solution strengthening both cause the mechanical property to increase.

Tensile Strength and Static Strength

a. Tensile Behavior of AM-Fabricated Ferrous Alloys
Tensile behavior of the AM-manufactured steel often satisfies the required specifications for technical usage. Formation of finer grains precedes a substantial rise in yield strength and ultimate tensile strength. As for the ductility of the AM samples, a minor amount of porosity results in ductile fracture with elongation values similar to wrought alloys. On the other hand, a greater amount of porosity influences brittle failure, which considerably lowers elongation. The AM-manufactured precipitation strengthening steels are relatively soft, as there is no precipitation formation due to inadequate time for faster solidification. In martensitic grade steels, the amount of retained austenite and austenite reversion phenomenon impacts the tensile properties.

b. Tensile Behavior of AM-Fabricated Al Alloys
The finer grains developed in AM-processed Al alloys promote increased strength in the as-built condition. However, the precipitation strengthens the AM-fabricated AlSi10Mg alloy, which shows similar tensile properties to the solution-strengthened $AlSi_{12}$ alloy. During heat treatment of AM-fabricated AlSi10Mg alloys, the earlier fine grain becomes coarser, and precipitation formation takes place. The coarse grains deteriorate the tensile strength, whereas precipitates strengthen the alloy. The AM-manufactured scandium-containing alloy aids to retain fine grain structure and also completely coherent precipitates after aging

heat treatment. However, in the AA 2139 (Al–Cu, Mg) alloy, loss of Mg occurs during AM, which afterward lowers the precipitate volume as well as drops the tensile strength.

c. Tensile Properties of AM-Manufactured Ni Alloys

The tensile behavior of AM-fabricated Ni alloys is comparable to the wrought one, while the ductility is low because of the precipitation of γ' and γ'' phases in the austenite matrix, and δ phases around the grain boundaries.

d. Tensile Properties of AM-Manufactured Ti Alloys

In AM, Ti-6Al-4V is the most comprehensively studied group of alloys. As Ti is an appropriate material for different AM techniques, the process input parameters influencing microstructures and tensile behaviors have been considered systematically, specifically for Ti-6Al-4V alloys. The better tensile strength is correlated with the finer martensitic structure resulting from rapid cooling. Finer grains always enhance yield strength and ductility. The deformed hexagonal lattice of α' martensite is stronger compared to lamellar α, which is due to the finer lath width, without reducing the ductility.

Typically, AM-fabricated Ti-6Al-4V alloy has better tensile strength than cast or wrought alloys, i.e., $\alpha + \beta$ alloys, but lower ductility than pure Ti, because of the impeding of the twinning deformation phenomenon.

It is concluded that AM-manufactured Ti-6Al-4V alloy is equivalent to cast or wrought products. It is important to note that the tendency of anisotropy is divergent for tensile strength and ductility using different techniques. The lower ductility of Ti-6Al-4V alloy manufactured using LPBF and laser-directed energy deposition techniques are ascribed to the development of brittle martensite phases. Ductility is the anisotropic property, which is different in the horizontal and vertical direction of the building and can be improved through post-process heat treatment.

Fatigue Behavior of AM-Manufactured Alloys

The fatigue property depends on the isotropic behavior of the AM-fabricated samples. Usually, fatigue strengths are greater in the horizontal built direction than the vertical direction in the LPBF process. The fatigue life of the as-fabricated AM samples is considerably lower than the wrought ones, which is due to the surface roughness and internal defects influencing the cracks to initiate. The fatigue property of AM products can be enhanced by post-processing heat treatment, hot isostatics pressing, and surface quality improvement. Besides surface features and internal defects, fatigue crack growth also depends on the crystallographic direction of grains that hold the crack tip, the number of grain boundaries around it, and the type of residual core stress. Post-processing like surface grinding and heat treatment may significantly enhance the mechanical properties of AM-fabricated parts to be similar or even superior to conventional counterparts.

a. Factors Influencing Fatigue Behavior in AM

The well-known defects to introduce fatigue cracks in AM components are the pores and voids generated from entrapped gas and/or lack of fusion, as well as inadequate fusion. There is a controversy about the build orientation anisotropy on the mechanical properties of AM products. The difference in thermal profile experienced in different build directions control the morphology of the microstructure, defects, and eventually the ductility.

Tensile residual stresses are disadvantageous to fatigue properties; their impact may be reduced or prevented through suitable process parameters, corrected build direction, or releasing them by applying post-processing heat treatment (PPHT).

b. Fatigue Performance of AM-Manufactured Ferrous Alloys

The fatigue property of 316L alloy is influenced by its monotonic strength. The building orientation shows a significant impact on the fatigue life of 17-4 PH steel. Usually, the horizontally built samples show higher fatigue properties because of the structural configuration along the loading direction. However, in vertical samples, defects are detrimental as they create stress accumulation during loading.

The fatigue life of ferrous alloys is influenced by the alloying element and the post-processing techniques. Moreover, PPHT can expand fatigue life through the recovery of ductility and toughness of the alloy.

c. Fatigue Behavior of AM-Fabricated Al Alloys

Although Al alloys have different physical properties than ferrous and Ti alloys, in the areas of thermal conductivity, surface reflectivity, and melt viscosity, the AM-fabricated proper-

ties are comparable. For example, in eutectic AlSi12 and AlSi10Mg alloys, the faster cooling rate develops a finer lamellar dendritic network of eutectic phases. The formation of strengthening phases of Mg2Si as well as the distribution of Si particles in the Al matrix contributes to the tensile strength of the AM alloy compared to the conventional sand-cast or die-cast alloys. Throughout the plastic deformation, the dendrite structure acts as load-bearing elements by breaking through the dendritic arms, followed by the ultimate delamination of the Al matrix. The rapid cooling rate results in the growth of residual pores and eventually forms initial cracks at vital pores. Therefore, the joining of several cracks causes a rapid fracture while dropping the ductility.

The application of heat treatment usually reduces residual porosity, and thereby fatigue inconsistency. In high cycle fatigue (HCF), the fatigue property is influenced by the resistance to the crack origination rather than growth. Materials performance is connected to the fatigue scheme under consideration. Materials that have an improved tensile strength are stronger in the low cycle fatigue scheme, which is different from HCF.

d. Fatigue Property of AM-Manufactured Nickel Alloys

Wrought IN718 contains δ phases, whereas the AM-fabricated IN718 comprises Laves phases. It is known that the wrought IN718 shows a better fatigue crack resistance than the AM-processed IN718 because of the absence of the detrimental Laves phase.

e. Fatigue Behavior of Additive-Manufactured Ti Alloy

A comparison of the fatigue property with the wrought alloy specifies that AM-manufactured alloys have a shorter fatigue life. It is already identified that the fatigue property of AM alloy is greatly influenced by internal defects, which perform as micro-notches and result in stress accumulation. The application of post-processing treatment is important to remove or shrink pores to a far smaller size, which makes them unable to influence fatigue behavior.

REFERENCES:

[1] *J. Dawes, R. Bowerman, and R. Trepleton, "Introduction to the additive manufacturing powder metallurgy supply chain," Johnson Matthey Technol. Rev., vol. 59, no. 3, pp. 243–256, 2015, doi: https://doi.org/10.1595/205651315X688686.*

[2] *G. Egger, P. E. Gygax, R. Glardon, and N. P. Karapatis, "Optimization of powder layer density in selective laser sintering," 10th Solid Free. Fabr. Symp., pp. 255–263, 1999*

[3] *W. E. Frazier, "Metal additive manufacturing: A review," J. Mater. Eng. Perform. 2014, doi: https://doi. org/10.1007/s11665-014-0958-z.*

[4] *Y. J. Liang, X. Cheng, and H. M. Wang, "A new microsegregation model for rapid solidification multicomponent alloys and its application to single-crystal nickel-base superalloys of laser rapid directional solidification," Acta Mater., vol. 118, pp. 17–27, 2016, doi: https://doi.org/10.1016/j. actamat.2016.07.008.*

[5] *B. Cantor, W. T. Kim, B. P. Bewlay, and A. G. Gillen, "Microstructure – cooling rate correlations in meltspun alloys," J. Mater. Sci., vol. 26, no. 5, pp. 1266–1276, 1991, doi: https://doi.org/10.1007/BF00544465.*

[6] *D. D. Gu, W. Meiners, K. Wissenbach, and R. Poprawe, "Laser additive manufacturing of metallic components: Materials, processes and mechanisms," Int. Mater. Rev., vol. 57, no. 3, pp. 133–164, 2012, doi: https://doi.org/10.1179/1743280411Y.0000000014.*

[7] *A. Y. Uzan, Y. Kozak, Y. Korin, I. Harary, H. Mehling, and G. Ziskind, "A novel multi-dimensional model for solidification process with supercooling," Int. J. Heat Mass Transf., vol. 106, pp. 91–102, 2017, doi: https://doi.org/10.1016/j.ijheatmasstransfer.2016.10.046.*

[8] *W. Kurz and D. Fisher, Fundamentals of solidification, Trans Tech Publications, Switzerland, Germany, UK, USA, 1986.*

[9] *M. E. Glicksman, "Principles of solidification: An introduction to modern casting and crystal growth concepts," no. 2, Springer, New York, pp. 1–520, 2011, doi: https://doi.org/10.1007/978-1-4419-7344-3.*

[10] *S. Kou, Metallurgy, Welding Metallurgy, 2nd edition, vol. 822, no. 1–3, John Wiley & Sons,,2003.*

[11] *T. DebRoy et al., "Additive manufacturing of metallic components – Process, structure and properties," Prog. Mater. Sci., vol. 92. pp. 112–224, 2018, doi: https://doi.org/10.1016/j.pmatsci.2017.10.001.*

[12] *H. Zhao, "Microstructure Heterogeneity in Additive ManufacturedTi-6Al-4V," Thesis, 2017.*

[13] *W. Callister and D. Rethwisch, Materials science and engineering: an introduction, 8th edition, vol. 94, John Wily & Sons, Inc, 2007.*

[14] *S. Das, "Physical aspects of process control in selective laser sintering of metals," Adv. Eng. Mater., vol. 5, no. 10, pp. 701–711, 2003, doi: https://doi.org/10.1002/adem.200310099.*

[15] *D. A. Porter and K. E. Easterling, "Phase transformations in metals and alloys, 3rd edition," CRC Press, p. 138, 2014, doi: https://doi.org/10.1146/annurev.ms.03.080173.001551.*

[16] *A. Basak and S. Das, "Epitaxy and microstructure evolution in metal additive manufacturing," Annu. Rev. Mater. Res., vol. 46, no. 1, pp. 125–149, 2016, doi: https://doi.org/10.1146/annurev-matsci-070115-031728.*

[17] *S. A. David and J. M. Vitek, "Correlation between solidification parameters and weld microstructures," Int. Mater. Rev., vol. 34, no. 1, pp. 213–245, 1989, doi: https://doi.org/10.1179/imr.1989.34.1.213.*

[18] *M. Garibaldi, I. Ashcroft, M. Simonelli, and R. Hague, "Metallurgy of high-silicon steel parts produced using selective laser melting," Acta Mater., vol. 110, pp. 207–216, 2016, doi: https://doi.org/10.1016/j. actamat.2016.03.037.*

[19] *A. Yadollahi, N. Shamsaei, S. M. Thompson, and D. W. Seely, "Effects of process time interval and heat treatment on the mechanical and microstructural properties of direct laser deposited 316L stainless steel," Mater. Sci. Eng. A, vol. 644, pp. 171–183, 2015, doi: https://doi.org/10.1016/j.msea.2015.07.056.*

[20] *X. Zhao, L. Liu, and J. Zhang, "Investigation of grain competitive growth during directional solidification of single-crystal nickel-based superalloys," Appl. Phys. A Mater. Sci. Process., vol. 120, no. 2, pp. 793–800, 2015, doi: https://doi.org/10.1007/s00339-015-9290-1.*

[21] *T. Wang, Y. Y. Zhu, S. Q. Zhang, H. B. Tang, and H. M. Wang, "Grain morphology evolution behavior of titanium alloy components during laser melting deposition additive manufacturing," J. Alloys Compd., vol. 632, pp. 505–513, 2015, doi: https://doi.org/10.1016/j.jallcom.2015.01.256.*

[22] *L. Thijs, M. L. Montero Sistiaga, R. Wauthle, Q. Xie, J. P. Kruth, and J. Van Humbeeck, "Strong morphological and crystallographic texture and resulting yield strength anisotropy in selective laser melted tantalum," Acta Mater., vol. 61, no. 12, pp. 4657–4668, 2013, doi: https://doi.org/10.1016/j.actamat.2013.04.036.*

[23] *A. Weisheit, A. Gasser, G. Backes, T. Jambor, N. Pirch, K. Wissenbach, Direct laser cladding, current-status and future scope of application. In: Majumdar J., Manna I. (eds) Laser-assisted fabrication of materials. Springer series in materials science, vol 161, Springer, Berlin, Heidelberg, 2013. https://doi.org/10.1007/978-3-642-28359-8_5. pp. 221–240.*

[24] *H. Gong, K. Rafi, H. Gu, T. Starr, and B. Stucker, "Analysis of defect generation in Ti-6Al-4V parts made using powder bed fusion additive manufacturing processes," Addit. Manuf., vol. 1, pp. 87–98, 2014, doi: https://doi.org/10.1016/j.addma.2014.08.002.*

[25] *M. Pastor, H. Zhao, and T. Debroy, "Pore formation during continuous wave Nd:YAG laser welding of aluminium for automotive applications," Weld. Int., vol. 15, no. 4, pp. 275–281, 2001, doi: https://doi.org/10.1080/09507110109549355.*

[26] *K. Schmidtke, F. Palm, A. Hawkins, and C. Emmelmann, "Process and mechanical properties: Applicability of a scandium modified Al-alloy for laser additive manufacturing," Phys. Procedia, 2011, vol. 12, no. PART 1, pp. 369–374, doi: https://doi.org/10.1016/j.phpro.2011.03.047.*

[27] *X. Cao, W. Wallace, J. P. Immarigeon, and C. Poon, "Research and progress in laser welding of wrought aluminum alloys. II. Metallurgical microstructures, defects, and mechanical properties," Mater. Manuf. Process., vol. 18, no. 1, pp. 23–49, 2003, doi: https://doi.org/10.1081/AMP-120017587.*

[28] *C. P. Paul, P. Ganesh, S. K. Mishra, P. Bhargava, J. Negi, and A. K. Nath, "Investigating laser rapid manufacturing for Inconel-625 components," Opt. Laser Technol., vol. 39, no. 4, pp. 800–805, 2007, doi: https://doi.org/10.1016/j.optlastec.2006.01.008.*

[29] *V. Shankar, K. Bhanu Sankara Rao, and S. Mannan, "Microstructure and mechanical properties of Inconel 625 superalloy," J. Nucl. Mater., vol. 288, no. 2, pp. 222–232, 2001, doi: https://doi.org/10.1016/S0022-3115(00)00723-6.*

[30] *B. Farber et al., "Correlation of mechanical properties to microstructure in Metal Laser Sintering Inconel 718," Mater. Sci. Eng. A, vol. 712, pp. 539–547, 2018, doi: https://doi.org/10.1016/j.msea.2017.11.125.*

[31] *G. C. Li, J. Li, X. J. Tian, X. Cheng, B. He, and H. M. Wang, "Microstructure and properties of a novel titanium alloy Ti-6Al-2V-1.5Mo-0.5Zr-0.3Si manufactured by laser additive manufacturing," Mater. Sci. Eng. A, vol. 684, pp. 233–238, 2017, doi: https://doi.org/10.1016/j.msea.2016.11.084.*

[32] *T. Ahmed and H. J. Rack, "Phase transformations during cooling in α+β titanium alloys," Mater. Sci. Eng. A, vol. 243, no. 1–2, pp. 206–211, 1998, doi: https://doi.org/10.1016/S0921-5093(97)00802-2.*

[33] *E. A. Jägle, P. P. Choi, J. Van Humbeeck, and D. Raabe, "Precipitation and austenite reversion behavior of a maraging steel produced by selective laser melting," J. Mater. Res., vol. 29, pp. 2072–2079, 2014, doi: https://doi.org/10.1557/jmr.2014.204.*

03 Material Parameter Measurement in EVIDENT Microscopy Software Solutions – PRECiV

SUMMARY

Additive manufacturing (AM) and 3D printing are novel manufacturing processes that build metallic or non-metallic parts by adding material, layer by layer, based on computer-aided design models. Evident's PRECiV™ software offers flexible solutions for additive manufacturing quality assurance. With a guided workflow for different measurement tasks, PRECiV image analysis software provides easy-to-use, reliable solutions to conduct complex analyses according to international standards in the field of material qualification and evaluation.

For example, with the Porosity solution, it is possible to measure different porosity-related parameters that help to quickly identify whether the material meets quality requirements. In addition, PRECiV software provides both intercept and planimetric measurements of the grain size structure of AM pieces. Moreover, monitoring the solidification time in titanium or aluminum alloys is a key factor in improved mechanical properties (such as tensile strength and elongation). The locally different energy input on the surface during the additive manufacturing process often causes grains in the material to grow unevenly. This can cause dendrites, a tree-like branching structure. The dendrite arm spacing (DAS) is directly connected to the solidification time. With a known DAS provided by PRECiV software and a specific material-dependent constant, it is easy to calculate the solidification time and tailor the final quality of parts.

Additive manufacturing and 3D printing have been used as standard terms to indicate a novel manufacturing process that builds a metallic or non-metallic part by adding material, layer by layer, based on a computer-aided design (CAD) model. The three-dimensional CAD model is sliced vertically into several two-dimensional sections. These two-dimensional layers will be used as a path for powerful energy sources, which could be welding torches, electron beams or lasers to melt the material onto each other, either wire or metal powder, to form the final component.

PRECiV offers flexible solutions that can be used for additive manufacturing quality assurance. With a guided workflow for different measurement tasks PRECiV provides easy-to-use and highly reliable solutions to conduct complex analysis according to international standards (ISO, ASTM, JIS, DIN) in the field of material qualification and evaluation (Metal, Ceramics, Coatings, Weldments, Aluminum alloys, Cast Iron …). Analysis is possible on live or already recorded images. As the used measuring conditions can be saved, it is easy to recall them at a later stage. Storing the measurement conditions increases the reproducibility of the results. If one has several images of the same type that need to be measured, the workflow provides batch processing. This improves the statistical measurement data.

POROSITY

Additive manufacturing techniques using optimized process parameters can build parts with relative density higher than 99.8%. Even when using optimized process parameters and operational conditions, it is reported that there is an uncontrolled and unavoidable percentage of porosity in additive manufactured parts. Porosity directly influences the mechanical properties and operational performance of the part.

There are at least three sources for porosity in AM manufactured parts: gas porosity, lack-of-fusion, and keyholing.

With the "Porosity" solution in PRECiV image analysis software, it is possible to measure different porosity-related parameters. Porosity describes any void or hole found in a material. The morphology of pores in terms of their size, shape, surface constituents, location and frequency, help to ascertain the defect's origin.

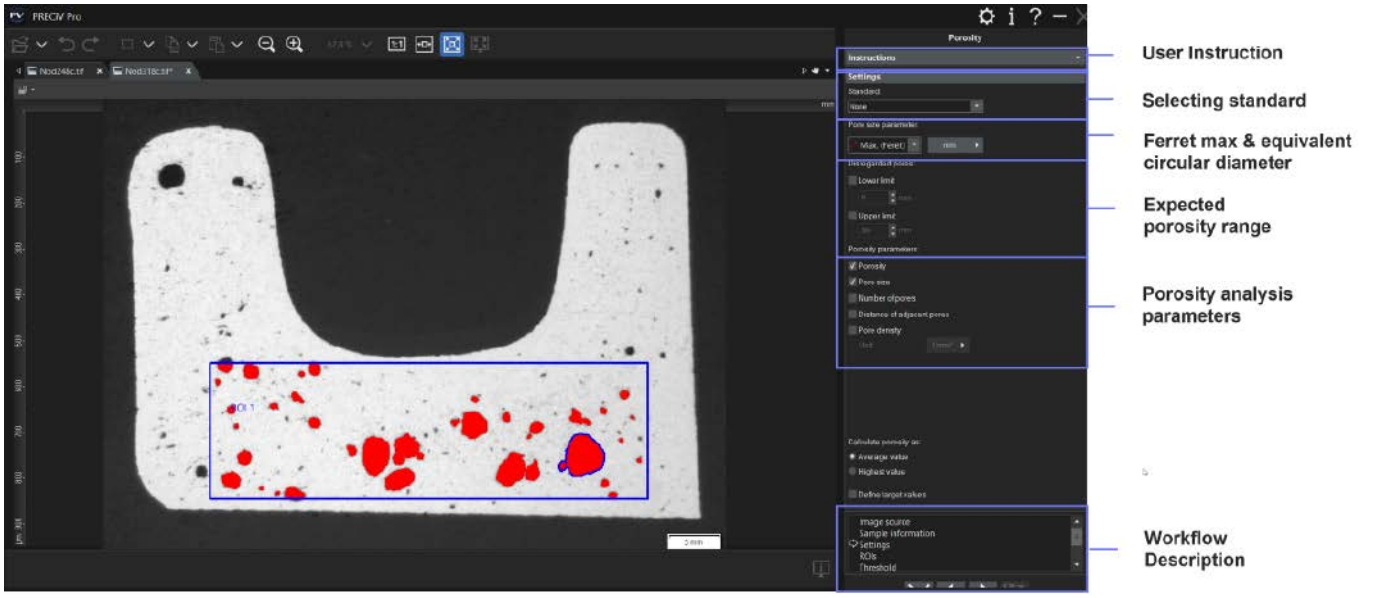

Figure 1: Workflow-based pore analysis in a region of interest (ROI)

Pore analysis parameters
With a threshold-based measurement of pore content per ROI, the software calculates the following parameters: Porosity, Pore Size, Number of pores, Distance of adjacent pores and the pore density. The setting of limits helps to quickly identify whether the material meets quality requirements.

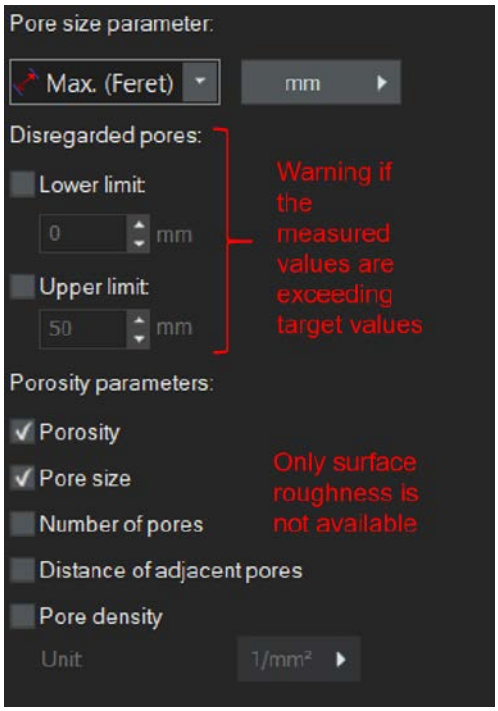

GRAINS

Additive manufacturing will melt material layers onto each other with powerful energy sources to form the final product. Melting processes change the microstructure of the material used.

For metals and ceramics, grain size is one of the most significant metallographic measurements as it directly affects mechanical properties. Common grain size measurements include grains per unit area/volume, average diameter or grain size number. Grain size number can be calculated or compared to standardized grain size charts.

To make the grain boundaries visible, sample preparation must be carried out. Grinding, polishing and etching are necessary steps for good results.

PRECiV software provides both intercept and planimetric measurements, covering the latest version of the most commonly used standards in academic and industrial environments.

Since these are materials solutions of the software, a guided workflow with batch processing is available as well as the ability to save the settings. However, it is also possible to manually intervene if necessary, e.g. if intersections of the measuring grid with the grain boundaries are not correctly detected or are falsified by inclusions within the grains.

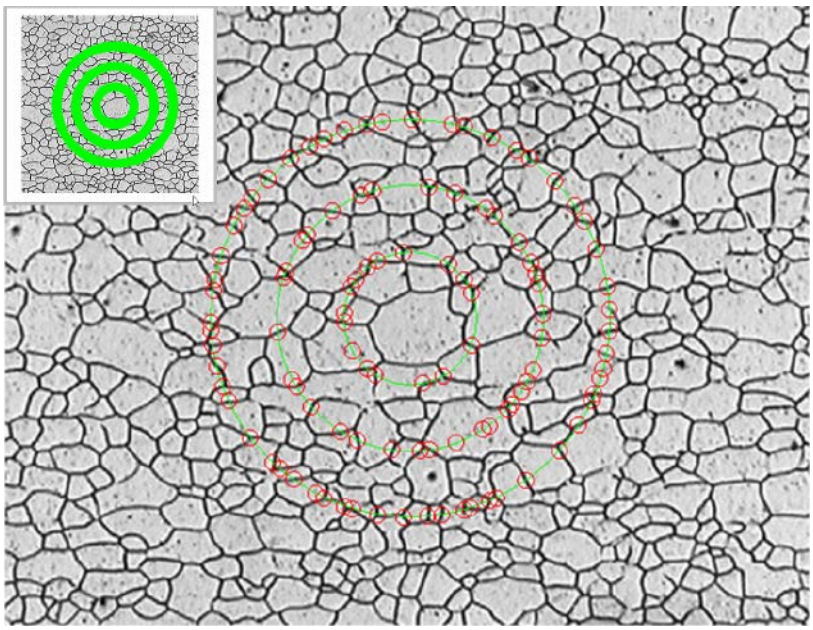

Figure 2: Example grains intercept measurement with circular measuring grid

In the "Grains Intercept" solution different measuring grids help to consider the geometry of the micro structure like the following examples show:

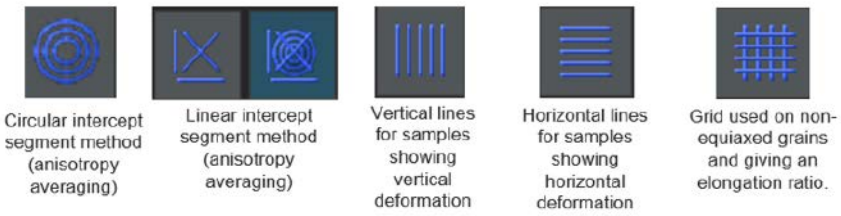

Circular intercept segment method (anisotropy averaging)

Linear intercept segment method (anisotropy averaging)

Vertical lines for samples showing vertical deformation

Horizontal lines for samples showing horizontal deformation

Grid used on non-equiaxed grains and giving an elongation ratio.

Due to the averaging over the pattern length, the software solution delivers precise results (+/– 0.1 G). The precision is always a function of the number of images measured – batch processing can speed up the analysis. In addition, various available patterns make it possible to obtain the elongation value for non-equiaxed microstructures. So for Grains Intercept measurements, PRECiV provides a single value G, the mean intercept length, the average number of intercepts, the number of intercepts per unit length (1/mm) and if measured, the value for the elongation.

In contrast to the intercept method, "Grains Planimetric" refers to the entire area of grains. After reconstruction, the grain boundaries—the area of all grains—is calculated. Originally, a test circle was used for this purpose, as the first analyses were carried out in the eyepieces of the microscope.

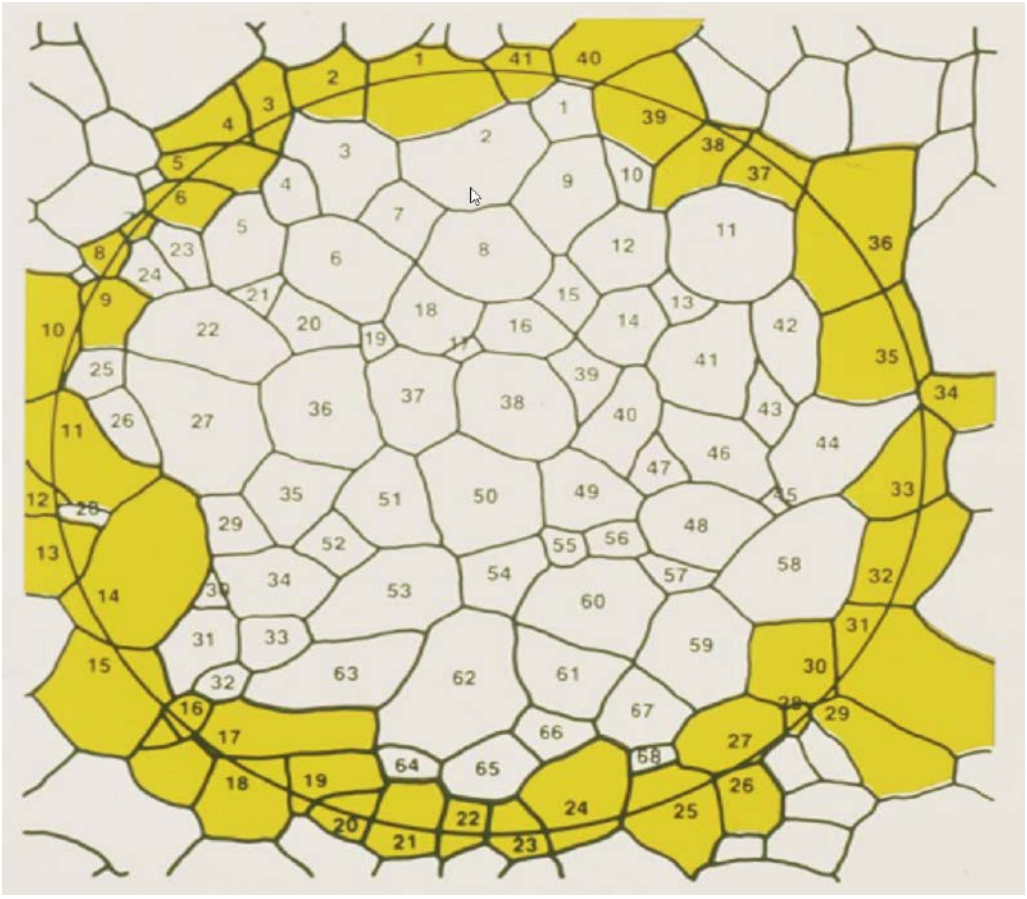

Figure 3: Historical test circle for planimetric analysis

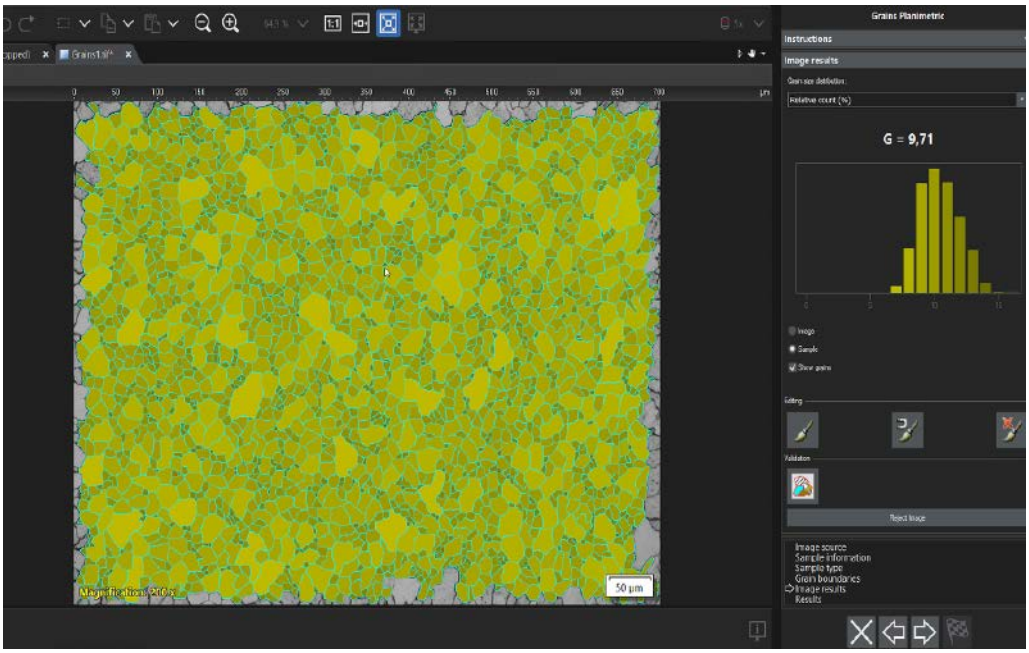

Figure 4: Grains Planimetric analysis in PRECiV

In our modern world, we can leave that approach and use the entire image instead.

The advantage of the planimetric method is that it provides the full information about all grains, the grain size distribution on the evaluated area and geometric information like elongation. A second phase can be considered and evaluated.

DENDRITE ARM SPACING

Dendrite arm spacing is an interesting method. Originally known from light metals like Aluminum and Magnesium, it is an important analysis method for additive manufactured materials. Due to the locally different energy input on the surface during manufacturing process, the grains in the mate-

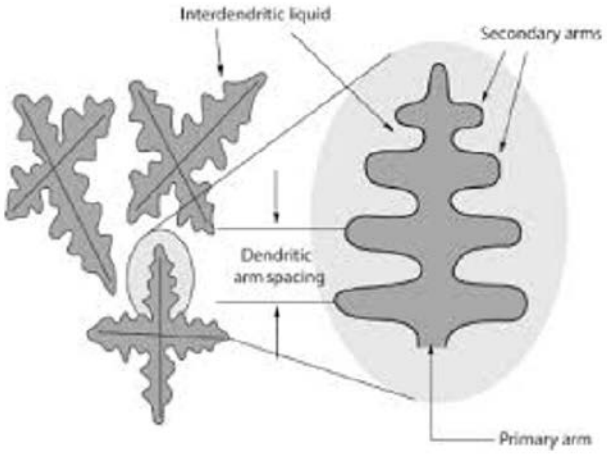

Figure 5: Crystal growth in dendrite form

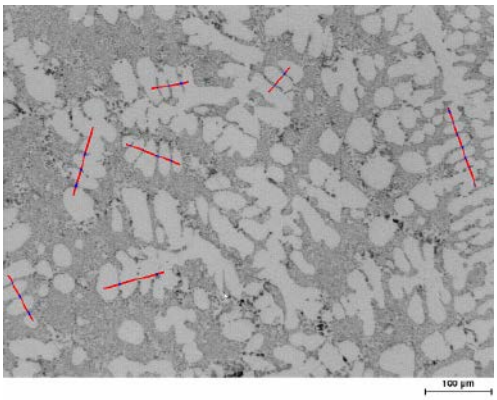

Figure 6: Manual measurement of Dendrite Arm Spacing

rial often grow unevenly. That results in dendrites, a tree-like branching structure.

The monitoring of the solidification time in such alloys is a key factor to improved mechanical properties (like tensile strength and elongation). The Dendrite Arm Spacing is directly connected to the solidification time.

With a known Dendrite Arm Spacing (DAS) and a specific material-dependent constant it is easy to calculate the solidification time.

A precondition for a dendrite arm spacing measurement is that the dendrites differ from the rest of the sample, for example by contrast. In this case, dendrites will have different intensity values from the rest of the sample, making automatic analysis of the image possible. Setting thresholds for detecting the dendrites is a good and quick solution in this case. On the other hand, a manual measurement can be conducted.

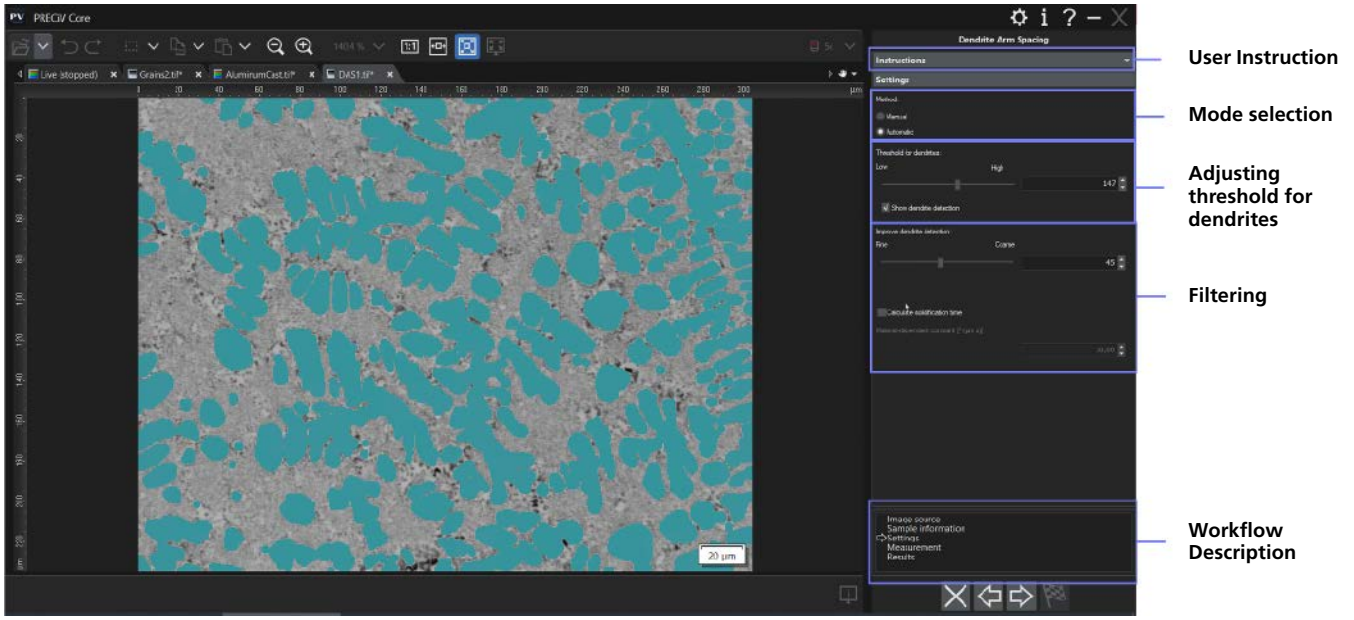

Figure 7: Automatic measurement using threshold inside of the guided workflow